Modeling of Nonlinear Medical Diagnostic Ultrasound

ISBN 978-90-9023462-5
NUR 950

Cover illustration: Gaussie by G. Huijssen – Artist's impression of a medical acoustic wave

Figure 1.1a depicts a GE Vivid3^{TM} echo system. Reproduced with kind permission of General Electric Healthcare Nederland.
The origin of Figure 1.2a is unknown. Please inform the author in case of any copyright issues.

Printed in The Netherlands on FSC Mixed Sources paper
by PrintPartners Ipskamp B.V., Enschede

MODELING OF NONLINEAR MEDICAL DIAGNOSTIC ULTRASOUND

Proefschrift

ter verkrijging van de graad van doctor
aan de Technische Universiteit Delft,
op gezag van de Rector Magnificus prof. dr. ir. J.T. Fokkema,
voorzitter van het College van Promoties,
in het openbaar te verdedigen
op dinsdag 14 oktober 2008 om 10:00 uur
door

Jacobus HUIJSSEN

elektrotechnisch ingenieur
geboren te Oud-Beijerland

Dit proefschrift is goedgekeurd door de promotor:
Prof. dr. ir. P.M. van den Berg

Copromotor: Dr. Ir. M.D. Verweij

Samenstelling promotiecommissie:

Rector Magnificus	voorzitter
Prof. dr. ir. P.M. van den Berg	Technische Universiteit Delft, promotor
Dr. ir. M.D. Verweij	Technische Universiteit Delft, copromotor
Prof. dr. ir. A. Gisolf	Technische Universiteit Delft
Prof. V.F. Humphrey, PhD	University of Southampton, UK
Prof. dr. ir. N. de Jong	Universiteit Twente
Prof. dr. ir. C. Vuik	Technische Universiteit Delft
Dr. ir. M.R.T. Roest	VORtech Computing

Acknowledgements:

This research was financially supported by the Dutch Technology Foundation STW (06790).

This research was sponsored by the ICT Delft Research Centre.

This work was sponsored by the Stichting Nationale Computerfaciliteiten (National Computing Facilities Foundation, NCF) for the use of supercomputer facilities, with financial support from the Nederlandse Organisatie voor Wetenschappelijk Onderzoek (Netherlands Organization for Scientific Research, NWO).

Aan de belangrijkste personen in mijn leven:

Mijn ouders
Elise, maatje
Fig. 1.1b

Contents

1 Introduction **1**

1.1 Medical diagnostic ultrasound imaging 2

1.2 Nonlinear acoustics and its application to echography 4

1.3 Modeling of nonlinear medical ultrasound 7

1.4 This thesis 10

2 Basic equations for the acoustic field in nonlinear media **13**

2.1 Basic considerations regarding the continuum model 14

2.2 Acoustic field equations 17

2.3 Acoustic constitutive equations 21

2.4 Second-order nonlinear wave equation 27

2.5 Discussion 31

3 Solution of the basic nonlinear equations employing the INCS method **35**

3.1 Neumann iterative solution 36

3.2 Green's function method 37

3.3 Discretization at the Nyquist rate 38

3.4 Filtering of the Green's function 53

3.5 Evaluation of the sources 57

3.6 Discussion 64

4 Application of the INCS method to one-dimensional wave problems 69

4.1 Configuration 69

4.2 Implementation 71

4.3 Numerical simulations 73

4.4 Discussion 86

5 Application of the INCS method to three-dimensional wave problems 89

5.1 Configuration 89

5.2 Implementation 92

5.3 Numerical simulations 98

5.4 Discussion 126

6 Experimental verification of the INCS method 129

6.1 Experimental setup 129

6.2 Measurements and comparison 131

6.3 Discussion 143

7 Conclusions and discussion 145

7.1 Conclusions 145

7.2 Discussion 147

A Evaluation of the lossless Burgers equation based on a time-base transformation 151

B Computational approaches for the efficient evaluation of the INCS method in case of large-scale problems 155

C Derivation of the linear acoustic field of a cylindrical piston transducer causing a pressure jump 165

D Extension of the INCS method to media with attenuation of a frequency power law type **171**

E Extension of the INCS method to media with inhomogeneity **187**

Bibliography **195**

Samenvatting **203**

Acknowledgements **207**

About the author **209**

Publications **211**

Chapter 1

Introduction

This thesis is concerned with the formulation, implementation and validation of a numerical method that may contribute to the design of new medical diagnostic ultrasound equipment. The method predicts the nonlinear acoustic wavefield emitted by an ultrasound transducer and thus assists in understanding the physical phenomena of nonlinear acoustic propagation and in estimating the performance of new transducer designs and imaging methods. The method is referred to as the Iterative Nonlinear Contrast Source (INCS) method, and it is based on a Green's function representation of the forward source problem. This formulation yields a convolution integral over the spatiotemporal source domain. The convolution integral is evaluated by means of an efficient numerical method that employs an equidistantly sampled grid with a coarse discretization.

This introduction discusses the background and context of this thesis. In Section 1.1, we introduce the application of medical diagnostic ultrasound. Section 1.2 is concerned with the phenomenology of nonlinear acoustics and its utilization in medical ultrasound. Section 1.3 treats the numerical modeling of nonlinear acoustic fields, the challenges to be met, the work that has been done by other researchers and the aim of the current research. Finally, Section 1.4 gives an overview of the subjects treated in this thesis.

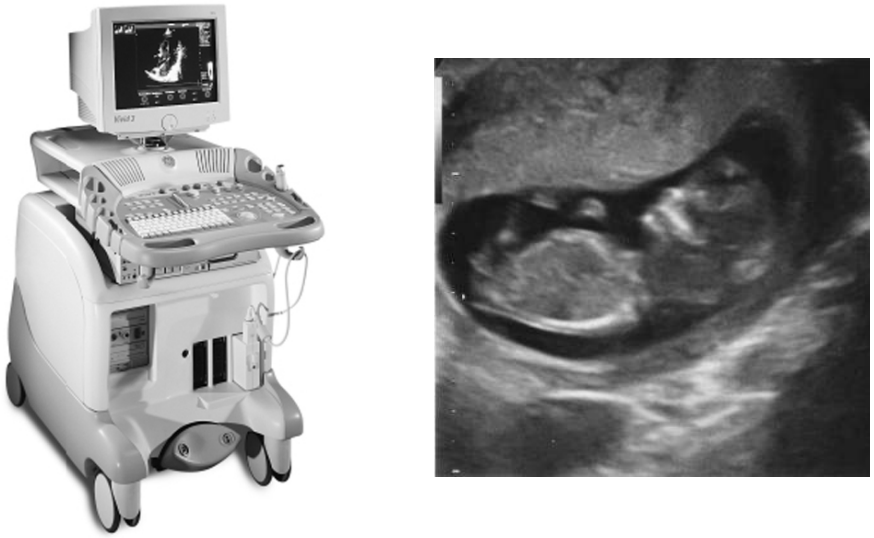

(a) (b)

Figure 1.1. (a) Picture of an echography machine.
(b) Echography image of an 11 week fetus.

1.1 Medical diagnostic ultrasound imaging

In the last 40 years, the application of high-frequency acoustic waves, or ultrasound waves, for echographic purposes has become an all-round standard in the medical diagnostic practice [65]. The basic principle behind this application is the generation of an acoustic field in the human body and the reception of the wavefield coming back from reflections on tissue layers and body structures, or from volume scattering within the tissue. With the information that is present in this backscattered wavefield, an image can be constructed of the inner organs like the heart, liver and spleen, or of a fetus in the uterus, thus uncovering their structures and (dys)functionalities that are of interest to the clinician. An example of an echography machine and a typical echography image of a fetus are shown in Fig. 1.1. Compared to other imaging modalities like X-ray, Computerized Tomography (CT) and Magnetic Resonance Imaging (MRI), the main advantages of echography are its versatility, its ability to present a real-time and moving image, its relatively low cost and its harmlessness. It has been estimated that in the year 2000, each week 5 million ultrasound examinations were performed world-

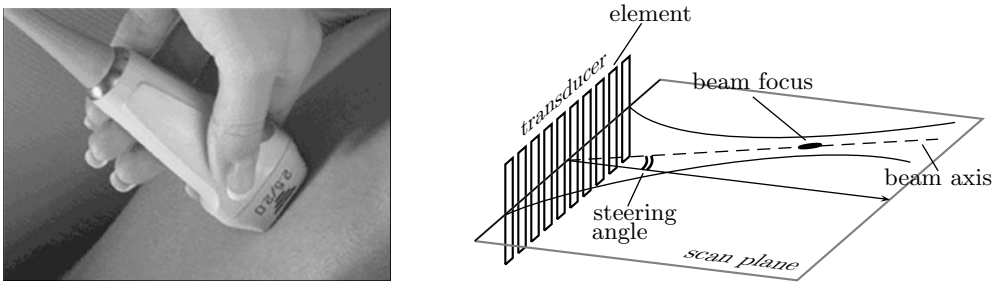

Figure 1.2. (a) Picture of a medical phased array transducer.
(b) Schematic configuration of the phased array transducer, showing a row of active elements and a sketched profile of a steered and focused ultrasound beam in the scan plane.

wide [65]. In obstetrics, echography is the single preferred imaging method. Many parents have stood in wonder looking at their yet unborn child and seeing the beat of its heart and the activities that it is employing. In cardiography, ultrasound has enabled cardiologists to diagnose a score of heart diseases and abnormalities, thus saving thousands of lives each year. And in many other applications, echography has provided a means for obtaining information on the patient's health without the need for an alternative technique that is more inconvenient for the patient or more elaborate for the clinician.

In most present-day echography equipment, an ultrasound image is obtained by scanning an acoustic beam over a certain plane through the body. Most often, the acoustic beam is generated with a phased array transducer, which is a piezoelectric device consisting of up to 256 separately excitable elements arranged in a row. The phased array excites a wavefield that can be focused and steered in any desired direction in the so-called scan plane, as is shown in Fig. 1.2. The size of a typical transducer is in the order of centimeters and it can be easily operated with one hand. For this type of transducer, the employed ultrasound frequencies are in the range of $1 - 15$ MHz. The spatial resolution of the ultrasound image and the penetration depth of the acoustic beam are both dependent on the imaging frequency, in such a way that a higher imaging frequency yields a higher resolution but a lower penetration depth. At a frequency of 1 MHz, the resolution is about 3 mm and the penetration depth is in the range of $10 - 20$ cm. For intravascular

ultrasound, the imaging frequency can go up to 30 MHz, giving a resolution of about 0.1 mm and a penetration depth up to 5 mm. The used imaging frequency is thus determined by the specific application and the transducer type. The maximum amplitude of the acoustic pressure fields used in echography is generally in the range of $0.1 - 1$ MPa.

The recent decade has seen a number of revolutions in echography that have further enhanced its applicability and imaging quality. Firstly, the employment of contrast agents has given a new dimension to the echo image by showing the degree of perfusion of the tissue. Secondly, a spatial dimension has been added to the ultrasound image by the development of three-dimensional echography methods, which are able to scan an entire volume instead of only a certain scan plane. Finally, the utilization of the nonlinear distortion of the ultrasound field has resulted in a significant improvement of the image quality. The latter development will be discussed in more detail in the next section.

1.2 Nonlinear acoustics and its application to echography

The mathematical-physical equations that describe the propagation of acoustic waves are inherently nonlinear. This nonlinearity is caused by field-dependent medium behavior that shows up in the derivatives as well as in the medium parameters in the acoustic equations. For most phenomena and applications involving acoustic wavefields, the amplitude of the acoustic disturbances is relatively small, and therefore a linear approximation of the nonlinear equations yields sufficiently accurate results. However, for increasing amplitude and frequency the nonlinear terms may not be neglected anymore, and the resulting nonlinear distortion grows from just observable to strong.[1]

Consider an acoustic wavefield that is excited by a certain source. In the case of linear propagation, a scaling of the excitation amplitude by a certain factor results in a scaling of the wavefield amplitude by the same factor, and the wavefield of a combination of several sources is equal to a superposition of the wavefields of the separate sources. For a plane-wave, homogeneous and lossless situation, the linear propagation of an acoustic

[1] In parallel to the linear description of sound propagation being referred to as small-signal, the nonlinear description is often referred to as *finite amplitude*.

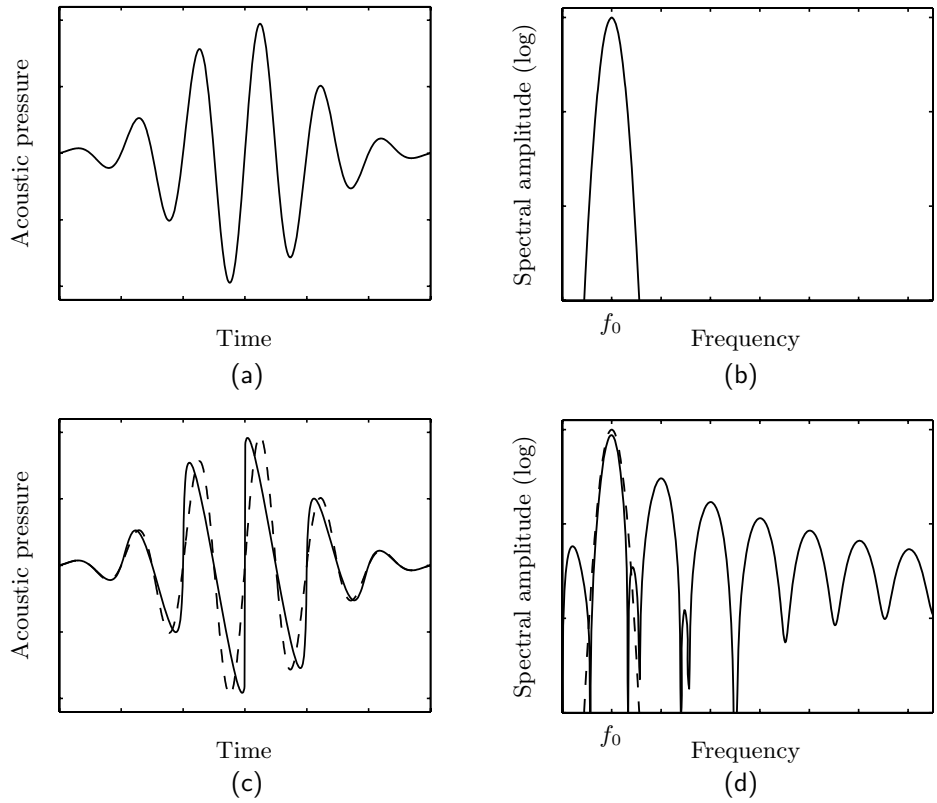

Figure 1.3. Pulse shape of a plane wave in a lossless, homogeneous medium at the source (dashed) and at a certain distance from the source (solid), under linear and nonlinear propagation. (a) Time signature, linear propagation. (b) Frequency spectrum, linear propagation. (c) Time signature, nonlinear propagation. (d) Frequency spectrum, nonlinear propagation. In (b) and (d), f_0 is the center frequency of the source pulse.

pulse with a certain amplitude and center frequency over a certain distance yields a waveform which shape and spectrum remain the same. This is shown in Figs. 1.3a and b, where the pulse shape at a certain distance completely overlaps the pulse shape at the source. In the case of nonlinear propagation, the scaling and superposition rules do not apply, and we will observe a cumulative deformation of the pulse shape. This deformation depends on the amplitude and the center frequency of the excitation, as well as on the propagation distance. An example of a rather strong nonlinear deformation can be seen in Figs. 1.3c and d. In the spectrum we observe that besides the fundamental frequency component, which is located around the center

frequency, also a number of harmonic frequency components occur around multiples of the center frequency, and that a frequency component appears between zero and the center frequency. Examples of phenomena and applications for which nonlinearity is important can be found in aircraft noise, underwater acoustics, parametric arrays, non-destructive testing and medical therapeutic and diagnostic ultrasound. The waveform distortion may lead to shock formation, increased attenuation of the acoustic wave and the consequent increased heating of the medium. Other nonlinear phenomena are scattering of sound by sound and acoustic streaming [32]. Cavitation effects can also be considered as nonlinear acoustic behavior, but they are generally treated as a separate phenomenon.

It has been recognized in the 1980's that for the frequencies and magnitudes that are common in medical diagnostic ultrasound, the occurring acoustic fields undergo an observable cumulative nonlinear distortion when propagating through tissue [21, 50]. Originally considered as a side-effect when studying the nonlinear response of contrast agents, in the 1990's it was realized that this effect could be employed to improve the imaging quality of echography [4, 76]. The current imaging modality based on nonlinear distortion is known as Tissue Harmonic Imaging (THI), and it constructs an echo image by specifically considering the second harmonic frequency component of the nonlinear wavefield. Since its introduction THI has gained rapid acceptance and popularity, and currently all echo machines are able to image with the THI which has become the first choice in many echography examinations. The improved image quality of THI is attributed to an improved beamforming compared to the traditional fundamental imaging [20, 65].

Recently, Bouakaz and De Jong [7] have suggested an approach to further benefit from nonlinear acoustic propagation in medical ultrasound by taking into account the third till the fifth harmonics. This modality is called SuperHarmonic Imaging (SHI). It is a topic of ongoing research to develop a dedicated phased array transducer and imaging method that enable the full exploitation of the possibilities of SHI. For this research, a method for the accurate prediction of the nonlinear acoustic field excited by phased array transducers with an arbitrary geometry and element steering is of vital importance. The lack of a suitable method to assist in the further development of SHI has motivated the research described in this thesis.

1.3 Modeling of nonlinear medical ultrasound

In order to understand the character of nonlinear wave propagation and to predict its behavior, numerical models are essential tools. The cumulative nonlinear distortion effect cannot be understood as an isolated phenomenon, but it depends on the magnitude and shape of the field on each position along the propagation path between the source and the point of observation. In order to correctly reproduce the nonlinear acoustic field, the source configuration and excitation, and all effects that significantly influence the propagation of the wave need to be accounted for in a realistic and consistent way. With the rise in computational speed and memory size, numerical modeling of nonlinear wave propagation has become feasible for situations of increasing size and complexity.

The research described in this thesis aims at the accurate prediction of the pulsed acoustic pressure field generated by a medical diagnostic phased array transducer in a nonlinear acoustic medium. The nonlinear distortion involved in this application is weak to moderate. Special interest goes to the development of higher harmonic frequency components that arise during the nonlinear propagation of the acoustic pulse through the medium. Since these components may be very small compared to the linear field, the nonlinear pressure field must be predicted with great accuracy. The source may have a complex geometry that requires the resulting wavefield to be considered in a three-dimensional configuration. Since the shape of the excited acoustic pulse strongly determines the nonlinear distortion of the field, we need to evaluate the transient wavefield. For these reasons the resulting computational domain consists of four dimensions. In view of the frequencies and the typical sizes and durations employed in medical diagnostic applications, this is a large-scale domain (e.g. in the order of 100 wavelengths/periods in each spatiotemporal direction). To enable the study of wide-angle effects like grating lobes and steered acoustic beams, the field prediction needs to be accurate for nonlinear acoustic fields propagating in arbitrary forward directions and observed from arbitrary angles. The acoustic properties of soft tissue, which is the medium for which the ultrasound equipment is ultimately used, are in the order of the properties of water, except for the acoustic attenuation which is generally much larger in tissue than in water [65]. Nevertheless, water is considered as a good first approximation of human tissue. Medical transducers are generally designed on the basis of their performance in a water tank, and therefore in this thesis water is taken as the propagation medium.

In the recent decades, several groups of researchers have invested their effort in developing a numerical method that meets the challenge of accurately predicting the nonlinear ultrasound field. Most currently used 3D nonlinear acoustic models assume forward-wave propagation and are based on an evolution equation that, starting from a certain source plane, march the solution from plane to plane in the main direction of propagation. Within this group of models, a first line of research is based on the Kuznetsov-Zabolotskaya-Khokhlov (KZK) equation [45, 84]. The KZK equation is a nonlinear wave equation derived from the basic nonlinear acoustic equations under a parabolic approximation [32], and it accounts for the nonlinear terms up to the second order in the field quantities. Because of its parabolic approximation it is valid for beams with quasi-plane wavefields. For this reason, the region of validity is generally taken not too far off the main transducer axis and not too close to the source. One numerical implementation of the KZK equation, called the Bergen code [1], was originally designed to deal with circular transducers, and subsequently it has been adapted to cope with non-axisymmetric sources [5, 11]. A similar development applies to the Texas code [46], which has been adapted by Bouakaz et al. [8, 9], Khokhlova et al. [40, 41], and Yang and Cleveland [82] to deal with rectangular and phased-array transducers. The latter two versions allow for tissue-like attenuation, and Cleveland and Jing [14] further extended the last version to deal with slightly inhomogeneous media as well. A second line of forward-wave models uses a phenomenological approach and splits each marching step into separate operations that account for the effects of diffraction, absorption and nonlinearity. The diffraction step is incorporated without using a paraxial approximation. Based on the work of Christopher and Parker [12, 13], Tavakkoli et al. [66] improved the algorithm and Zemp et al. [85] further developed it for use with non-axisymmetric sources and tissue-like attenuation, employing an angular spectrum approach. Recently, Wojcik et al. [44, 81] proposed a similar approach, where the nonlinear step is performed using a wave envelope expansion of the field. Finally, Varslot and Taraldsen [72] developed a forward-wave propagating method for heterogeneous media, and within this context they compared both a paraxial and an angular spectrum approach. For the nonlinear propagation step, all of the above authors use a plane-wave solution in the time domain or in the frequency domain, thus assuming that the main nonlinear distortion is in the direction of the transducer axis. Although at each diffraction step the nonlinear distortion is spreaded again, this may not be accurate for wavefields that are strongly focused or that propagate at an angle significantly different from the transducer axis.

A correction method has been proposed by Christopher and Parker [12], and Fox et al. [26] implemented a KZK method with a steered propagation axis. However, when studying wide-angle phenomena like grating lobes or propagation through heterogeneous media, we need to account for nonlinear distortion in all directions. A method that handles nonlinear propagation in all forward directions was proposed by Varslot et al. [71], but this method is limited by its quasilinear approximation.

Apart from the forward-wave propagation models, a number of models has been developed for full-wave nonlinear propagation of acoustic fields. Because of the computational effort involved, these models have been limited to 2D cartesian or cylindrical implementations. Sparrow and Raspet [60] and Yano and Inoue [83] studied nonlinear effects in air and in ideal gas, respectively, both with a finite difference solution of a set of first-order conservation laws. Liebler et al. [30, 48] developed a similar approach for transient fields in water and tissue. Hallaj and Cleveland [31] employed a finite difference method to solve the Westervelt equation [1, 32], which is another second order nonlinear wave equation derived from the basic acoustic equations [32]. Wojcik et al. [80] and Hoffelner et al. [34] based their solution on a finite element approach. None of these models have an assumed directionality in the wave propagation or in the nonlinear distortion. Whereas most authors include nonlinear medium behavior in a constitutive equation and directly obtain the nonlinear field by solving the differential equations, Hoffelner used an iterative correction of the linearized wave problem to obtain the nonlinear field. A problem of the mentioned full-wave models is the large number of points per wavelength and per period (referred to as PPW) in space and time that is needed for an accurate computation. The Nyquist-Shannon sampling theorem for bandlimited signals prescribes a minimum of 2 PPW at the highest harmonic frequency component of interest. Finite Difference and Finite Element methods need a much higher number of PPW, and this makes these methods particularly unfavorable for application to large-scale, three-dimensional problems. The best effort in this respect has been made by Wojcik et al. [79], who present a pseudospectral method that handles the spatial differentiation in the k-space domain and includes propagation in inhomogeneous media. It needs 4 PPW in the spatial dimensions, and with a Courant number of 0.2 it employs at least 20 PPW in the temporal dimension.

The numerical method developed in this thesis, the Iterative Nonlinear Contrast Source (INCS) method, can be classified as a full-wave model, and

it does not suffer from an assumption on the directionality of the wavefield as made with all described forward-wave models. The INCS method employs an integral equation formulation of the wave problem, instead of a differential equation formulation, which is the basis of all other methods. For the solution of the integral equation, the INCS method applies an iterative scheme that involves the spatiotemporal convolution of a contrast source with a Green's function. The issue that full-wave models usually require a large number of points per wavelength is resolved by employing an approach that enables a discretization of the convolution integral at the limit of 2 PPW in all dimensions. Because of these characteristics, we believe that the developed numerical method is a worthwhile contribution to the challenge of predicting the nonlinear ultrasound wavefield from a medical diagnostic transducer. The method is capable of handling a four-dimensional spatiotemporal domain with a size in the order of 100 wavelengths/periods in each dimension. The source is included as a plane geometry with an arbitrary amplitude and delay time distribution across the source plane, exciting a pulsed waveshape. In the derivation, the propagation medium is considered lossless in order to focus our full attention to the accurate incorporation of the nonlinear distortion effect. This approximation makes the method fit for nonlinear propagation in water. Due to the general formulation, the method may be easily extended to deal with, e.g. tissue-like attenuation[2] and inhomogeneities of the medium.[3]

1.4 This thesis

This thesis describes in detail the development of the INCS method. Here we give an overview of the subjects treated in this thesis.

In Chapter 2, we present the formulation of the mathematical-physical basis of nonlinear acoustic wave phenomena. We derive a pair of first order, nonlinear basic equations and the accompanying constitutive equations, and we show that under certain assumptions these basic equations simplify to a nonlinear wave equation that is identified as the lossless Westervelt equation with a source term.

In Chapter 3, we discuss the solution of the Westervelt equation by the Iterative Nonlinear Contrast Source (INCS) method. The method is based on an iterative scheme that addresses the nonlinear terms in the Westervelt

[2]See Appendix D.
[3]See Appendix E.

equation as contrast sources. The recurring linear field problem is solved with a Green's function method, which yields a convolution integral that is approximated by a discrete convolution sum. The latter can efficiently be evaluated by means of a numerical method based on the Fast Fourier Transform (FFT). Special interest goes to the discretization of the convolution integral, and an approach is presented that enables a coarse discretization in all spatiotemporal dimensions.

In Chapter 4, we discuss the implementation of the INCS method for one-dimensional nonlinear wave problems, and we present simulation results for linear and nonlinear wave problems. We will compare these results with those from analytical solutions and from an alternative numerical method.

In Chapter 5 we discuss the implementation of the INCS method as applied to three-dimensional nonlinear wave problems, and we compare the model results with several numerical methods that have been discussed in Section 1.3.

In Chapter 6, we describe laboratory measurements that we have performed for the validation of the INCS method.

Chapter 7 completes this thesis with a presentation of the final conclusions that may be drawn from the described research, and the discussion of a number of perspectives for future development.

Chapter 2

Basic equations for the acoustic field in nonlinear media

We start our study with the basic equations of nonlinear acoustic wave propagation, viz. the pertaining field equations and constitutive equations. These equations form the relations between the basic quantities that describe the acoustic wavefield. The field equations describe the fundamental relations between the basic wavefield quantities in a continuum, and they have the form of conservation laws. The constitutive equations specify the behavior of the specific medium that constitutes the continuum. Together, they form a complete set of equations for the acoustic field. As will become clear, the nonlinearity in the equations is caused by field-dependent medium behavior that shows up in the derivatives as well as in the medium parameters in the constitutive equations. In Section 2.1 we set up the framework in which we will derive our equations. Next, in Section 2.2 we study the basic field equations with special attention to the nonlinear aspects. In Section 2.3 we discuss a number of constitutive equations for different media. The field equations and a particular set of constitutive equations lead to a set of first order partial differential equations, from which in Section 2.4 we derive a second order nonlinear wave equation that is accurate up to the second order in the wavefield quantities. In the closing Section 2.5 we place some remarks on specific aspects of the derivation.

Throughout this chapter, we employ the subscript notation for all vec-

tor quantities. For instance, a vector is written as a_j, where the subscript j is an index variable that denotes the different components of the vector $\boldsymbol{a}$. Therefore, in a threedimensional space the index variable can vary from 1 to 3. Moreover, we use the Einstein summation convention, which states that multiplication of two quantities with an identical subscript variable signifies an addition of the products of components with an identical subscript; e.g. for the vectors a_i and b_j, in a threedimensional space we have

$$a_k b_k = a_1 b_1 + a_2 b_2 + a_3 b_3. \tag{2.1}$$

We will adopt the following shorthand notations for the partial temporal and spatial derivatives:

$$\partial_t \, \cdot = \frac{\partial \, \cdot}{\partial t}, \tag{2.2}$$

$$\partial_j \cdot = \frac{\partial \, \cdot}{\partial x_j}. \tag{2.3}$$

The first three sections of this chapter draw heavily on the studies on continuum mechanics by De Hoop [17] and by Thompson [67].

2.1 Basic considerations regarding the continuum model

The acoustic field equations and the acoustic constitutive equations will be derived under the *continuum hypothesis*, formulated as follows:

Assumption 1 *The field quantities and medium parameters that describe the macroscopic acoustic phenomena vary piecewise continuously with position.*

When studied on a microscopic scale, all physical media exhibit a non-continuous structure consisting of discrete atoms or molecules interacting with each other. Since these interactions determine the acoustic behavior of the medium, the basis of acoustic phenomena is of a discrete nature. However, the scale at which the acoustic phenomena occur, i.e. the macroscopic scale, is so large that the observations always involve the statistical, spatial averages of a large number of discrete particles or interactions, and these averages are by Assumption 1 considered to behave as piecewise continuous

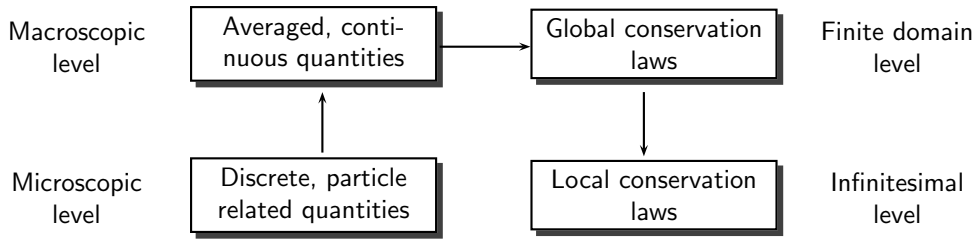

Figure 2.1. Procedure to derive continuous quantities and their local interrelations from discrete particle systems.

quantities. A typical microscopic spatial dimension in gases is the mean free path length, which is in the order of 10^{-7} m for gases under normal condition. For liquids, we can use as a typical microscopic spatial dimension the intermolecular spacing, giving an order of 10^{-10} m. The wavelengths of the ultrasound wavefields we are concerned with are in the order of 10^{-3} m in liquids. The vast difference between these two scales ensures that the averaging may always involve sufficient particles or interactions to assure the validity of the continuum hypothesis while the occupied domain is still small on the macroscopic scale. For these spatially averaged quantities we will formulate conservation laws in the form of global laws over a certain domain. And because of the continuity of the field quantities and medium parameters, we can then consider them on an infinitesimal scale by reducing the global laws to local conservation laws in the form of partial differential equations. This procedure is outlined in Fig. 2.1.

The continuum is spanned in a Euclidean background space $\mathbb{R}^3$, where a Cartesian right-handed reference frame with orthonormal base vectors $\boldsymbol{i}_x$, $\boldsymbol{i}_y$, $\boldsymbol{i}_z$ is given. The position vector $\boldsymbol{x}$ of a point, or x_j in subscript notation, is denoted as

$$\boldsymbol{x} = x_1\boldsymbol{i}_x + x_2\boldsymbol{i}_y + x_3\boldsymbol{i}_z. \tag{2.4}$$

In the continuum, we define a continuous number density of particles, denoted by $n(x_j, t)$ [m^{-3}]. As the particles are allowed to move through space, the number density varies with space and time, and we can observe in each point an average *drift velocity* $v_k(x_j, t)$ [$\mathrm{m\,s}^{-1}$]. When each particle is assigned a mass m [kg], we obtain a continuous mass distribution in each point, denoted by the *mass density* $\rho(x_j, t)$ [$\mathrm{kg\,m}^{-3}$]. The flow of mass in each point is denoted by the *mass flow density* $\Phi_k(x_j, t)$ [$\mathrm{kg\,m}^{-2}\mathrm{s}^{-1}$]. In the continuum, we may have different types of particles, each type identified by a superscript

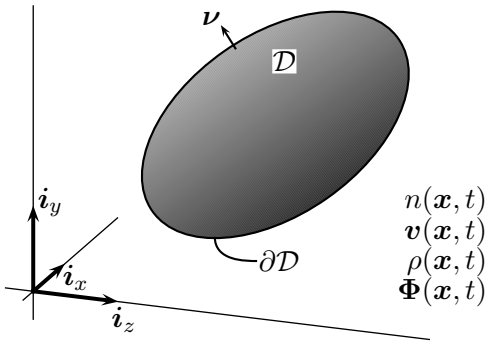

Figure 2.2. Background space $\mathbb{R}^3$ with base vectors $\boldsymbol{i}_x$, $\boldsymbol{i}_y$ and $\boldsymbol{i}_z$, the continuous quantities n, $\boldsymbol{v}$, ρ and $\boldsymbol{\Phi}$ defined within $\mathbb{R}^3$, and the material volume $\mathcal{D}$ with its boundary $\partial\mathcal{D}$ and unit normal $\boldsymbol{\nu}$.

B and distinguished by its particle mass m^B. The behavior of the particles with mass m_B is described by the set of quantities $\{n^B, \rho^B, v_k^B, \Phi_k^B\}$. The relations between the quantities describing the behavior of the continuum as a whole and their componentwise counterparts are

$$n = \sum_B n^B, \tag{2.5}$$

$$\rho = \sum_B \rho^B = \sum_B m^B n^B, \tag{2.6}$$

$$v_k = [\sum_B n^B]^{-1} \sum_B n^B v_k^B, \tag{2.7}$$

$$\Phi_k = \sum_B \Phi_k^B = \sum_B \rho^B v_k^B. \tag{2.8}$$

Examples of media where the different components play a distinct role are two-phase media like bubbly liquid or porous rock. In the current thesis, we will restrict ourselves to media where all components share the same average drift velocity $v_k^B = v_k$, which assumption is known as *common collective motion*:

Assumption 2 *Particles with different mass m^B everywhere share the same average drift velocity v_k.*

This assumption ensures that we only have to account for the total quantities instead of all their componentwise counterparts. A consequence that will be

employed in the upcoming discussion is the fact that under this assumption we have $\Phi_k = \rho\, v_k$.

An important concept within the continuum model is the *material volume*, which is a volume that follows a fixed, identified collection of particles. The material volume, denoted as $\mathcal{D}(t)$, can vary continuously in time with respect to its shape, position and volume. The boundary of the material volume is denoted as $\partial\mathcal{D}(t)$, and since $\mathcal{D}(t)$ should follow a specific amount of matter, there is supposed to be no transport of matter across $\partial\mathcal{D}(t)$. On the microscopic level, this could not hold in a strict sense, since the molecular diffusion would give rise to a fading of the boundary and after sufficient time the material volume would lose its identity. We will restrict ourselves to treating the material volume on the macroscopic level, using only averaged or global quantities without reference to a specific identity of the particles. Thus, we define the material volume as a certain domain $\mathcal{D}(t)$ at $t = t_0$ within the continuum, whose boundary $\partial\mathcal{D}(t)$ follows the average drift velocity v_k. With Assumption 2 we can then conclude that *on average* there is no mass flow across the boundary.

2.2 Acoustic field equations

2.2.1 Reynold's transport theorem

When we formulate conservation laws for the continuum, we will consider the rate of change over time of some quantity, integrated over a certain domain. Both the domain, in this thesis always chosen to be the material volume $\mathcal{D}(t)$, and the quantity, being some continuous function $\Psi(x_j, t)$ defined in $\mathcal{D}(t)$, may change with respect to time, and therefore the total time derivative consists of two terms, giving *Reynold's transport theorem*

$$\mathrm{d}_t \int_{\mathcal{D}(t)} \Psi \,\mathrm{d}V = \int_{\mathcal{D}(t)} \partial_t \Psi \,\mathrm{d}V + \int_{\partial\mathcal{D}(t)} \Psi\, v_k\, \nu_k \,\mathrm{d}A, \tag{2.9}$$

where d_t denotes the total time derivative and ν_k is the unit normal to $\partial\mathcal{D}(t)$, pointed outwards. The quantity $\Psi(x_j, t)$ is a scalar field, but Eq. (2.9) is equally valid for a vector field, which would be denoted by $\Psi_m(x_j, t)$.

2.2.2 Gauss' divergence theorem

A mathematical theorem that will be used extensively to derive the local equations from their global forms is *Gauss' divergence theorem*. This theorem gives the relation between the integration of a quantity over a domain and its integration over the domain boundary. In this thesis, the domain is always chosen to be the material volume $\mathcal{D}(t)$, and the quantity is a continously differentiable function $\Psi(x_j, t)$ defined in $\mathcal{D}(t)$. Then Gauss' divergence theorem states

$$\int_{\mathcal{D}(t)} \partial_k \Psi \, \mathrm{d}V = \int_{\partial\mathcal{D}(t)} \Psi \, \nu_k \, \mathrm{d}A. \tag{2.10}$$

The quantity $\Psi(x_j, t)$ may be a (continously differentiable) vector field as well, denoted by $\Psi_m(x_j, t)$, or a tensor field, denoted by $\Psi_{mn}(x_j, t)$.

2.2.3 Conservation of volume

A fundamental conservation law describing the behavior of the continuum lays down its deformation. As we are only interested in acoustics, which is concerned with compressional waves, we will restrict ourselves in deriving a relation for volume dilatation and compression, thus disregarding any deviatoric deformations that may occur in the continuum as well. We consider a material volume $\mathcal{D}(t)$ and we study its volume $V(t)$ [m^3] given as

$$V(t) = \int_{\mathcal{D}(t)} \mathrm{d}V. \tag{2.11}$$

Since the velocity of the boundary $\partial\mathcal{D}(t)$ is v_k, and since the only change over time in the volume V can occur by expansion or reduction at the boundary, we can write down the *global law of volume conservation* as

$$\mathrm{d}_t V(t) = \int_{\partial\mathcal{D}(t)} v_k \, \nu_k \, \mathrm{d}A. \tag{2.12}$$

This relation can be derived from Reynold's transport theorem, Eq. (2.9), by substituting $\Psi(x_j, t) \equiv 1$. The volume change $\mathrm{d}_t V$ can be split up in an induced part that is caused by internal action arising from stresses within the medium – to be described by the constitutive equations – and an injected, source part that is caused by external action. In order to derive a local equivalent of Eq. (2.12) we would like to have local measures for the induced

and injected parts of the volume change. Therefore, we define a function that describes the volume density of the induced part of the time rate of change of the volume, the *induced cubic dilatation rate* $\dot{\theta}(x_j, t)$ [s^{-1}]. In the same way, the injected part of the volume change is represented by the *volume density of volume injection rate* $q(x_j, t)$ [s^{-1}]. The integration of these quantities over $\mathcal{D}(t)$ yields $\mathrm{d}_t V(t)$, and thus $\dot{\theta}$ and q are given by

$$\int_{\mathcal{D}(t)} \left(\dot{\theta} + q\right) \mathrm{d}V = \mathrm{d}_t V. \tag{2.13}$$

The physical meaning of $(\dot{\theta} + q)$ may be better understood by dividing both sides of Eq. (2.13) by V and by considering an infinitesimally small domain $\mathcal{D}(t)$. Now we can remove the domain integral and Eq. (2.13) yields

$$\dot{\theta} + q = \lim_{V \to \mathrm{d}V} \frac{1}{V} \mathrm{d}_t V, \tag{2.14}$$

i.e. the local volume change per unit volume of an infinitesimally small material volume.

With these two local quantities, we can rewrite Eq. (2.12) as

$$\int_{\mathcal{D}(t)} \left(\dot{\theta} + q\right) \mathrm{d}V = \int_{\partial\mathcal{D}(t)} v_k \, \nu_k \, \mathrm{d}A. \tag{2.15}$$

When we ensure that v_k is continuously differentiable in $\mathcal{D}(t)$ we can apply Gauss' divergence theorem, Eq. (2.10), to the right-hand term of Eq. (2.15). This gives

$$\int_{\mathcal{D}(t)} \left(\dot{\theta} + q\right) \mathrm{d}V = \int_{\mathcal{D}(t)} \partial_k v_k \, \mathrm{d}V. \tag{2.16}$$

Considering that $\mathcal{D}(t)$ can be chosen arbitrarily, we can then remove the domain integrals and we obtain the *local form* of the *deformation equation*

$$\partial_k v_k - \dot{\theta} = q. \tag{2.17}$$

2.2.4 Conservation of linear momentum

A second fundamental conservation law within the continuum model is the *conservation law of linear momentum*, better known as Newton's second law. It is stated as follows:

Axiom 1 *Within the material volume, the rate of change over time of the linear momentum is equal to the force exerted on it.*

The total linear momentum of the material within $\mathcal{D}(t)$ is given by the mass flow density Φ_k integrated over $\mathcal{D}(t)$. Since there is no average mass flow across $\partial\mathcal{D}(t)$, as was noted in Section 2.1 on the basis of Assumption 2, we do not have to account for any inflow or outflow of momentum through mass transport across the boundary. The total force on the material within $\mathcal{D}(t)$ consists of surface forces and volume forces. The surface forces operate on the domain boundary $\partial\mathcal{D}(t)$ and are represented by the force surface density or traction $t_k(x_j, t)$ [$\mathrm{N\,m^{-2}}$]. At this stage we make another assumption regarding the nature of the medium:

Assumption 3 *For acoustic propagation, the medium can be considered non-viscous.*

Under this assumption, the surface forces are always directed normal to the boundary, and we can write the traction as

$$t_k = -p\,\nu_k, \tag{2.18}$$

where $p(x_j, t)$ [$\mathrm{N\,m^{-2}}$] is the mechanical pressure on $\partial\mathcal{D}$. The minus sign is explained by the fact that for positive p the traction on $\mathcal{D}(t)$ is directed inwards while the normal ν_k is always directed outwards. The volume forces exert a force on each point inside $\mathcal{D}(t)$ and are represented by the volume force density $f_k(x_j, t)$ [$\mathrm{N\,m^{-3}}$]. We reserve p to account for internal action, which will be further described by the constitutive equations, and with f_k we account for any external actions. Thus, f_k acts as a source term that excites the acoustic field. The conservation of linear momentum in the material volume $\mathcal{D}(t)$ can now be formulated as the *equation of motion*

$$\int_{\partial\mathcal{D}(t)} -p\,\nu_k\,\mathrm{d}A + \int_{\mathcal{D}(t)} f_k\,\mathrm{d}V = \mathrm{d}_t \int_{\mathcal{D}(t)} \Phi_k\,\mathrm{d}V. \tag{2.19}$$

If we ensure that p is continuously differentiable in $\mathcal{D}(t)$ we can apply Gauss' divergence theorem, Eq. (2.10), to the first term of Eq. (2.19). When subsequently we consider that $\mathcal{D}(t)$ can be chosen arbitrarily and when we define the *mass flow density rate* $\dot{\Phi}(x_j, t)$ [$\mathrm{kg\,m^{-2}s^{-2}}$] as

$$\int_{\mathcal{D}(t)} \dot{\Phi}_k\,\mathrm{d}V = \mathrm{d}_t \int_{\mathcal{D}(t)} \Phi_k\,\mathrm{d}V, \tag{2.20}$$

then we can remove the domain integrals and we obtain the *local form* of the *equation of motion*

$$\partial_k p + \dot{\Phi}_k = f_k. \tag{2.21}$$

2.3 Acoustic constitutive equations

The local equations of deformation and motion, Eqs. (2.17) and (2.21), will serve as the field equations for the acoustic field. In these equations we see four dependent variables, namely v_k, $\dot{\theta}$, p and $\dot{\Phi}_k$, and two source terms, q and f_k. In order to obtain a complete set of equations we need two extra equations, which will be introduced in this section. They are called the constitutive equations as they are presumed to specify the medium-specific acoustic behavior. The distinction between field equations and constitutive equations should not be interpreted too strictly, since in the derivation of the field equations we already made some assumptions with regard to the constitution of the medium, Assumptions 2 and 3. The first constitutive equation will be obtained from the principle of mass conservation, and the second constitutive equation will be derived using the equation of state of an adiabatical gas. Subsequently, we will derive the medium parameters for a generalized equation of state.

2.3.1 Material time derivative

An operator that will arise in the constitutive equations is the *material time derivative*, also called the co-moving time derivative, denoted as D_t. It is defined as

$$\mathrm{D}_t \cdot = \partial_t \cdot + v_k \partial_k \cdot. \tag{2.22}$$

The first term on the right-hand side is called the unsteady part, the second term is called the convective part. The material time derivative can be interpreted as the time rate of change of a certain quantity that an observer sees when he moves through the fluid with the drift velocity $v_k(x_j, t)$, i.e. along with the material.

2.3.2 Conservation of mass

The principle of the conservation of mass is based on the axiom of *conservation of particles*:

Axiom 2 *In the absence of processes that create or annihilate particles within the continuum, the total number of particles remains constant.*

These processes will indeed remain outside the scope of our study. With the substitution of the mass density $\rho(x_j, t)$ as the field quantity into Reynold's transport theorem, Eq. (2.9), we can therefore write down the *mass conservation law* as

$$\int_{\mathcal{D}(t)} \partial_t \rho + \int_{\partial\mathcal{D}(t)} \rho\, v_k\, \nu_k \,\mathrm{d}A = \mathrm{d}_t \int_{\mathcal{D}(t)} \rho \,\mathrm{d}V = 0. \tag{2.23}$$

Upon application of Gauss' divergence theorem, Eq. (2.10), to the second term on the left-hand side, and with the realization that $\mathcal{D}(t)$ can be chosen arbitrarily, we arrive at the *continuity equation of mass flow*

$$\partial_t \rho + \partial_k(\rho\, v_k) = 0. \tag{2.24}$$

By applying the spatial derivative to the quantities within parentheses we can write this equation in an alternative form as

$$\mathrm{D}_t \rho + \rho\, \partial_k v_k = 0. \tag{2.25}$$

2.3.3 First constitutive equation

The first constitutive equation relates the mass flow density rate $\dot{\Phi}_k$ to the drift velocity v_k. We start with the definition of $\dot{\Phi}_k$, Eq. (2.20), and we substitute Reynold's transport theorem, Eq. (2.9), with Φ_k as the field quantity in the right-hand side of Eq. (2.20) to obtain

$$\int_{\mathcal{D}(t)} \dot{\Phi}_k \,\mathrm{d}V = \int_{\mathcal{D}(t)} \partial_t \Phi_k \,\mathrm{d}V + \int_{\partial\mathcal{D}(t)} \Phi_k\, v_m\, \nu_m \,\mathrm{d}A. \tag{2.26}$$

Next we apply Gauss' theorem, Eq. (2.10), to the second term on the right-hand side and we get

$$\int_{\mathcal{D}(t)} \dot{\Phi}_k \,\mathrm{d}V = \int_{\mathcal{D}(t)} \partial_t \Phi_k \,\mathrm{d}V + \int_{\mathcal{D}(t)} \partial_m(\Phi_k v_m) \,\mathrm{d}V. \tag{2.27}$$

Since $\mathcal{D}(t)$ can be chosen arbitrarily, we can remove the domain integrals, and with $\Phi_k = \rho\, v_k$ we get

$$\dot{\Phi}_k = \partial_t(\rho\, v_k) + \partial_m(\rho\, v_k v_m). \tag{2.28}$$

When we apply the partial derivatives to the terms within parentheses we can rewrite this equation as

$$\dot{\Phi}_k = \rho \mathrm{D}_t v_k + v_k \mathrm{D}_t \rho + v_k \rho \partial_m v_m, \tag{2.29}$$

and with the application of the equation of mass flow in its alternative form, Eq. (2.25), the last two terms cancel and we arrive at

$$\dot{\Phi}_k = \rho \mathrm{D}_t v_k. \tag{2.30}$$

This is the *first constitutive equation*. It is general for all media obeying Assumption 2.

2.3.4 Hydrostatic equation of state

To formulate the second constitutive equation, we need to introduce thermodynamic considerations into our discussion. In order for them to be valid within the context of sound propagation, we must assume that the medium is everywhere in *instantaneous local thermodynamic equilibrium* [43, 67]. This can be formulated as follows:

Assumption 4 *All quantities that describe the thermodynamic and acoustic state of the continuum vary slowly enough in time and space, so that in each point and at each instant an equilibrium is established between the thermodynamic state variables within a small neighborhood around that point.*

If this assumption holds then we can formulate an *equation of state* (EOS) that interrelates a number of thermodynamic state variables for the medium. This EOS is in general only valid for a single phase of the medium, and to be useful for our considerations we assume the absence of changes in phase:

Assumption 5 *There are no phase changes of the medium.*

Phase changes like cavitation and condensation may occur because of strong acoustic fluctuations of the total pressure. We thus assume that these fluctuations have such a magnitude that the phase of the medium is not affected by them.

A well-known EOS is the *ideal gas law*, which states

$$p = \rho R T, \tag{2.31}$$

where R is the specific gas constant and T [K] is the temperature. The pressure p is the hydrostatic pressure, which we take to be equal to the mechanical pressure.[1] Many gases obey this EOS in first order. From Eq. (2.31) we can obtain the so-called *adiabatical gas law*, see e.g. [59],

$$\frac{p}{p_0} = \left(\frac{\rho}{\rho_0}\right)^{\gamma}, \tag{2.32}$$

where γ is the ratio of specific heats at constant pressure and at constant volume, and p_0 and ρ_0 are the pressure and density at the ambient state. This equation is useful as a basis to describe the medium behavior for acoustic phenomena in gases, as it is well-known that for gases in first order sound propagation can be considered as an adiabatic process [32, 67]. We extend the applicability of Eq. (2.32) by making a generalization:

Assumption 6 *For acoustic propagation, the medium can be considered to behave adiabatic, i.e. non-thermally conducting.*

We will not go into detail on the derivation of Eq. (2.32) from Eq. (2.31), but a fundamental axiom that is employed and that cannot remain unmentioned is the *first law of thermodynamics*:

Axiom 3 *Within the material volume, the rate of change over time of the internal energy plus the kinetic energy is equal to the work upon the material volume plus the amount of heat transferred to it.*

2.3.5 Second constitutive equation

We start the derivation of the second constitutive equation with the local deformation equation, Eq. (2.17), with $q = 0$. Using the alternative form of the mass equation, Eq. (2.25), we see that Eq. (2.17) can be written as

$$\dot{\theta} = \partial_r v_r = \frac{-\mathrm{D}_t \rho}{\rho}. \tag{2.33}$$

[1] For viscous fluids, there is a subtle difference between mechanical and hydrostatic pressure; for non-viscous fluids, the distinction vanishes. See e.g. [77] for a further discussion.

When we take the natural logarithm of the adiabatical gas law, Eq. (2.32), we get

$$\ln(p) - \ln(p_0) = \gamma \left[\ln(\rho) - \ln(\rho_0)\right], \tag{2.34}$$

and taking the material derivative of Eq. (2.34) gives us

$$\frac{\mathrm{D}_t p}{p} = \frac{\gamma \mathrm{D}_t \rho}{\rho}. \tag{2.35}$$

When we substitute this in Eq. (2.33), we obtain

$$\dot{\theta} = \frac{-\mathrm{D}_t p}{\gamma p}. \tag{2.36}$$

For sound propagation in gases it makes sense to define a parameter κ [Pa^{-1}] by

$$\kappa = \frac{1}{\gamma p}, \tag{2.37}$$

which is fairly constant for common acoustic phenomena. With this parameter, called the *compressibility*, Eq. (2.36) results in

$$\dot{\theta} = -\kappa \mathrm{D}_t p. \tag{2.38}$$

This is the *second constitutive equation.*

2.3.6 Medium parameters for the adiabatical gas EOS and for a Taylor approximation of the EOS

In the constitutive equations Eqs. (2.30) and (2.38), we have the field quantities $\dot{\Phi}_k$, v_k, $\dot{\theta}$ and p. The quantities ρ and κ are considered as medium parameters. For an ideal gas, ρ and κ are related to the pressure by Eqs. (2.32) and (2.37), rewritten here as

$$\rho = \rho_0 \left(\frac{p}{p_0}\right)^{1/\gamma}, \tag{2.39}$$

$$\kappa = \kappa_0 \left(\frac{p_0}{p}\right), \tag{2.40}$$

where $\kappa_0 = 1/\gamma p_0$ is the compressibility at the ambient state. For small acoustic pressures, the variations of κ and ρ in p are small and they are generally neglected, as will be shown in Section 2.4. However, for the nonlinear acoustic field they are essential.

The ideal gas law is valid for gases in first order. Liquids do not obey this law since the ideal gas law neglects the intermolecular attractive forces that are so significantly present in a liquid. There have been proposed many equations of state for liquids based on fittings of empirical data, on simplified medium models or on a combination of them [10, 37, 67]. We refrain from picking a specific EOS, but we join in with the common practice of formulating the EOS as a Taylor series expansion of p as a function of ρ around the ambient state (p_0, ρ_0) and under isentropic condition. For acoustic propagation the employment of the isentropic form of the EOS is valid only when we neglect the heat flow and the dissipation in the medium. The absence of the heat flow has already been stated in Assumption 6. The absence of dissipation is covered by:

Assumption 7 *For our purpose of deriving the dependency of the constitutive parameters on the field quantities, the dissipation can be neglected.*

The use of a Taylor series expansion is appropriate when the following assumption holds [32]:

Assumption 8 *The equation of state of the medium behaves sufficiently smooth around the ambient state so that it can be adequately approximated by a two-term Taylor approximation.*

This gives an approximation of the EOS of the form

$$p(\rho) = p_0 + \left(\frac{\partial p}{\partial \rho}\right)_{\rho=\rho_0} (\rho - \rho_0) + \frac{1}{2!}\left(\frac{\partial^2 p}{\partial \rho^2}\right)_{\rho=\rho_0} (\rho - \rho_0)^2, \tag{2.41}$$

or equivalently

$$p(\rho) = p_0 + c_0^2(\rho - \rho_0) + \frac{1}{2}\frac{c_0^2}{\rho_0}\frac{B}{A}(\rho - \rho_0)^2, \tag{2.42}$$

where

$$c_0^2 = \left(\frac{\partial p}{\partial \rho}\right)_{\rho=\rho_0}, \tag{2.43}$$

$$\frac{B}{A} = \frac{\rho_0}{c_0^2}\left(\frac{\partial^2 p}{\partial \rho^2}\right)_{\rho=\rho_0}, \tag{2.44}$$

are the small-signal sound speed and the B/A ratio, respectively. Inversion of Eq. (2.42) gives

$$\rho = \rho_0 + \rho_0 \frac{A}{B}\left(\sqrt{1 + 2\frac{B}{A}\frac{p-p_0}{\rho_0 c_0^2}} - 1\right). \tag{2.45}$$

Combining Eqs. (2.33) and (2.38) shows us that

$$\kappa = \frac{1}{\mathrm{D}_t p}\frac{\mathrm{D}_t \rho}{\rho} = \frac{1}{\rho}\frac{\mathrm{d}\rho}{\mathrm{d}p}, \tag{2.46}$$

and with Eq. (2.45) we arrive at

$$\kappa = \frac{1}{\rho_0 c_0^2}\left(1 + 2\frac{B}{A}\frac{p-p_0}{\rho_0 c_0^2}\right)^{-1/2}\left[1 + \frac{A}{B}\left(\sqrt{1 + 2\frac{B}{A}\frac{p-p_0}{\rho_0 c_0^2}} - 1\right)\right]^{-1}. \tag{2.47}$$

The first-order forms of Eqs. (2.45) and (2.47) are obtained by approximating these expressions around the ambient state $p = p_0$, giving

$$\rho = \rho_0\left[1 + \kappa_0(p - p_0)\right], \tag{2.48}$$

$$\kappa = \kappa_0\left[1 + \kappa_0(1 - 2\beta)(p - p_0)\right], \tag{2.49}$$

where $\beta = 1 + B/2A$ is the so-called coefficient of nonlinearity and $\kappa_0 = 1/\rho_0 c_0^2$ is the compressibility at the ambient state.

2.4 Second-order nonlinear wave equation

The four equations that form the starting point for our subsequent analysis are the deformation equation (2.17), the equation of motion (2.21) and the

first and second constitutive equations (2.30) and (2.38). These equations lead to a set of first order partial differential equations in p and v_k,

$$\partial_k p \ + \rho \mathrm{D}_t v_k = f_k, \tag{2.50}$$
$$\partial_r v_r + \kappa \mathrm{D}_t p \ = q. \tag{2.51}$$

In the derivation of the second constitutive equation we have already introduced the ambient states for p, ρ and κ. We will now write the latter quantities as the summation of their ambient states p_0, ρ_0 and κ_0, and an acoustic perturbation p', ρ' and κ',

$$p = p_0 + p', \tag{2.52}$$
$$\rho = \rho_0 + \rho', \tag{2.53}$$
$$\kappa = \kappa_0 + \kappa', \tag{2.54}$$

where p' is also known as the *acoustic pressure*. The velocity v_k is in itself a perturbed quantity since in the ambient state $v_k = 0$.

When we substitute the forms Eqs. (2.52)–(2.54) in Eqs. (2.50) and (2.51) and we only keep terms that are of first order in the perturbed quantities, and we also let the symbol p denote the acoustic pressure instead of the total pressure, we get the *linear acoustic equations*

$$\partial_k p \ + \rho_0 \partial_t v_k = f_k, \tag{2.55}$$
$$\partial_r v_r + \kappa_0 \partial_t p \ = q. \tag{2.56}$$

From these equations we derive a linear wave equation in p under the assumption that ρ_0 is homogeneous:

Assumption 9 *The ambient density ρ_0 is not varying with respect to position.*

If we subtract the divergence of Eq. (2.55) from ρ_0 times the temporal derivative of Eq. (2.56), we obtain the *linear acoustic wave equation*

$$c_0^{-2} \partial_t^2 p - \partial_k^2 p = S, \tag{2.57}$$

where

$$S = \rho_0 \partial_t q - \partial_k f_k \tag{2.58}$$

is the source term and $c_0^{-2} = \rho_0 \kappa_0$.

Next we derive a wave equation that accounts for the nonlinearity up to the second-order terms in the perturbed quantities. A principle that will be employed throughout is that we can substitute first-order relations like Eqs. (2.48), (2.49) and (2.55)-(2.57) into a second-order term and retain second-order accuracy. When we write out all terms in Eqs. (2.50) and (2.51), where for ρ and κ we take the expressions derived from the two-term Taylor approximation Eqs. (2.48) and (2.49), and we discard the terms that are of third and higher order in the perturbed quantities, we get

$$\partial_k p \; + \rho_0 \partial_t v_k = f_k - \rho_0 \kappa_0 p \, \partial_t v_k - \rho_0 v_j \partial_j v_k, \tag{2.59}$$

$$\partial_j v_j + \kappa_0 \partial_t p \; = q \; - \kappa_0^2 (1 - 2\beta) p \, \partial_t p - \kappa_0 v_j \partial_j p. \tag{2.60}$$

From these equations it can be proven that up to second order we can consider the acoustic velocity to be free of rotation. Firstly, this gives us the opportunity to substitute $\partial_j v_k = \partial_k v_j$ in the final term in Eq. (2.59). Secondly, this enables us to write the velocity outside any source domain by means of a *velocity potential* ϕ, defined by

$$v_k = \partial_k \phi. \tag{2.61}$$

If we substitute this into the linear acoustic equation (2.55), then for regions where ρ_0 is constant we obtain a relation between ϕ and p that is valid up to first order

$$p = -\rho_0 \partial_t \phi. \tag{2.62}$$

With Eqs. (2.61) and (2.62) we obtain from Eq. (2.56) a wave equation in ϕ, that is valid up to first order

$$c_0^{-2} \partial_t^2 \phi - \partial_k^2 \phi = 0. \tag{2.63}$$

Substituting $\partial_j v_k = \partial_k v_j$ and Eqs. (2.61) and (2.62) in all the second-order terms of Eqs. (2.50) and (2.51) except in the term with the factor 2β, gives

$$\partial_k p \; + \rho_0 \partial_t v_k = f_k + \rho_0^2 \kappa_0 \, \partial_t \phi \, \partial_t \partial_k \phi - \rho_0 \, \partial_j \phi \, \partial_k \partial_j \phi, \tag{2.64}$$

$$\partial_j v_j + \kappa_0 \partial_t p \; = q \; + 2\beta \kappa_0^2 \, p \, \partial_t p - \rho_0^2 \kappa_0^2 \, \partial_t \phi \, \partial_t^2 \phi + \rho_0 \kappa_0 \, \partial_j \phi \, \partial_j \partial_t \phi. \tag{2.65}$$

We obtain a second-order nonlinear wave equation by subtracting the divergence of Eq. (2.64) from ρ_0 times the time derivative of Eq. (2.65). This yields

$$\begin{aligned} c_0^{-2} \partial_t^2 p - \partial_k^2 p = S + \rho_0 \kappa_0^2 \beta \partial_t^2 p^2 \\ + \frac{\rho_0}{2} \left[-c_0^{-2} \partial_k^2 (\partial_t \phi)^2 + \partial_k^2 (\partial_j \phi)^2 \right. \\ \left. - c_0^{-4} \partial_t^2 (\partial_t \phi)^2 + c_0^{-2} \partial_t^2 (\partial_j \phi)^2 \right]. \end{aligned} \tag{2.66}$$

The term between square brackets can be rewritten as

$$\begin{aligned}\left[-c_0^{-2}\partial_k^2\ (\partial_t\phi)^2 + \partial_k^2(\partial_j\phi)^2 - c_0^{-4}\partial_t^2(\partial_t\phi)^2 + c_0^{-2}\partial_t^2(\partial_j\phi)^2\right] \\ = \left[\partial_k^2 + c_0^{-2}\partial_t^2\right]\left[(\partial_j\phi)^2 - c_0^{-2}(\partial_t\phi)^2\right] \\ = \left[\partial_k^2 + c_0^{-2}\partial_t^2\right]\left[\frac{1}{2}(\partial_j^2 - c_0^{-2}\partial_t^2)\phi^2 - \phi(\partial_j^2 - c_0^{-2}\partial_t^2)\phi\right]. \qquad (2.67)\end{aligned}$$

The factor $(\partial_j^2 - c_0^{-2}\partial_t^2)\phi$ in the last term is zero up till first order in view of Eq. (2.63), and omitting the entire last term will therefore give only a third order error, which may be neglected. When the bracketed term in Eq. (2.66) is thus rewritten, we can straightforwardly see that in second order this equation is equal to

$$c_0^{-2}\partial_t^2\tilde{p} - \partial_k^2\tilde{p} = S + \rho_0\kappa_0^2\beta\partial_t^2\tilde{p}^2, \qquad (2.68)$$

where

$$\tilde{p} = p + \frac{\rho_0}{4}(\partial_k^2 + c_0^{-2}\partial_t^2)\phi^2. \qquad (2.69)$$

Suppose that we can solve $\tilde{p}$ from Eq. (2.68), then by applying the transformation of Eq. (2.69) we obtain the nonlinear acoustic pressure estimate from the second order equation. Following the arguments put forward by Aanonsen et al. [1] and Naze Tjotta and Tjotta [32, 52], we notice that both the transformation of Eq. (2.69) as well as the nonlinear term in Eq. (2.68) give rise to nonlinear distortion of the acoustic pressure field. However, the nonlinearity in the transformation is of a local and instantaneous nature, whereas the nonlinear term in Eq. (2.68) accounts for cumulative nonlinear distortion that builds up gradually during the propagation of the acoustic field. We can neglect the nonlinear term in the transformation Eq. (2.69) if we assume that the local nonlinear effect is negligible:

Assumption 10 *In the nonlinear distortion of the acoustic field, the cumulative nonlinear effect dominates the local nonlinear effect.*

Under this assumption, $\tilde{p}$ may be taken equal to p and we end up with the lossless *Westervelt equation* [1, 32]

$$c_0^{-2}\partial_t^2 p - \partial_k^2 p = S + \frac{\beta}{\rho_0 c_0^4}\partial_t^2 p^2. \qquad (2.70)$$

2.5 Discussion

In this section we will highlight a number of issues related to the derivations discussed in this chapter.

Firstly, we note that for the derivation of the local laws we have employed Gauss' divergence theorem more than once under the assumption that the quantities p, ρ and v_k were continuously differentiable across the entire domain. However, as implied by Assumption 1, these quantities may exhibit jumps across certain boundaries, and therefore the local laws are not valid here. As a consequence, we should derive nonlinear *boundary conditions* from the global laws to adequately describe the acoustic field across these boundaries. The reason that this exercise has not been undertaken here is two-fold. First, in this thesis we will not consider media with spatial jumps in their constitutive parameters. Second, the method that we will develop for the numerical evaluation of the acoustic field will turn such jumps into continuous changes.

Secondly, we remark that in the derivation of the momentum equation in Section 2.2.4 the pressure is used to describe the internal mechanical force, and the volume force is used to describe the external mechanical force. When we would like to apply a pressure as an external excitation, then this may be performed through an infinite volume force acting on an infinitely thin source surface and oriented perpendicular to that surface. This issue will be further discussed in Chapter 3.

Thirdly, we briefly review the assumptions that were made in the course of the discussion. The five assumptions identified as the continuum hypothesis (1), common collective motion (2), instantaneous local thermodynamic equilibrium (4), absence of phase change (5) and smoothness of the EOS (8) are commonly and often silently accepted. The effectiveness and predictive force of the resulting theories and equations in the past centuries is a clear hint to their all-round validity, although we may always come up with examples where under specific or extreme conditions some of them are violated.

Three assumptions showed that in our analysis we have not accounted for possible loss mechanisms. These are Assumptions 3 and 6, which assume that viscosity and thermal conduction can be neglected, and Assumption 7, which supposes that dissipation can be treated separately from the nonlinear behavior. Our main concern in this chapter has been to show the origin of the nonlinear terms in the equations, and for simplicity and clarity on

this aspect we have neglected the loss mechanisms. For the description of shockwaves [32] it has been realized in the past century that attenuation mechanisms have to be included in the analysis. However, at the same time they have always been treated separately from the nonlinear terms, and all coupled terms have been considered to be of third order and were thus neglected in a second-order derivation. We justify our approach of neglecting loss phenomena in the derivation of the nonlinear acoustic equations by three observations. Firstly, the separate treatment of nonlinear and loss phenomena in studies for modeling acoustic shockwaves has shown to be effective. In the examples in this thesis we will use pressures, configurations and media in which the nonlinear effect is clearly observable but does not lead to shockwaves, which is all the more justifying the separate treatment of acoustic losses. Secondly, for our first medium of interest, water, the thermoviscous absorption is in fact negligible for the pressure levels and distances occurring in our examples. Thirdly, for the medium which is our final target, i.e. human tissue, it is empirically known that the attenuation is of a kind that cannot be adequately described with a simplified model that could have been included straightforwardly in the analysis. This is due to absorption processes in human tissue like relaxation, dissipation and scattering[2] that are of a different nature than the thermoviscous absorption that is normally accounted for. As explained in e.g. [19, 22, 65], thermoviscous models end up with an order f^2 power law attenuation, f denoting the frequency, while in tissue we have a frequency-dependency that is more accurately described by an order f^α power law with $1 < \alpha < 2$. Therefore, our approach is to adopt a phenomenological approach and to account for acoustic loss in a later stage.[3]

The assumption of constant density for deriving the linear and nonlinear wave equations, Assumption 9, is one that puts indeed a serious limit to the applicability of the theory, as it excludes all heterogeneous media including human tissue. It would be a considerable improvement to include medium inhomogeneity into the model, and in Appendix E it is show that inhomogeneity may be included into our approach in a straightforward way.

The remaining Assumption 10, stating negligible local nonlinearity, was employed in the derivation of the Westervelt equation and excludes the description of nonlinear effects like nonlinear radiation pressure, nonlinear distortion in compound wavefields such as standing or guided waves, and

[2]Scattering is not a loss mechanism, but for a distribution of scatterers the effect on the acoustic field is not distinguishable from dispersion due to acoustic loss. It can thus be accounted for through an attenuation function.

[3]See Appendix D.

nonlinear fields in intersecting beams [32]. In these phenomena, local nonlinear effects contribute significantly to the nonlinear distortion of the acoustic wavefield. The local nonlinear effect is also not negligible within a wavelength of a boundary or a source domain. When these nonlinear phenomena need to be accounted for in the model we should revert to the set of first order equations, Eqs. (2.50) and (2.51), with appropriate expressions for ρ and κ. However, in this thesis we will be concerned with the nonlinear distortion effects of progressive fields from a source plane, in which case the cumulative nonlinear effects dominate and for which we can safely employ the Westervelt equation.

Chapter 3

Solution of the basic nonlinear equations employing the INCS method

---

In the previous chapter we presented the mathematical-physical basis for the nonlinear acoustic wavefield. We found that the basic equations can be formulated in two ways. Firstly, by the set of two coupled, first-order, partial differential equations given by Eqs. (2.50) and (2.51),

$$\partial_k p + \rho \mathrm{D}_t \boldsymbol{v} = \boldsymbol{f}, \tag{3.1}$$

$$\boldsymbol{\nabla} \cdot \boldsymbol{v} + \kappa \mathrm{D}_t p = q. \tag{3.2}$$

Here ρ and κ are given by one of the sets of equations (2.39)-(2.40), (2.45)-(2.47) or (2.48)-(2.49), depending on the medium and on the accuracy needed. Secondly, and with one further assumption, the nonlinear acoustic wavefield can be described by the single, second-order, partial differential equation which is known as the lossless Westervelt equation, and which is given by Eq. (2.70),

$$c_0^{-2} \partial_t^2 p - \boldsymbol{\nabla}^2 p = S + \frac{\beta}{\rho_0 c_0^4} \partial_t^2 p^2. \tag{3.3}$$

In this chapter we will develop a strategy to compute the nonlinear acoustic pressure field from Eq. (3.3) for a homogeneous medium. The strategy will consist of four steps. Firstly, in Section 3.1 the nonlinear acoustic wave problem will be formally solved by a Neumann iterative solution, in which the

nonlinear terms in the basic equations act as nonlinear contrast sources and provide iterative corrections to the linear wave problem. Secondly, in Section 3.2 the linear wave problem is solved by a spatiotemporal convolution of the (primary or contrast) source with the Green's function of the linear background medium. Thirdly, in order to numerically evaluate the convolution integral, in Sections 3.3-3.5 the terms under the integral are filtered and windowed in all spatiotemporal dimensions, where the filtering allows for a discretization at the minimum rate of two points per wavelength and per period. Fourthly, as also discussed in Section 3.3, the discretized convolution sum is efficiently evaluated using a Fast Fourier Transform (FFT) method. In the closing Section 3.6 we discuss some further issues related to the analysis in this chapter.

In this chapter we present the solution strategy that applies to Eq. (3.3), although it can equally well be applied to the set of equations (3.1) and (3.2). Using these equations instead of Eq. (3.3) would be useful for employing a different form for the constitutive parameters, for inhomogeneous media or for validating the assumptions made in the derivation of the Westervelt equation. In this chapter we will no longer use the subscript notation and the Einstein summation convention associated with it.

3.1 Neumann iterative solution

The main purpose of this chapter is to develop a strategy for solving the nonlinear acoustic pressure field $p(\boldsymbol{x}, t)$ from the Westervelt equation (3.3). We consider the nonlinear field in a homogeneous medium, i.e. ρ_0, κ_0 and β are assumed to be constant. The nonlinear pressure field is interpreted as a summation of the linear field solution, denoted as $p^{(0)}(\boldsymbol{x}, t)$, and a nonlinear correction, denoted as $\delta p(\boldsymbol{x}, t)$. The linear field solution $p^{(0)}$ can be obtained by solving the wave equation (2.57) for the homogeneous, lossless and linear background medium in which the external term S acts as the *primary source*. We will denote the solution method for the wave equation for the given background medium as the operator $\mathcal{L}$, so $p^{(0)} = \mathcal{L}[S]$. Equivalently, the nonlinear field correction δp can be obtained by letting $\mathcal{L}$ work on the second term on the right-hand side of Eq. (3.3), which we will define as the *nonlinear contrast source*

$$S^{NL}(p) = \frac{\beta}{\rho_0 c_0^4} \partial_t^2 p^2. \tag{3.4}$$

When we assume that the total nonlinear pressure field p is dominated by $p^{(0)}$, then a good first estimate of $S^{NL}(p)$ is $S^{NL}(p^{(0)})$. The operator $\mathcal{L}$ can now be employed to obtain a first estimate of the nonlinear field correction as $\delta p^{(1)} = \mathcal{L}[S^{NL}(p^{(0)})]$. Repeating these steps, the contrast source formulation enables the computation of a successive estimate $p^{(j)} = p^{(0)} + \delta p^{(j)}$ to p and results in the *Neumann iterative solution* [23]

$$p^{(0)} = \mathcal{L}[S^{(0)}], \qquad S^{(0)} = S, \tag{3.5}$$

$$p^{(j)} = p^{(0)} + \mathcal{L}[S^{(j)}], \quad S^{(j)} = S^{NL}(p^{(j-1)}), \quad j \geq 1. \tag{3.6}$$

This scheme is the formal equivalent of the approach used by Hoffelner et al. [34]. Moreover, it can be interpreted as a perturbation scheme [32], where $p^{(1)}$ in our scheme is identified as the quasilinear solution. With $j > 1$, we improve this quasilinear solution towards the full nonlinear wavefield, assuming that the scheme indeed converges.

3.2 Green's function method for the primary and contrast source problem

One method to compute $\mathcal{L}[S^{(j)}]$ is the evaluation of the convolution integral [58]

$$\begin{aligned}\mathcal{L}[S^{(j)}] &= G(\boldsymbol{x}, t) *_{\boldsymbol{x},t} S^{(j)}(\boldsymbol{x}, t) \\ &= \int_{\mathcal{D}_S^{(j)}} \int_{\mathcal{T}_S^{(j)}} G(\boldsymbol{x}-\boldsymbol{x}', t-t')\, S^{(j)}(\boldsymbol{x}', t')\, \mathrm{d}t'\, \mathrm{d}\boldsymbol{x}',\end{aligned} \tag{3.7}$$

where $G(\boldsymbol{x}, t)$ is the Green's function of the homogeneous, lossless and linear background medium. For many background media the Green's function is known in closed form, see e.g. [17, 18]. In this thesis we will employ the one-dimensional and the three-dimensional free-space Green's functions, given by [18]

$$G(x, t) = \frac{c_0}{2} H(t - |x|/c_0), \qquad \text{(1D)} \tag{3.8}$$

$$G(\boldsymbol{x}, t) = \frac{\delta(t - \|\boldsymbol{x}\|/c_0)}{4\pi \|\boldsymbol{x}\|}, \qquad \text{(3D)} \tag{3.9}$$

where $H(t)$ is the Heaviside step function and $\delta(t)$ is the Dirac delta distribution. In Eq. (3.7) $\mathcal{D}_S^{(j)}$ and $\mathcal{T}_S^{(j)}$ denote the relevant spatial and temporal

domains of integration. For $p^{(0)}$, the spatial integration is over the support $\mathcal{D}_S^{(0)}$ of the primary source S and may involve zero to three integrations, depending on whether $S^{(0)}$ contains a point, line, surface or volume source. For the successive estimates $p^{(j)}$, the integration is over the three-dimensional domain $\mathcal{D}_S^{(j)}$ that supports the contrast source $S^{(j)}$, which is equal to the support of $p^{(j-1)}$. In principle, the latter support spans the entire space where an acoustic pressure is observed. In practice however, the domain in which the contrast sources contribute significantly to $p^{(j)}$ is limited. We will further investigate this issue in Chapters 4 and 5.

3.3 Discretization at the Nyquist rate: spatiotemporal filtering and windowing

Except in the simplest cases, the convolution integral in Eq. (3.7) must be discretized and evaluated by numerical means. When we employ a straightforward approach, we will need a fine discretization and a corresponding large number of samples to obtain sufficient accuracy. However, especially when dealing with multi-dimensional, large-scale convolutions, as will be the case in computing the nonlinear acoustic field of medical phased array transducers, this will result in a prohibitively large grid size. A coarse discretization is therefore essential for the tractability of the computation. In addition to this, most iterative methods, like the Neumann iterative scheme, require the storage of the computed pressure field at the full spatiotemporal grid, which makes the employment of a coarse discretization all the more necessary. In Subsection 3.3.1 we will first discuss the straightforward discretization of a one-dimensional convolution integral and its efficient evaluation. To analyze the approximation error in the discretization, in Subsection 3.3.2 we recall a number of basic properties of the Fourier transform of a continuous signal and its discretized version. Next, in Subsection 3.3.3 we present an improved discretization method that allows for the accurate evaluation of the convolution integral at a discretization down to the limit of 2 points per period for band-limited signals, as prescribed by the Nyquist-Shannon theorem. We discuss an alternative procedure within the proposed method in Subsection 3.3.4, and finally in Subsection 3.3.5 we discuss the application of the developed method to the multi-dimensional convolution of Eq. (3.7).

3.3.1 Straightforward discretization and efficient evaluation of a convolution integral

We first consider the numerical evaluation of a one-dimensional convolution integral

$$F(t) = G(t) *_t S(t) = \int_{-\infty}^{\infty} G(t - t')\, S(t')\, \mathrm{d}t'. \tag{3.10}$$

A straightforward approach is to use a trapezoidal quadrature rule with a sampling distance Δt to approximate the convolution integral by the convolution sum [2, p. 885]

$$F_n^* = \Delta t\, G_n * S_n = \Delta t \sum_m G_{n-m} S_m, \tag{3.11}$$

where it is assumed that the integrand is zero at the endpoints. Here, $G_{n-m} = G[(n-m)\Delta t]$ and $S_m = S(m\Delta t)$ exactly, but F_n^* is an approximation of $F_n = F(n\Delta t)$. The exclusive use of the function values at the collocation points $t = n\Delta t$ implies that the functions have been sampled. To keep the number of samples finite, $n - m$ and m must be limited to a finite number, which means the windowing of $G(t)$, $S(t)$ and, consequently, $F(t)$. Let us assume that the interval of interest of F_n ranges from $n = 0$ to $N-1$ and the support of S_m also ranges from $m = 0$ to $N-1$.[1] Then the support of G_q may be restricted to the points $q = n - m = -N+1$ to $N-1$, giving $2N-1$ points. For reason of efficiency, the convolution sum is usually evaluated by applying a Fast Fourier Transform (FFT) method [54]. Since this implies a circular convolution instead of a linear one as in Eq. (3.11), a wraparound error in the interval of interest must be avoided by extending the support of S_m with at least $N-1$ zeros (zero-padding) [57]. For an efficient FFT and for simplifying the upcoming discussions, the number of points is rounded up to $2N$ by zero-padding S_m with N points and G_q with one point. The computational effort of the FFTs thus employed is of the order $2N \log(2N)$.

The approximation error is given by $F_n^* - F_n$ and is controlled by the step size Δt. Often, the step size is compared to the wavelength of a harmonic signal that is characteristic for the problem under investigation. To this end

[1] For ease of the discussion we take the interval of interest in $F(t)$ and the support of $S(t)$ to coincide. The generalization to non-coinciding intervals is straightforward and is not explicitly treated in this thesis.

we introduce the *number of points per period*

$$D_\phi = \frac{2\pi}{\phi\,\Delta t}, \tag{3.12}$$

where ϕ is the angular frequency of the chosen characteristic signal.[2] When we employ a discretization procedure based on the trapezoidal rule, usually 10 to 20 points per period are needed for a sufficiently accurate evaluation. We illustrate this with the integration of a switched harmonic function, given by

$$F(t) = \int_{-\infty}^{\infty} G(t-t')S(t')\,\mathrm{d}t' \tag{3.13}$$

with

$$G(t) = H(t), \tag{3.14}$$

$$S(t) = \sin(\Omega_0\,t)[H(t-T_b) - H(t-T_e)]. \tag{3.15}$$

The exact result for $F(t)$ is

$$F(t) = \begin{cases} 0, & t \le T_b \\ \Omega_0^{-1}[\cos(\Omega_0\,T_b) - \cos(\Omega_0\,t)], & T_b < t \le T_e \\ \Omega_0^{-1}[\cos(\Omega_0\,T_b) - \cos(\Omega_0\,T_e)], & T_e < t \end{cases} \tag{3.16}$$

and the approximation of Eqs. (3.13)–(3.15) with the trapezoidal rule gives us

$$F_n^* = \frac{\Delta t}{2}S(n\Delta t) + \Delta t \sum_{m=-\infty}^{n-1} S(m\Delta t). \tag{3.17}$$

In the present case we take $\Omega_0 = 1$, $\{T_b, T_e\} = \{2\pi, 8\pi\}$, and we consider the region of interest $t \in [0, 10\pi]$. For this problem we choose the characteristic frequency to be $\phi = \Omega_0 = 1$ in Eq. (3.12), so for a given D_{Ω_0} the step size will be $\Delta t = 2\pi/D_{\Omega_0}$. We obtain estimates F_n^* on the points $t = n\Delta t$, $n \in [0, N-1]$ with $N - 1 = 10\pi/\Delta t$. We further define a relative root mean square (RRMS) error

$$\mathrm{Err} = \sqrt{\frac{\sum_{n=0}^{N-1}(F_n^* - F_n)^2}{\sum_{n=0}^{N-1} F_n^2}}. \tag{3.18}$$

[2]The subscript ϕ on D acknowledges the fact that D_ϕ is related to a specific characteristic frequency ϕ, which is not always unambiguously determined. D_ϕ can be converted between different choices of the characteristic frequency according to $D_{\phi_1}/D_{\phi_2} = \phi_2/\phi_1$.

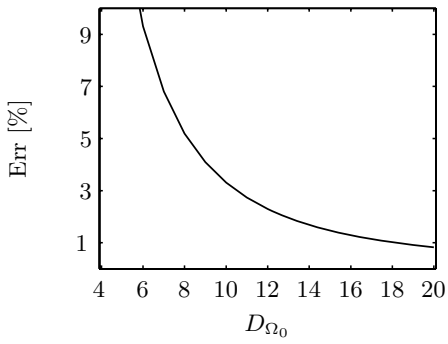

Figure 3.1. RRMS error for the trapezoidal rule approximation Eq. (3.17) versus the number of points per period.

The behavior of the error as a function of D_{Ω_0} is given in Fig. 3.1. In the figure we see that to arrive at an error equal to or less than 1% with the trapezoidal rule, we have to take $D_{\Omega_0} \geq 18$.

3.3.2 Basic Fourier theorems

We further investigate the approximation error $F_n^* - F_n$ from a Fourier domain perspective and formulate a method to arrive at the same error with a coarser discretization. We first recall three basic properties of an arbitrary function $f(t)$ and its Fourier transform $\hat{f}(\omega)$ defined by the Fourier transformation pair

$$\hat{f}(\omega) = \int_{-\infty}^{\infty} f(t)\, \exp(-j\omega t)\, \mathrm{d}t, \tag{3.19}$$

$$f(t) = \frac{1}{2\pi} \int_{-\infty}^{\infty} \hat{f}(\omega)\, \exp(j\omega t)\, \mathrm{d}\omega. \tag{3.20}$$

The first basic property is the *convolution theorem*, which states that the Fourier transform of a convolution is given as [55]

$$f(t) = a(t) *_t b(t) \qquad \leftrightarrow \qquad \hat{f}(\omega) = \hat{a}(\omega)\, \hat{b}(\omega). \tag{3.21}$$

This property forms the basis of the FFT method mentioned in the previous Subsection. In the dual case, for a convolution in the Fourier domain, the

equivalent in the original domain is given as

$$\hat{f}(\omega) = \hat{a}(\omega) *_\omega \hat{b}(\omega) \quad \leftrightarrow \quad f(t) = 2\pi\, a(t)\, b(t). \tag{3.22}$$

The second property involves the process of equidistant sampling of $f(t)$ and $\hat{f}(\omega)$. The sampled version of $f(t)$ is defined as

$$f^{\Delta t}(t) = \sum_{n=-\infty}^{\infty} f(n\Delta t)\ \delta\left(\frac{t - n\Delta t}{\Delta t}\right), \tag{3.23}$$

where Δt is the sampling distance. With the impulse train defined as

$$\delta_{\Delta t}(t) = \Delta t \sum_{n=-\infty}^{\infty} \delta\left(t - n\Delta t\right) = \sum_{n=-\infty}^{\infty} \delta\left(\frac{t - n\Delta t}{\Delta t}\right), \tag{3.24}$$

we can rewrite Eq. (3.23) as

$$f^{\Delta t}(t) = f(t)\ \delta_{\Delta t}(t). \tag{3.25}$$

Since the Fourier transform of $\delta_{\Delta t}(t)$ is

$$\hat{\delta}_{\Delta t}(\omega) = 2\pi \sum_{m=-\infty}^{\infty} \delta\left(\omega - \frac{2\pi\, m}{\Delta t}\right), \tag{3.26}$$

the Fourier transform of $f^{\Delta t}(t)$ is given as

$$\hat{f}^{\Delta t}(\omega) = \hat{f}(\omega) *_\omega \hat{\delta}_{\Delta t}(\omega) = \sum_{m=-\infty}^{\infty} \hat{f}(\omega + m\,\Omega_{\text{per}}), \tag{3.27}$$

which is periodic with $\Omega_{\text{per}} = 2\pi/\Delta t$. Overlap of the terms in Eq. (3.27) makes that whenever $\hat{f}(\omega)$ is nonzero for $|\omega| > \frac{1}{2}\Omega_{\text{per}}$, then $\hat{f}^{\Delta t}(\omega) \neq \hat{f}(\omega)$ for $|\omega| < \frac{1}{2}\Omega_{\text{per}}$. This effect is called *aliasing* and it is illustrated in Fig. 3.2. The quantity $\frac{1}{2}\Omega_{\text{per}} = \pi/\Delta t = \Omega_{\text{nyq}}$ is the angular Nyquist frequency. In the dual case, sampling of $\hat{f}(\omega)$ with a sampling distance $\Delta\omega$ results in a function $f^{\Delta\omega}(t)$ that is periodic with $T_{\text{per}} = 2\pi/\Delta\omega$. For this case we observe that whenever $f(t)$ is nonzero for $|t| > \frac{1}{2}T_{\text{per}}$, we have a similar overlap of terms in $f^{\Delta\omega}(t)$ for $|t| < \frac{1}{2}T_{\text{per}}$ as in Eq. (3.27). We will refer to this effect as *time-domain aliasing*.

The third property involves rectangular windowing of $f(t)$ and $\hat{f}(\omega)$. If a windowed version of $f(t)$ is given by

$$f^{T}(t) = f(t)\,[H(t+T) - H(t-T)], \tag{3.28}$$

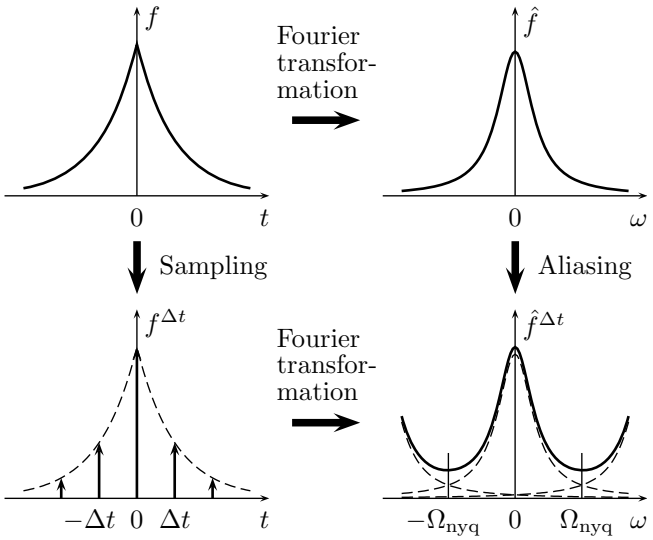

Figure 3.2. Illustration of aliasing in the Fourier domain due to the sampling of a function in the original domain.

where $2T$ is the width of the window, then the Fourier transform of this function is

$$\hat{f}^T(\omega) = \frac{T}{\pi}\hat{f}(\omega) *_\omega \operatorname{sinc}(T\,\omega), \tag{3.29}$$

in which $\operatorname{sinc}(x) = \sin(x)/x$. In the dual case, windowing of $\hat{f}(\omega)$ with a window of width 2Ω,

$$\hat{f}^\Omega(\omega) = \hat{f}(\omega)\,[H(\omega+\Omega) - H(\omega-\Omega)], \tag{3.30}$$

results in a function $f^\Omega(t)$ that is given by

$$f^\Omega(t) = \frac{\Omega}{\pi} f(t) *_t \operatorname{sinc}(\Omega\,t). \tag{3.31}$$

Windowing in the original domain always leads to a function of infinite support in the Fourier domain, and vice versa. In this thesis, we will refer to the operation to obtain $f^T(t)$ or $\hat{f}^T(\omega)$ as *windowing*, and to the operation to obtain $f^\Omega(t)$ or $\hat{f}^\Omega(\omega)$ as *filtering*. The parameters T and Ω are referred to as half window width and cutoff angular frequency, respectively.

The notation introduced in this subsection for the sampling, windowing and filtering operations will be used extensively in the subsequent discussion. Table 3.1 summarizes the definitions in the original domain as well as in the Fourier domain.

Sampling in the original domain

$$f^{\Delta t}(t) = \sum_{n=-\infty}^{\infty} f(n\Delta t)\ \delta\left(\frac{t - n\Delta t}{\Delta t}\right) \qquad \hat{f}^{\Delta t}(\omega) = \sum_{m=-\infty}^{\infty} \hat{f}(\omega + m\,\Omega_{\text{per}}) \quad (\Omega_{\text{per}} = 2\pi/\Delta t)$$

Sampling in the Fourier domain

$$f^{\Delta\omega}(t) = \sum_{m=-\infty}^{\infty} f(t + m\,T_{\text{per}}) \quad (T_{\text{per}} = 2\pi/\Delta\omega) \qquad \hat{f}^{\Delta\omega}(\omega) = \sum_{n=-\infty}^{\infty} \hat{f}(n\Delta\omega)\ \delta\left(\frac{\omega - n\Delta\omega}{\Delta\omega}\right)$$

Windowing

$$f^{T}(t) = f(t)\,[H(t+T) - H(t-T)] \qquad \hat{f}^{T}(\omega) = \frac{T}{\pi}\hat{f}(\omega) *_{\omega} \operatorname{sinc}(T\,\omega)$$

Filtering

$$f^{\Omega}(t) = \frac{\Omega}{\pi} f(t) *_{t} \operatorname{sinc}(\Omega\,t) \qquad \hat{f}^{\Omega}(\omega) = \hat{f}(\omega)\,[H(\omega+\Omega) - H(\omega-\Omega)]$$

Table 3.1. Summary of the definitions of the sampling, filtering and windowing operations in the temporal dimension.

3.3.3 Improved discretization of a convolution integral

In Subsection 3.3.1 we already observed that the straightforward discretization of Eq. (3.10) implies the sampling of $G(t)$ and $S(t)$ with a step size Δt. To analyze this process we first observe that

$$\begin{aligned} G^{\Delta t} *_t S^{\Delta t} &= \int_{-\infty}^{\infty} \sum_q G(q\Delta t)\ \delta\!\left(\frac{t-t'-q\Delta t}{\Delta t}\right) \\ &\qquad \times \sum_m S(m\Delta t)\ \delta\!\left(\frac{t'-m\Delta t}{\Delta t}\right)\ \mathrm{d}t' \\ &= \Delta t \sum_m \sum_q G_q\, S_m\ \delta\!\left(\frac{t-(q+m)\Delta t}{\Delta t}\right) \\ &= \Delta t \sum_m \sum_n G_{n-m}\, S_m\ \delta\!\left(\frac{t-n\Delta t}{\Delta t}\right) \\ &= \sum_n F_n^*\ \delta\!\left(\frac{t-n\Delta t}{\Delta t}\right) \\ &= F^{*,\Delta t}(t), \end{aligned} \tag{3.32}$$

where we have used Eq. (3.11) and the fact that $q = n - m$. As we already noted, in general $F_n^* \neq F_n$ and therefore in general $F^{*,\Delta t}(t) \neq F^{\Delta t}(t)$. This can be seen better when $F^{\Delta t}(t)$ and $F^{*,\Delta t}(t)$ are studied in the Fourier domain and are written out as

$$\hat{F}^{\Delta t}(\omega) = \left(\hat{G}\hat{S}\right)^{\Delta t} = \sum_m \hat{G}(\omega + m\,\Omega_{\mathrm{per}})\ \hat{S}(\omega + m\,\Omega_{\mathrm{per}}), \tag{3.33}$$

$$\begin{aligned} \hat{F}^{*,\Delta t}(\omega) = \hat{G}^{\Delta t}\hat{S}^{\Delta t} &= \sum_m \hat{G}(\omega + m\,\Omega_{\mathrm{per}}) \sum_q \hat{S}(\omega + q\,\Omega_{\mathrm{per}}) \\ &= \hat{F}^{\Delta t}(\omega) + \sum_m \hat{G}(\omega + m\,\Omega_{\mathrm{per}}) \sum_{q\neq m} \hat{S}(\omega + q\,\Omega_{\mathrm{per}}). \end{aligned} \tag{3.34}$$

The remaining sum term in the last expression is caused by the multiplication of the aliased spectra $\hat{G}^{\Delta t}(\omega)$ and $\hat{S}^{\Delta t}(\omega)$, and it forms the actual difference between $\hat{F}^{*,\Delta t}(\omega)$ and $\hat{F}^{\Delta t}(\omega)$. The term is zero when $\hat{G}(\omega)$ and $\hat{S}(\omega)$ are zero outside the region $\omega \in [-\frac{1}{2}\Omega_{\mathrm{per}}, \frac{1}{2}\Omega_{\mathrm{per}}] = [-\Omega_{\mathrm{nyq}}, \Omega_{\mathrm{nyq}}]$. This is in fact the Nyquist-Shannon sampling theorem for bandlimited signals [55], and it forms the basis of our method for the efficient discretization of the convolution integral.

The underlying assumption of our method is that we are only interested in the contributions in $\hat{F}$ with frequencies $|\omega| \leq \Phi$, Φ being the maximum angular frequency of interest. As a consequence of our limited interest, before we sample $G(t)$ and $S(t)$, we limit their spectra by filtering these functions according to Eq. (3.31) with a cutoff angular frequency $\Omega \geq \Phi$, and we use the bandlimited versions $G^{\Omega}(t)$ and $S^{\Omega}(t)$ instead of the original functions $G(t)$ and $S(t)$. Next we sample $G^{\Omega}(t)$ and $S^{\Omega}(t)$ at a sampling distance $\Delta t = \pi/\Omega$, so the situation $\Omega = \Omega_{\text{nyq}}$ occurs and the aliasing error reduces to zero. This means that we obtain F_n^* as the exact value of $F^{\Omega}(n\Delta t)$ for any Ω. The approximation error is then entirely due to the difference between $F^{\Omega}(n\Delta t)$ and $F(n\Delta t)$, and as long as $\Omega \geq \Phi$, i.e. $D_{\Phi} = 2\Omega/\Phi \geq 2$, this difference manifests itself only in the part of the spectrum that we are not interested in. With the proposed method we thus prefer to discard the contributions from the frequencies $|\omega| > \Omega$ over making an aliasing error in the frequency range $|\omega| \leq \Omega$.

So far, everything seems rather ideal. However, computational reality requires us to work with a finite number of samples, and this enforces the windowing of the functions involved, as we did in Subsection 3.3.1. The windowing operation is formally represented by Eq. (3.28) and it ensures that we have at most $2N$ nonzero samples in $G(t)$ and $S(t)$. This is realized by taking a half window width $T < N\Delta t$.[3] The application of the window to $G^{\Omega}(t)$ and $S^{\Omega}(t)$ may re-introduce an infinite support of $\hat{G}^{\Omega,T}(\omega)$ and $\hat{S}^{\Omega,T}(\omega)$ – the order of the superscripts indicating the order of corresponding operations – that leads to an aliasing error when the functions are sampled. This error is however of second order and in general much smaller than the aliasing error which would have been caused by the direct sampling of the functions $G(t)$ and $S(t)$.

When the filtering and windowing operations have been applied to $G(t)$ and $S(t)$, we continue with the procedure as given in Subsection 3.3.1. To summarize, our method for the improved discretization and evaluation of a one-dimensional convolution integral is:

[3] We exclude $T = N\Delta t$ as this gives $2N + 1$ points. For the supports $t \in [0, (N-1)\Delta t]$ of $S(t)$ and $t \in [(-N+1)\Delta t, (N-1)\Delta t]$ of $G(t)$, as in Subsection 3.3.1, the windows are in fact defined with $T = N\Delta t/2$ and $T = (N-1/2)\Delta t$, respectively, where for $S(t)$ the center of the window is shifted to $t = (N-1)\Delta t/2$. This window translation is not incorporated in our definition of the windowing operation Eq. (3.28), but it is not essential to the discussion of Subsections 3.3.2-3.3.4.

1. Subject $G(t)$ and $S(t)$ to a filter with cutoff angular frequency $\Omega \geq \Phi$.
2. Subject $G^{\Omega}(t)$ and $S^{\Omega}(t)$ to suitable time windows with half window width $T < N\Delta t$.
3. Sample $G^{\Omega,T}(t)$ and $S^{\Omega,T}(t)$ on $2N$ points with step size $\Delta t = \pi/\Omega$.
4. Obtain the FFT coefficients of $G_n^{\Omega,T}$ and $S_n^{\Omega,T}$ using an FFT.
5. Multiply the FFT coefficients, return to the original domain using an inverse FFT and scale the result with Δt.

This yields $F^{\Omega,T}(n\Delta t)$ as an approximation for $F(n\Delta t)$. The proposed method will be referred to as the *Filtered Convolution* (FC) method.

To show the improvement with the Filtered Convolution method, let us go back to the integral of the switched harmonic function in Eqs. (3.13)–(3.15). When we apply the filtering operation of Eq. (3.31) to $G(t)$, we obtain

$$G^{\Omega}(t) = \frac{1}{\pi}\left[\mathrm{Si}(\Omega\, t) + \frac{\pi}{2}\right], \tag{3.35}$$

where $\mathrm{Si}(z)$ is the sine integral [2, p. 231]

$$\mathrm{Si}(z) = \int_0^z \frac{\sin(t')}{t'}\,\mathrm{d}t'. \tag{3.36}$$

For $\Omega > \Omega_0$, the filtered form of $S(t)$ becomes

$$\begin{aligned} S^{\Omega}(t) = \quad & \frac{\sin(\Omega_0 t)}{2\pi}\Big\{\mathrm{Si}[(\Omega{+}\Omega_0)(t{-}T_b)] + \mathrm{Si}[(\Omega{-}\Omega_0)(t{-}T_b)] \\ & \qquad - \mathrm{Si}[(\Omega{+}\Omega_0)(t{-}T_e)] - \mathrm{Si}[(\Omega{-}\Omega_0)(t{-}T_e)]\Big\} \\ & - \frac{\cos(\Omega_0 t)}{2\pi}\Big\{\mathrm{Cin}[(\Omega{+}\Omega_0)(t{-}T_b)] - \mathrm{Cin}[(\Omega{-}\Omega_0)(t{-}T_b)] \\ & \qquad - \mathrm{Cin}[(\Omega{+}\Omega_0)(t{-}T_e)] + \mathrm{Cin}[(\Omega{-}\Omega_0)(t{-}T_e)]\Big\}, \end{aligned} \tag{3.37}$$

where $\mathrm{Cin}(z)$ is entire cosine integral [2, p. 231]

$$\mathrm{Cin}(z) = \int_0^z \frac{1-\cos(t')}{t'}\,\mathrm{d}t'. \tag{3.38}$$

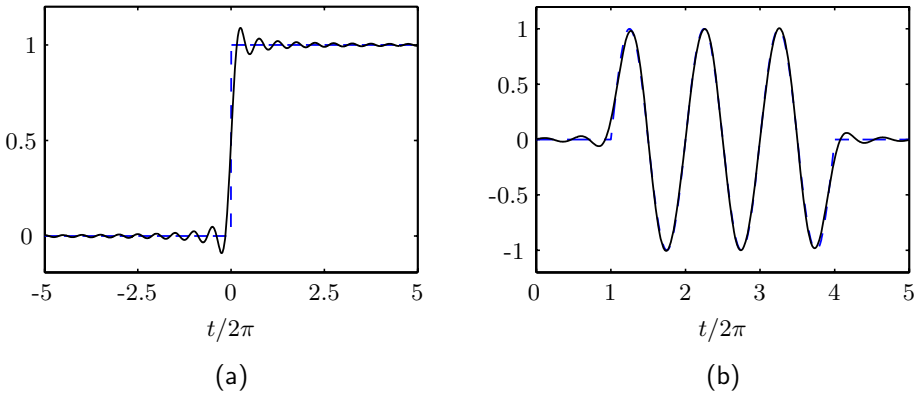

Figure 3.3. (a) Original form (dashed) and filtered form (solid) of $G(t)$ and (b) Original form (dashed) and filtered form (solid) of $S(t)$, both with a cutoff angular frequency $\Omega = 2\,\Omega_0$.

As an example, Fig 3.3 shows the original and filtered functions $G(t)$ and $S(t)$ for $\Omega = 2\,\Omega_0$. Since we apply the FC method, Ω is related to Δt by $\Omega = \Omega_{\text{nyq}} = \pi/\Delta t$. If we vary D_{Ω_0},[4] we get $\Delta t = 2\pi/\Omega_0 D_{\Omega_0}$ and $\Omega = \Omega_0 D_{\Omega_0}/2$, and we obtain estimates $F_n^{\Omega,T}$ on the points $t = n\Delta t$, $n \in [0, N-1]$, with $N - 1 = 10\pi/\Delta t$. The support of S_n^Ω is taken to coincide with the region of interest of F_n^Ω and the support of G_n^Ω is therefore $n \in [-N+1, N-1]$. To prevent the wraparound error in the region of interest and to obtain an FFT with $2N$ points, we zero-pad S_n^Ω with N points and G_n^Ω with one point. Figure 3.4a shows the error in the results of the convolution as obtained with the trapezoidal rule and with the FC method. From the figure we observe a reduction of the error by a factor 30 for the FC method, resulting in an RRMS error below 1% at $D_{\Omega_0} = 5$.[5] The remaining error in the FC method results from the difference between F_n^Ω and F_n and the difference between $F_n^{\Omega,T}$ and F_n^Ω. Figure 3.4b shows the latter two errors plotted separately. We observe that the total error in the FC method is mainly determined by the difference between F_n^Ω and F_n, i.e. the filtering operation. As assumed previously, the difference between $F_n^{\Omega,T}$ and F_n^Ω, i.e. the second-order error introduced by the windowing of the filtered signals, is indeed very small.

[4] As in Subsection 3.3.1, here we describe the discretization in terms of the characteristic frequency Ω_0 instead of the the maximum frequency of interest Φ.

[5] Obviously, for this example the maximum frequency of interest Φ should be taken larger than the chosen characteristic frequency Ω_0. Conform footnote 2 we have $D_\Phi = D_{\Omega_0}\Omega_0/\Phi$.

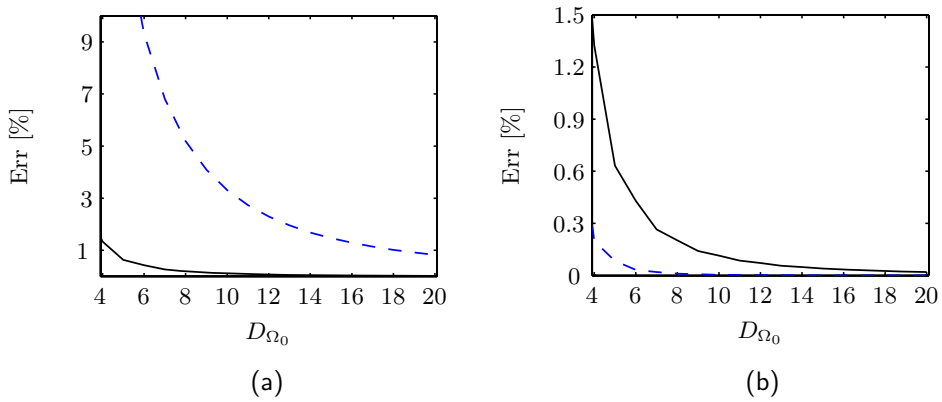

Figure 3.4. (a) RRMS error for the trapezoidal rule (dashed) and the FC method (solid) versus D_{Ω_0}. (b) RRMS error of the FC method splitted up in the error in F_n^{Ω} as compared to F_n (solid) and the error in $F_n^{\Omega,T}$ as compared to F_n^{Ω} (dashed).

An important property of the error for the FC method can be observed from Figure 3.5, where the error $F_n^* - F_n$ corresponding to the trapezoidal rule and the error $F_n^{\Omega,T} - F_n$ corresponding to the FC method are shown for $D_{\Omega_0} = 10$. With the trapezoidal rule the error retains a constant fluctuation, while with the FC method the error is localized mainly around $n = T_b/\Delta t$ and $n = T_e/\Delta t$. As already noted, the error in $F_n^{\Omega,T}$ is explained mostly by the difference between $F^{\Omega}(t)$ and $F(t)$, which is localized around the transitions in $F(t)$ and which is recognized as a Gibbs phenomenon [25].

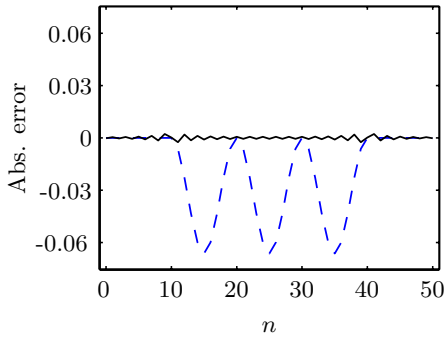

Figure 3.5. Absolute errors $F_n^* - F_n$ for the trapezoidal rule (dashed) and $F_n^{\Omega,T} - F_n$ for the FC method (solid), both with $D_{\Omega_0} = 10$.

3.3.4 Alternative procedure for obtaining the FFT coefficients of the filtered and windowed functions

In the procedure described in the previous subsection we sample the filtered and windowed $G^{\Omega,T}(t)$ and $S^{\Omega,T}(t)$ in the temporal domain and then transform these with an FFT. As an alternative, we can obtain the FFT coefficients of $G^{T,\Omega}(t)$ or $S^{T,\Omega}(t)$ by a direct sampling of their Fourier domain equivalents. When the step size and number of coefficients in the original domain are Δt and $2N$, as in Subsection 3.3.1, then in the Fourier domain the sample points are $\omega = n\Delta\omega$, with $\Delta\omega = \pi/N\Delta t$ and $n \in [-N, N-1]$. To obtain the correct magnitude and format for the application of the inverse FFT, the coefficients need to be scaled with a factor $1/\Delta t$ and they have to be placed in the order $\{[0, N-1], [-N, -1]\}$.

When we intend to adopt this alternative procedure, we need to perform the windowing and filtering in the Fourier domain. In this domain, these operations play a dual role as compared to the original domain. The filtering operation in Eq. (3.30) limits the support of the functions in the Fourier domain to $\omega \in [-\Omega, \Omega]$ and it ensures that we obtain a finite number of samples. The windowing operation, Eq. (3.29), limits the support of the functions in the original domain to $t \in [-T, T]$, where $T < N\Delta t$ as in Subsection 3.3.3, and it ensures that the time-domain aliasing error, which is the dual of the aliasing error, does not occur when the function is sampled in Fourier domain with a step size $\Delta\omega \leq \pi/T$.

In the Fourier domain the filtering is a trivial task. However, as discussed in Subsection 3.3.3, the windowing of $\hat{G}^{\Omega}(\omega)$ and $\hat{S}^{\Omega}(\omega)$ may reintroduce an infinite support and therefore leads to an infinite number of samples. Because of this, in the Fourier domain we need to interchange the order of the filtering and windowing and derive $\hat{G}^{T,\Omega}(\omega)$ and $\hat{S}^{T,\Omega}(\omega)$. Of course, in a dual way to the procedure in Subsection 3.3.3, the filtering of $\hat{G}^{T}(\omega)$ and $\hat{S}^{T}(\omega)$ may re-introduce an infinite support of $G^{T,\Omega}(t)$ and $S^{T,\Omega}(t)$ that leads to a time-domain aliasing error when the functions are sampled in the Fourier domain. This error is however of a second order and in general much smaller than the time-domain aliasing error that would have been caused by the direct sampling of the functions $\hat{G}(\omega)$ and $\hat{S}(\omega)$ in the Fourier domain.

Our aim to remove the aliasing error and thus enable a sampling down to two points per period can thus be attained by the alternative procedure as well as by the original procedure. In summary, the Filtered Convolution

method with the original and alternative procedure is stated as follows:

Original FC method	**Alternative FC method**
1. Subject $G(t)$ and $S(t)$ to a filter with cutoff angular frequency $\Omega \geq \Phi$.	1. Subject $\hat{G}(\omega)$ and $\hat{S}(\omega)$ to suitable time windows with half window width $T < N\Delta t$ with $\Delta t = \pi/\Omega$.
2. Subject $G^{\Omega}(t)$ and $S^{\Omega}(t)$ to suitable time windows with half window width $T < N\Delta t$ with $\Delta t = \pi/\Omega$.	2. Subject $\hat{G}^{T}(\omega)$ and $\hat{S}^{T}(\omega)$ to a filter with cutoff angular frequency $\Omega \geq \Phi$.
3. Sample $G^{\Omega,T}(t)$ and $S^{\Omega,T}(t)$ on $2N$ points with step size $\Delta t = \pi/\Omega$.	3. Sample $\hat{G}^{T,\Omega}(\omega)$ and $\hat{S}^{T,\Omega}(\omega)$ on $2N$ points with step size $\Delta\omega = \Omega/N$.
4. Obtain the FFT coefficients of $G_n^{\Omega,T}$ and $S_n^{\Omega,T}$ using an FFT.	4. Obtain the FFT coefficients of $G_n^{T,\Omega}$ and $S_n^{T,\Omega}$ by scaling with $1/\Delta t$ and reordering.
5. Multiply the FFT coefficients, return to the original domain using an inverse FFT and scale the result with Δt.	5. Multiply the FFT coefficients, return to the original domain using an inverse FFT and scale the result with Δt.

We can of course also choose to derive and sample the filtered and windowed forms of $G(t)$ in the one domain and of $S(t)$ in the other. This freedom will be a benefit when applying the filtering and windowing operations to the specific Green's functions and source functions, as will be shown in Sections 3.4 and 3.5.

3.3.5 Improved discretization and efficient evaluation of the multi-dimensional convolution integral

In order to discretize and evaluate the multi-dimensional convolution integral in Eq. (3.7) using the Filtered Convolution method, we have to apply the filtering and windowing operations to all spatiotemporal dimensions of $G(\boldsymbol{x}, t)$ and $S^{(j)}(\boldsymbol{x}, t)$ before we sample them. The order in which the dimensions

are addressed is not important, and for each dimension we have the freedom to either sample in the original domain or in the Fourier domain. We use the superscripts Ω and T to denote the filtering and windowing operations in the temporal dimension. For the spatial dimension, the filtering and windowing operations will be denoted by the subscripts K and X, respectively. The employed notations and the operations they refer to are summarized for the temporal dimension in Table 3.1, and their spatial counterparts can be straightforwardly derived from them.

The prime parameter for both the spatial and the temporal discretization is the temporal angular cutoff frequency Ω. As explained in Subsection 3.3.3, this quantity directly determines the temporal sampling distance $\Delta t = \pi/\Omega$. For waves in three spatial dimensions, the length of the vectorial wavenumber or the vectorial spatial angular frequency is $\|\boldsymbol{k}\| = (k_x^2+k_y^2+k_z^2)^{1/2}$. Under the assumption that at the cutoff frequency Ω we are only interested in the contribution of propagating (i.e. non-evanescent) waves, we have $\|\boldsymbol{k}\| \leq \Omega/c_0$ and the maximum possible wavenumber in each spatial dimension is $K = \Omega/c_0$. This, in turn, yields the spatial sampling distance in each spatial dimension as $\Delta x = \pi/K = c_0\Delta t$.

Assuming a problem involving one temporal and three spatial dimensions, sampling of the source and Green's function reduces the convolution integral Eq. (3.7) to the convolution sum

$$\mathcal{L}[S^{(j)}]_{a,b,c,n} = \Delta x^3 \Delta t \sum_{d,e,f} \sum_{m} G_{a-d,b-e,c-f,n-m}\, S^{(j)}_{d,e,f,m}, \tag{3.39}$$

where $\mathcal{L}[S^{(j)}]$, G and $S^{(j)}$ denote the spatiotemporally filtered and windowed forms. The evaluation of Eq. (3.39) can be done efficiently with either the original or alternative Filtered Convolution method as summarized in the previous subsection, using the parameters given abouve. In both cases we encounter a four-dimensional FFT and $S^{(j)}_{d,e,f,m}$ has to be zero-padded in all four dimensions to avoid the wraparound error. If $A \times B \times C \times N$ is the total number of points in the discrete domain of interest, the number of operations required for the convolution is of the order $16\, A \times B \times C \times N \log(16\, A \times B \times C \times N)$. Appendix B describes a number of memory-efficient methods for evaluating Eq. (3.39).

The success of the Filtered Convolution method depends on the ability to perform the filtering and windowing operations on the Green's function and on the primary and contrast sources in all spatiotemporal dimensions. This will be the subject of the subsequent sections.

3.4 Spatiotemporal filtering and windowing of the Green's function

In this section we will consider the spatiotemporal filtering and windowing of the Green's functions in Eqs. (3.8) and (3.9) in all occurring dimensions. We will obtain expressions for $\hat{G}_{K,X}^{T,\Omega}$ in the temporal Fourier domain. In Eqs. (3.19) and (3.20) we have already introduced the temporal Fourier transformation pair. In addition, here we introduce the one-dimensional spatial Fourier transformation pair

$$\tilde{F}(k_x,\omega) = \int_{-\infty}^{\infty} \hat{F}(\,x\,,\omega)\,\exp(jk_x x)\,\mathrm{d}x, \tag{3.40}$$

$$\hat{F}(\,x\,,\omega) = \frac{1}{2\pi}\int_{-\infty}^{\infty} \tilde{F}(k_x,\omega)\,\exp(-jk_x x)\,\mathrm{d}k_x, \tag{3.41}$$

and the three-dimensional spatial Fourier transform pair

$$\tilde{F}(\boldsymbol{k},\omega) = \int_{\mathbb{R}^3} \hat{F}(\boldsymbol{x},\omega)\,\exp(j\boldsymbol{k}\cdot\boldsymbol{x})\,\mathrm{d}\boldsymbol{x}, \tag{3.42}$$

$$\hat{F}(\boldsymbol{x},\omega) = \frac{1}{8\pi^3}\int_{\mathbb{R}^3} \tilde{F}(\boldsymbol{k},\omega)\,\exp(-j\boldsymbol{k}\cdot\boldsymbol{x})\,\mathrm{d}\boldsymbol{k}. \tag{3.43}$$

3.4.1 One-dimensional Green's function

The one-dimensional, space-time domain free space Green's function of Eq. (3.8) is repeated here as

$$G(x,t) = \frac{c_0}{2}H(t-|x|/c_0). \tag{3.44}$$

Its temporal Fourier domain equivalent is

$$\hat{G}(x,\omega) = \frac{\exp(-jk\,|x|)}{2jk}, \tag{3.45}$$

where $k = \omega/c_0$ is the wavenumber, and its spatial Fourier domain counterpart is

$$\tilde{G}(k_x,\omega) = \frac{1}{k_x^2 - k^2}. \tag{3.46}$$

We start with the spatial filtering operation. The spatial angular cutoff frequency K is determined by the maximum temporal angular cutoff frequency Ω through $K = \Omega/c_0$. The filtered form of $\tilde{G}(k_x, \omega)$ can then be written as

$$\tilde{G}_K(k_x, \omega) = \tilde{G}(k_x, \omega) H(K - |k_x|). \tag{3.47}$$

With the application of the inverse spatial Fourier transform we obtain the spatially filtered Green's function in the temporal Fourier domain for $|k| < K$ as [69][6]

$$\begin{aligned}\hat{G}_K(x, \omega) = \hat{G}(x, \omega) \\ &- \frac{\cos(k\,|x|)}{2\pi k} \left\{ \mathrm{Cin}[(K-k)\,|x|] - \mathrm{Cin}[(K+k)\,|x|] - \ln\left(\frac{K-k}{K+k}\right) \right\} \\ &- \frac{\sin(k\,|x|)}{2\pi k} \left\{ \mathrm{Si}[(K-k)\,|x|] + \mathrm{Si}[(K+k)\,|x|] - \pi \right\}. \end{aligned} \tag{3.48}$$

Next, we perform the temporal windowing in the temporal Fourier domain. For the *unfiltered* Green's function, temporal windowing yields

$$\begin{aligned} G^T(x, t) &= \frac{c_0}{2} H(t - |x|/c_0) \left[H(t+T) - H(t-T) \right] \\ &= \frac{c_0}{2} \left[H(t - |x|/c_0) - H(t-T) \right] H(c_0 T - |x|), \end{aligned} \tag{3.49}$$

and therefore

$$\hat{G}^T(x, \omega) = \frac{\exp(-jk\,|x|) - \exp(-jk\,c_0 T)}{2jk} H(c_0 T - |x|). \tag{3.50}$$

We may directly apply this result to the first term of Eq. (3.48). The time windowing of the other terms in Eq. (3.48), which represent the spatial filtering operation, is more involving. When we omit the time windowing of these terms, we are bound to make a time-domain aliasing error during the evaluation of the temporal convolution sum. As explained in Subsection 3.3.4, the temporal filtering of $\hat{G}_K^T(x, \omega)$ that must still take place will force us to make a similar time-domain aliasing error anyhow, so we decide to restrict the temporal windowing to the first term of Eq. (3.48) and to leave the other terms in the equation unaffected. Thus, we have obtained an approximation of the spatially filtered, temporally windowed form of $\hat{G}(x, \omega)$, valid for

[6] The differences between Eq. (3.48) and the form used in [69] are due to an alternative definition of the temporal Fourier transform and the use of $\mathrm{Cin}(t)$ instead of $\mathrm{Ci}(t)$.

$|k| < K$,

$$\begin{aligned}\hat{G}_K^T(x,\omega) =& \frac{\exp(-jk\,|x|) - \exp(-jk\,c_0T)}{2jk}\,H(c_0T - |x|) \\ &- \frac{\cos(k\,|x|)}{2\pi k}\left\{\mathrm{Cin}[(K-k)\,|x|] - \mathrm{Cin}[(K+k)\,|x|] - \ln\left(\frac{K-k}{K+k}\right)\right\} \\ &- \frac{\sin(k\,|x|)}{2\pi k}\left\{\mathrm{Si}[(K-k)\,|x|] + \mathrm{Si}[(K+k)\,|x|] - \pi\right\}. \end{aligned} \tag{3.51}$$

In the limit $k \to 0$, Eq. (3.51) reduces to

$$\hat{G}_K^T(x,\omega) = \frac{c_0T - |x|}{2}\,H(c_0T - |x|) - \frac{\cos(K\,|x|)}{\pi K} - \frac{|x|}{2\pi}[2\,\mathrm{Si}(K\,|x|) - \pi]. \tag{3.52}$$

Now we may perform the remaining temporal filtering and spatial windowing operations by straightforward multiplications with the appropriate windows, resulting in $\hat{G}_{K,X}^{T,\Omega}(x,\omega)$. This function can subsequently be sampled in x and ω.

3.4.2 Three-dimensional Green's function

The three-dimensional, space-time, free-space Green's function of Eq. (3.9) is repeated here as

$$G(\boldsymbol{x},t) = \frac{\delta(t - \|\boldsymbol{x}\|/c_0)}{4\pi\,\|\boldsymbol{x}\|}, \tag{3.53}$$

Its temporal Fourier domain equivalent is

$$\hat{G}(\boldsymbol{x},\omega) = \frac{\exp(-jk\,\|\boldsymbol{x}\|)}{4\pi\,\|\boldsymbol{x}\|}, \tag{3.54}$$

where $k = \omega/c_0$ is the wavenumber, and its spatiotemporal Fourier domain counterpart is

$$\tilde{G}(\boldsymbol{k},\omega) = \frac{1}{\|\boldsymbol{k}\|^2 - k^2}. \tag{3.55}$$

We find it most convenient to first perform the spatial filtering in the spatiotemporal Fourier domain. There is a subtlety connected to the filtering

with respect to the three spatial dimensions. To prevent spatial aliasing at Ω with the given spatial sampling, it is *necessary* to ensure that we only have nonzero content in the Green's function at $|k_x| \leq K$, $|k_y| \leq K$ and $|k_z| \leq K$, i.e. to apply a cube-shaped filter in the spatial Fourier domain. This may be achieved by separately applying a filter with cutoff wavenumber K in each spatial dimension. Since at Ω we are only interested in propagating waves, it is *sufficient* to ensure that we only have nonzero frequency content in the Green's function $(k_x^2+k_y^2+k_z^2)^{1/2} \leq K$ with $K = \Omega/c_0$, i.e. to apply a spherical filter with cutoff wavenumber K in the spatial Fourier domain. When employing the spherical filter, we obtain

$$\tilde{G}_K(\boldsymbol{k},\omega) = \tilde{G}(\boldsymbol{k},\omega)\, H(K - \|\boldsymbol{k}\|). \tag{3.56}$$

With the application of the inverse spatial Fourier transform we obtain the spatially filtered Green's function in the temporal Fourier domain for $|k| < K$ as [70][7]

$$\begin{aligned}\hat{G}_K(\boldsymbol{x},\omega) &= \hat{G}(\boldsymbol{x},\omega) \\ &- \frac{\sin(k\,\|\boldsymbol{x}\|)}{4\pi^2\,\|\boldsymbol{x}\|}\left\{\mathrm{Cin}[(K-k)\,\|\boldsymbol{x}\|] - \mathrm{Cin}[(K+k)\,\|\boldsymbol{x}\|] - \ln\left(\frac{K-k}{K+k}\right)\right\} \\ &+ \frac{\cos(k\,\|\boldsymbol{x}\|)}{4\pi^2\,\|\boldsymbol{x}\|}\left\{\mathrm{Si}[(K-k)\,\|\boldsymbol{x}\|] + \mathrm{Si}[(K+k)\,\|\boldsymbol{x}\|] - \pi\right\}.\end{aligned} \tag{3.57}$$

Next, we perform the temporal windowing in the temporal Fourier domain. For the *unfiltered* Green's function, temporal windowing yields

$$\begin{aligned}G^T(\boldsymbol{x},t) &= \frac{\delta(t - \|\boldsymbol{x}\|/c_0)}{4\pi\,\|\boldsymbol{x}\|}\,[H(t+T) - H(t-T)] \\ &= \frac{\delta(t - \|\boldsymbol{x}\|/c_0)}{4\pi\,\|\boldsymbol{x}\|}\,H(c_0T - \|\boldsymbol{x}\|),\end{aligned} \tag{3.58}$$

and therefore

$$\hat{G}^T(\boldsymbol{x},\omega) = \frac{\exp(-jk\,\|\boldsymbol{x}\|)}{4\pi\,\|\boldsymbol{x}\|}\,H(c_0T - \|\boldsymbol{x}\|). \tag{3.59}$$

We may directly apply this result to the first term of Eq. (3.57). Using an identical reasoning as for the one-dimensional Green's function we leave the other terms in the equation unaffected. Thus, we have obtained an

[7] The differences between Eq. (3.57) and the form used in [70] are due to an alternative definition of the temporal Fourier transform and the use of $\mathrm{Cin}(t)$ instead of $\mathrm{Ci}(t)$.

approximation of the spatially filtered, temporally windowed form of $\hat{G}(\boldsymbol{x},\omega)$, valid for $|k| < K$,

$$\begin{aligned}\hat{G}_K^T(\boldsymbol{x},\omega) =& \frac{\exp(-jk\,\|\boldsymbol{x}\|)}{4\pi\,\|\boldsymbol{x}\|}\,H(c_0T-\|\boldsymbol{x}\|)\\ &-\frac{\sin(k\,\|\boldsymbol{x}\|)}{4\pi^2\,\|\boldsymbol{x}\|}\left\{\mathrm{Cin}[(K-k)\,\|\boldsymbol{x}\|]-\mathrm{Cin}[(K+k)\,\|\boldsymbol{x}\|]-\ln\left(\frac{K-k}{K+k}\right)\right\}\\ &+\frac{\cos(k\,\|\boldsymbol{x}\|)}{4\pi^2\,\|\boldsymbol{x}\|}\left\{\mathrm{Si}[(K-k)\,\|\boldsymbol{x}\|]+\mathrm{Si}[(K+k)\,\|\boldsymbol{x}\|]-\pi\right\}. \end{aligned} \tag{3.60}$$

In the limit $\|\boldsymbol{x}\| \to 0$, Eq. (3.60) reduces to

$$\hat{G}_K^T(\boldsymbol{x},\omega) = -\frac{jk}{4\pi}+\frac{k}{4\pi^2}\ln\left(\frac{K-k}{K+k}\right)+\frac{K}{2\pi^2}. \tag{3.61}$$

Now we may perform the remaining temporal filtering and spatial windowing operations by straightforward multiplications with the appropriate rectangular windows, resulting in $\hat{G}_{K,X}^{T,\Omega}(\boldsymbol{x},\omega)$. This function can subsequently be sampled in $\boldsymbol{x}$ and ω.

3.5 Evaluation of the primary and contrast sources

In the previous section we focused on the treatment of the Green's functions. In this section we will discuss the definition, filtering, windowing and evaluation of the primary and contrast sources. Special attention is paid at the evaluation on a coarse grid of the derivatives in the source terms. The discussion focuses on the three-dimensional case, from which the one-dimensional case can straightforwardly be extracted.

3.5.1 Definition, filtering and evaluation of the primary source

The primary source $S^{(0)}(\boldsymbol{x},t)$ is identified as the source term $S(\boldsymbol{x},t)$ in the Westervelt equation (3.3). Conform Eq. (2.58) it is written as

$$S = \rho_0\partial_t q - \boldsymbol{\nabla}\cdot\boldsymbol{f}, \tag{3.62}$$

where q [s^{-1}] is the volume density of the volume injection rate and $\boldsymbol{f}$ [$\mathrm{N\,m}^{-3}$] is the volume density of the external volume force. The two terms in

Eq. (3.62) can be employed to describe jump conditions in $\boldsymbol{v}$ and p across a certain surface. A *velocity jump condition* can be imposed as a volume injection q on an infinitely thin source surface. A velocity jump ΔV in the z-direction across the plane $z = 0$ requires a source term $q = \Delta V\,\delta(z)$, i.e.

$$S = \rho_0 \partial_t [\Delta V\,\delta(z)]. \tag{3.63}$$

Equivalently, a *pressure jump condition* across a surface can be imposed as an external force on an infinitely thin source surface, directed perpendicular to that surface. A pressure jump ΔP across the plane $z = 0$ requires a source term $\boldsymbol{f} = \boldsymbol{i}_z \Delta P\,\delta(z)$, i.e.

$$S = -\partial_z [\Delta P\,\delta(z)]. \tag{3.64}$$

For the problems in this thesis we will describe the primary source with either Eq. (3.63) or Eq. (3.64), and therefore we will focus on these source types and discuss the filtering and windowing for all spatiotemporal dimensions, as well as the evaluation of the occurring derivatives.

In the three-dimensional situation, the excitation functions ΔV or ΔP may depend on x, y and t. Subsection 3.5.2 will be devoted to the spatiotemporal filtering of $\Delta V(x, y, t)$ and $\Delta P(x, y, t)$ in these dimensions. In the z-dimension, filtering of the delta pulse $\delta(z)$ gives, in view of Eq. (3.31),

$$\delta_K(z) = \frac{K}{\pi} \operatorname{sinc}(Kz), \tag{3.65}$$

which for $K = \pi/\Delta x$ gives $1/\Delta x$ for $z = 0$ and 0 for $z = n\Delta x,\ n \neq 0$. Thus, in the calculation of the linear field solution the four-dimensional convolution reduces to a convolution in x, y and t.

The evaluation of the derivatives in the velocity and pressure jump conditions can be performed as follows. The temporal derivative in Eq. (3.63) applies to $\Delta V(x, y, t)$ and may be performed analytically on its time signature if it is known analytically. Alternatively, we could first filter and sample ΔV and then apply a discrete method to approximate the temporal derivative. However, since ΔV is discretized on a coarse grid, a straightforward approach like a second order centered finite difference will not exhibit sufficient accuracy. The issue of evaluating a derivative on a coarse grid will be further discussed in Subsection 3.5.3.

The spatial derivative in Eq. (3.64) applies to the delta pulse $\delta(z)$. We could apply the derivative to the filtered pulse $\delta_K(z)$, but this would turn

the surface source in z into a volume source. Instead, since for a convolution we have the commutative property

$$A *_z (\partial_z B) = (\partial_z A) *_z B = \partial_z (A *_z B), \tag{3.66}$$

we may postpone the evaluation of the derivative until after the convolution of the Green's function with the source. The derivative must then be performed on a function that has been discretized on a coarse grid. For this we need a similar discrete method as for the temporal derivative in the velocity jump condition, which will be discussed in Subsection 3.5.3.

In the discussion up till now we silently assumed that the filtering and windowing operations applied on S commute with the derivatives within S. For the filtering operation this can be easily shown to be true with the aid of Eq. (3.31) and Eq. (3.66). For the windowing operation this is not true, and this may result in an error in the temporal dimension for the velocity jump source and in the z-dimension for the pressure jump source. Regarding the velocity jump source, as long as the time signature has a support that is smaller than the time window, the windowing of the filtered pulse will be applied only to the tails that are due to the filtering and the error will be of a similar smallness as those already made in the approximations of Subsection 3.3.3 and Section 3.4. Regarding the pressure jump source, we observed from Eq. (3.65) that the filtered delta pulse in z only has a value at $z = 0$, and the windowing can therefore be omitted, thus removing the commutativity issue.

3.5.2 Spatiotemporal filtering and windowing of the primary source geometry and signature

The approach for the spatiotemporal filtering of the excitation function, being either $\Delta V(x, y, t)$ or $\Delta P(x, y, t)$, depends on its spatial geometry and its temporal signature. When, apart from the amplitude and the time delay, every point of the source emits the same signature, we can treat the temporal dimension independently from the spatial dimensions. In all practical cases, the spatial support of the source is limited and the explicit spatial windowing for preventing time-domain aliasing error is therefore not necessary. Likewise, all practical sources have a limited temporal support that makes explicit temporal windowing superfluous.

When the source signature has a bandwidth that is already below Ω, the temporal filtering may be skipped as well. In many other situations,

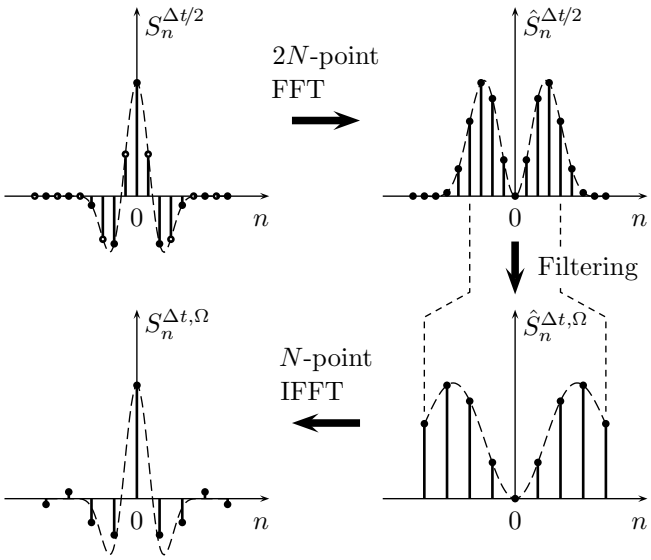

Figure 3.6. Numerical procedure for filtering. In this example, the intended number of gridpoints is $N = 9$ and an oversampling factor $a = 2$ has been used. In the upper left graph, the intermediate samples are indicated with open circles.

the Fourier transform of the signature is known analytically, so the temporal filtering may conveniently be performed in the temporal Fourier domain. In a similar way, the spatial filtering is easily applied whenever the spatial Fourier domain equivalent is available in analytical form, as for rectangular or cylindrical piston sources, or for phased array transducers [85]. In such cases, the sampling is first applied in the Fourier domain, after which an inverse FFT is employed to return to the original domain. By using the spatial filtering we conveniently circumvent problems like staircase effects or the missing out of very small sources that are located in between the gridpoints.

When the filtering of the source cannot be employed before the sampling, e.g. when the source can only be characterized through discrete measurements, aliasing must be avoided in a numerical way. For this we propose the procedure as exemplified in Fig. 3.6 for the time coordinate. This procedure is equally applicable to any of the spatial coordinates. The procedure starts with oversampling the relevant source window at aN points instead of the intended N points. Subjection of the samples to an aN-point FFT yields a discrete version of the Fourier domain function over an interval that is a

times as long as intended but, for a properly chosen oversampling factor a, with negligible aliasing at the N points around the origin. Next, all points except those N around the origin are discarded, thus getting the Fourier domain function over an interval of the intended length. This restriction is the actual filtering step since the remaining discrete interval corresponds with the continuous angular frequency interval $[-\Omega, \Omega]$. Finally, an N-point inverse FFT is performed, and the result is scaled with a factor $1/a$. This yields N samples in the original domain, at the intended sampling distance and with negligible aliasing.

3.5.3 Computing derivatives on a coarse grid

Assume that we have available the values of a certain function $f(t)$ on the points $t = n\Delta t$, $n \in [0, N-1]$. A straightforward method to approximate the derivative $\partial f(t)/\partial t$ on the points $t = n\Delta t$ is to employ a second order centered finite difference (FD) scheme [63]

$$\left.\frac{\mathrm{d}f(t)}{\mathrm{d}t}\right|_{n\Delta t} = \frac{f((n+1)\Delta t) - f((n-1)\Delta t)}{2\Delta t} + \mathcal{O}(\Delta t^2). \tag{3.67}$$

The accuracy of this scheme is such that for a contribution with angular frequency ϕ, as a rule of thumb we would need $D_\phi \geq 10$ for sufficient accuracy. To obtain sufficient accuracy at smaller D_ϕ, as in our case where $\phi = \Omega = \Omega_{\mathrm{nyq}}$ and $D_\phi = D_\Omega = D_{\Omega_{\mathrm{nyq}}} = 2$, we have two alternatives: a high-order FD scheme, or a spectral difference method. A high-order FD scheme is realized by including more sample points in the FD stencil than the two points in Eq. (3.67). The stencil weights can be obtained through the method of undetermined coefficients [51] or via a fast algorithm developed by Fornberg [24, 25]. The limiting case for these high-order FD schemes is the spectral difference, which uses all N points in the interval [25]. It is based on the fact that in the Fourier domain a derivative of a function $f(t)$ turns into a scaling of $\hat{f}(\omega)$ with $j\omega$. The spectral difference method is efficiently implemented with the help of the FFT conform the following procedure:

1. Apply the FFT to the coefficients $f(n\Delta t)$, $n \in [0, N-1]$.
2. Scale the FFT coefficients with $j\,n\Delta\omega$, where $\Delta\omega = 2\pi/N\Delta t$ and n takes on the values $\{[0, (N-1)/2], [-(N/2), -1]\}$ (division rounded down).
3. Apply the inverse FFT.

The spectral difference assumes circular boundary conditions, in other words it assumes that the function $f(t)$ is periodic in $N\Delta t$. If, upon cyclic continuation, there is a nonsmooth transition between the period boundaries, the spectral difference will give rise to a Gibbs phenomenon at the boundary.

The high-order FD scheme gives us more freedom in the treatment at the boundaries. We can of course assume circular boundary conditions, but these give similar problems as with the spectral difference. Alternatively, if we can supply the function values $f(n\Delta t)$ on a larger interval $n \in [-q, N-1+q]$, then we can apply a centered FD scheme of order $2q$ and obtain the derivative on the interval $n \in [0, N-1]$ without extra tricks. A third option is to use asymmetric FD schemes at the boundaries. However, for high-order schemes the magnitudes of some weights become extremely large when the asymmetry increases. This will amplify the numerical errors at the boundary and destroy the accuracy of the FD scheme. A trade-off in accuracy is reached by employing a reduced order at the boundaries when the asymmetry grows.

In conclusion, the spectral difference is the favorite choice as long as we can assure that the transition between end and beginning of the interval of $f(t)$ is smooth. Otherwise we should revert to a high-order FD and treat the boundaries preferably by supplying a longer interval of points than the interval for which the derivative will be needed. If this is not possible, then we will need to satisfy ourselves with asymmetric FD schemes of lower order at the boundaries.

3.5.4 Definition, filtering, windowing and evaluation of the nonlinear contrast source

The contrast source $S^{(j)}(\boldsymbol{x}, t)$ follows from Eqs. (3.4) and (3.6) as

$$S^{(j)} = S^{NL}(p^{(j-1)}) = \frac{\beta}{\rho_0 c_0^4} \partial_t^2 (p^{(j-1)})^2. \tag{3.68}$$

In discussing the filtering of the contrast source, we assume that $p^{(j-1)}$ is bandlimited in all dimensions with a cutoff temporal angular frequency Ω and a cutoff wavenumber K, and we assume that it is given over the domain of interest, which implies the windowing to that domain. When $p^{(j-1)}$ has been obtained as a sampled function with the Filtered Convolution method, these assumptions are always satisfied. The multiplication of a bandlimited signal with itself results in a signal with a bandwidth that is twice as large as the bandwidth of the original signal, while subsequent differentiation has no

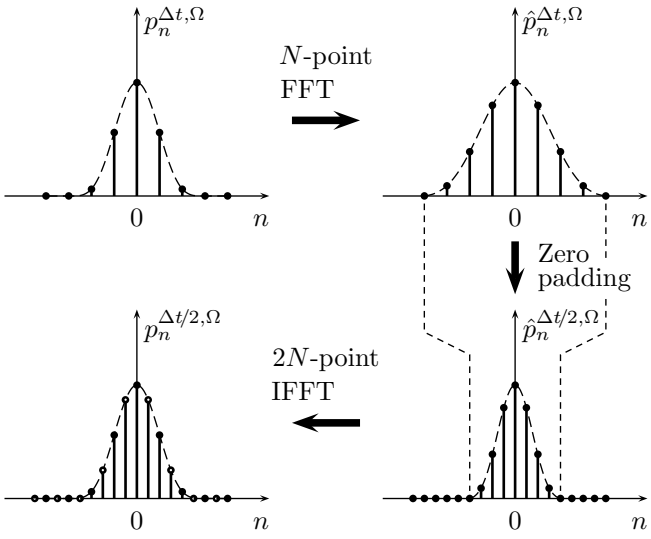

Figure 3.7. Numerical procedure for interpolation. In this example, the available number of gridpoints is $N = 9$. In the lower left graph, the intermediate samples are indicated by open circles.

influence on the bandwidth. Therefore *in principle* the squaring operation in Eq. (3.4) causes the need to filter the contrast source in all spatiotemporal dimensions to avoid aliasing. However, *in fact* the filtering is only necessary for a reduced number of dimensions, as we will discuss in Chapters 4 and 5.

For a given sampled function $p^{(j-1)}$, the following method can be used to perform a temporal filtering of the contrast source. This method is equally applicable to any of the spatial coordinates. When the samples of $p^{(j-1)}$ are multiplied with themselves, the original sampling distances $\Delta t = \pi/\Omega$ and $\Delta x = \pi/K$ are no longer sufficient for the increased bandwidth of the result. To avoid aliasing, we must decrease the relevant sampling distances by a factor 2 before the multiplication takes place. This must be performed by interpolating the available samples of $p^{(j-1)}$ without distorting the corresponding spectral values. To achieve this, we suggest the procedure of spectral interpolation as depicted in Fig. 3.7 for the time coordinate. First, an N-point FFT is applied to the available N sample points. The discrete Fourier domain is then extended from N to $2N$ points by zero-padding. Finally, an $2N$-point inverse FFT is performed and the result is scaled with a factor 2. This yields $2N$ samples in the original domain, without distorting the relevant spectral values. Using the interpolated samples of $p^{(j-1)}$ thus

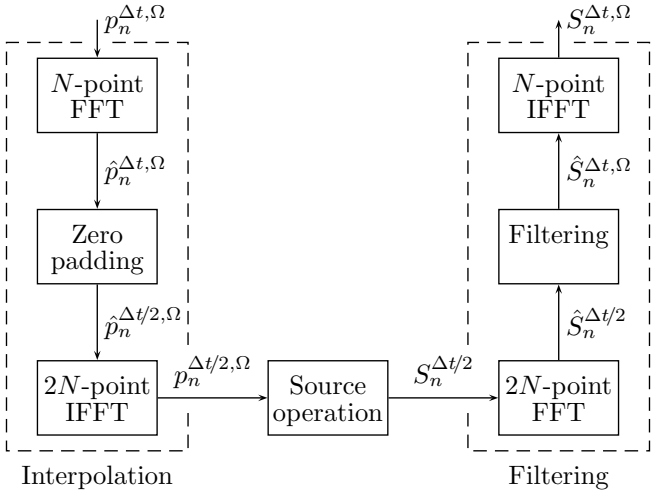

Figure 3.8. The entire numerical procedure for the evaluation of the contrast source.

obtained, we may perform the squaring operation and obtain $2N$ samples of $(p^{(j-1)})^2$. This densely sampled function is then directly amenable for a subsequent numerical filtering according to Fig. 3.6 with $a = 2$. The entire numerical procedure for the evaluation of the contrast source is summarized in Fig. 3.8. An issue of special attention in the procedure is that in a similar fashion as for the spectral difference method discussed in Subsection 3.5.3, the filtering procedure assumes a circular boundary and is therefore sensitive to strong jumps on the boundaries. These jumps may give rise to Gibbs phenomenon at the boundary.

When the product $(p^{(j-1)})^2$ has been obtained, we can calculate the second-order temporal derivative by employing one of the methods already discussed in Subsection 3.5.3. The spectral derivative may be obtained with negligible extra computational cost by benefiting from the availability of the FFT coefficients in the filtering procedure.

3.6 Discussion

In this chapter, we have presented a method to compute an estimate of the nonlinear acoustic pressure. The aim of the method is to enable the evaluation of the nonlinear acoustic pressure on a coarse grid. The nonlinear acoustic pressure was obtained with a Neumann iterative solution of the Westervelt

equation, with the nonlinear term acting as a contrast source. In the scheme, the wavefield estimates were obtained through a convolution of the relevant source terms with the Green's function of the linear background medium. The discretization of this convolution involved spatiotemporal filtering, windowing and sampling of both the Green's function and the sources. It was shown that with this method a discretization of $D_\Phi = 2$ at the maximum angular frequency of interest Φ is feasible in all dimensions with sufficient accuracy. In the upcoming chapters, we will refer to the complete method as the *Iterative Nonlinear Contrast Source* (INCS) method. The part of the method concerning the discretization and evaluation of the convolution will be referred to as the Filtered Convolution (FC) method. In the next chapters, we will use the INCS method for one-dimensional and three-dimensional problems, and we will analyze the ability of the scheme to correctly and accurately predict the nonlinear acoustic pressure.

In the course of the derivation of the INCS method, we have used a number of approximations which may result in global or local errors:

1. In Section 3.1, the nonlinear acoustic pressure $p(\boldsymbol{x}, t)$ is approximated with the iterative estimates $p^{(j)}(\boldsymbol{x}, t)$, resulting in a global error. Provided that the scheme converges, this error is controlled by the number of iterations.

2. In Section 3.3, the pressure estimate $p^{(j)}(\boldsymbol{x}, t)$ is approximated with its spatiotemporally filtered form $p_K^\Omega(\boldsymbol{x}, t)$. As was seen for the example at the end of Subsection 3.3.3, this will mainly establish itself as a localized error at places where sudden transitions in $p^{(j)}(\boldsymbol{x}, t)$ occur. This error is inherent to our choice of focusing on the frequencies $|\omega| < \Omega$, with $\Omega \geq \Phi$.

3. In Section 3.4, errors are introduced in the Green's functions by 1) the application of the spatial window after the application of the spatial filter, 2) the application of the temporal filter after the application of the temporal window, and 3) by not applying the temporal window to the terms in the Green's functions that result from the spatial filter. These approximations may result in global as well as local errors in the pressure estimate, but they are all second-order effects.

4. In Subsection 3.5.2, an error may be introduced if the primary source describes a velocity jump condition. This error is caused by the commutation of the windowing operation and the temporal derivative, and

may establish itself at the beginning and end of the interval in t. It is of a second order and is controllable by choosing a sufficiently long time window.

5. In the numerical evaluation of the derivatives in the primary and contrast sources, as proposed in Subsection 3.5.3, we may also introduce a global error in the entire field and a local error at the beginning and end of the spatial or temporal intervals. The global error is controlled by the order of the numerical scheme, and the local errors can be prevented by choosing a sufficiently long time window.

6. In Subsection 3.5.4, application of the filtering procedure of Fig. 3.8 in the evaluation of the nonlinear contrast source may result in a local error in the form of a Gibbs phenomenon at the boundaries of the temporal or spatial interval. This error is controlled by choosing a sufficiently long time window. Alternatively, when we omit the procedure we may end up with a global error due to aliasing if the nonlinear distortion is strong.

The global errors caused by the approximations 1, 5 and 6 mentioned above affect the nonlinear field distortion, and they will be best visible in the spectral domain. The local errors are mostly located at the boundaries of the spatiotemporal grid. These regions will therefore have our special attention in the numerical experiments in the coming chapters.

We further analyze approximation 2 and its consequences for the modeling of the physical problem at hand. With approximation 2 we project the entire acoustic field problem, i.e. the primary and contrast sources, the Green's function and the resulting acoustic pressure, on a bandlimited space which is governed by the angular cutoff frequency Ω. For the primary source this means that sharp details in the geometry and the signature are blurred. This gives some advantages from the discretization point of view in that we do not suffer from the staircase effect and from the missing out of very small sources that are located in between the grid points. On the other hand, the acoustic field resulting from these sources will also be reproduced only up to Ω in the temporal dimension and up to $K = \Omega/c_0$ in the spatial dimensions. Therefore, sharp transitions in the wavefield in time or space cannot be entirely accounted for, and we expect to observe Gibbs phenomena in the calculated wavefield. Looking back to Fig. 2.1, we could say that beyond the infinitesimal domain we have created another domain, the bandlimited domain, in which the quantities are always continuous instead of piecewise

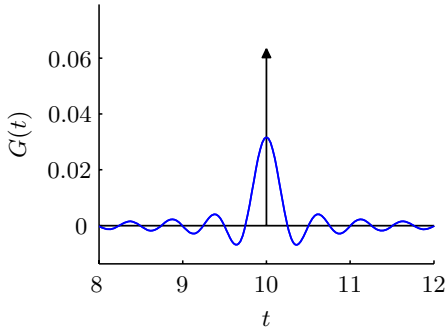

Figure 3.9. Plot of the filtered three-dimensional Green's function versus time for $\|\boldsymbol{x}\|/c_0 = 10$ and $\Omega = 4\pi$.

continuous. In this domain, the differential equations derived in the previous chapter are therefore valid everywhere. This suggests that it is not necessary to formulate boundary conditions since in this domain a boundary will not show up as a discontinuity but as a smooth transition, albeit with the accompanying Gibbs phenomenon.

Apart from the loss of strict localization, another consequence of the projection onto the bandlimited space is the loss of strict causality. This can be demonstrated for the Green's function. Fig. 3.9 shows the three-dimensional spatiotemporally filtered Greens function for $\|\boldsymbol{x}\|/c_0 = 10$, where $\Omega = 4\pi$ and where T is taken sufficiently large. For strict causality, we would expect the Green's function at $t < 10$ to be zero. For the filtered Green's function, this is not the case. If we would like to reproduce the strict causality, this would require an infinitely large maximum frequency of interest. However, this would also give us back the delta pulse and the singularity at $\|\boldsymbol{x}\| = 0$ in the three-dimensional Greens function and the accompanying difficulties in their evaluation. In the bandlimited domain, there is no such thing as a sharp pulse from a sharp point source, but only their filtered equivalents with a level of precision governed by Ω, and for these filtered forms the filtered Green's function suffices. Although in the bandlimited domain causality cannot be defined as strictly as in the infinitesimal domain, we still recognize that a filtered effect cannot precede its filtered cause.

A third consequence of Approximation 2 is that in the projection on the bandlimited space we remove a part of the energy from the original acoustic field. This is performed before the numerical iterative scheme is invoked,

and is thus of a controlled nature that is governed by Ω. In the convolution sum that is subsequently evaluated, no energy is lost, but in the evaluation of the nonlinear contrast source we may again remove some acoustic energy by the procedure to prevent aliasing. The effects of this will be visible in the evaluation of strong nonlinearity, to be studied in the upcoming chapters.

Chapter 4

Application of the INCS method to one-dimensional wave problems

---

In this chapter the INCS method will be applied to one-dimensional, nonlinear acoustic wave problems. We will present numerical results and compare these with results from reference solutions. We will investigate general properties of the nonlinear propagation of plane acoustic waves and we will test the performance of the INCS method for a number of aspects. In Section 4.1, the configuration under study will be described, and in Section 4.2 the implementation of the one-dimensional INCS method is discussed. In Section 4.3 we will present numerical results and discuss observations from those results. The chapter closes with a short discussion in Section 4.4.

Throughout this chapter we will employ the spatial coordinate x. When referring to equations in which the vectorial coordinate $\boldsymbol{x}$ or the coordinate z is used, their replacement by x is implicitly assumed.

4.1 Configuration

We consider the nonlinear propagation of a plane acoustic wave that is excited by a plane surface source at $x = 0$ and that propagates up to a certain distance of interest X in the positive x-direction. The source action is described either by a velocity jump $\Delta V(t)$ as in Eq. (3.63), or by a pressure jump $\Delta P(t)$

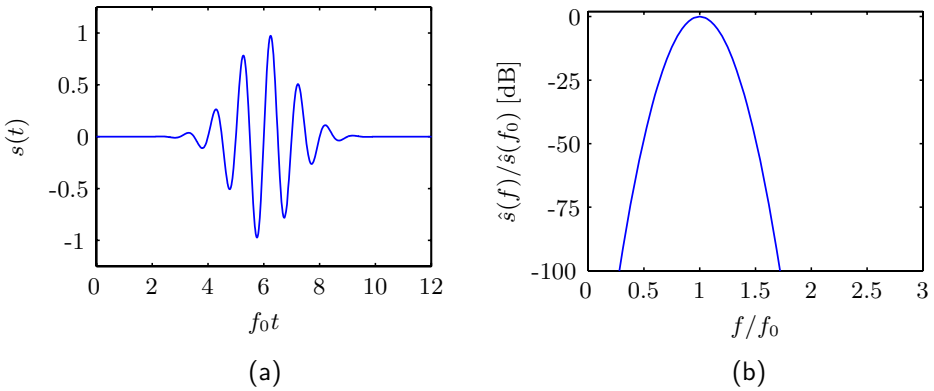

Figure 4.1. (a) Source signature for $T_w = 3/f_0$ and $T_d = 6/f_0$. (b) Spectrum of the source signature.

as in Eq. (3.64). With either of these source types and the one-dimensional Green's function of Eq. (3.8) substituted in Eq. (3.7), the exact solution of the linear pressure field becomes

$$p_L(x,t) = \begin{cases} \rho_0 c_0 & \frac{1}{2}\Delta V(t - |x|/c_0) \\ \\ \operatorname{sign}(x) & \frac{1}{2}\Delta P(t - |x|/c_0) \end{cases}, \quad x \neq 0. \tag{4.1}$$

This shows that for $x > 0$ the linear pressure field from the two source types differs only by the acoustic impedance $\rho_0 c_0$. For a pressure field with an amplitude P_0, the excitation functions are given as

$$\rho_0 c_0 \, \Delta V(t) = \Delta P(t) = 2P_0 \, s(t), \tag{4.2}$$

where $s(t)$ is the source signature. For $s(t)$ we choose a harmonic signal with a Gaussian envelope,

$$s(t) = \exp\left[-\left(\frac{t - T_d}{T_w/2}\right)^2\right] \sin[2\pi f_0 (t - T_d)], \tag{4.3}$$

where T_w and T_d are the width and the delay of the envelope, and f_0 is the fundamental frequency. Representative values of P_0 and f_0 for diagnostic ultrasound are $P_0 = 500$ kPa and $f_0 = 1$ MHz. We set the width and delay of the envelope at $T_w = 3/f_0$ and $T_d = 6/f_0$, giving a pulse of about six cycles as shown in Fig. 4.1.

The medium in which the wave propagates is water, with a small-signal sound speed $c_0 = 1492\ \mathrm{m\,s^{-1}}$, a density of mass $\rho_0 = 998\ \mathrm{kg\,m^{-3}}$ and a coefficient of nonlinearity $\beta = 3.52$. All values apply to an ambient pressure of 10^5 Pa and a room temperature of 23 °C [32, 47, 49]. In all simulations, attenuation will be neglected.

4.2 Implementation

In this section we will discuss the implementation of the INCS method on a number of aspects. We will address the evaluation of the Green's function, the primary source and the nonlinear contrast source, and we discuss the step sizes and domain sizes that will be used in the field calculations.

For the calculation of the nonlinear acoustic field we employ the INCS method with the spatiotemporally filtered and windowed one-dimensional Green's function that has been obtained in Subsection 3.4.1. For the evaluation of the Green's function on the sample points, values for $\mathrm{Cin}(x)$ and $\mathrm{Si}(x)$ can be obtained by implementations found in standard mathematical libraries like NAG [53] or IMSL [75], or they can be obtained by an implementation of the procedure described in [57].

The filtering and evaluation of the primary source is performed as outlined in Subsection 3.5.1–3.5.3. As can be seen from Fig. 4.1b, the chosen source signature has a narrow-band spectrum that at $f = 1.5 f_0$ gives a power level of -48 dB relative to the level at f_0. Thus for $\Omega \geq 3\pi f_0$ the temporal filtering of the primary source is considered superfluous and is omitted. The spatial filter in the x-dimension results in Eq. (3.65). For the velocity jump source, the temporal derivative is applied directly to the source signature in Eq. (4.3). For the pressure jump source, the spatial derivative is applied after the convolution with the Green's function. The spatial derivative is implemented as a centered FD scheme of order 30, where the boundaries are treated by making the x-axis 15 points longer on each side of the spatial interval of interest.

The nonlinear contrast source of Eq. (3.4) is evaluated by using the procedure of Fig. 3.8 in the temporal dimension only. If we assume that the nonlinear pressure field only propagates in the positive x-direction, then spatial filtering of the nonlinear contrast source can be omitted. To show this, we will first study the nonlinear contrast source $S^{NL}(p)$ for a pressure field $p(\boldsymbol{x}, t)$ that consists of two steady-state, plane waves that are traveling in the

positive x-direction and that have frequencies ω_1 and ω_2, with $0 \leq \omega_2 \leq \omega_1$,

$$p(\boldsymbol{x}, t) = \sin\left[\omega_1 t - \frac{\omega_1}{c_0} x\right] + \sin\left[\omega_2 t - \frac{\omega_2}{c_0} x\right]. \tag{4.4}$$

The square of $p(\boldsymbol{x}, t)$ that occurs in $S^{NL}(p)$ consists of five terms

$$p^2(\boldsymbol{x}, t) = I_0 + I_{2\omega_1} + I_{2\omega_2} + I_{\omega_1+\omega_2} + I_{\omega_1-\omega_2}, \tag{4.5}$$

where

$$I_0 = 1, \tag{4.6}$$

$$I_{2\omega_1} = -\frac{1}{2}\cos\left[2\omega_1 t - \frac{2\omega_1}{c_0} x\right], \tag{4.7}$$

$$I_{2\omega_2} = -\frac{1}{2}\cos\left[2\omega_2 t - \frac{2\omega_2}{c_0} x\right], \tag{4.8}$$

$$I_{\omega_1+\omega_2} = -\cos\left[(\omega_1 + \omega_2) t - \frac{\omega_1 + \omega_2}{c_0} x\right], \tag{4.9}$$

$$I_{\omega_1-\omega_2} = \cos\left[(\omega_1 - \omega_2) t - \frac{\omega_1 - \omega_2}{c_0} x\right]. \tag{4.10}$$

In the nonlinear contrast source we have to take the second order temporal derivative of p^2, and therefore the term I_0 yields no contribution. If ω_1 and ω_2 are smaller than the temporal cutoff frequency Ω, as will be the case for a pressure field obtained with the Filtered Convolution method, then the term $I_{\omega_1-\omega_2}$ always contains temporal frequencies $(\omega_1 - \omega_2) \leq \Omega$ and spatial frequencies $(\omega_1 - \omega_2)/c_0 \leq K = \Omega/c_0$. The three remaining terms may actually possess temporal frequencies larger than Ω and spatial frequencies larger than K, which could give rise to aliasing in the temporal and spatial dimensions. The application to p^2 of a temporal filter with a cutoff frequency Ω entirely removes those terms $I_{2\omega_1}$, $I_{2\omega_2}$ and $I_{\omega_1+\omega_2}$ for which $2\omega_1 > \Omega$, $2\omega_2 > \Omega$ and $\omega_1 + \omega_2 > \Omega$, respectively. This implies that those terms $I_{2\omega_1}$, $I_{2\omega_2}$ and $I_{\omega_1+\omega_2}$ that pass the temporal filter automatically have $2\omega_1/c_0 \leq K$, $2\omega_2/c_0 \leq K$ and $(\omega_1+\omega_2)/c_0 \leq K$. Consequently, after the temporal filtering all the spatial frequencies of the terms in Eq. (4.5) are below K and the spatial filter is superfluous. The considered case can be readily generalized to the nonlinear contrast source in a realistic situation where the nonlinear pressure field p consists of a continuum of plane waves, all with temporal frequencies below Ω. Therefore, we conclude that, assuming the nonlinear pressure field propagates in a forward direction and the temporal filtering is applied, spatial filtering of the nonlinear contrast source can be safely omitted.

The temporal derivative in the nonlinear contrast source is evaluated using the spectral difference method. For this, the temporal region of interest is taken such that the linear field solution does not cross the beginning or end of the interval, so that in a cyclic continuation of the contrast source the transition at the period boundaries is sufficiently smooth. This aspect requires that the pulse delay T_d is large enough to have a negligible excitation level at $t = 0$, which is realized by taking $T_d = 6/f_0$, as can be seen from Fig. 4.1. The spatial domain of the contrast source is taken as the entire interval from the primary source up to the distance of interest.

For a given value of D_F[1] at a given maximum frequency of interest F, the step sizes Δt and Δx are given by $\Delta t = \Delta x/c_0 = 1/D_F F$, and the temporal and spatial cutoff angular frequencies Ω and K follow as $\Omega = c_0 K = \pi/\Delta t = \pi\, D_F F$. In the Green's function, K is taken slightly larger than Ω/c_0 to avoid the integrable singularities $k = \pm K$, see Eq. (3.51). For the domain of interest, the chosen distance of interest X also determines the temporal window size T through $T = X/c_0 + T_p$, where T_p is the length of the excitation pulse. For the presented pulse we use $T_p = 12/f_0$. The Green's function is sampled in (x, ω), and the primary source is sampled in (x, t).

The complete algorithm is implemented in Matlab and is evaluated on a laptop PC with a 1.7 GHz processor and 1.25 GB memory. The implementation was done straightforwardly, and the memory requirements for the simulations in this chapter were satisfied without any problems by the applied computer system. Typical run times under Matlab 7.1 ranged from seconds to several minutes.

4.3 Numerical simulations

In this section we will present results of simulations performed with the INCS method as applied to one-dimensional acoustic wave problems. Several cases will be discussed, ranging from the linear field solution in Subsection 4.3.1 to strong nonlinear distortion in Subsection 4.3.4.

[1]Here, the number of points per period is not expressed in terms of the angular frequency ϕ but in terms of the ordinary frequency f, replacing the definition in Eq. (3.12) by $D_f = 1/f\,\Delta t$. Clearly, since $\phi = 2\pi f$, we have $D_f = D_\phi$.

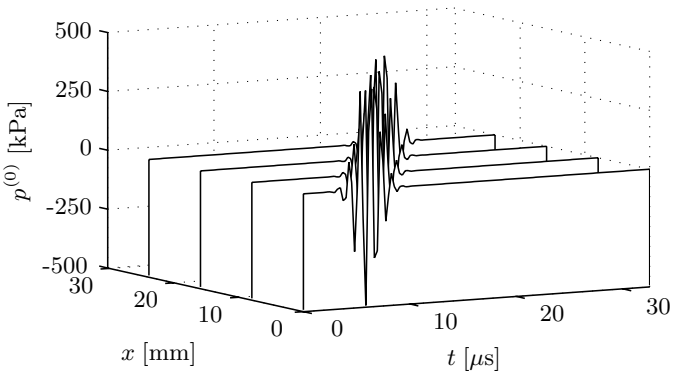

Figure 4.2. Linear pressure field up to $X = 30$ mm obtained by the INCS method with the velocity jump source and $D_F = 4$.

4.3.1 Linear field solution

To first investigate the performance of the INCS method for linear propagation, we compare $p^{(0)}$ with the analytical solution of Eq. (4.1). We use the source and medium parameters as supplied in Section 4.1. For the pulse of Eq. (4.3) we choose a maximum frequency of interest $F = 1.5f_0$. For our domain of interest we take $X = 30$ mm and $T = 32$ μs. Figure 4.2 shows the linear pressure field as obtained by the INCS method with the velocity jump source and with $D_F = 4$, and Table 4.1 summarizes the RRMS errors for various values of D_F, with p_L from Eq. (4.1) as the reference solution. The RRMS error is obtained from Eq. (3.18) by summing over all samples in the domain $(0, X] \times [0, T]$. In the first and second column we list the RRMS errors for the velocity jump source and the pressure jump source. In the third column we list the RRMS errors for $p^{(0)}$ as obtained by the direct approach based on the trapezoidal rule, i.e. by omitting the spatiotemporal filtering and directly sampling the Green's function in Eq. (3.8).[2] From the table we observe that the INCS method shows a considerable improvement compared to the direct method. Already at $D_F = 2.5$ we have an RRMS error below 1% for both source types. We recall that this error includes the intended error that arises from the filtering operation. The large difference in error between the velocity jump source and the pressure jump source for $D_F = 2$ is explained by the limited accuracy of the 30th order FD scheme employed with the latter source type. As can be observed from Fig. 4.3, the absolute

[2]For evaluation purposes, we represent the filtered version of the delta pulse $\delta(x)$ that appears in the source by a value $1/\Delta x$ at $x = 0$ and zero at other sample points.

Table 4.1. RRMS errors in the linear pressure field $p^{(0)}$ for various D_F, listed for the INCS method with either a velocity jump source ΔV or a pressure jump source ΔP, and for the direct approach with a velocity jump source. The reference is the solution p_L from Eq. (4.1).

	RRMS Error [%]		
D_F	INCS ΔV	INCS ΔP	Direct ΔV
2.0	1.6	4.0	41
2.5	0.8	0.4	25
3.0	0.5	0.2	17
4.0	0.3	0.2	10
5.0	0.2	0.2	6

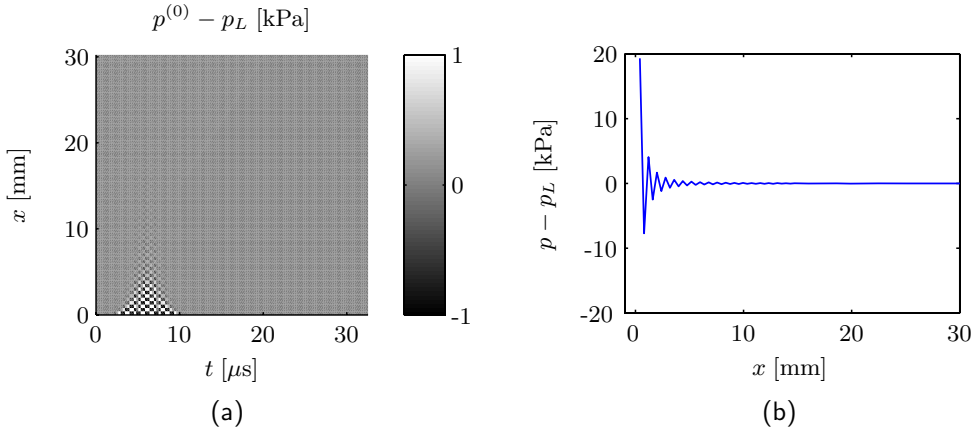

Figure 4.3. (a) Absolute error in the linear pressure field $p^{(0)}$ obtained by the INCS method with the velocity jump source and $D_F = 2.5$. The greyscale axis has been limited to $[-1, 1]$ kPa to focus on the spatiotemporal development of the error. (b) Detail of the absolute error along the x axis at $t = 6.1$ μs. The reference is the solution p_L from Eq. (4.1).

error $p^{(0)} - p_L$ in the INCS method is localized mainly at $x = 0$ and at the time that the source is excited. As Fig. 4.3a shows, we also have a global oscillating error on the entire x-axis at the time of excitation. However, as Fig. 4.3b shows, this global error is 25 times smaller around $x = 0$ than the linear acoustic field solution, and it is rapidly decreasing for increasing x.

4.3.2 Nonlinear field solution

The INCS method is employed to obtain estimates $p^{(j)}$, $j = 1, 2, \ldots$ of the nonlinear pressure field from the velocity jump source. The source and medium parameters as supplied in Section 4.1 are used. The maximum frequency of interest is set at $F = 6.5f_0$ and we keep the discretization at $D_F = 2$, which gives us $\Delta t = 1/13f_0$ and $\Delta x = c_0/13f_0$. For our domain of interest we take $X = 100$ mm and $T = 78$ μs. As a reference we employ the solution p_B of the lossless Burgers equation [15], which is outlined in Appendix A. For the solution of the Burgers equation we use a temporal step size of $\Delta t = 1/200f_0$ and the same spatial step size as is used for the INCS method. Figure 4.4 shows the spectrum of $p^{(j)}$ at $x = 100$ mm for $j = 0$ to 7, and Fig. 4.5 shows a detail of the spectrum of $p^{(7)}$ at the highest harmonic that is accounted for. For higher iterations we observe no significant improvement.

The nonlinear effect causes the appearance of the second and higher harmonic frequency components around multiples of the fundamental frequency f_0, and a component around a frequency below f_0. We denote the fundamental component as F0 and the harmonic components as 2H, 3H etc. The nonlinear component around the frequency below f_0 is known as the self-demodulation part [3]. This component is reproduced by the INCS method, but it will not be considered further in this thesis except for the discussion in Section 4.4. From Fig. 4.4 we observe that each iteration gives a better estimate for increasingly higher harmonics. As both Figs. 4.4 and 4.5 show, the peaks of the higher harmonic frequency components are located at frequencies somewhat higher than the exact multiples of f_0. For the h-th higher harmonic, the peak frequency will be denoted as f_h, and as can be seen from Fig 4.4 this is the frequency at which the $(h+1)$-th maximum of $\hat{p}(f)$ is located. From Fig. 4.5 we observe a slight overestimation of the sixth harmonic as well as the Fourier domain equivalent of a Gibb's phenomenon that is superimposed on the solution. The Gibb's phenomenon has to be attributed to the error made by the spatial windowing of the spatially filtered Green's

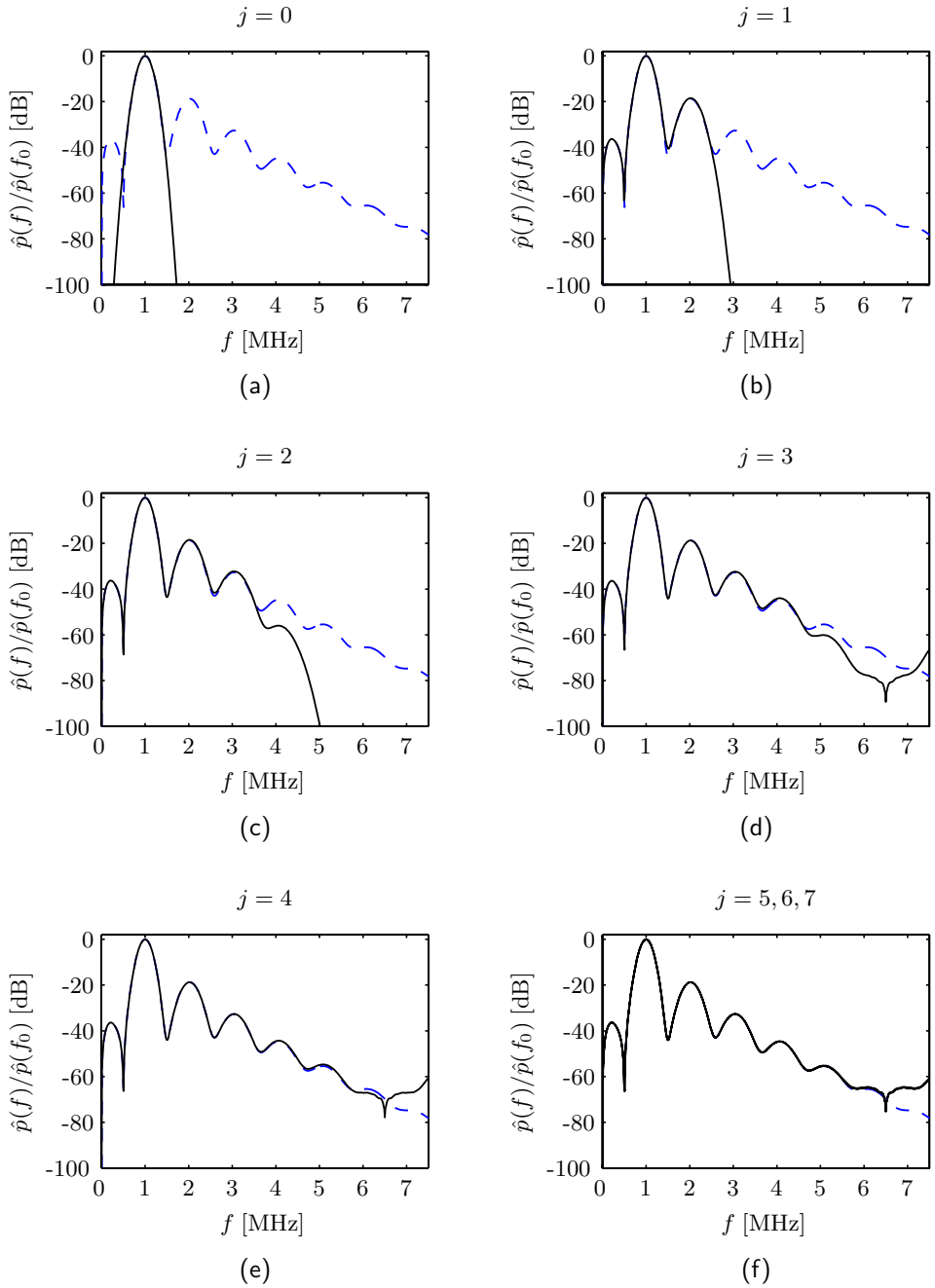

Figure 4.4. (a)-(f) Spectrum of $p^{(j)}$ at $x = 100\,\mathrm{mm}$ as obtained by the INCS method with $j = 0$ to 7 (solid). The reference (dashed) is the solution p_B of the Burgers equation.

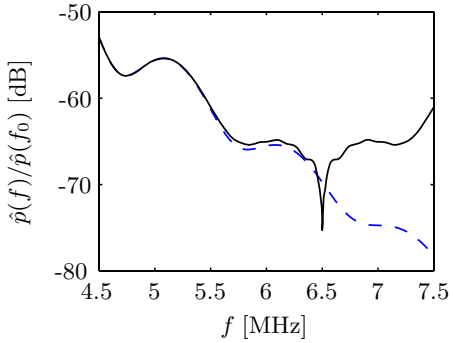

Figure 4.5. Detail at the sixth harmonic of the spectrum of $p^{(7)}$ at $x = 100$ mm as obtained by the INCS method with $F = 6.5$ MHz (continuous). The reference (dashed) is the solution p_B of the Burgers equation.

function. For 6.5 MHz $< f <$ 7.5 MHz, we see the periodical continuation of the spectrum at the negative frequencies $-6.5 < f < -5.5$ MHz due to the fact that the temporal sampling frequency is $2F = 13$ MHz.

Table 4.2 gives the relative errors $[\hat{p}^{(j)}(f_h) - \hat{p}_B(f_h)]/\hat{p}_B(f_h)$ for the peaks $\hat{p}^{(j)}(f_h)$ of the fundamental and the higher harmonics at $x = 100$ mm, for iterations up to $j = 7$. This error follows from comparison with the corresponding solution $\hat{p}_B(f_h)$ of the Burgers equation. From the table we observe that, except for the last harmonic, at an iteration $j = h-1$ we obtain an overestimated approximation of the h-th harmonic with a relative error less than 9%. In the next two iterations the approximations are improved further. As the boldface entries show, for a relative error less than 1% we need iteration $j = h + 1$. This behavior is explained as follows. It appears that as soon as we obtain a rough estimate of the h-th harmonic in iteration $j = h-1$, then in iteration $j = h$ the $(h+1)$-th harmonic is also approximately included in the solution. As soon as this $(h + 1)$-th harmonic is present, in iteration $j = h + 1$ it will lead to a correction of h-th harmonic. The latter correction will significantly reduce the error level. This mechanism also partially explains the persistent error in the sixth harmonic. Apart from the Gibb's phenomenon already noted, this error has to be attributed to the absence of the seventh and higher harmonics that would otherwise lead to corrections of the sixth harmonic.

To further investigate the relation between the different harmonics, Fig. 4.6 shows the spatial development of the higher harmonics up to

Table 4.2. Relative errors in the peaks of the fundamental and the higher harmonics at $x = 100$ mm, as predicted by the INCS method with $j = 0$ to 7. The reference is the solution p_B of the Burgers equation.

j	Relative error [%]					
	f_0	f_2	f_3	f_4	f_5	f_6
0	0.8	-100	-100	-100	-100	-100
1	0.8	2.8	-96	-100	-100	-100
2	**0.0**	2.8	5.2	-69	-89	-100
3	0.0	**0.0**	3.8	7.5	-30	-54
4	0.0	0.0	**-0.1**	3.6	8.5	1.9
5	0.0	0.1	-0.1	**-0.2**	3.1	11
6	0.0	0.1	0.0	0.0	**0.3**	6.7
7	0.0	0.1	0.0	0.1	0.4	**6.3**

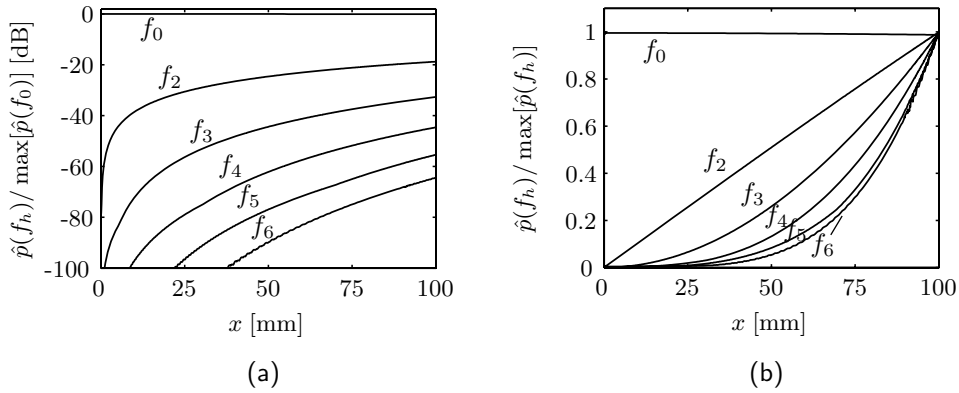

Figure 4.6. Progressive development of the fundamental and the first five harmonic frequency components for $x = 0$ to 100 mm, as predicted by the INCS method with $j = 7$. (a) Logarithmic plot relative to the maximum of $\hat{p}(f_0)$ at $x = 0$ mm. (b) Linear plot, each harmonic relative to its own spatial maximum level.

$x = 100$ mm as predicted by the INCS method with $j = 7$. From Fig. 4.6b we observe a slight decrease in level of $\hat{p}(f_0)$ over distance. Physically, this can be attributed to the transfer of energy from the fundamental component to the harmonic components. The level of the second harmonic component $\hat{p}(f_2)$ shows a nearly linear growth over distance. This indicates that the level of the second harmonic is mainly determined by the accumulation of contributions arising from the fundamental component.[3] Both observations support the conclusions from Table 4.2 that in general a harmonic is mainly determined by its lower harmonic predecessors and is to a lesser degree corrected by its higher harmonic offspring.

4.3.3 Domain of the contrast source

Up to now we have without motivation used a contrast source domain that coincides with the domain of interest of $p(x, t)$. As we saw in the previous subsection, this results in an accurate estimate of the nonlinear pressure field. To test the assumption that it is sufficient to include the nonlinear contrast sources between the primary source at $x = 0$ and the observation point x, we re-run the simulation of the previous subsection, but in each iteration we put the contrast source equal to zero for $x > 50$ mm. Figure 4.7 shows the spatial development of the higher harmonics up to $x = 100$ mm for this situation. We observe that as a result of the removal of the contrast sources beyond $x = 50$ mm the development of all higher harmonics stagnates. A corresponding view is offered in Fig. 4.8, where in the subfigures a and b the linear field solution $p^{(0)}$ and the nonlinear field correction $\delta p^{(7)} = p^{(7)} - p^{(0)}$ are shown up for $x = 0$ to 50 mm. We observe that the correction grows over distance and travels along with the pulse of the linear field solution. Up to $x = 50$ mm, the magnitude of the correction is in the order of 10% of $p^{(0)}$. All separate contrast sources contribute in such a way that the correction field remains in step with the linear pulse. Let us denote the field correction of the simulation with the contrast source domain up to $x = 50$ mm as $\delta p_{50}^{(7)}$. If we subtract from $\delta p_{50}^{(7)}$ the field correction $\delta p_{100}^{(7)}$ of the simulation with the contrast source domain up to $x = 100$ mm, then we observe a small pulse traveling in the negative x-direction, as pictured in Fig. 4.8c. It seems as though the sharp boundary of the contrast source results in a reflection, or

[3] This observation forms the basis for the usability of quasilinear theory to obtain a first approximation for the second harmonic component [32]. The nearly linear growth over distance of the second harmonic component can also be observed from the Fubini solution for harmonic waves [56].

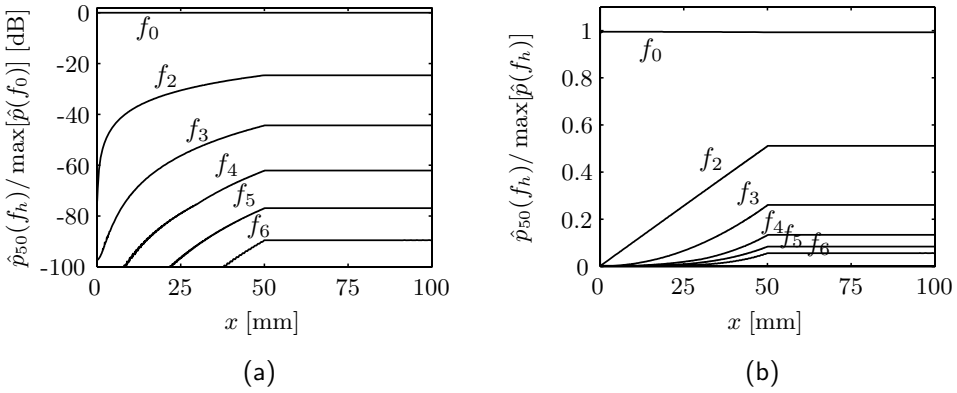

Figure 4.7. Progressive development of the fundamental and the first five harmonic frequency components for $x = 0$ to 100 mm, as predicted by the INCS method with $j = 7$ when the contrast source is put to zero for $x > 50$ mm. (a) Logarithmic plot relative to the maximum of $\hat{p}(f_0)$ at $x = 0$ mm. (b) Linear plot, each harmonic relative to the spatial maximum level it obtains in case of an unmasked contrast source, as in Fig. 4.6.

stated otherwise, as though the contrast sources just before the boundary are missing out the corrective effect that the contrast sources beyond the boundary would have when they would have been included. The reflection is small, and therefore it does not noticeably influence the nonlinear pressure field when the contrast source domain is restricted to the domain from the primary source up to the observation point x.

4.3.4 Behavior at strong nonlinear distortion

The magnitude of the nonlinear distortion of the acoustic field is determined by a number of parameters, whose relation to the occurrence of strongly nonlinear distortion is best shown through the expression for the plane-wave shock formation distance [32]

$$\bar{x} = \frac{\rho_0 \, c_0^3}{2\pi f_0 \beta \, P_0}. \tag{4.11}$$

This expression gives the distance $\bar{x}$ at which a plane-wave pressure field, starting as a harmonic excitation with frequency f_0 and amplitude P_0, and propagating in a homogeneous, lossless, nonlinear medium with parameters ρ_0, c_0 and β, is transformed into a shockwave, i.e. when it has obtained

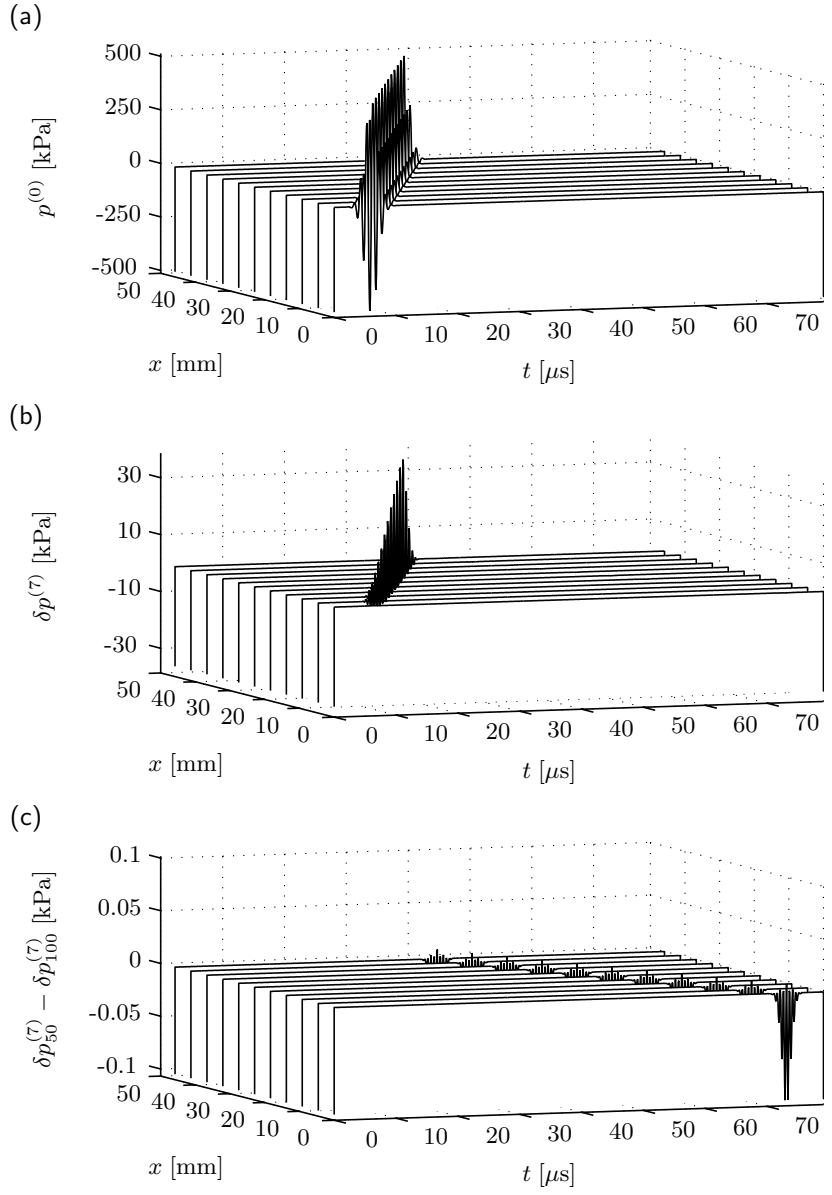

Figure 4.8. (a) Linear field solution $p^{(0)}$ up to $x = 50$ mm. (b) Field correction $\delta p^{(7)}$ up to $x = 50$ mm. (c) Difference between the field correction $\delta p_{50}^{(7)}$ as given by a nonlinear contrast source chopped off at $x = 50$ mm and the field correction $\delta p_{100}^{(7)}$ running up to $x = 100$ mm.

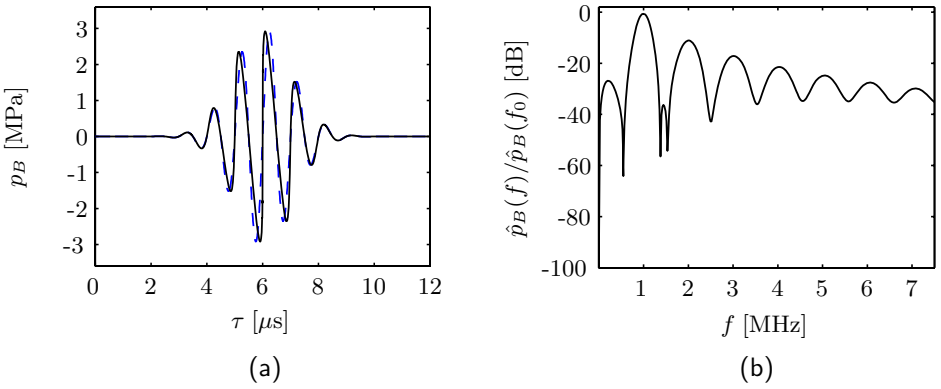

Figure 4.9. (a) Nonlinear waveform steepening for a pulse with $P_0 = 3$ MPa. The dashed line shows the pulse at $x = 0$ mm, the solid line shows the pulse at $\bar{x} = 50$ mm. The pulse is obtained with the solution of Burgers' equation. The time axis is in the comoving time frame $\tau = t - x/c_0$. (b) Spectrum of the pulse at $\bar{x} = 50$ mm.

an infinite slope in its signature. The shock is the result of the effect of nonlinear waveform steepening. This is illustrated in Fig. 4.9, where we have depicted the nonlinear pressure field at $x = \bar{x} = 50$ mm of a pulse with $P_0 = 3$ MPa and with the other parameters taken as in the previous sections. The results have been obtained by using the solution of the Burgers equation with $\Delta t = 1/200 f_0$ and $\Delta x = c_0/13 f_0$. The expression for $\bar{x}$ shows that the strength of the nonlinear distortion increases with increasing β, f_0 and P_0. The lossless nonlinear theory is invalid for $x > \bar{x}$, which makes that the field at $\bar{x}$ is in principle the one with the strongest possible nonlinear distortion that can be studied within the context of this thesis. Still, as Fig. 4.9b shows, the second and higher harmonic frequency components stay below 10 dB relative to the fundamental component, signifying that the nonlinear field can be considered as a nondominant correction to the linear field.

Although the INCS method has not been designed to include shock waves, it is instructive to study the behavior of the method under such a strong nonlinear distortion. Figure 4.10 shows the pressure field and its spectrum at $x = \bar{x} = 50$ mm resulting from a pulse with $P_0 = 3$ MPa and with the other parameters as in the previous sections. The maximum frequency of interest is chosen as $F = 6.5$ MHz, we keep the discretization at $D_F = 2$, and we iterate up to $j = 11$. For higher iterations we observe no significant improvement. The time signature in Fig. 4.10a shows that the

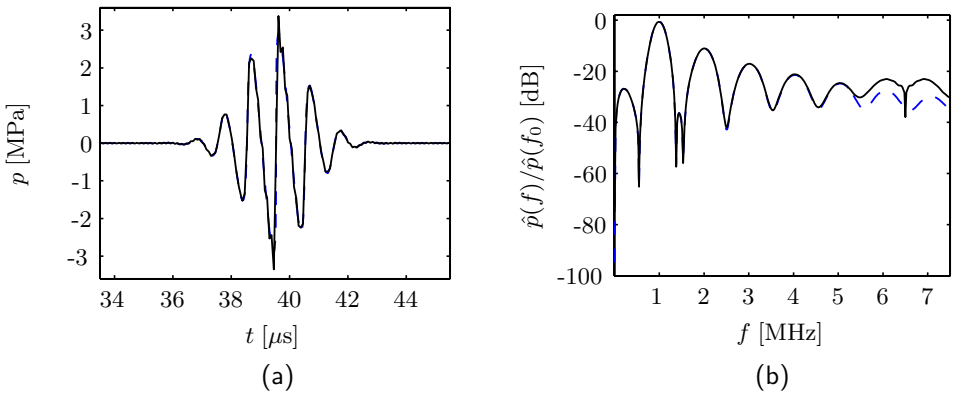

Figure 4.10. (a) Acoustic pressure at $x = \bar{x} = 50$ mm for a pulse with $P_0 = 3$ MPa, as predicted by the INCS method (solid) with $j = 11$, and the solution of the Burgers equation (dashed). (b) Spectrum of the same pulses.

waveform steepening is well accounted for up to a level of detail governed by F. Around the sharpest edge in the center of the pulse we may observe a Gibbs phenomenon superimposed on the signal.

From the spectrum in Fig. 4.10b we observe a significant overestimation of the sixth harmonic and some overestimation of the lower harmonics. This is also observed from Table 4.3, where, for iterations up to $j = 11$, we have listed the relative errors $[\hat{p}^{(j)}(f_h) - \hat{p}_B(f_h)]/\hat{p}_B(f_h)$ for the peaks $\hat{p}^{(j)}(f_h)$ of the fundamental and the higher harmonics at $x = \bar{x} = 50$ mm. This error follows from comparison with the corresponding solution $\hat{p}_B(f_h)$ of the Burgers equation. From the table we observe that for the strongly nonlinear field it takes more iterations for the Neumann scheme to converge than for the weakly nonlinear field. For each harmonic except the sixth we observe at first a strong overestimation of the harmonic peak level, then a smaller underestimation and finally an even smaller overestimation with a relative error up to 3%. The persistent error in the sixth harmonic is 68%. This overestimation can be explained by the inability of the scheme to generate the harmonics above $F = 6.5$ MHz, i.e. the seventh and higher harmonics. Thus, the corrective effect of these higher harmonics on the lower harmonics, especially on the sixth harmonic, is not incorporated. Or, in physical terms, the amount of energy that would otherwise have been transferred from the lower harmonics to the higher ones is not extracted and the lower harmonics, especially the sixth, retain an amplitude that is too large.

Table 4.3. Relative errors in the peaks of the fundamental and the higher harmonics of the acoustic field at $x = 50$ mm of a pulse with $P_0 = 3$ MPa, as predicted by the INCS method with $j = 0$ to 11. The reference is the solution p_B of the Burgers equation.

j	Relative error [%]					
	f_0	f_2	f_3	f_4	f_5	f_6
0	7.6	-100	-100	-100	-100	-100
1	7.6	28	-98	-100	-100	-100
2	-0.3	28	59	-49	-90	-100
3	-1.2	-2.6	41	94	35	29
4	-0.3	-5.4	-12	32	103	110
5	0.0	0.1	-8.9	-24	12	132
6	0.1	1.3	3.0	-7.3	-27	68
7	0.0	0.5	3.0	7.4	-2.5	53
8	0.0	0.2	0.9	4.6	7.0	66
9	0.0	0.3	0.8	2.1	3.0	70
10	0.0	0.3	1.0	2.5	1.6	68
11	0.0	0.3	1.1	2.8	2.2	68

As explained in Section 4.2, to prevent aliasing we employ the filtering procedure of Fig. 3.8 in the evaluation of the nonlinear contrast source. If we omit the filtering procedure and if we revert to a direct evaluation of the contrast source, then the nonlinear pressure field of Fig. 4.11 results. We observe a strong overestimation of the highest harmonics, which reveals itself in the time domain signal as an oscillation around the time signature. Yet, the iterative scheme remains stable even for the shock wave.

In conclusion, although the INCS method is not designed to account for strong nonlinearity, it reproduces the harmonics reasonably well except for the highest harmonic that is accounted for. With these strong nonlinear distortions, the Neumann iterative scheme remains stable up to the shock formation distance $\bar{x}$, although the convergence is somewhat slower than for the weakly nonlinear case. The accuracy of the scheme can be improved by accounting for a larger number of harmonics, which is achieved by increasing F. To obtain an accurate result for the h-th harmonic in the case of strong nonlinearity, the number of iterations has to be taken larger than the rule of thumb $j = h + 1$ as mentioned in Subsection 4.3.2.

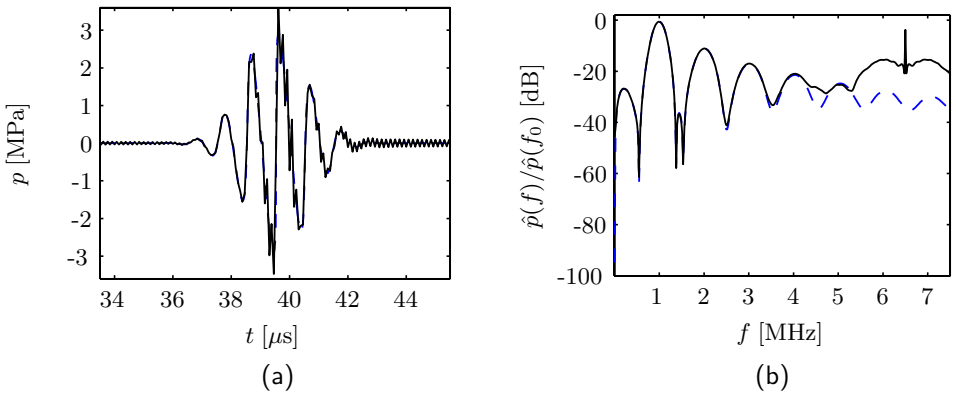

Figure 4.11. (a) Acoustic pressure at $x = \bar{x} = 50$ mm for a pulse with $P_0 = 3$ MPa, as predicted by the INCS method with $j = 11$ and without filtering of the nonlinear contrast source (solid), and the solution of the Burgers equation (dashed). (b) Spectrum of the same pulses.

4.4 Discussion

In this chapter we have investigated the performance of the INCS method for plane, nonlinear acoustic waves. It has been shown that the INCS method is able to accurately generate the linear field solution, as well as the nonlinear field distortion, with a discretization down to two points per period at the maximum frequency of interest. We saw that for moderate nonlinear distortion an accurate estimate of the h-th harmonic frequency component was obtained by including $h+1$ harmonics and by iterating up to $j = h+1$. A rough estimate of the harmonic was already obtained with the inclusion of h harmonics and by iterating up to $j = h-1$. The iterative scheme has been shown to be stable up to the plane-wave shock formation distance. It proved to be necessary and sufficient to employ the filtering procedure in time in the evaluation of the nonlinear contrast source. In all situations the highest harmonic component showed to be more or less overestimated. In the simulations we observed some of the local and global errors that were summarized in Section 3.6, like the artifacts shown in Figs. 4.3 and 4.4b, but none of them showed to have a severe impact on the presented results in the case of moderately nonlinear distortion.

In Subsection 4.3.2 we noted a strong dependence of the harmonics on their preceding and following neighbors. The lower harmonics mainly determined the level of the specific component and the higher harmonics

corrected it to a lesser degree. The generation of higher harmonics may be explained further by considering the nonlinear contrast source

$$S^{NL}(p^{(j-1)}) = \frac{\beta}{\rho_0 c_0^4}\,\partial_t^2 (p^{(j-1)})^2. \tag{4.12}$$

When this expression is transformed to the temporal Fourier domain, we obtain

$$\hat{S}^N(\hat{p}^{(j-1)}) = \frac{-\beta}{\rho_0 c_0^4}\,\omega^2\,(\hat{p}^{(j-1)} *_\omega \hat{p}^{(j-1)}). \tag{4.13}$$

This expression shows that the higher harmonics are introduced into the contrast source by the auto-convolution of the spectrum of the previous nonlinear field estimate. This explains the generation of increasingly higher harmonics in each successive iteration, as pictured in Fig. 4.4. In the linear field solution $p^{(0)}$ we only have the fundamental frequency component around $f = f_0$ and a corresponding component around $f = -f_0$. For the first nonlinear estimate we obtain the self-demodulation component around $f = 0$ and the second harmonic component around $f = 2f_0$ and $f = -2f_0$. Subsequent multiplication with $-\omega^2$ makes that the self-demodulation component is zero at $f = 0$ and that at the other frequencies it is much smaller than the second harmonic component. In each successive iteration, the present harmonics are convolved with themselves and with all other components, and thus we obtain new harmonics and correct the lower ones. This effect explains the iterative behavior as observed with INCS scheme.

From Eq. (4.13) we can also explain the observation that the peaks of the harmonic components are not exactly at the multiples of the fundamental frequency f_0, as was observed from Fig. 4.4. For the first nonlinear contrast source estimate from the linear field solution $p^{(0)}$, the second harmonic component generated by the auto-convolution is at first symmetric around $2f_0$. However, the multiplication with ω^2 favors the higher frequencies within the harmonic component and thus shifts the peak to a frequency that is larger than $2f_0$. For the higher harmonics, this effect results in an increasing deviation of the peak frequency from the integer multiple of the fundamental frequency.

Chapter 5

Application of the INCS method to three-dimensional wave problems

---

In this chapter the INCS method will be applied to a variety of three-dimensional, nonlinear acoustic wave problems. We will present numerical results and compare these with results from reference solutions. General properties of the nonlinear propagation of acoustic fields from various sources will be investigated and the performance of the INCS method will be tested on a number of aspects. In Section 5.1 the configuration under study is described. In Section 5.2 the implementation of the INCS method is discussed. In Section 5.3 we will present the numerical results and discuss observations from those results. The chapter closes with a short discussion in Section 5.4.

5.1 Configuration

We consider the nonlinear propagation of an acoustic wave that is excited by a source located in the plane $z = 0$ and with its center at the origin. We are interested in the nonlinear acoustic pressure field propagating from the source up to a distance of interest $\|\boldsymbol{X}\|$ and propagating in an outward direction, for which often the positive z-direction is taken. The source action is described either by a velocity jump as in Eq. (3.63), or by a pressure jump as in Eq. (3.64). The excitation functions $\Delta V(x, y, t)$ and $\Delta P(x, y, t)$ are

given by

$$\rho_0 c_0 \, \Delta V(x,y,t) = \Delta P(x,y,t) = 2P_0 \, s(t) *_t A(x,y,t), \tag{5.1}$$

where P_0 is the source pressure amplitude, $s(t)$ is the source signature and $A(x,y,t)$ describes the source geometry and time delay. For $s(t)$ we choose a harmonic signal with a Gaussian envelope,

$$s(t) = \exp\left[-\left(\frac{t-T_d}{T_w/2}\right)^2\right] \sin[2\pi f_0 (t-T_d)], \tag{5.2}$$

where T_w and T_d are the width and the delay of the envelope, and f_0 is the fundamental frequency. Representative values of P_0 and f_0 for diagnostic ultrasound are $P_0 = 100$ kPa and $f_0 = 1$ MHz. We set the width and delay of the envelope at $T_w = 3/f_0$ and $T_d = 6/f_0$, giving a pulse of about six cycles as shown in Fig. 4.1. The geometry and delay function may be written as

$$A(x,y,t) = a(x,y) \, \delta[t - t_d(x,y)], \tag{5.3}$$

in which $a(x,y)$ is an geometry function ranging between 0 and 1, and $t_d(x,y)$ is a time delay. Combination of Eqs. (5.1) and (5.3) yields

$$\rho_0 c_0 \, \Delta V(x,y,t) = \Delta P(x,y,t) = 2P_0 \, s[t - t_d(x,y)] a(x,y). \tag{5.4}$$

In the one-dimensional case that was treated in the previous chapter, the velocity and pressure jump conditions yield pressure fields that for $x > 0$ differ only in magnitude by the acoustic impedance $\rho_0 c_0$. In the three-dimensional case that we are dealing with in this chapter, the two source descriptions yield pressure fields that differ in magnitude as well as in shape. The velocity jump condition can be related to the boundary value problem of a transducer mounted in a perfectly rigid baffle in the plane $z = 0$, and prescribes a normal velocity $v_z(x,y,t) = \Delta V(x,y,t)/2$. The pressure jump condition can be related to the boundary value problem of a transducer mounted in a perfectly compliant baffle in the plane $z = 0$, and prescribes a pressure $p(x,y,t) = \Delta P(x,y,t)/2$.[1]

We will consider several types of sources, viz. a point source, an unfocused or focused cylindrical source, a rectangular source, and a steered and

[1] Since we use velocity and pressure jump conditions, our solution applies to a *saltus* problem. Most reference solutions employed in this thesis are based on a *boundary value* problem. A discussion on the difference between saltus problems and boundary value problems can be found in e.g. [6, 17].

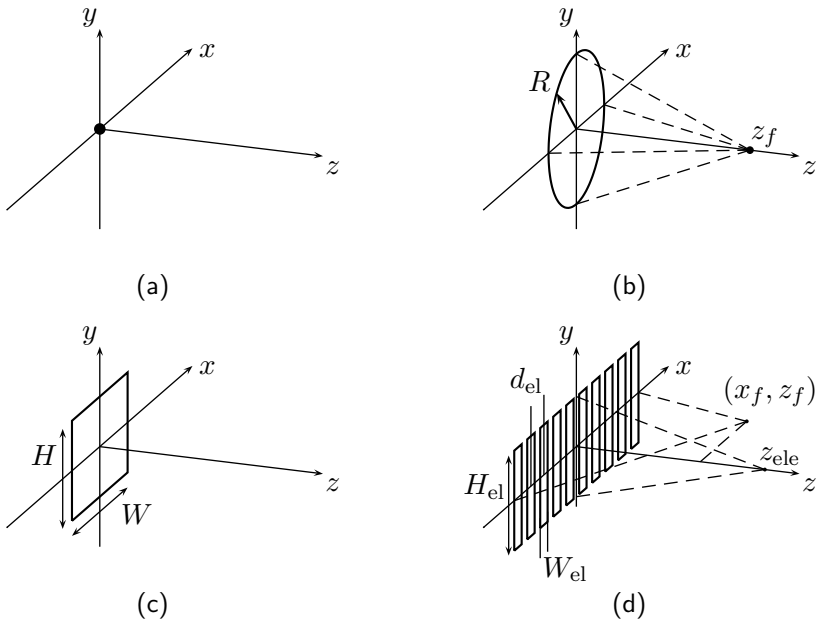

Figure 5.1. Four different source geometries: (a) Point source. (b) Cylindrical source with radius R and focal distance z_f. (c) Rectangular source with width W and height H. (d) Phased array transducer with N_{el} elements of width W_{el}, height H_{el} and pitch d_{el}, and lateral focus (x_f, z_f) and elevation focus z_{ele}, where z_{ele} is not necessarily equal to z_f.

focused phased array transducer. These geometries are shown in Fig. 5.1, together with their respective parameters. For each geometry we obtain a geometry function $a(x, y)$ and a time delay function $t_d(x, y)$. For unfocused sources, $t_d(x, y)$ is zero everywhere. For the focused cylindrical source, the time delay function is

$$t_d(x, y) = \frac{1}{c_0}\left[\sqrt{R^2 + z_f^2} - \sqrt{x^2 + y^2 + z_f^2}\right]. \tag{5.5}$$

For a defocused cylindrical source, the time delay function becomes

$$t_d(x, y) = \frac{1}{c_0}\left[\sqrt{x^2 + y^2 + z_f^2} - |z_f|\right]. \tag{5.6}$$

For the phased array source, in the x-dimension $t_d(x, y)$ is determined by (x_f, z_f) and it varies elementwise. In the y-dimension $t_d(x, y)$ is determined

by z_{ele} and it varies continuously in y. This results in

$$t_d(x,y) = \frac{1}{c_0}\left[\sqrt{(W/2+|x_f|)^2+z_f^2} - \sqrt{(x_{\text{el}}-x_f)^2+z_f^2} + \sqrt{(H_{\text{el}}/2)^2+z_{\text{ele}}^2} - \sqrt{y^2+z_{\text{ele}}^2}\right], \tag{5.7}$$

where W is the total transducer width and x_{el} is the center of the element to which x belongs. Typical geometry sizes range from millimeters to centimeters.

The medium in which the wave propagates is water, with a small-signal sound speed $c_0 = 1492\ \text{m}\,\text{s}^{-1}$, a density of mass $\rho_0 = 998\ \text{kg}\,\text{m}^{-3}$ and a coefficient of nonlinearity $\beta = 3.52$. All values apply to an ambient pressure of 10^5 Pa and a room temperature of 23 °C [32, 47, 49]. In all simulations, attenuation will be neglected.

5.2 Implementation

In this section we will discuss the implementation of the INCS method. We start with specific aspects like the evaluation of the Green's function, the primary source and the nonlinear contrast source. We discuss the step sizes and domain sizes that will be used in the field calculations. Finally, we discuss the general implementation of the method as a Fortran program on a parallel computer.

For the computation of the nonlinear acoustic field we employ the INCS method with the spatiotemporally filtered and windowed three-dimensional Green's function that has been obtained in Subsection 3.4.2. For the evaluation of $\text{Cin}(x)$ and $\text{Si}(x)$ occurring in $\hat{G}^{T,\Omega}_{K,X}(\boldsymbol{x},\omega)$, implementations are available in standard mathematical libraries like NAG [53] or IMSL [75], or they can be obtained by an implementation of the procedure described in [57]. However, since the evaluation of the Green's function contributes significantly to the overall evaluation time of the INCS method, we have developed our own, optimized implementations of these functions.

The primary source is filtered and evaluated with the approaches outlined in Section 3.5. The convolution in Eq. (5.1) is evaluated in the Fourier domain by multiplying $\hat{s}(\omega)$ with $\hat{A}(x,y,\omega)$, where the latter follows from Eq. (5.3) as

$$\hat{A}(x,y,\omega) = a(x,y)\exp[-j\omega\, t_d(x,y)]. \tag{5.8}$$

Equivalent to the situation in the one-dimensional case, the temporal filtering of the source signature $s(t)$ is considered superfluous for $\Omega \geq 3\pi f_0$ and is omitted. Filtering of the primary source in the z-dimension results in Eq. (3.65). The approach for the spatial filtering of $\hat{A}(x, y, \omega)$ in x and y depends on the type of source. Spatial filtering of the point source geometry is performed analytically and leads to Eq. (3.65) in both x and y. For $K = \pi/\Delta x$ and with the x, y and z-dimension all filtered, the point source therefore results in the value $1/\Delta x^3$ at the sample point $(x, y) = (0, 0)$ and zero at the other sample points. The cylindrical source is filtered in x and y by the oversampling procedure outlined in Subsection 3.5.2 with an oversampling factor of eight. The filtering of the rectangular source is performed analytically in x and y employing the filtered form of the Heaviside step function as given in Eq. (3.35). For the phased array source, filtering in the x-dimension is realized by using the filtered form of the Heaviside function for each element since the phase delay function is constant in x over the element. In the y-dimension, we may apply the oversampling procedure with an oversampling factor of eight. The contributions of all elements are subsequently summed.

For the velocity jump source, the temporal derivative is applied directly to the source signature in Eq. (5.2). For the pressure jump source, the spatial derivative is applied after the convolution with the Green's function. The spatial derivative is implemented as a centered FD scheme of order 30, where the boundaries are treated by making the z-axis 15 points longer on each side of the interval of interest.

The nonlinear contrast source of Eq. (3.4) is evaluated by using the procedure of Fig. 3.8 in the temporal dimension only, since the aliasing error caused by omitting the filtering in the spatial dimensions is only small. To show this, we will first study the nonlinear contrast source $S^{NL}(p)$ for a pressure field $p(\boldsymbol{x}, t)$ that consists of two steady-state, two-dimensional, plane waves that are traveling in the plane $y = 0$ that have frequencies ω_1 and ω_2 with $0 \leq \omega_2 \leq \omega_1$, and that cross each other at an angle $0 \leq \alpha \leq \pi$,

$$\begin{aligned} p(\boldsymbol{x}, t) = &\sin\left[\omega_1 t - \frac{\omega_1}{c_0}\sin\left(\frac{\alpha}{2}\right)x - \frac{\omega_1}{c_0}\cos\left(\frac{\alpha}{2}\right)z\right] \\ &+ \sin\left[\omega_2 t + \frac{\omega_2}{c_0}\sin\left(\frac{\alpha}{2}\right)x - \frac{\omega_2}{c_0}\cos\left(\frac{\alpha}{2}\right)z\right]. \end{aligned} \tag{5.9}$$

The square of $p(\boldsymbol{x}, t)$ that occurs in $S^{NL}(p)$ consists of five terms

$$p^2(\boldsymbol{x}, t) = I_0 + I_{2\omega_1} + I_{2\omega_2} + I_{\omega_1+\omega_2} + I_{\omega_1-\omega_2}, \tag{5.10}$$

where

$$I_0 = 1, \tag{5.11}$$

$$I_{2\omega_1} = -\frac{1}{2}\cos\left[2\omega_1 t - \frac{2\omega_1}{c_0}\sin\left(\frac{\alpha}{2}\right)x - \frac{2\omega_1}{c_0}\cos\left(\frac{\alpha}{2}\right)z\right], \tag{5.12}$$

$$I_{2\omega_2} = -\frac{1}{2}\cos\left[2\omega_2 t - \frac{2\omega_2}{c_0}\sin\left(\frac{\alpha}{2}\right)x - \frac{2\omega_2}{c_0}\cos\left(\frac{\alpha}{2}\right)z\right], \tag{5.13}$$

$$I_{\omega_1+\omega_2} = -\cos\left[(\omega_1+\omega_2)t - \frac{\omega_1-\omega_2}{c_0}\sin\left(\frac{\alpha}{2}\right)x - \frac{\omega_1+\omega_2}{c_0}\cos\left(\frac{\alpha}{2}\right)z\right], \tag{5.14}$$

$$I_{\omega_1-\omega_2} = \cos\left[(\omega_1-\omega_2)t - \frac{\omega_1+\omega_2}{c_0}\sin\left(\frac{\alpha}{2}\right)x - \frac{\omega_1-\omega_2}{c_0}\cos\left(\frac{\alpha}{2}\right)z\right]. \tag{5.15}$$

In the nonlinear contrast source we have to take the second order temporal derivative of p^2, and therefore the term I_0 yields no contribution. If ω_1 and ω_2 are smaller than the temporal cutoff frequency Ω, as will be the case for a pressure field obtained with the Filtered Convolution method, then the four remaining terms may actually possess temporal frequencies larger than Ω and spatial frequencies larger than $K = \Omega/c_0$, which could lead to aliasing in the temporal and spatial dimensions. The application to p^2 of a temporal filter with a cutoff frequency Ω entirely removes those terms $I_{2\omega_1}$, $I_{2\omega_2}$ and $I_{\omega_1+\omega_2}$ for which $2\omega_1 > \Omega$, $2\omega_2 > \Omega$ and $\omega_1+\omega_2 > \Omega$, respectively. This implies that those terms $I_{2\omega_1}$, $I_{2\omega_2}$ and $I_{\omega_1+\omega_2}$ that pass the temporal filter automatically have $2\omega_1/c_0 \leq K$, $2\omega_2/c_0 \leq K$, $(\omega_1-\omega_2)/c_0 \leq K$ and $(\omega_1+\omega_2)/c_0 \leq K$. Consequently, after the temporal filtering all the spatial frequencies of these terms are always below K and the spatial filter is superfluous. However, the term $I_{\omega_1-\omega_2}$ may contain a temporal frequency $(\omega_1-\omega_2) \leq \Omega$ and a spatial frequency $(\omega_1+\omega_2)\,c_0^{-1}\,\sin(\alpha/2) > K$ in the x-dimension, and for this term the spatial filter in x would therefore be necessary. The issue is now for which ω_1, ω_2 and α we would still obtain a spatial frequency smaller than or equal to K in this term. Or in other words, given $\omega_1 = \beta\,\Omega$ and $\omega_2 = \gamma\,\omega_1$, for which $0 \leq \alpha \leq \pi$, $0 \leq \beta \leq 1$ and $0 \leq \gamma \leq 1$ we would get

$$(1+\gamma)\,\beta\,\sin\left(\frac{\alpha}{2}\right) \leq 1. \tag{5.16}$$

We observe that this always occurs if $\beta \leq 1/2$, i.e. for frequencies $\omega_2 \leq \omega_1 \leq \Omega/2$, and if $\alpha \leq \pi/3$, i.e. for a crossing angle smaller than 60°. For other values of α and β, only specific ranges of γ yield a spatial frequency larger

than K. For the case of two crossing plane waves we therefore conclude that temporal filtering with a cutoff frequency Ω implies spatial filtering with a cutoff frequency $K \leq \Omega/c_0$ for all frequencies smaller than $\Omega/2$ and for all crossing angles smaller than 60°.

The considered case of two crossing plane waves can be generalized to the nonlinear contrast source in a realistic three-dimensional situation where the nonlinear pressure field p consists of a continuum of plane waves, all with temporal frequencies below Ω. In this realistic situation, we can distinguish between the pressure field in points that are close to the source and the pressure field in points that are some distance away from the source. For points close to the source, the cumulative nature of nonlinear propagation results in a pressure field in which the higher harmonic components are virtually absent, and the field only consists of the fundamental frequency components in a small frequency band around f_0. In any computation involving nonlinear fields, the maximum frequency of interest F is chosen such that at least the second harmonic is incorporated, i.e. $F \geq 2f_0$. As a consequence, for the temporal frequencies involved with the fundamental field we have $\beta \leq 0.5$ near the source, which makes that the spatial filtering will be superfluous here. For points at some distance from the source, the constituents of p will travel more or less parallel to each other and cross each other under an angle far below 60°. This causes that at some distance from the source the spatial filtering may safely be omitted as well. This completes the motivation for the omission of the spatial filtering of the contrast source.

The temporal derivative in the nonlinear contrast source is evaluated using the spectral difference method. For this, the temporal region of interest is taken such that the linear field solution does not extend beyond the beginning or end of the interval, so that in a cyclic continuation of the contrast source the transition at the period boundaries is sufficiently smooth. This aspect requires that the pulse delay T_d is large enough to have a negligible excitation level at $t = 0$, which is realized by taking $T_d = 6/f_0$, as can be seen from Fig. 4.1. As far as the spatial domain of the contrast source is concerned, we observed in the previous chapter that for the one-dimensional case it was sufficient to include the nonlinear contrast sources between the primary source at $x = 0$ and an observation point x. In the current three-dimensional case, we therefore assume that the conical region spanned by a point of observation $\boldsymbol{x}$ (top of the cone) and the primary source (base of the cone) is sufficient as a contrast source domain for yielding an accurate estimate of the nonlinear pressure field in $\boldsymbol{x}$. In other words, from $\boldsymbol{x}$ the

entire source aperture has to be visible through the contrast source domain. We will investigate this assumption in Subsection 5.3.3.

For a given value of D_F[2] at a given maximum frequency of interest F, the step sizes Δt and Δx are given by $\Delta t = \Delta x/c_0 = 1/D_F F$, and the temporal and spatial cutoff angular frequencies Ω and K follow as $\Omega = c_0 K = \pi/\Delta t = \pi\, D_F F$. In the Green's function, K is taken slightly larger than Ω/c_0 to avoid the integrable singularities $k = \pm K$, see Eq. (3.60). The spatial domain of interest follows from the domain of the nonlinear contrast source as described in the previous paragraph, and it spans the entire three-dimensional domain from the primary source to all the points of observation. The temporal window size T is taken as $T = L/c_0 + T_d + T_p$ where L is the largest distance from any point in the spatial domain of interest to any point on the source aperture, T_d is the largest time delay on the source and T_p is the excitation pulse length, which is taken as $T_p = 12/f_0$ for the given pulse.

The complete INCS method has been implemented in Fortran90, both as a sequential program to run on a single processor desktop computer, and as a parallel program to run on a large-scale, clustered multiprocessor system. To realize flexibility and speed we have employed the FFTW library for the evaluation the multi-dimensional FFT's in the algorithm [27]. A significant benefit of this library is that it contains efficient routines for multi-dimensional FFT's, where each dimension can consist of $2^{n_2}3^{n_3}5^{n_5}7^{n_7}11^{n_{11}}13^{n_{13}}$ points , n_2 to n_{13} being arbitrary integers, instead of only being efficient for sizes 2^n as for a standard FFT [28]. In the sequential program as well as in the parallel program, careful attention needs to be given to the memory management in order to enable the evaluation of the nonlinear pressure field in a large four-dimensional domain. Appendix B describes several approaches to reduce either the total grid size or the size of the arrays that need to be stored temporarily during the evaluation of the convolution. In the parallel program, the array that stores the nonlinear contrast source $S^{(j)}(\boldsymbol{x}, t)$ or the pressure field estimate $p^{(j)}(\boldsymbol{x}, t)$ is always distributed evenly over all processors. Depending on the operation to be applied, we employ a T-local distribution, where each processor is allocated a complete time trace for a limited number of spatial points, or an X-local distribution, where each processor is allocated the entire spatial domain for a number of time instances

[2]Here, the number of points per period is not expressed in terms of the angular frequency ϕ but in terms of the ordinary frequency f, replacing the definition in Eq. (3.12) by $D_f = 1/f\,\Delta t$. Clearly, since $\phi = 2\pi f$, we have $D_f = D_\phi$.

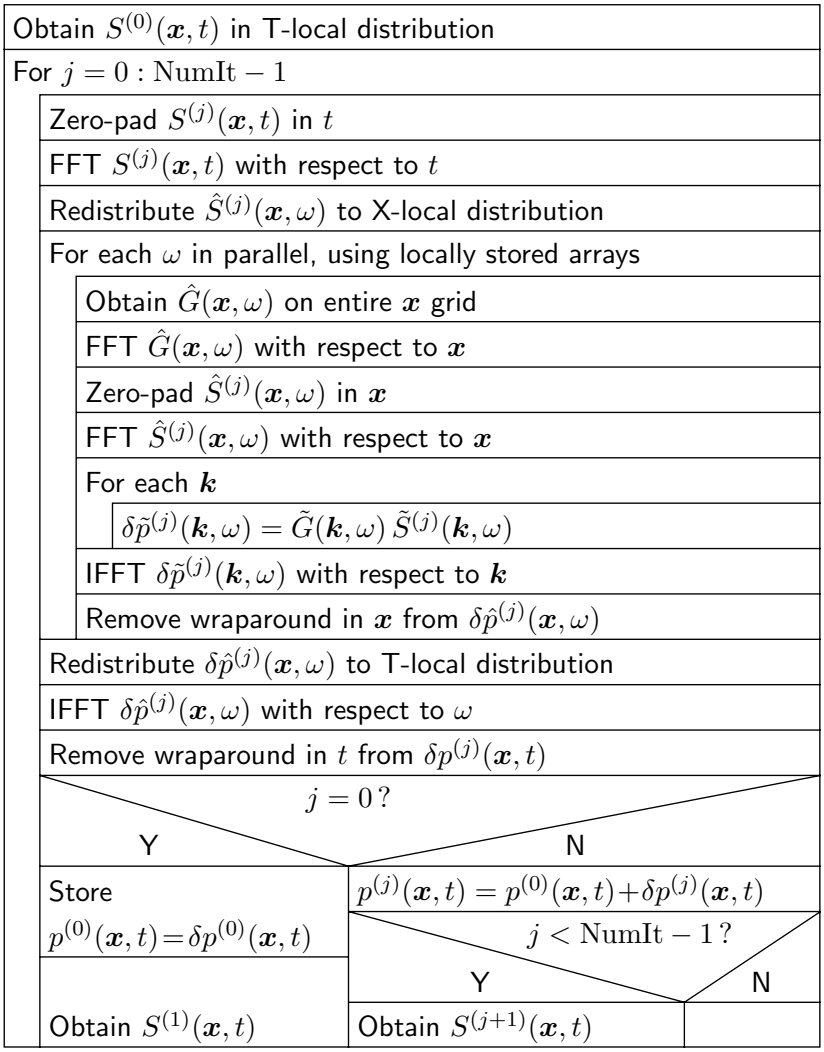

Figure 5.2. Structure diagram for the parallel implementation of the INCS method. The symbols indicating the field solution and correction, the Green's function, and the primary and contrast sources, refer to the filtered, windowed and sampled quantities.

or angular frequencies [42]. In Figure 5.2 we show the structure diagram of the parallel program, in which the focus lies on the evaluation of the convolution. Inside the outer loop over j, first $S^{(j)}(\boldsymbol{x}, t)$ is zero-padded, transformed in the temporal dimension, and redistributed to X-local. In this way, inside the nested loop over ω, the local temporary arrays, which will include the spatial zero-padding regions, need only be three-dimensional arrays. Another advantage of this approach is that the redistribution steps occur outside the loop over ω. Inside this loop, $\hat{G}(\boldsymbol{x}, \omega)$ is evaluated for each angular frequency and each spatial point. The parallel program was run on the Aster computer at SARA in Amsterdam, which is an SGI Altix 3700 clustered multiprocessor system consisting of 416 Intel Itanium 2 processors running at 1.3 GHz and with 2 GB memory per processor.

5.3 Numerical simulations

In this section we will present results of simulations performed with the INCS method as applied to three-dimensional acoustic wave problems. Several cases will be discussed, ranging from a linear field solution in Subsection 5.3.1 to strong nonlinear distortion in Subsection 5.3.5. For the discretization of the linear field problem, we will fix a specific maximum frequency of interest F and we will vary the number of points per wavelength D_F down to $D_F = 2$. For all nonlinear field problems, we will vary F depending on the number of harmonic frequency components to be included, and we will keep D_F fixed at $D_F = 2$. In all situations we will focus on the field in the plane $y = 0$, as this plane contains the characteristic features of the spatial field distribution.

We will employ four methods for the presentation of the results:

1. To compare the linear field solution p of the INCS method with a corresponding reference solution p_{ref}, we apply the RRMS error

$$\mathrm{Err} = \sqrt{\frac{\sum \left[p(x,0,z,t) - p_{\mathrm{ref}}(x,0,z,t)\right]^2}{\sum p_{\mathrm{ref}}^2(x,0,z,t)}}, \tag{5.17}$$

where the summations are taken over all sample points $(x, 0, z, t)$ in the plane $y = 0$ and within the domain of interest.

2. For the visualization of the spatial characteristics of the linear field solution and the nonlinear field correction we define the *profile* $P[p](\boldsymbol{x})$ as the

maximum of the envelope of the acoustic pressure $p(\boldsymbol{x}, t)$ in a point $\boldsymbol{x}$, obtained with

$$P[p](\boldsymbol{x}) = \max_t\{|p(\boldsymbol{x}, t) + j\,\mathcal{H}_t[p(\boldsymbol{x}, t)]|\}, \tag{5.18}$$

where $\mathcal{H}_t[p(\boldsymbol{x}, t)]$ denotes the temporal Hilbert transform of $p(\boldsymbol{x}, t)$. To obtain an accurate pressure profile, the coarse discretization employed in the INCS method may require the pressure signature to be interpolated in time with the procedure of Fig. 3.7, before Eq. (5.18) is applied.

3. For the visualisation of the frequency contents of the nonlinear field solutions, we transform the pressure field to the time Fourier domain and we define the h-th harmonic *spectral profile* as the peak level $\hat{p}(\boldsymbol{x}, f_h)$. For the higher harmonics, f_h is defined as the frequency where the $(h+1)$-th maximum of the spectrum of p is located. To assess the accuracy of the nonlinear field solution of the INCS method, its spectral profiles $\hat{p}(\boldsymbol{x}, f_h)$ will be compared to the spectral profiles $\hat{p}_{\text{ref}}(\boldsymbol{x}, f_h)$ obtained by other methods.

4. In some cases however, the spectral profile does not yield a representative view of the higher harmonic frequency contents generated by nonlinear distortion. For example, this is the case if the three-dimensional linear acoustic field has several arrivals due to the finite source geometry. In such cases, we will extract the harmonic component by applying a bandpass filter to the pressure field $p(\boldsymbol{x}, t)$ and subsequently obtain the profile of the filtered pressure field component by applying Eq. (5.18). For the h-th harmonic, we will use an eighth-order Butterworth filter with cutoff frequencies $(h-0.3)f_0$ and $(h+0.3)f_0$. The main advantage of this *filtered profile* $P_h[p](\boldsymbol{x})$ is that it is more robust than the spectral profile in case of a multiple arrival, in case of a long pulse in combination with a short temporal window, or in case of experimental artifacts. An extra advantage may be that it yields a time domain quantity rather than a frequency domain quantity, as the latter makes sense only in relative terms. Since it is less straightforward to compute than the spectral profile, we will employ the filtered profile only in cases where the spectral profile would yield ambiguous results.

In the upcoming sections, all profiles will be shown on a dB-scale relative to a certain characteristic field profile level.

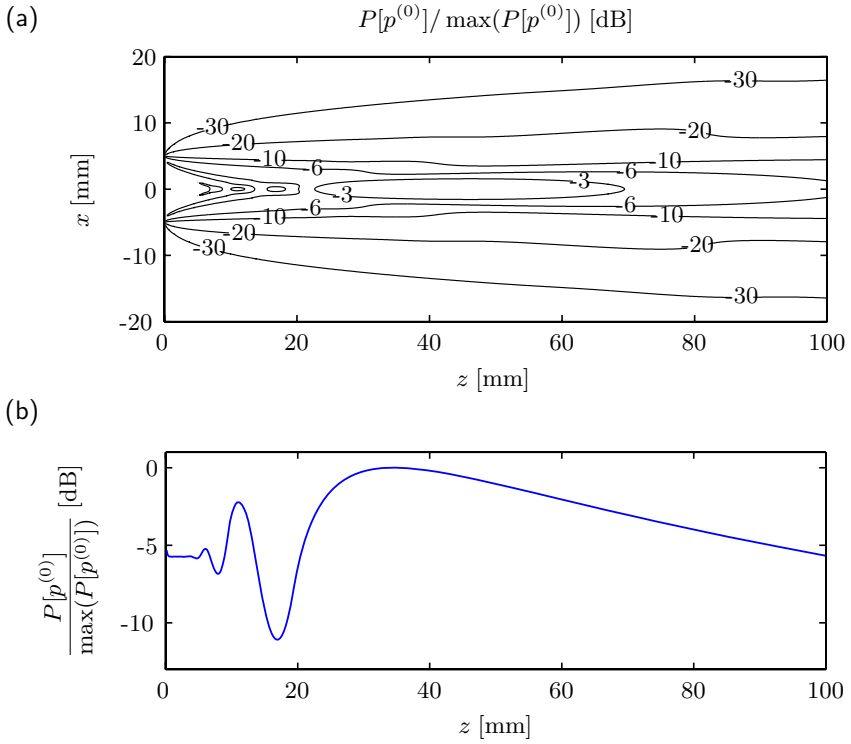

Figure 5.3. Linear profile $P[p^{(0)}]$ for the cylindrical piston source. (a) In the plane $y = 0$. (b) On the z-axis. The discretization is $D_F = 2.33$.

5.3.1 Linear field solution

We start the investigation of the performance of the INCS method by considering linear propagation. We will use the method to obtain $p^{(0)}$ for two different source types. For both source types, we use the source signature of Eq. (5.2) with $f_0 = 2$ MHz and $P_0 = 100$ kPa. Further we choose a maximum frequency of interest $F = 1.5 f_0$.

Our first source type is an unfocused cylindrical source with a radius $R = 5$ mm, causing a pressure jump. The linear field solution $p^{(0)}(\boldsymbol{x}, t)$ is obtained in a domain of interest with a spatial size of 40 mm$\times$2 mm$\times$100 mm and a comoving temporal window of 10 μs. Figure 5.3a shows several contours of the linear profile $P[p^{(0)}]$ in the plane $y = 0$ for $D_F = 2.33$. Figure 5.3b shows the profile on the axis of the transducer, which coincides with the z-axis. The maximum of $P[p^{(0)}]$ equals 193 kPa and is found at the natural

Table 5.1. RRMS error in the linear pressure field $p^{(0)}(\boldsymbol{x}, t)$ of the unfocused cylindrical source, obtained by the INCS method with various D_F. The reference is the solution as derived in Appendix C. Also listed are the grid size, the wall clock time needed for the evaluation and the number of processors.

D_F	Err [%]	4D grid size $\times 10^6$ points	Wall clock time [s]	Number of processors
2.00	4.0	25.72	143	4
2.33	1.0	39.26	230	4
2.67	0.8	60.24	393	4
3.33	0.5	155.7	873	4
4.00	0.5	345.6	686	8
5.33	0.4	1150	1203	48

focus $(x, y, z) = (0, 0, 34)$ mm.

Our results are compared to results from a reference solution for the pressure field of a cylindrical piston source causing a pressure jump. This has been obtained using a Lobatto quadrature integration of the Kirchhoff-Huygens integral across the source surface, which is derived in Appendix C. Table 5.1 presents the RRMS error for various D_F. Also listed are the corresponding grid size, the evaluation time and the number of processors used by the INCS method. From these simulations we observe that the results for $D_F = 2.33$, with an RRMS error of 1%, compare very well with the reference solution. The arrival times of the body waves and the edge waves[3] are reproduced correctly. The latter is also the case for $D_F = 2$, although for this discretization the RRMS error is 4%. For higher D_F, the error decreases quickly to a level of 0.4% at $D_F = 5.33$. The main contribution to the latter error comes from the first plane beyond the source plane $z = 0$ at the time that the source is excited. If the first plane is left out of the RRMS error, the RRMS errors for $D_F = \{3.33, 4.00, 5.33\}$ respectively decrease to $\{0.2\%, 0.1\%, 0.1\%\}$.

The second source type presented in this subsection is a phased array source causing a velocity jump. The transducer is a 64 element array with element parameters $W_{\text{el}} \times H_{\text{el}} = 0.25$ mm $\times$ 12 mm and $d_{\text{el}} = 0.3$ mm. The array is focused at $(x_f, z_f) = (0, 60)$ mm and $z_{\text{ele}} = z_f$. The linear field

[3] see Appendix C

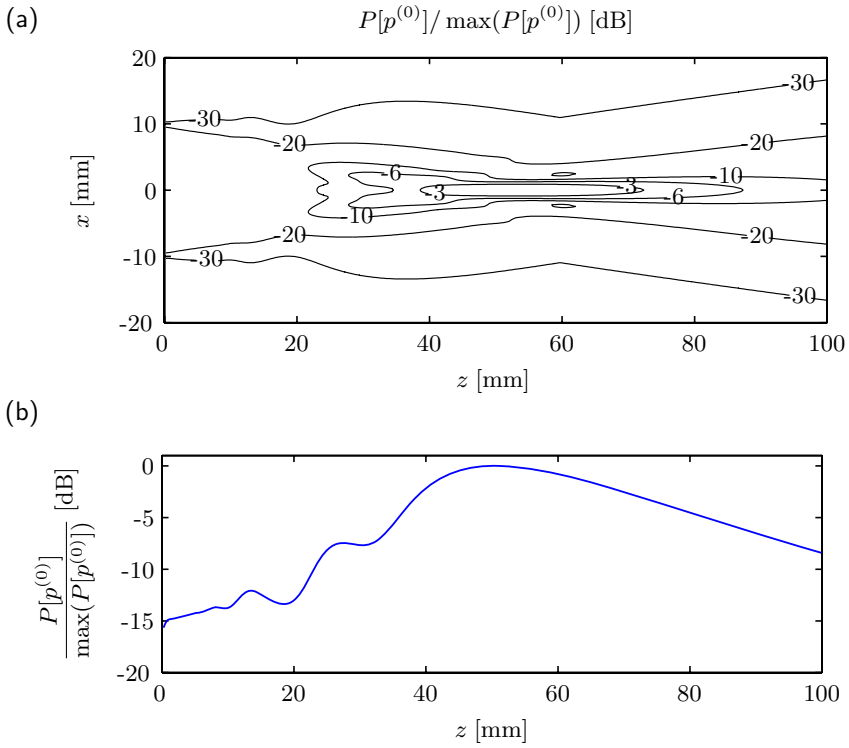

Figure 5.4. Linear profile $P[p^{(0)}]$ for the phased array source. (a) In the plane $y = 0$. (b) On the z-axis. The discretization is $D_F = 2$.

solution $p^{(0)}(\boldsymbol{x}, t)$ is obtained in a domain of interest with a spatial size of 80 mm $\times$ 1 mm $\times$ 100 mm and a comoving temporal window of 20 μs. Figure 5.4a shows the profile $P[p^{(0)}]$ in the plane $y = 0$ for $D_F = 2$. Figure 5.4b shows the profile on the axis of the transducer. The profile level close to the source is about 83 kPa,[4] and the maximum of $P[p^{(0)}]$ equals 470 kPa and is found at the realized focus $(x, y, z) = (0, 0, 51)$ mm.[5]

Our results are compared with results from the FieldII program [38, 39]. FieldII solves the Rayleigh integral [61], which applies to a source in a per-

[4]The ratio of the profile level of 83 kPa close to the source and the source pressure $P_0 = 100$ kPa is the same as the ratio of the element width $W_{\mathrm{el}} = 0.25$ mm and the pitch $d_{\mathrm{el}} = 0.3$ mm.

[5]The realized focal distance $z = 51$ mm is smaller than the theoretical focal distance $z_f = 60$ mm. This is due to the fact that the phased array source has a limited height and number of elements, whereas in the calculation of the element delays from the theoretical focal distance we assume that these parameters are infinite.

Table 5.2. RRMS error in the linear pressure field $p^{(0)}(\boldsymbol{x}, t)$ of the phased array source, obtained by the INCS method with various D_F. The reference solution is the result given by the FieldII program. Also listed are the grid size, the wall clock time needed for the evaluation and the number of processors.

D_F	Err [%]	4D grid size $\times 10^6$ points	Wall clock time [s]	Number of processors
2.00	1.6	67.0	352	4
2.67	1.0	161.6	510	8
3.33	0.7	318.1	1380	8

fectly rigid baffle. Table 5.2 presents the RRMS error for various D_F, in combination with the grid size, the evaluation time and the number of processors used by the INCS program. The FieldII solution has been obtained with a temporal sampling frequency of 400 MHz and with 20 by 40 mathematical elements for each transducer element in the x and y-dimensions. From Table 5.2 we observe that the results from both programs show excellent comparison already for $D_F = 2$. The large difference in error between the cylindrical source and the phased array source for $D_F = 2$, being respectively 4% and 1.6%, is explained by the limited accuracy of the 30th order FD scheme employed in the evaluation of the pressure jump condition for the cylindrical source.

From these cases we observe that large domains, with up to the order of 500×10^6 grid points, can be handled successfully with the parallel program employing a limited number of processors. This problem size is equivalent to a four-dimensional computational domain of 75 wavelengths/periods at $f_{\max}$ in each spatiotemporal dimension. This gives a clear indication of the applicability of our method to large-scale problems. As can be seen from the last line of Table 5.1, the problem size and computation time grow massively for increasing D_F. This illustrates once more the necessity of a coarse discretization. The second case shows that our method is capable of accurately computing the linear acoustic pressure field of complex planar sources, even when discretized with $D_F = 2$.

5.3.2 Directional independence

As discussed in Section 1.3, most models used to predict the nonlinear acoustic field of medical transducers assume that the wavefield is quasi-plane. Compared to these models, an important benefit of the INCS method is the directional independence of the linear and nonlinear field solution. We will demonstrate this by using the INCS method to compute the nonlinear pressure field from a point source located at $\boldsymbol{x} = \boldsymbol{0}$. The point source is defined as[6]

$$S = S_0\, S(t)\, \delta(\boldsymbol{x}). \tag{5.19}$$

The linear field solution for the point source is found by substituting Eq. (5.19) and the three-dimensional Green's function of Eq. (3.9) in Eq. (3.7). This yields

$$p_L(\boldsymbol{x}, t) = \frac{S_0\, S(t - \|\boldsymbol{x}\|/c_0)}{4\pi\, \|\boldsymbol{x}\|}, \quad \boldsymbol{x} \neq 0. \tag{5.20}$$

The signature of the point source is the harmonic signal with $f_0 = 1$ MHz and a Gaussian envelope as used before, and S_0 is taken such that at $\|\boldsymbol{x}\| = 1$ mm the linear profile is $P_1 = 500$ kPa, i.e. $S_0 = 2\pi \times 10^3$ N m^{-1}. We compute the nonlinear pressure field in a domain of interest of size 8.6 mm $\times$ 8.6 mm $\times$ 8.6 mm, centered at the origin, and a temporal window of 12 μs. The maximum frequency of interest is $F = 5$ MHz, we sample at $D_F = 2$ and we use iteration $j = 3$.

Figure 5.5a shows the linear profile $P[p^{(0)}]$ in the plane $y = 0$, and Fig 5.5b shows $P[p^{(0)}]$ on the z-axis, together with the profile $P[p_L]$ of the linear field solution from Eq. (5.20). As observed from this figure, the INCS method reproduces the linear field profile accurately except for a very small region around the point source.

To investigate the directional independence of the INCS method, we check the profile $P[p^{(0)}]$ of the linear field solution and the profile $P[\delta p^{(3)}] = P[p^{(3)} - p^{(0)}]$ of the nonlinear field correction on the half circle with radius $\|\boldsymbol{x}\| = 4$ mm that is indicated in Fig. 5.5a. The mean levels of the linear field profile and the nonlinear field correction profile on that radius are $\overline{P}[p^{(0)}] = 123$ kPa and $\overline{P}[\delta p^{(3)}] = 0.97$ kPa, respectively. Figure 5.6 shows

[6] The point source thus defined can be interpreted as a velocity jump source, and it can be translated to the form of Eq. (5.1) by taking $P_0 = c_0 S_0/2$, $s(t) = \int_{-\infty}^{t} S(t')\,\mathrm{d}t'$, $a(x, y) = \delta(x)\delta(y)$ and $t_d = 0$.

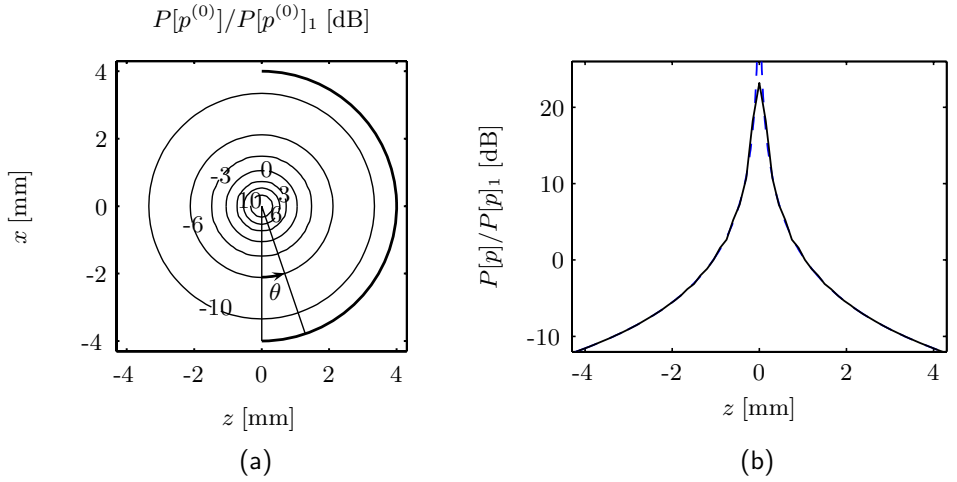

Figure 5.5. Profile $P[p^{(0)}]$ for the point source. (a) In the plane $y = 0$, together with the half-circle referred to in the text. (b) On the z-axis, as obtained from the INCS method (solid) and from the analytical solution in Eq. (5.20) (dashed).

the relative variation of the mentioned radial profiles around their mean levels, versus the angle θ. We observe that the relative directional variation is less than 0.05 dB, which is equal to 0.6%. This forms a good illustration for the directional independence of the INCS method, both for the linear field solution as well as for the nonlinear field correction.

In Fig. 5.6 we have used the entire domain of interest as the contrast source domain for the nonlinear field corrections. If the contrast source domain is limited in the z-direction to the interval $[-0.8, 4.3]$ mm, we get the profiles as shown in Figs. 5.7a and c. The variation in the profile of the nonlinear field correction around its mean level is increased but it is still less than 0.2 dB. However, if the contrast source domain is limited in the z-direction to the interval $[0, 4.3]$ mm, as in Figs. 5.7b and d, the variation in the nonlinear field correction profile around its mean levels increases to a magnitude of 3 dB with a trend towards $\theta = 0°$ and $\theta = 180°$. These results show that the nonlinear contrast source method model is indeed free of directional dependence as long as the nonlinear contrast source domain is chosen correctly.

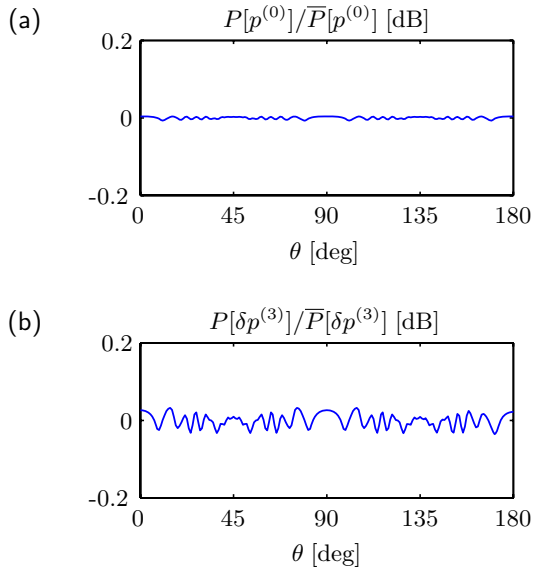

Figure 5.6. Radial profile levels at a radius $\|\boldsymbol{x}\| = 4$ mm, versus angle θ. (a) For the linear field solution $p^{(0)}$. (b) For the nonlinear field correction $\delta p^{(3)}$.

5.3.3 Domain of the contrast source

As we have observed in the previous subsection, it is essential to incorporate the nonlinear contrast sources that contribute significantly to the nonlinear distortion, in order to obtain an accurate estimate of the nonlinear acoustic field and to preserve the directional independence of the nonlinear operator. This fact determines the spatiotemporal domain of the contrast sources that must be accounted for. As we saw in Subsection 4.3.3, in the one-dimensional situation it was sufficient to take the domain of the contrast source from the primary source to the observation point. In the three-dimensional situation we expect a similar requirement. Therefore we assume that those nonlinear contrast sources that lie in the region between the primary source and the point of observation will mainly contribute to the nonlinear distortion, and that the influence of other contrast sources may be safely ignored.[7]

We will investigate this assumption by using the INCS method to com-

[7]For the point source in the previous subsection it showed to be necessary to stretch the contrast source domain out to the negative z-axis. For the plane surface source investigated in this and the upcoming subsections it is expected that this will not be necessary, as they resemble the situation of Chapter 4 more than they resemble the case of the point source.

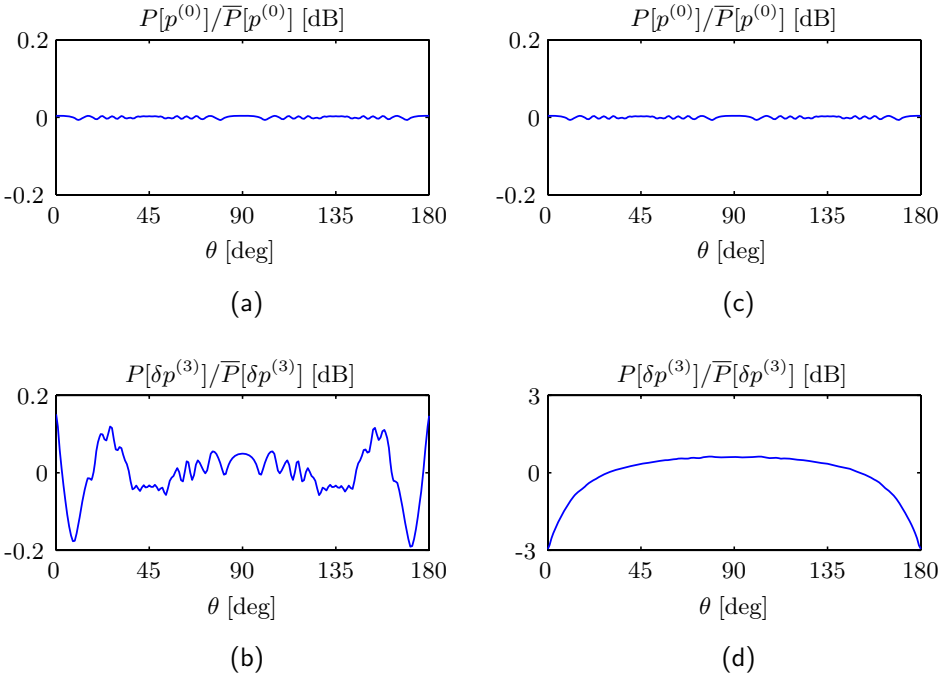

Figure 5.7. Radial profiles at a radius $\|\boldsymbol{x}\| = 4$ mm, versus angle θ for the profile of the linear field solution $p^{(0)}$ (a,c) and of the nonlinear field correction $\delta p^{(3)}$ (b,d). (a,b) With a contrast source domain limited in the z-direction to $[-0.8, 4.3]$ mm. and (c,d) With a contrast source domain limited in the z-direction to $[0, 4.3]$ mm.

pute the nonlinear field correction with a nonlinear contrast source that is masked in a part of the domain of interest. The primary source is a rectangular piston with dimensions $W \times H = 10$ mm $\times$ 10 mm, causing a pressure jump. The source emits a pulse with a frequency of $f_0 = 1$ MHz and a Gaussian envelope as used before, and the source pressure amplitude is $P_0 = 500$ kPa. The pressure field is obtained in a domain of interest with a spatial size of 15 mm $\times$ 15 mm $\times$ 52 mm and a temporal window of 22 μs. The maximum frequency of interest is $F = 3$ MHz, we discretize with $D_F = 2$ and we use iteration $j = 1$. The profile of the linear field solution $p^{(0)}$ is shown in Fig. 5.8, and the profile of the first nonlinear field correction $\delta p^{(1)}$ employing the entire region of interest for the contrast source is depicted in Fig. 5.9a. The maximum levels of $P[p^{(0)}]$ and $P[\delta p^{(1)}]$ are respectively 870 kPa and 73 kPa.

When we mask the contrast source in a region $X \times Z = [-7.5 \text{ mm}, -1 \text{ mm}] \times [z, 52 \text{ mm}]$ with $z = \{5, 20\}$ mm, as depicted in Fig. 5.8, we obtain an error $p_z^{(1)} - p^{(1)} = \delta p_z^{(1)} - \delta p^{(1)}$ in the first nonlinear field estimate, where the subscript z denotes the specific masking domain. In Fig. 5.9b, we see that the effect of this masking in the axial profile mainly manifests itself as an underestimation of the nonlinear field correction. This effect is larger for a masking domain starting closer to the primary source. The profiles of the errors $\delta p_z^{(1)} - \delta p^{(1)}$ are shown in Fig. 5.10. From these figures we observe that the more the masking blocks the view from an observation point to the primary source, the higher the error becomes in the nonlinear field correction. Moreover, close examination (not shown) reveals that besides the underestimation there is a similar small reflection from the contrast source domain boundary as observed for the one-dimensional wave problem in Fig. 4.8c. From this test we conclude that the contrast sources that contribute most significantly to the nonlinear field in a certain observation point indeed lie in the region in between the observation point and the primary source.

5.3.4 Nonlinear field solution

In this subsection we will present nonlinear field profiles that have been obtained with the INCS method for a variety of situations and we will compare these results with the results from three existing numerical models. The first model that is used for comparison purposes is a finite-difference implementation of the Westervelt equation for cylindrical source geometries [31, 36]. It will be referred to as the FD-WV model, and in contrast two the other

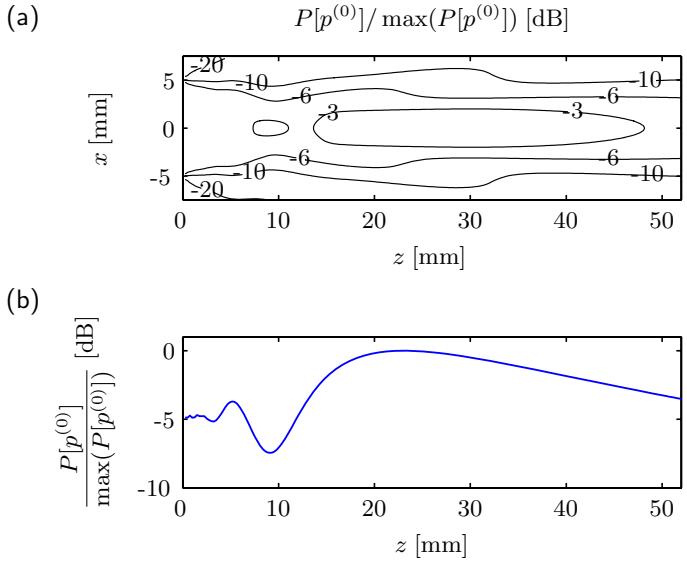

Figure 5.8. Profile of the linear field solution $p^{(0)}$ for the rectangular piston source. (a) In the plane $y = 0$. (b) On the z-axis.

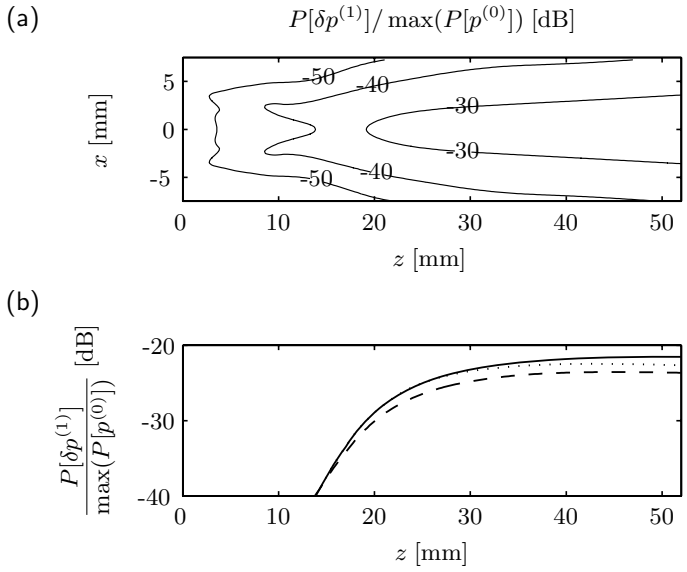

Figure 5.9. Profile of the nonlinear field correction $\delta p^{(1)}$. (a) In the plane $y = 0$. (b) On the z-axis. Shown are the axial profiles for the reference case (solid), for a masking domain starting at $z = 5$ mm (dashed) and for a masking domain starting at $z = 20$ mm (dotted).

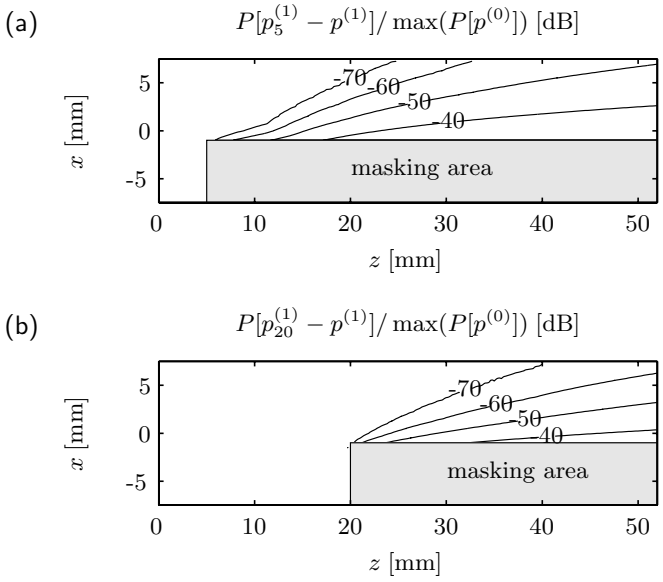

Figure 5.10. Profiles $P[\delta p_z^{(1)} - \delta p^{(1)}]$ of the error in the nonlinear field corrections caused by the masking of the contrast source domains. The plots show the profiles in the plane $y = 0$ for the masking domains starting at (a) $z = 5$ mm and (b) $z = 20$ mm.

two models it is a full-wave model. The second model we will employ for comparison is the angular spectrum nonlinear propagation (AS-NLP) model developed by Zemp et al. [85]. This model is based on a phenomenological approach to the nonlinear forward-wave problem [12]. In this approach, the acoustic diffraction, attenuation and nonlinear distortion phenomena are separately treated in a scheme that marches the field from the source plane at $z = 0$ to computational planes at $z + k\Delta z$, $k = 1, 2, 3 \ldots$, in the direction of the positive z-axis. The diffraction and attenuation operators are free of angle-dependent behavior up to an angle of $\pm 90°$ relative to the positive z-axis. The nonlinearity operator is based on a plane-wave algorithm, and therefore we expect to obtain reliable nonlinear field results as long as the field is propagating in a quasi-plane fashion and in a direction close to the positive z-axis. However, when the field significantly deviates from this characterization, we expect to observe deviations in the nonlinear field components. The third model we employ for comparison is a numerical model for cylindrically symmetric problems that is based on the KZK equation. The latter is a parabolic approximation of the Westervelt equation [7, 46].

Within the parabolic approximation, the field is also assumed to be quasi-planar and to propagate in a direction close to the positive z-axis, as with the AS-NLP model, but this assumption is already incorporated in the linear field solution and not only in the nonlinear field correction. For unfocused cylindrical piston sources, the KZK model should result in accurate answers in a region not too close to the source and not too far from the z-axis [29]. For the off-axis limit an angle of 15° is sometimes mentioned [72]. All three models use a boundary value condition prescribing an acoustic pressure in the plane $z = 0$, and therefore in this section we will everywhere apply the INCS method with a pressure jump source.

Unfocused cylindrical source

We will first employ all four methods to evaluate the nonlinear field of an unfocused cylindrical source with a radius $R = 5$ mm, exciting a pulse with a frequency of $f_0 = 1$ MHz, a Gaussian envelope as used before and a source pressure amplitude $P_0 = 500$ kPa. With the INCS method we consider a spatial region of interest of 17 mm $\times$ 11 mm $\times$ 45 mm and a temporal window of 39 μs. The maximum frequency of interest is $F = 4f_0$, we discretize with $D_F = 2$, resulting in step sizes $\Delta x = 0.19$ mm and $\Delta t = 0.13$ μs, and we use iteration $j = 4$. Based on our observations in the one-dimensional case, with these settings we expect to get an accurate estimate for the fundamental and the second harmonic frequency components, and a fair estimate of the third harmonic component. The FD-WV method uses a maximum radius of 40 mm, an axial distance of 50 mm and a temporal window of 19 μs. It employs spatial step sizes $\Delta r = 0.03$ mm and $\Delta z = 0.015$ mm, and a temporal step size $\Delta t = 0.004$ μs. The AS-NLP method uses 10 computational planes of size 60 mm $\times$ 60 mm to step from the source plane to the plane $z = 50$ mm, and a temporal window of 25 μs. Moreover, it employs spatial step sizes $\Delta x = \Delta y = 0.63$mm, $\Delta z = 5$mm and a temporal step size $\Delta t = 0.05$ μs. The KZK method uses step sizes in the radial and axial directions and a maximum radius. These all vary in relation with the axial distance as described in the original paper [46]. For the current problem the radial step size is between 0.05 mm and 0.2 mm, the axial step size is between 0.03 mm and 0.7 mm, the radius is between 27 mm and 107 mm and the maximum axial distance is $z = 50$ mm. The temporal window size is 25 μs and the temporal step size is $\Delta t = 0.01$ μs. The resulting axial spectral profiles and radial spectral profiles at $z = 20$ mm are shown in Fig. 5.11 for all four methods. With the INCS method, the maximum profile level is

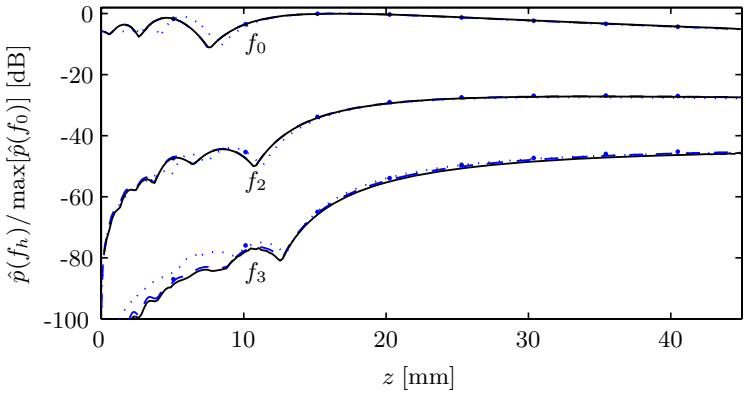

(a)

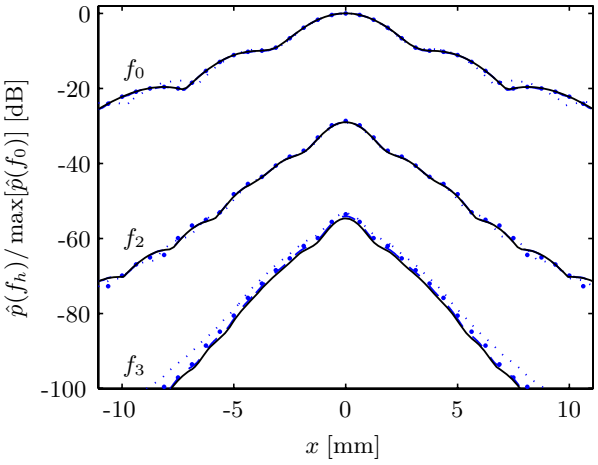

(b)

Figure 5.11. Spectral profiles for the cylindrical source as obtained by the INCS method (solid), the FD-WV method (dashed), the AS-NLP method (large, sparse dots) and the KZK method (small dots). (a) Axial spectral profiles. (b) Radial spectral profiles at $z = 20$ mm.

Table 5.3. Typical differences and variations in the spectral profiles in the plane $y = 0$ for the cylindrical source, as obtained by the INCS method and compared to those computed by the FD-WV method, the AS-NLP method and the KZK method.

Spectral profile	Typical deviation and variance [%] of INCS relative to		
	FD-WV	AS-NLP	KZK
f_0	1.1 ± 2.3	0.0 ± 1.1	0.0 ± 5.9
f_2	0.0 ± 2.3	-3.4 ± 5.9	3.5 ± 5.9
f_3	-6.7 ± 2.3	-16 ± 5.9	-16 ± 16

$P[p^{(4)}] = 983$ kPa at the natural focus $z = 17.6$ mm. The maximum second and third harmonic spectral profile levels are -27 dB and -46 dB relative to the maximum fundamental level. However, the third harmonic spectral profile has not yet reached its global maximum at $z = 45$ mm.

From these figures we observe a good agreement between the INCS method, the FD-WV method and the AS-NLP method for all three profiles. The differences with the KZK method in the axial profiles for $z < 13$ mm and in the radial profiles for $|x| > 6$ mm are due to the parabolic approximation, but elsewhere the fundamental, second and third harmonic profiles coincide well with those of the other models. In Table 5.3 we list typical differences and variations observed in the spectral profiles in Fig. 5.11a and b, as obtained by the INCS method and compared to those obtained by the other three methods. For the KZK method, we have only accounted for the region $z > 13$ mm and $|x| < 6$ mm. From the figures and the table we observe that for the fundamental component resemblance with the INSC results is best for the AS-NLP method, and for the second and third harmonic components this resemblance is best for the FD-WV method and second-best for the AS-NLP method. The second harmonic profile predicted by the INCS method is at the average level of the predictions by the other methods. For the third harmonic spectral profile we observe that the INCS method produces the lowest estimate of all three methods.

From this comparison, the question arises which method may serve as a benchmark for the other three methods. In Chapter 4 we observed that the nonlinear distortion is excellently accounted for by the INCS method in case

of one-dimensional wave propagation. When the results were compared to the results of the Burgers Equation, it turned out that for a sufficient number of iterations the relative errors as reported in Table 4.2 were an order of magnitude smaller than the relative errors reported in Table 5.3. Moreover, in Subsection 5.3.1 we added the observation that the linear field predicted by the INCS method is very accurate and that the three-dimensional diffraction is therefore well accounted for as well. From these facts we draw the conclusion that the INCS method serves as a benchmark for the other three methods. This implies that for the cylindrical transducer studied in this paragraph, the other methods overestimate the third harmonic component by a factor of about 7% for the FD-WV method and and 19% for the AS-NLP and KZK method.

Phased array, unsteered beam

Next, we will present a number of simulation results that have been obtained with the INCS method for a phased array geometry. With this source we can only use the AS-NLP method for a comparison, since the FD-WV and KZK methods are limited to sources with cylindrical symmetry. We simulate the nonlinear field of a 48 element phased array with element parameters $W_{\mathrm{el}} \times H_{\mathrm{el}} = 0.21$ mm $\times$ 12 mm and $d_{\mathrm{el}} = 0.5$ mm. The array is focused at $(x_f, z_f) = (0, 56.6)$ mm and $z_{\mathrm{ele}} = z_f$. We use a source pulse with a center frequency $f_0 = 1$ MHz, a Gaussian envelope as used before and a source pressure amplitude $P_0 = 250$ kPa. The nonlinear field solution is obtained with the INCS method in a domain of interest with a spatial size of 30 mm$\times$18 mm$\times$72 mm and a comoving temporal window of 36 μs. For these simulations we use $F = 4f_0$ and $D_F = 2$. We use the nonlinear field estimate for $j = 4$. Figure 5.12 shows the spectral profiles of the three frequency components f_0, f_2 and f_3 in the plane $y = 0$ and relative to their respective maximum levels, and the figure also shows the axial spectral profiles relative to the maximum fundamental level. The profile level close to the source is about $P[p^{(4)}] = 105$ kPa, and the maximum profile level is $P[p^{(4)}] = 414$ kPa at the realized focus $(x, y, z) = (0, 0, 45)$ mm. The maximum levels of the second and the third harmonic spectral profiles are -30 dB and -55 dB relative to the maximum fundamental level.

From these figures we observe that the higher harmonic spectral profiles attain their maxima at a larger distance in z than the fundamental profile. Moreover, when compared to their maximum levels, the relative harmonic

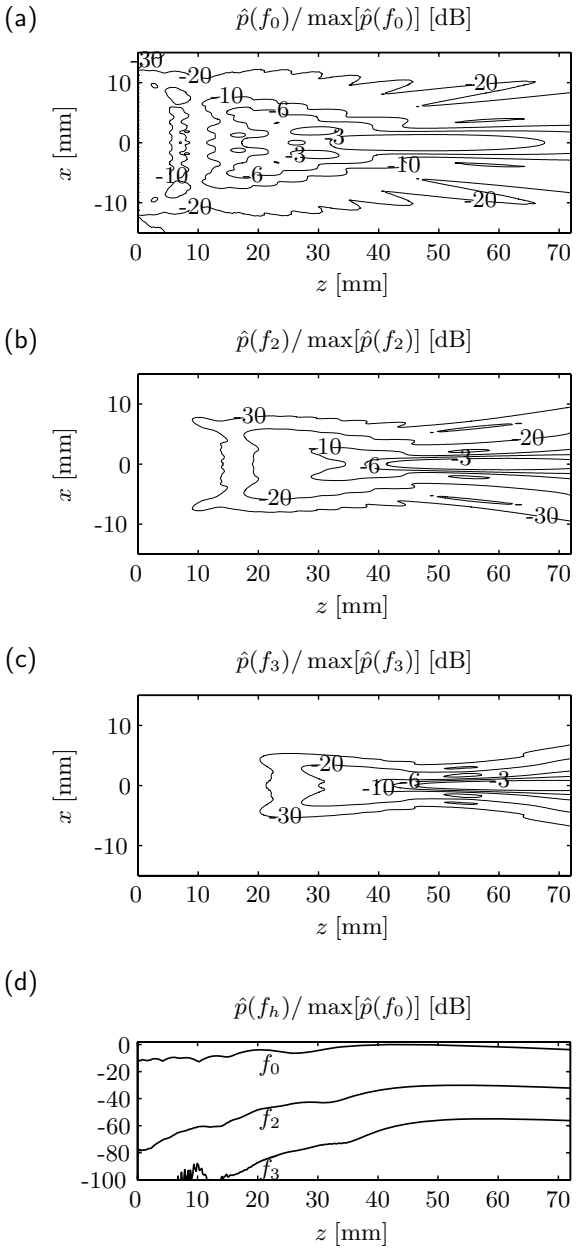

Figure 5.12. Spectral profiles for the phased array transducer exciting an unsteered beam. (a) Fundamental spectral profile in the plane $y = 0$. (b) Second harmonic spectral profile in the plane $y = 0$. (c) Third harmonic spectral profile in the plane $y = 0$. (d) On the beam axis.

spectral levels close to the source are much lower than for the fundamental component, and the levels fall off much faster to the side, yielding a narrower main beam and a smaller sidelobe level than for the fundamental component.

We compare the spectral profiles obtained by the INCS method with those obtained by the AS-NLP method. For the latter method we use 35 computational planes of size 60 mm × 60 mm to step from the source plane to the plane $z = 70$ mm, and a temporal window of 41 μs. Moreover, it employs spatial step sizes $\Delta x = \Delta y = 0.47$ mm and $\Delta z = 2$ mm, and a temporal step size $\Delta t = 0.05$ μs. In Fig. 5.13 the axial spectral profiles and the lateral spectral profiles for $y = 0$, $z = 58$ mm are shown. From these figures we observe an even better resemblance between the spectral profiles of the INCS method and the AS-NLP method than for the unfocused cylindrical source.

Phased array, steered beam

Employing the same phased array source, we have also used the INCS method to obtain the spectral profiles of the acoustic beam when its axis is steered 22.5° and 45° off the transducer axis. The focuses in these cases are $(x_f, z_f) = (22, 52)$ mm and $(x_f, z_f) = (40, 40)$ mm, with $z_{\text{ele}} = z_f$, giving the same focal distances as in the unsteered case. The domains of interest are parallellogram-shaped in the xz-plane, conform the beam angle, and these skew domains have a size of 30 mm × 18 mm × 60 mm and 30 mm × 18 mm × 53 mm, respectively. We use the nonlinear field estimate for $j = 4$. In Figures 5.14 and 5.15, the fundamental, the second harmonic and the third harmonic spectral profiles in the plane $y = 0$ are shown for both steering angles, as obtained with the INCS method with the same discretization as in the unsteered situation. Both figures also show the axial spectral profiles relative to the maximum fundamental level. The fundamental profiles clearly show the parallellogram-shaped domains. Based on the observations in Subsection 5.3.3 we expect that these contrast source domains will be adequate for the estimation of the nonlinear profiles. For 22.5° beam steering, the maximum level of the profile is $P[p^{(4)}] = 396$ kPa at the realized focus $(x, y, z) = (17, 0, 40)$ mm. The maximum second and third harmonic spectral profile levels are −31 dB and −56 dB relative to the maximum fundamental level. For 45° beam steering, the maximum level of the profile is $P[p^{(4)}] = 358$ kPa at the realized focus $(x, y, z) = (24, 0, 23)$ mm. The maximum second and third harmonic spectral profile levels are −33 dB

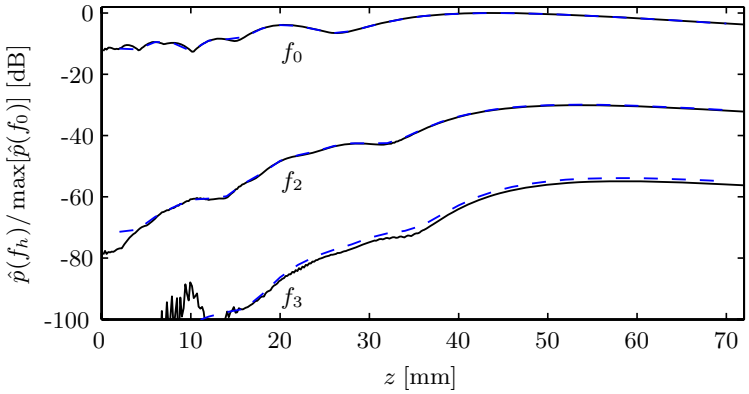

(a)

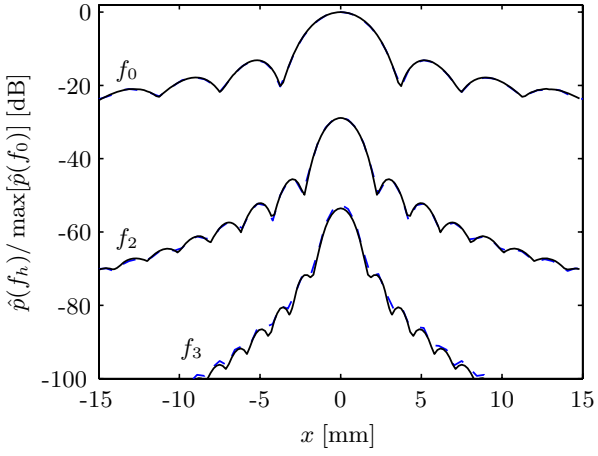

(b)

Figure 5.13. Spectral profiles for the phased array transducer exciting an unsteered beam, as obtained by the INCS method (solid) and by the AS-NLP method (dashed). (a) Axial spectral profiles. (b) Lateral spectral profiles for $y = 0$, $z = 58$ mm.

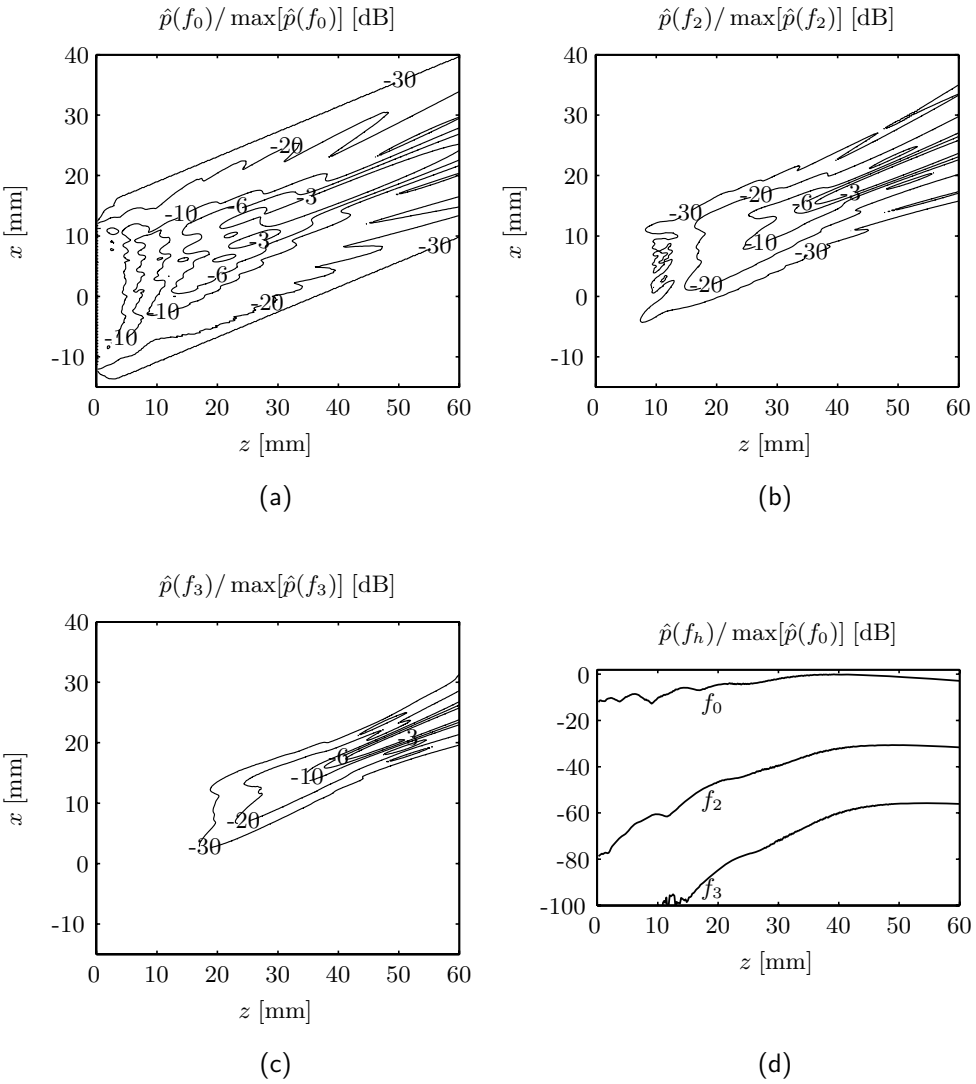

Figure 5.14. Spectral profiles for the phased array transducer exciting an beam steered at $22.5°$. (a) Fundamental spectral profile in the plane $y = 0$. (b) Second harmonic spectral profile in the plane $y = 0$. (c) Third harmonic spectral profile in the plane $y = 0$. (d) On the steered beam axis.

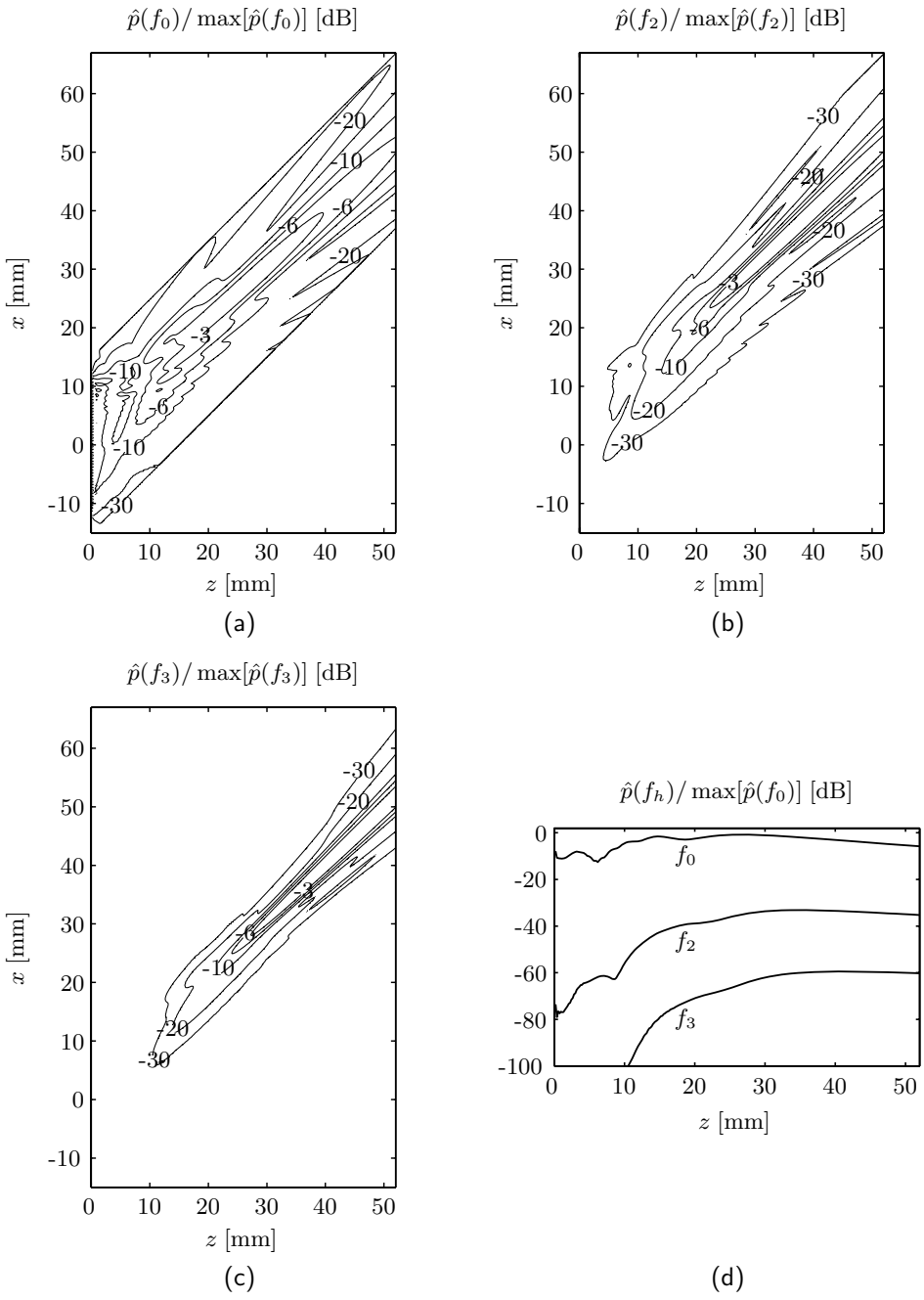

Figure 5.15. Spectral profiles for the phased array transducer exciting an beam steered at $45°$. (a) Fundamental spectral profile in the plane $y = 0$. (b) Second harmonic spectral profile in the plane $y = 0$. (c) Third harmonic spectral profile in the plane $y = 0$. (d) On the steered beam axis.

and -59 dB relative to the maximum fundamental level. When comparing the higher harmonic spectral profiles with the fundamental spectral profile, we observe from these figures similar characteristics as for the unsteered case.

We compare the results of the INCS method for the steered beams with those obtained by the AS-NLP method. To employ the latter method for 22.5° beam steering we use 30 computational planes of size 70 mm $\times$ 70 mm to step from the source plane to the plane $z = 60$ mm, and a temporal window of 50 μs. Moreover, we employ spatial step sizes $\Delta x = \Delta y = 0.55$ mm and $\Delta z = 2$ mm, and a temporal step size $\Delta t = 0.05$ μs. For 45° beam steering, we use 30 computational planes of size 90 mm $\times$ 90 mm to step from the source plane to the plane $z = 60$ mm, and a temporal window of 74 μs. Here we employ spatial step sizes $\Delta x = \Delta y = 0.35$ mm and $\Delta z = 2$ mm, and a temporal step size $\Delta t = 0.05$ μs. The computational planes are perpendicular to the transducer axis, as in the previous simulations. In Fig. 5.16 the lateral spectral profiles in the plane $y = 0$ are shown at $z = 52$ mm for 22.5° beam steering and at $z = 40$ mm for 45° beam steering. In both situations we observe a perfect agreement of both methods for the fundamental component. For 22.5° beam steering, the level of the second harmonic component at the main beam predicted by the AS-NLP method is 0.5 dB lower than the level predicted by the INCS method, and this difference increases for larger x. The third harmonic components obtained by both methods differ by 1.5 dB at the main beam, and the tails have a widely different shape and level. For 45° beam steering, the level of the second harmonic component at the main beam predicted by the AS-NLP is 2.6 dB lower than the level predicted by the INCS method. The third harmonic components differ by 7.5 dB at the main beam, and again its overall shape is much different for both methods.

From these simulations we clearly see the limitations of the quasi-planar wave assumption in the nonlinear step of the AS-NLP method. The results obtained with the AS-NLP method did not improve when the step size Δz was reduced to 1 mm, and this was also not the case when a smaller temporal step size of $\Delta t = 3.3$ μs was taken. The step sizes Δx and Δy were $\{0.47, 0.55, 0.35\}$ mm for the respective beam steering angles $\{0^\circ, 22.5^\circ, 45^\circ\}$, but the observed trends in the deviating second and third harmonic components for increasing steering angle did not show any dependence on them. This suggests that further reducing Δx and Δy would not have improved the obtained results of the AS-NLP method.

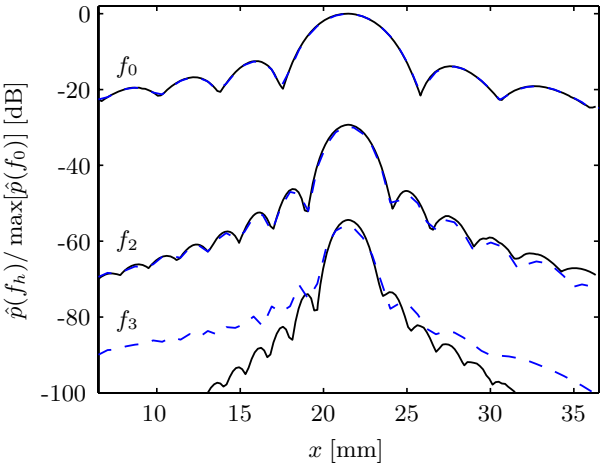

(a)

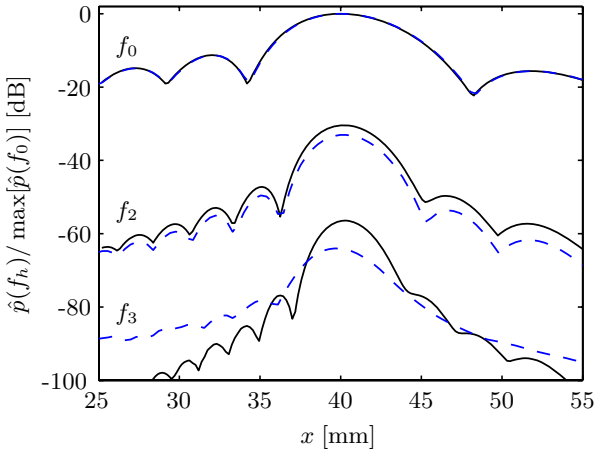

(b)

Figure 5.16. Lateral spectral profiles in the plane $y = 0$ for the phased array transducer exciting a steered beam as obtained by the INCS method (solid) and by the AS-NLP method (dashed). (a) Lateral profile at $z = 52$ mm for the beam steered at $22.5°$. (b) Lateral profile at $z = 40$ mm for the beam steered at $45°$.

Phased array, steered beam, grating lobe

In the following simulation we will demonstrate the ability of the INCS method to account for wide-angle phenomena like grating lobes. Grating lobes may appear in the field profile of a phased array transducer when $d_{\text{el}} > c_0/2f_0$. With $f_0 = 1\text{MHz}$ and $c_0 = 1500\ \text{ms}^{-1}$ we get $c_0/2f_0 = 0.75$ mm, and therefore for a 48 element phased array transducer with element parameters $W_{\text{el}} \times H_{\text{el}} = 0.42\ \text{mm} \times 12\ \text{mm}$ and $d_{\text{el}} = 1.0$ mm we expect a grating lobe. The acoustic beam is steered at 45° by focusing it at $(x_f, z_f) = (40, 40)$ mm, with $z_{\text{ele}} = z_f$. As in the previous situations we use a source pulse with a center frequency $f_0 = 1$ MHz, a Gaussian envelope and a source pressure amplitude $P_0 = 250$ kPa. The field profiles are obtained in two simulations where we employ two parallellogram-shaped domains of size $60\ \text{mm} \times 18\ \text{mm} \times 50$ mm, one of which making an angle of 45° and capturing the main bean, and the other making an angle of −45° and capturing the grating lobe. The comoving temporal window has a duration of 75 μs. For both simulations we use $F = 4.5f_0$ and $D_F = 2$, and we use iteration $j = 4$. The two skew beams are merged into one image for the spectral profiles, as shown in Fig. 5.17. The maximum profile level is 536 kPa at the realized focus $(x, y, z) = (38, 0, 37)$ mm. The maximum second and third harmonic spectral profile levels are −29 dB and −54 dB relative to maximum fundamental level. When comparing the higher harmonic spectral profiles with the fundamental spectral profile, we observe from this figure similar characteristics as for the case without grating lobe. Moreover, we observe a strong reduction of the grating lobe in the higher harmonic profiles.

We compare the results of the INCS method with those of the AS-NLP method employing the same settings as for the 45° beam steering without the grating lobe. In Fig. 5.18 the lateral spectral profiles for $y = 0$, $z = 40$ mm are shown. As in the case of the steered beam without the grating lobe, we observe a perfect agreement of the fundamental profile in the calculated regions. However, the higher harmonic spectral profiles are not at all accurately reproduced by the AS-NLP method, whereas the grating lobe shows a stronger deterioration than the main beam.

5.3.5 Behavior at strong nonlinear distortion

As a final study we will investigate the capabilities of the INCS method in the case of strong nonlinear distortion. For this we consider the nonlinear acoustic

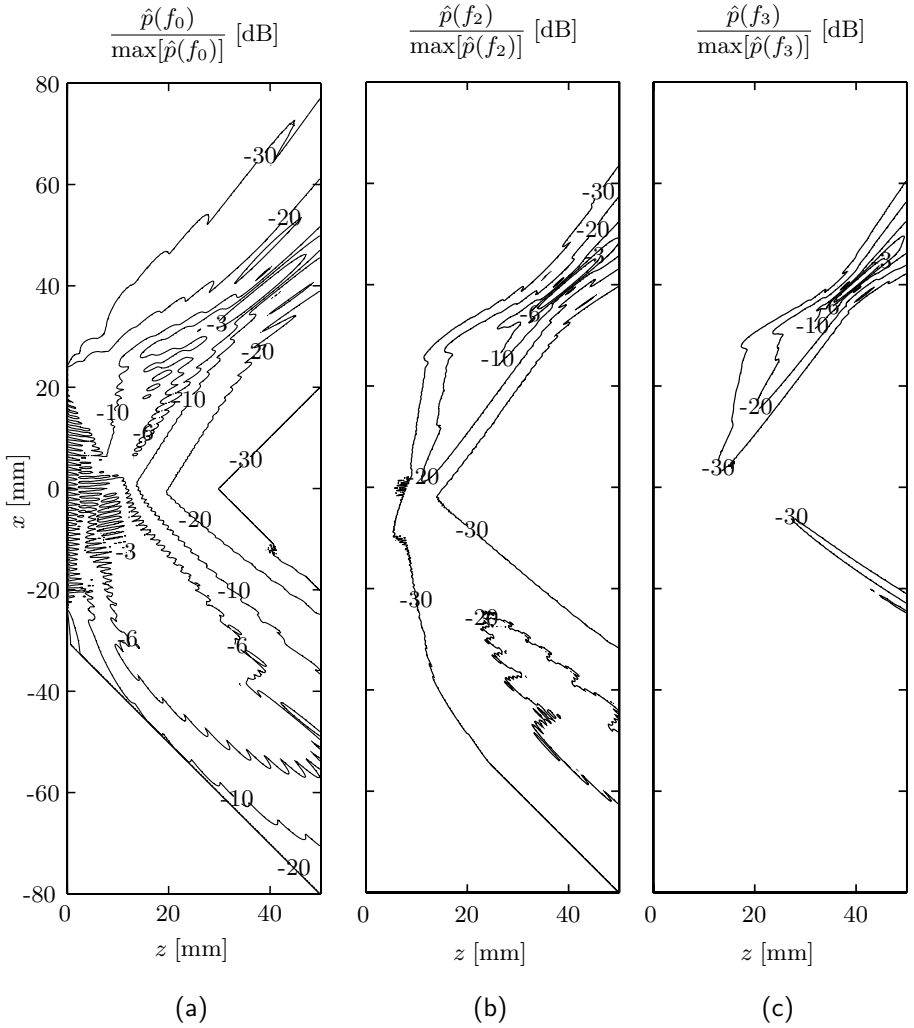

Figure 5.17. Spectral profiles in the plane $y = 0$ for the phased array transducer exciting a beam steered at $45°$ and a grating lobe. (a) Fundamental spectral profile. (b) Second harmonic spectral profile. (c) Third harmonic spectral profile.

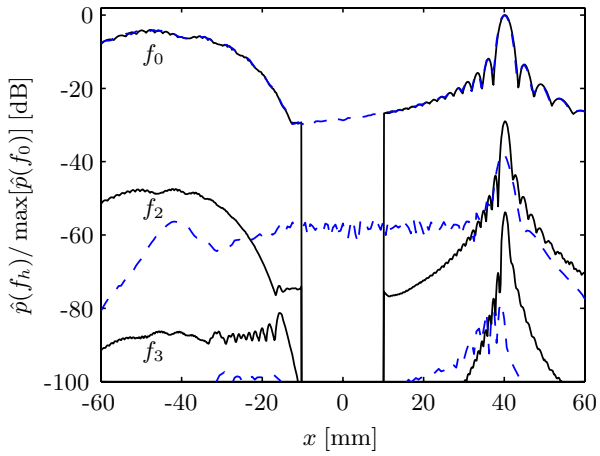

Figure 5.18. Lateral spectral profiles at $z = 40$ mm in the plane $y = 0$ for the phased array transducer exciting a beam steered at $45°$ and a grating lobe, as obtained by the INCS method (solid) and by the AS-NLP method (dashed).

pressure field from an unfocused cylindrical source with a radius $R = 6.9$ mm, excited by a pulse with $f_0 = 1$ MHz, a Gaussian envelope as used before and a source pressure amplitude $P_0 = 2$ MPa. The INCS method is employed using a spatial domain of size 20 mm $\times$ 20 mm $\times$ 100 mm and a comoving temporal window of 28 μs. The maximum frequency of interest is $F = 4.5$ MHz, we discretize with $D_F = 2$ and we use iteration $j = 4$. In Fig. 5.19 the axial spectral profiles of the fundamental and the second to the fourth harmonic spectral profiles are shown, as computed with the INCS method as well as with the KZK method. The maximum pressure of the filtered profile of the fundamental is $P_0[p^{(4)}] = 3.54$ MPa at $z = 31$ mm. In the figure, the acoustic pressure and its spectrum on the axis at $z = 40$ mm and at $z = 70$ mm are also shown. From the figures we observe for $z > 30$ mm a similar overestimation of the fourth harmonic component as we observed for the one-dimensional wave problem in Figs. 4.10 and 4.11. For $z > 70$ mm the third harmonic component shows a slight overestimation as well, and the pulseform has deteriorated significantly. This is caused partly by overestimation of the third and fourth higher harmonics, but more significantly by the the absence of the fifth and higher harmonics due to the filtering. From Figs. 5.19b and d we observe that, as far as the discretization allows, the INCS method correctly reproduces the waveform asymmetry which is a well-known effect in nonlinear ultrasound fields incorporating diffraction and focusing effects [65].

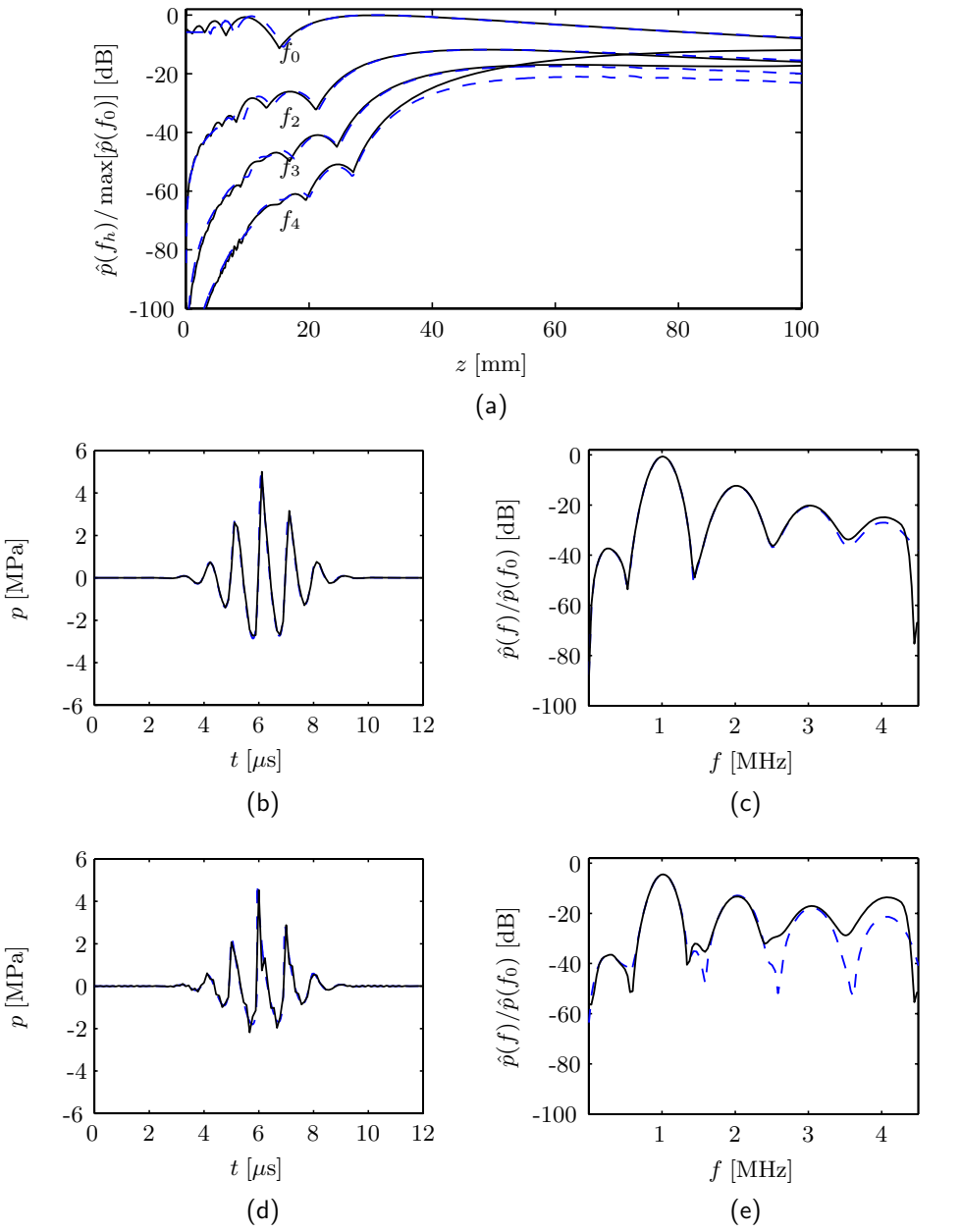

Figure 5.19. Results on the transducer axis for the unfocused cylindrical source exciting a strong acoustic pulse, as obtained with the INCS method (solid) and with the KZK method (dashed). (a) Axial spectral profiles. (b) Signature at $z = 40$ mm. (c) Spectrum at $z = 40$ mm. (d) Signature at $z = 70$ mm. (e) Spectrum at $z = 70$ mm.

5.4 Discussion

In this chapter we have investigated the performance of the INCS method for three-dimensional acoustic wave problems involving various plane sources. It has been shown that the INCS method is able to accurately predict the linear as well as the nonlinear acoustic pressure field with a discretization down to two points per period of the maximum frequency of interest. For the linear field solution, the comparison with two different linear models has shown excellent agreement. For the nonlinear field solution, we compared the spectral profiles of the fundamental component and of the higher harmonic components, as predicted by the INCS method, with those of three different nonlinear acoustic models, and we found very good agreement in a number of situations involving moderate nonlinear distortion. For the h-th harmonic frequency, it appeared to be sufficient to include h harmonics and iterate up to $j = h + 1$. It proved to be sufficient to employ a filtering procedure in time in the evaluation of the nonlinear contrast source. In the case of strong nonlinear distortion the waveform and the spectrum of the pressure showed a deviation due to the filtering, but INCS method did not show any instability. Regarding the local and global errors that were summarized in Section 3.6, we did observe some small effects like the error in the third harmonic spectral profile in Figs. 5.12 around $z = 10$ mm and in Fig. 5.19, but none of them showed to have a severe impact on the results in the case of moderate nonlinear distortion. From the observations in this and the previous chapter we conclude that the INCS method is a reliable, robust and general method for the prediction of the nonlinear acoustic pressure from surface sources exciting a wavefield propagating under an arbitrarily wide angle.

In the development of the INCS method we have paid specific attention to an efficient discretization down to the limit of two points per wavelength and per period. Yet, we observed that the resulting implementation may put a considerable claim on the available computational resources. For a full-wave method, discretization at the limit of two points per wavelength and per period is the best attainable result, and comparing the step sizes used for the first case in Subsection 5.3.4 with those of the FD-WV method for that case, we see that the discretization in the INCS method is coarser by a factor six in the radial direction and a factor 33 in the temporal direction. In forward-wave methods, the problem is solved in an entirely different way, which may give a considerable benefit in terms of the discretization. As compared to the AS-NLP method, we see that the temporal discretization is

a factor three coarser for the INCS method. However, the discretization in the lateral x and y-directions are finer by a factor three. Moreover, according to the paper by Zemp et al. [85] this discretization is not related to the highest harmonic frequency component to be included, as in the INCS method, but to the fundamental frequency. In the z-direction, the AS-NLP method has a large step size, being a factor 25 larger than the step size of the INCS method. This large step in z is a main advantage of the AS-NLP method. This, however, however comes with the drawbacks of a quasi-plane nonlinear propagator, as was shown in the examples. Compared to the KZK method, the temporal discretization of the INCS method was a factor 13 coarser. For the presented example, the spatial step sizes were in the same order as for the INCS method, but according to the paper by Lee et al. [46], the spatial step sizes in the KZK method are related to the geometry and the fundamental frequency and not so much to the highest harmonic component to be included. Therefore, the spatial discretization is more favorable with the KZK method in case of strong nonlinear fields with a high number of harmonic components. But this comes with the unfavorable consequences of the parabolic approximation for the nonlinear field prediction.

With regard to the computational requirements for the INCS method in terms of time and memory, we have seen that these varied strongly and depended on the specific implementation and situation. To give an idea of the scale that can be handled with the current program, we present some data on the largest problem that has been addressed up to now. The problem concerned a phased array excited with a center frequency $f_0 = 5$ MHz, generating a steered acoustic beam with a grating lobe. For this problem, the domain of interest was split up in two beams for the main beam and the grating lobe, and each beam had a size of 15 mm $\times$ 8 mm $\times$ 80 mm and a comoving temporal window of 7.6 μs. At the maximum frequency of interest $F = 12.5$ MHz the discretization took place with $D_F = 2$, resulting in an accurate estimate for the fundamental and the second harmonic frequency component. With $\lambda = c_0/F$ and $T = 1/F$, the domain size was equivalent to that of a cube with edges of length 100λ and a time period of $100T$. The computational grid size used in the parallel program, employing symmetry in the y-dimension and spatial decomposition in the z-dimension, was $252 \times 72 \times 672$ points in space and 191 points in time, yielding an array with a total size of 17 GB. For each of the two beams it took 2.5 hours to obtain iteration $j = 2$ with 96 processors and a maximum of 3.7 GB of memory on each processor. This example clearly shows that from a computational point of view these problems pose a considerable challenge to the programmer and to the

computational resources. However, we believe that the INCS method is the most efficient method to deal with these large, nonlinear, three-dimensional, pulsed problems.

Chapter 6

Experimental verification of the INCS method

In order to validate the nonlinear field predictions from the INCS method, measurements have been performed of the nonlinear acoustic pressure field of a rectangular transducer. These measurements are part of a set of experiments conducted at the Forschungszentrum Karlsruhe, Germany [35]. In this chapter we will discuss the measurements and we will make comparisons with the results from the INCS method. In Section 6.1 we will discuss the experimental setup used for the measurements. In Section 6.2 we will describe the measurements and the comparisons with the predictions from the INCS method and the FieldII program. The chapter ends with a discussion in Section 6.3.

6.1 Experimental setup

The acoustic field measurements have been performed with an automated measurement setup, which is shown in schematic form in Fig. 6.1. It comprises of a plexiglass water tank with a size of 45 cm $\times$ 30 cm $\times$ 30 cm. The water has been demineralized, and it has been degassed by letting it rest for 2–3 days prior to the measurements. The transducer under test (Tx) is positioned inside the water tank in a waterproof chamber. A needle hydrophone (Rx) measures the acoustic field generated by the transducer in

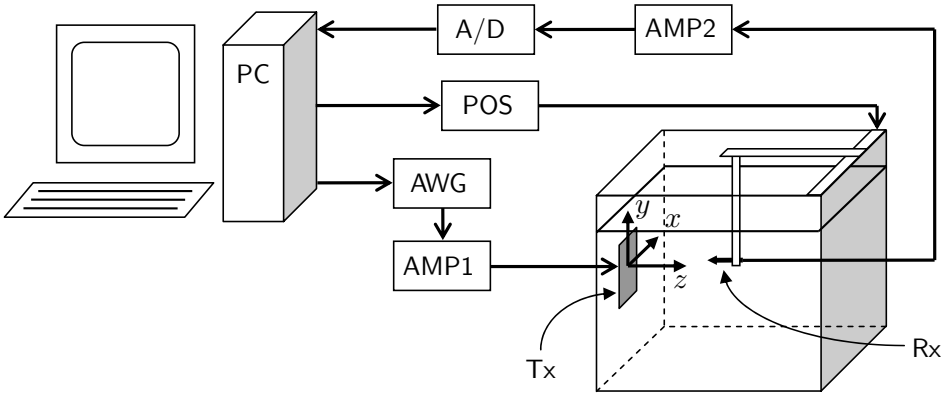

Figure 6.1. Schematic overview of the measurement setup.

the water. The hydrophone is attached to a three-dimensional translation device (POS) that enables an accurate positioning. The entire setup is controlled by a standard desktop PC which runs a control interface developed under LabWindows and written in C. The control program initializes a Sony Tektronix AWG2021 arbitrary waveform generator (AWG). The control program also passes the measurement positions to the positioning device (POS), a custom made system that controls the position. To indicate the position of the hydrophone, a Cartesian reference frame has been defined with its origin at the center of the transducer, as shown in Fig. 6.1. After positioning the hydrophone, the control program triggers the AWG, which generates a pulse that is amplified with a custom made amplifier (AMP1) based on a PA85A Op-amp. The amplifier is connected to the transducer under test, which is a custom made rectangular piezo piston transducer with dimensions $W \times H = 10$ mm $\times$ 15 mm, a center frequency of 1 MHz and a frequency bandwidth of 30%. The transducer employs a matching layer in between the piezo material and the water, and is air backed. The needle hydrophone is an Onda HNC-0400. The hydrophone output signal is amplified with an Onda AH-2010 20 dB preamplifier (AMP2) and converted to a digital signal with a GaGe CS1250 data acquisitioning board (A/D). To improve the overall signal-to-noise level, on each position the measurement is repeated 200 times and the measured signatures are subsequently averaged and stored on the hard disk of the control computer.

At the time of the measurements, the needle hydrophone and its preamplifier were newly purchased. The hydrophone showed an angular depen-

dency, with a −6 dB reduction of the sensitivity for pressure fields incident at an angle 30° off the center axis of the hydrophone. For pressure fields propagating perpendicularly to the hydrophone axis, the sensitivity of the hydrophone-preamplifier combination was in the order of 1 mV/Pa, and its frequency-dependent behavior was specified by the manufacturer over a frequency range of 1–15 MHz and within an accuracy of 1 dB. In the post-processing of the signatures we have applied this frequency-dependent behavior of the hydrophone to obtain the measured acoustic pressure. From the measured acoustic pressure we computed the filtered profiles $P_h[p]$ of the fundamental and the second and third harmonic components.

6.2 Measurements and comparison

Measurements of the acoustic pressure have been performed in the planes $x = 0$ and $y = 0$ and up to a distance $z = 100$ mm in the z-direction. The planes were scanned at a resolution of 1 mm and with an accuracy of 0.1 mm in each spatial direction. To determine the parameters of the acoustic medium, the water temperature was measured prior to each measurement session. The measurements were performed with the rectangular transducer being excited with a voltage pulse having a center frequency of 1 MHz and having either a low or a high level. A low excitation level involved a 3.5 V amplitude, resulting in an acoustic pressure amplitude in the order of 10 kPa, and a high excitation level was obtained by a 35 V amplitude, resulting in acoustic pressure amplitudes in the order of 100 kPa. For the low excitation level, we expect that the nonlinear acoustic distortion is so small that we can safely assume linear propagation. To simulate the pressure profile at the low excitation level, in Subsection 6.2.1 we will use the FieldII program [38, 39]. This program also has been employed in Subsection 5.3.1 for obtaining the linear acoustic pressure field of a surface source. For the high excitation level, we expect that the nonlinear acoustic distortion is observable by the occurrence of at least the second harmonic component. We will simulate the pressure profiles of the fundamental and the second and third harmonic components at the high-level field excitation by using the INCS method.

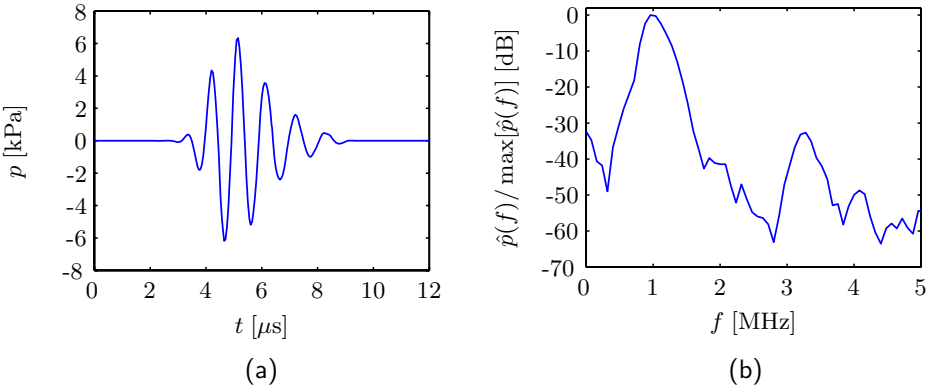

Figure 6.2. Measured pulse on the axis of the transducer at $z = 100$ mm for the low excitation. (a) Temporal signature. (b) Spectrum of the signature.

6.2.1 Low-level field measurements and comparison with the FieldII method

Fig. 6.2 shows the pulse signature measured on the axis of the transducer at $z = 100$ mm, at the low excitation level. In the spectrum we observe the fundamental frequency component around the center frequency at 1 MHz. Moreover, there is a significant third harmonic component that originates from electronic distortion in the input circuit and that is emitted because, apart from the narrow band around 1 MHz, the transducer also has pass-bands at the odd harmonic frequency components. We have measured the low-level acoustic pressure profiles, and we use the linear FieldII program to simulate the acoustic field and reproduce the measured profiles. In the FieldII program, we employ a plane rectangular source, and we derive a source signature that yields a pressure field exhibiting the same waveform as in Fig. 6.2. In the absence of nonlinear propagation, this source signature can be derived from the measured pressure signature on the axis of the transducer. In Appendix C it is shown that for large z the linear acoustic pressure on the axis of a cylindrical transducer can be approximated by

$$p(z,\tau) = P_0\, s(\tau) - P_0\, s(\tau - \frac{R^2}{2c_0 z}), \tag{6.1}$$

where P_0 is the source pressure amplitude, R is the source radius, $s(t)$ is the source signature and $\tau = t - z/c_0$ is a retarded time. The pressure on the axis can be used to obtain a scaled, first order finite difference (FD)

approximation of the time derivative of the source signature. To achieve this, we write

$$\frac{R^2}{2c_0 z} = \Delta\tau, \tag{6.2}$$

and we subsequently recast Eq. (6.1) into

$$\frac{p(z,\tau)}{\Delta\tau} = \frac{P_0\, s(\tau) - P_0\, s(\tau - \Delta\tau)}{\Delta\tau}. \tag{6.3}$$

From this equation we see that

$$\lim_{\Delta\tau\to 0} \frac{p(z,\tau)}{\Delta\tau} = \partial_\tau \left[P_0\ s(\tau)\right]. \tag{6.4}$$

The FieldII program requires its input condition to be provided in the form of the volume source description $c_0^{-1}\partial_t[P_0\, s(t)]$, and therefore we can directly employ the measured function $p(z,\tau)$, divided by $c_0\Delta\tau$, as an approximation to this input condition. This FD approximation of the input condition becomes better for increasing z. However, since at the same time for increasing z the pressure amplitude and therefore the signal-to-noise level reduces, we are compelled to make a trade-off. For the rectangular transducer, we expect a similar behavior as for the cylindrical transducer, so that for increasing z the pressure on the transducer axis resembles more and more the time derivative of the source signature. However, the equation $\Delta\tau = R^2/2c_0 z$ does not apply, and for the rectangular transducer we therefore obtain $\Delta\tau$ by matching the FieldII output level to the measured profile level.

We run the FieldII program with its input condition derived from the measured axial pressure at $z = 100$ mm, as shown in Fig. 6.2, and with a rectangular aperture of size $W \times H = 10$ mm $\times$ 15 mm, i.e. identical to the real transducer. During the measurements, the water temperature varied between 24 °C and 28 °C, corresponding to a sound speed between $c_0 = 1494\ \mathrm{m\,s^{-1}}$ and $1504\ \mathrm{m\,s^{-1}}$ at ambient pressure [49]. For the FieldII simulations we used an intermediate temperature of 26 °C, corresponding to $c_0 = 1499\ \mathrm{m\,s^{-1}}$. Further we use a sampling frequency of 150 MHz and we employ 50×50 mathematical elements for the rectangular source geometry. Figure 6.3a shows the filtered pressure profile of the fundamental component on the transducer axis, as obtained from the measurements[1] and from the FieldII program with $\Delta\tau = 0.099$ μs. The measured maximum

[1]The gaps at certain axial positions in the measured profile, which are visible in all measured axial and surface profiles in this chapter, are due to a technical problem with the positioning device. However, this issue does not seriously impair the observations based on the axial and the surface profiles.

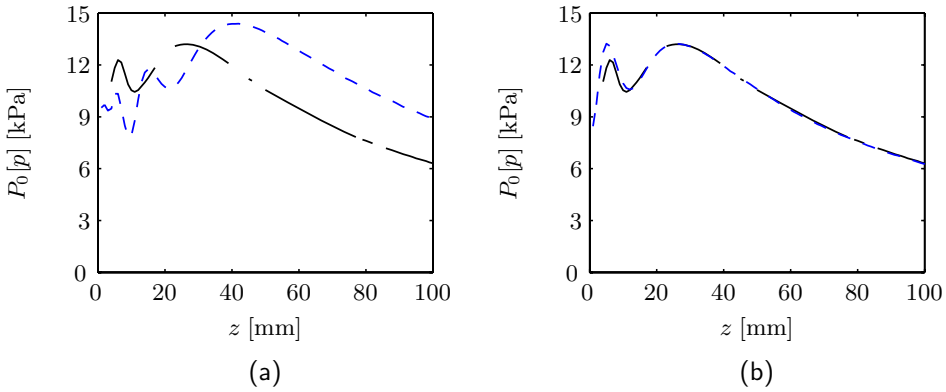

Figure 6.3. Filtered pressure profile $P_0[p]$ on the transducer axis for the low excitation level, obtained from the measurements (solid) and from the FieldII program (dashed). (a) With the source parameters $W \times H = 10$ mm $\times 15$ mm. (b) With the effective source parameters $W_{\text{eff}} \times H_{\text{eff}} = 8$ mm $\times 13.5$ mm and an offset $z_{\text{off}} = -6$ mm.

fundamental profile level on the axis is 13.2 kPa. It is clear from Fig. 6.3a that the measured profile is not correctly reproduced by the FieldII program. This mismatch must be attributed to the fact that the real transducer is inadequately described by the plane surface source. The acoustic disturbance excited in the transducer does not only originate at the surface at $z = 0$, but arises from the deformation of the entire piezo element. Most likely this does not result not in a constant amplitude across the entire transducer, and tapering near the edges is expected. Moreover, before the disturbance reaches the transducer surface, it travels through the piezo material and through the matching layer which causes time delays. In order to account for the tapering effects and the time delays and still retain the surface source description, we introduce effective width and height parameters W_{eff} and H_{eff} instead of the real ones, and we offset the source plane in the z-direction by z_{off}. Tuning of these parameters gives us a best match of the axial profile and of the lateral profiles at $z = 4$ mm, $z = 30$ mm and $z = 100$ mm with $W_{\text{eff}} = 8$ mm, $H_{\text{eff}} = 13.5$ mm, $z_{\text{off}} = -6$ mm and $\Delta\tau = 0.099$ μs. The results are shown in Figs. 6.3b and 6.4. In the axial profile obtained by the FieldII program, the maxima and minima are reproduced at the correct distances, although the first maximum at $z = 4$ mm is slightly overestimated. This should be attributed to the sharp edge of the transducer as used in the FieldII simulation, from which a rather ideal edge wave originates that interferes with the body wave and thus causes the minima and maxima in the axial profile. For the

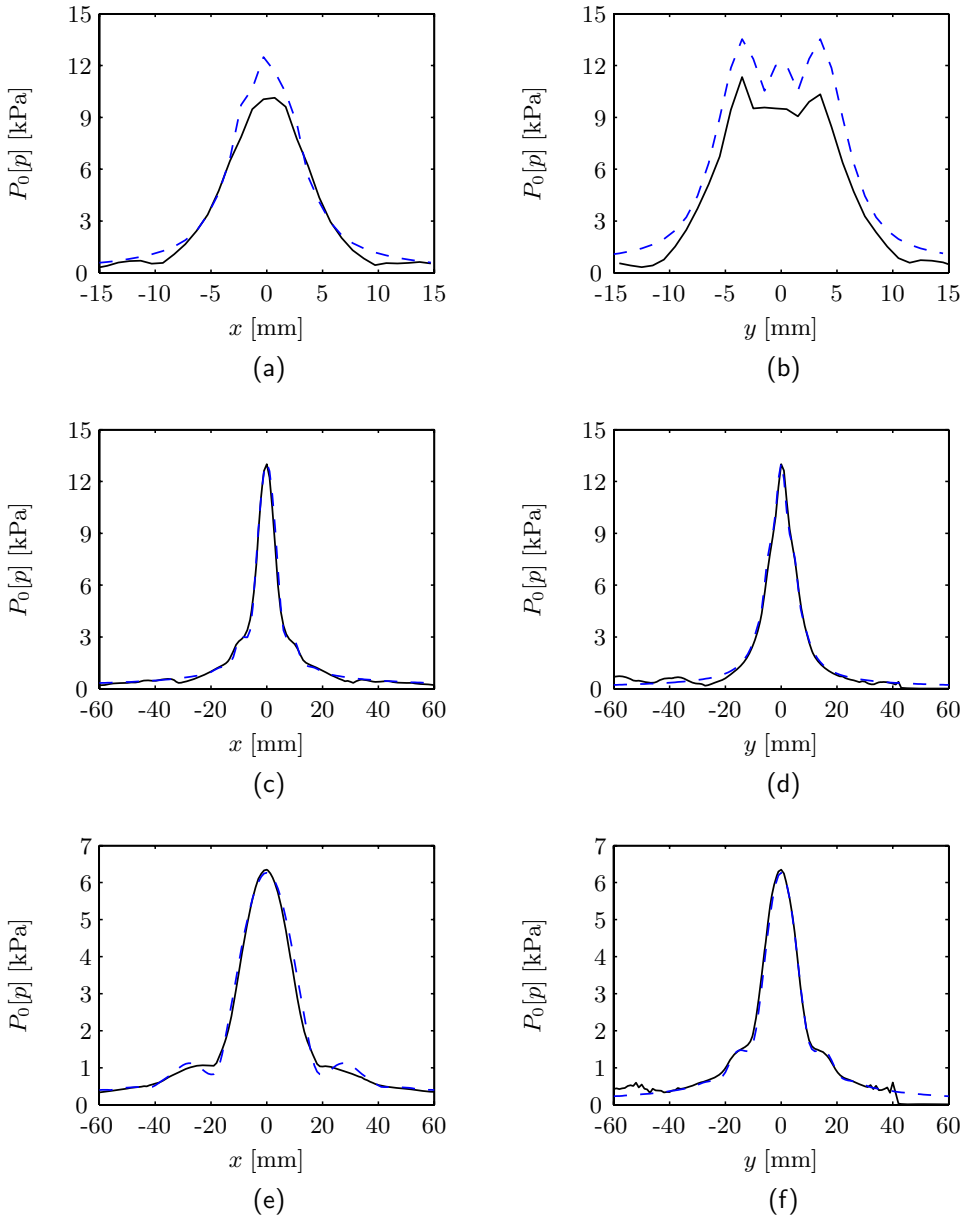

Figure 6.4. Filtered lateral pressure profiles $P_0[p]$ for the low excitation level, obtained from the measurements (solid) and from the FieldII program (dashed) with the effective source parameters $W_{\text{eff}} \times H_{\text{eff}} = 8$ mm$\times 13.5$ mm and an offset $z_{\text{off}} = -6$ mm. (a) $(y, z) = (0\text{ mm}, 4\text{ mm})$. (b) $(x, z) = (0\text{ mm}, 4\text{ mm})$. (c) $(y, z) = (0\text{ mm}, 30\text{ mm})$. (d) $(x, z) = (0\text{ mm}, 30\text{ mm})$. (e) $(y, z) = (0\text{ mm}, 100\text{ mm})$. (f) $(x, z) = (0\text{ mm}, 100\text{ mm})$.

real transducer, the edge is less sharp due to tapering effects, and the edge wave is therefore less ideal, giving a reduced level at the first axial maximum. In the lateral profiles, the beam widths are also reproduced correctly. The sidelobes in Figs. 6.4e and 6.4f are more pronounced in the simulations than in the measurement, but their location is again correct.

6.2.2 High-level field measurements and comparison with the INCS method

In Fig. 6.5 we compare the measured fundamental and harmonic filtered pressure profiles on the transducer axis for the low and high-level excitation. For the high-level excitation, the maximum fundamental profile level is 128 kPa, which is 19.7 dB higher than for the low-level excitation. From Fig. 6.5a we observe that at small z the second harmonic component has a comparable level for the low-level and high-level measurements. For $z > 16$ mm, the high-level measurements show a considerable enhancement of the second harmonic component as compared to the low-level measurements, up to a level of 14 dB at $z = 100$ mm. This is caused by the generation of the second harmonic component during the nonlinear propagation of the wavefield. In Fig. 6.5b we observe that for small z the third harmonic component of the high-level measurements is 3 dB higher than for the low-level excitation, and this increases to 6 dB at $z = 100$ mm. The 3 dB increase for small z indicates that the third harmonic component for the high-level excitation is already enhanced in the source signature due to nonlinear behavior of the transducer and/or the electronics. The 3 dB increase of the third harmonic component over distance is again caused by the nonlinear propagation of the wavefield. However, this effect is much smaller than for the second harmonic component.

We compare the axial and lateral pressure profiles measured for the high-level excitation with results from the INCS method. For the inclusion of the source signature and geometry, we use a similar approach as in Subsection 6.2.1 for the FieldII simulations. We use the volume source description according to Eq. (3.63), prescribing a velocity jump $\Delta v(x, y, t)$ over the plane $z = 0$. This results in the source term

$$S = \rho_0 \partial_t [\Delta V(x, y, t)\, \delta(z)], \tag{6.5}$$

where $\Delta V(x, y, t) = (2/\rho_0 c_0) P_0\, s(t)\, a(x, y)$, as in Eq. (5.1). With this source we also need the time derivative $\partial_t [P_0\, s(t)]$, for which we employ $p(z, \tau)/\Delta\tau$

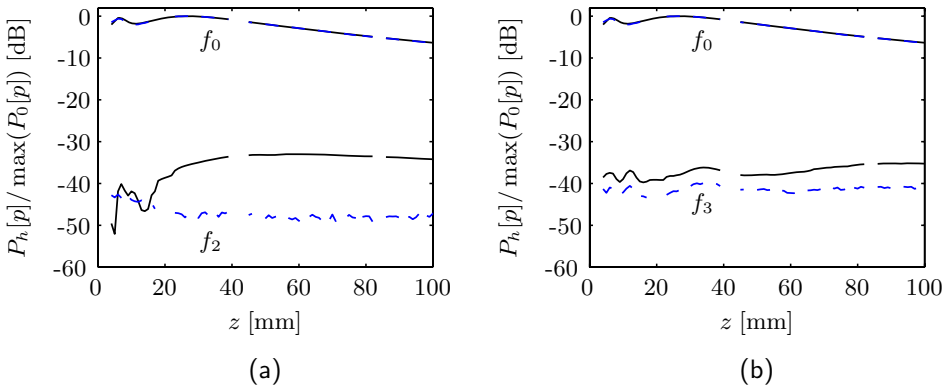

Figure 6.5. Filtered pressure profiles $P_h[p]$ on the transducer axis, measured with the high excitation level (solid) and with low excitation level (dashed), relative to their respective maximum fundamental levels. (a) Fundamental and second harmonic component. (b) Fundamental and third harmonic component.

as an approximation. In this way we obtain the source excitation from the measured low-level axial pressure at $z = 100$ mm, shown in Fig. 6.2, with $\Delta\tau = 0.0103$ μs. As for the low-level case, the source geometry is described by the effective parameters $W_{\text{eff}} \times H_{\text{eff}} = 8$ mm $\times$ 13.5 mm and $z_{\text{off}} = -6$ mm. During the measurements the water temperature varied between 24 °C and 28 °C, corresponding to a variation in the sound speed between $c_0 = 1494\ \text{m}\,\text{s}^{-1}$ and $1504\ \text{m}\,\text{s}^{-1}$ [49], a mass density between $\rho_0 = 997.3\ \text{kg}\,\text{m}^{-3}$ and $996.2\ \text{kg}\,\text{m}^{-3}$ [47] and a nonlinearity parameter between $\beta = 3.54$ and 3.58 [32], all values given at ambient pressure. For the INCS simulations we use an intermediate temperature of 26 °C, yielding $c_0 = 1499\ \text{m}\,\text{s}^{-1}$, $\rho_0 = 996.8\ \text{kg}\,\text{m}^{-3}$ and $\beta = 3.56$. The INCS method is used to predict the axial and lateral filtered pressure profiles of the fundamental and the second and third harmonic components. With the INCS method, we obtain the nonlinear field solution in a domain of interest with a spatial size of 81 mm $\times$ 18 mm $\times$ 102 mm and a comoving temporal window of 24 μs, a maximum frequency of interest $F = 4f_0$ and a discretization with $D_F = 2$. We use the nonlinear field estimate for $j = 2$. Figure 6.6 shows the measured and predicted axial filtered pressure profiles for the fundamental and the second and third harmonic components. From Fig. 6.6a we observe that the second harmonic profile is reproduced very well by the INCS method. The difference between the level of the measured profiles and the profiles from the INCS simulation is at most 1.2 dB, which is close to the 1 dB measurement

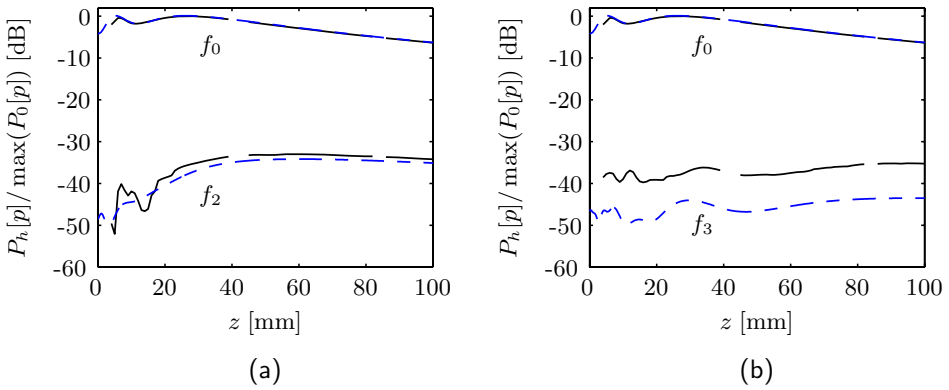

Figure 6.6. Filtered pressure profiles $P_h[p]$ on the transducer axis for the high excitation level, as obtained from the measurements (solid) and from the INCS method (dashed). (a) Fundamental and second harmonic component. (b) Fundamental and third harmonic component.

accuracy. From Fig. 6.6b we observe that the INCS method provides the shape of the axial profile of the third harmonic component, but its level is underestimated by 8 dB. As we observed in Fig. 6.2, the third harmonic component is already present in the source signature, and as we observed in Fig. 6.5, it propagates mainly in a linear fashion. The underestimation of the level of the third harmonic component is caused by the procedure to obtain the derivative of the source signature from the measured axial pressure at $z = 100$ mm. This procedure acts as a finite difference approximation, and a well-known effect of the FD approximation is an increasing underestimation of the higher frequencies [25].

Figure 6.7 shows the lateral profiles of the fundamental and second harmonic component at $z = 30$ mm and at $z = 100$ mm, as obtained from the measurements and from the INCS simulations. From these profiles we also observe that the second harmonic frequency component is reproduced very well by the INCS method, which shows that the INCS method accurately predicts the nonlinear distortion.

In Figs. 6.8 and 6.9, the filtered pressure profiles for the fundamental and the second and third harmonic components in the lateral plane $x = 0$ and on the transducer axis are shown, as obtained from the measurements and from the INCS simulations. We observe a good resemblance between all fundamental and harmonic profiles. Although the level of the third harmonic predicted by the INCS method is too low, as was already noted, the shape

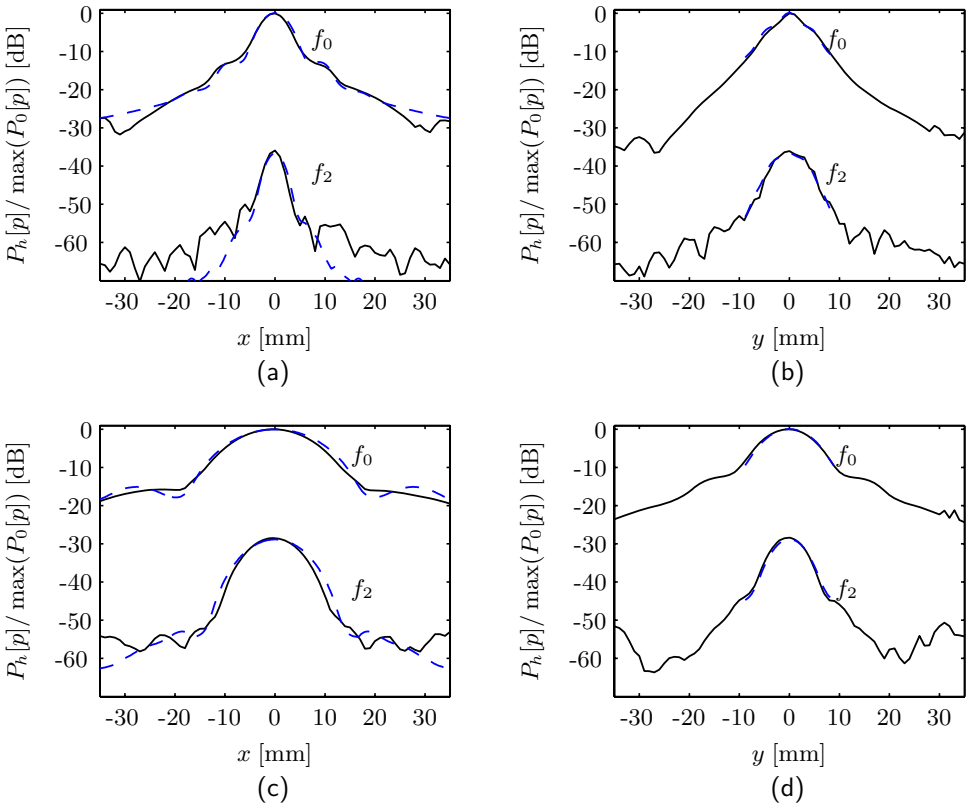

Figure 6.7. Filtered lateral profiles $P_h[p]$ for the fundamental and the second and third harmonic component at the high excitation level, as obtained from the measurements (solid) and from the INCS method (dashed).
(a) $(y, z) = (0\text{ mm}, 30\text{ mm})$. (b) $(x, z) = (0\text{ mm}, 30\text{ mm})$.
(c) $(y, z) = (0\text{ mm}, 100\text{ mm})$. (d) $(x, z) = (0\text{ mm}, 100\text{ mm})$.

of the profile is still reproduced very well.

Finally, in Fig. 6.10 the filtered pressure signatures for the fundamental and the second and third harmonic components on the transducer axis at $z = 50$ mm are shown, as measured and as predicted by the INCS method. Again we note an excellent resemblance of the signature of the fundamental and the second harmonic components. While the level of the signature of the third harmonic component is again underestimated, its shape is still reproduced very well.

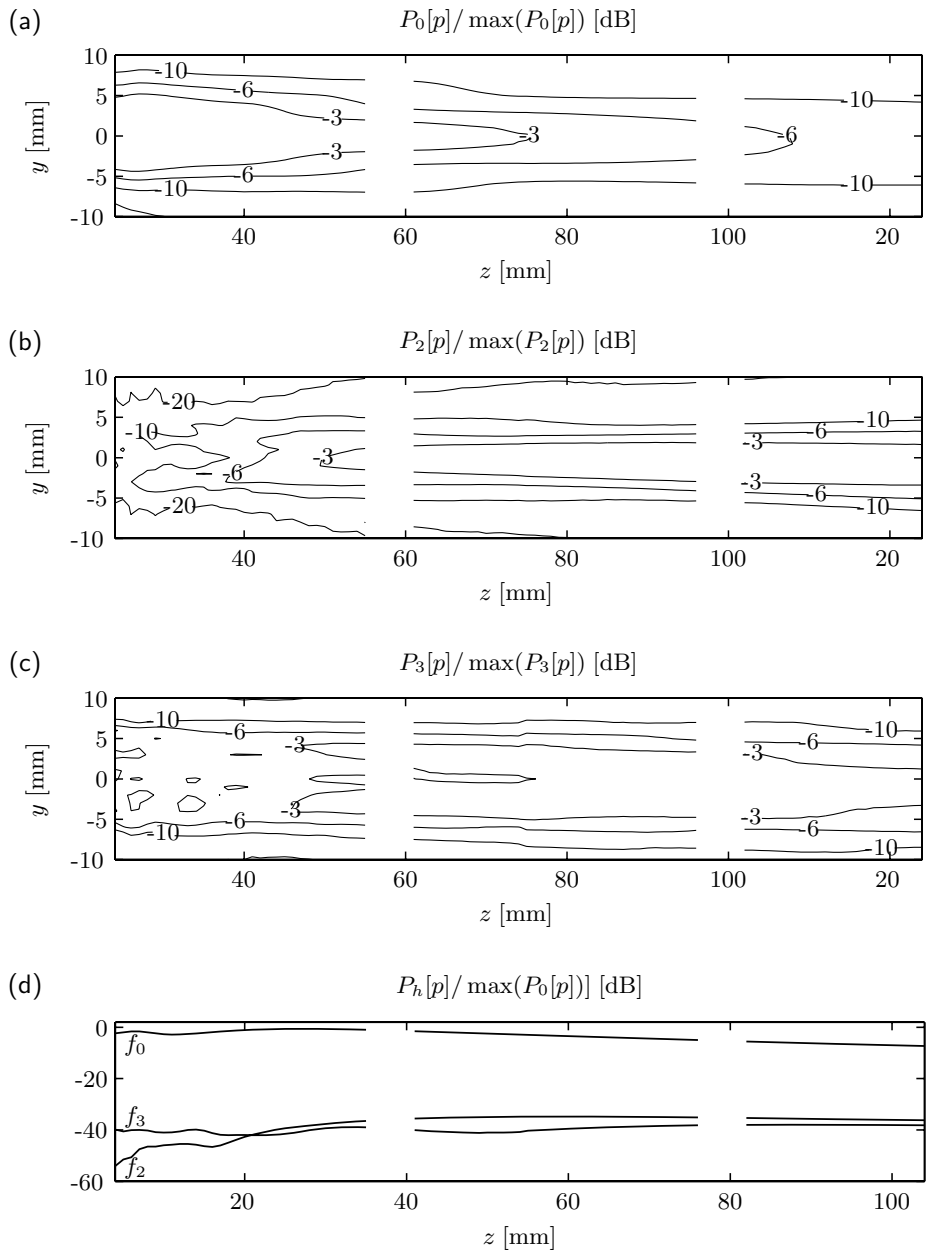

Figure 6.8. Filtered pressure profiles for the rectangular transducer with high-level excitation, obtained from the measurements. (a) Fundamental profile in the plane $x = 0$. (b) Second harmonic profile in the plane $x = 0$. (c) Third harmonic profile in the plane $x = 0$. (d) On the transducer axis.

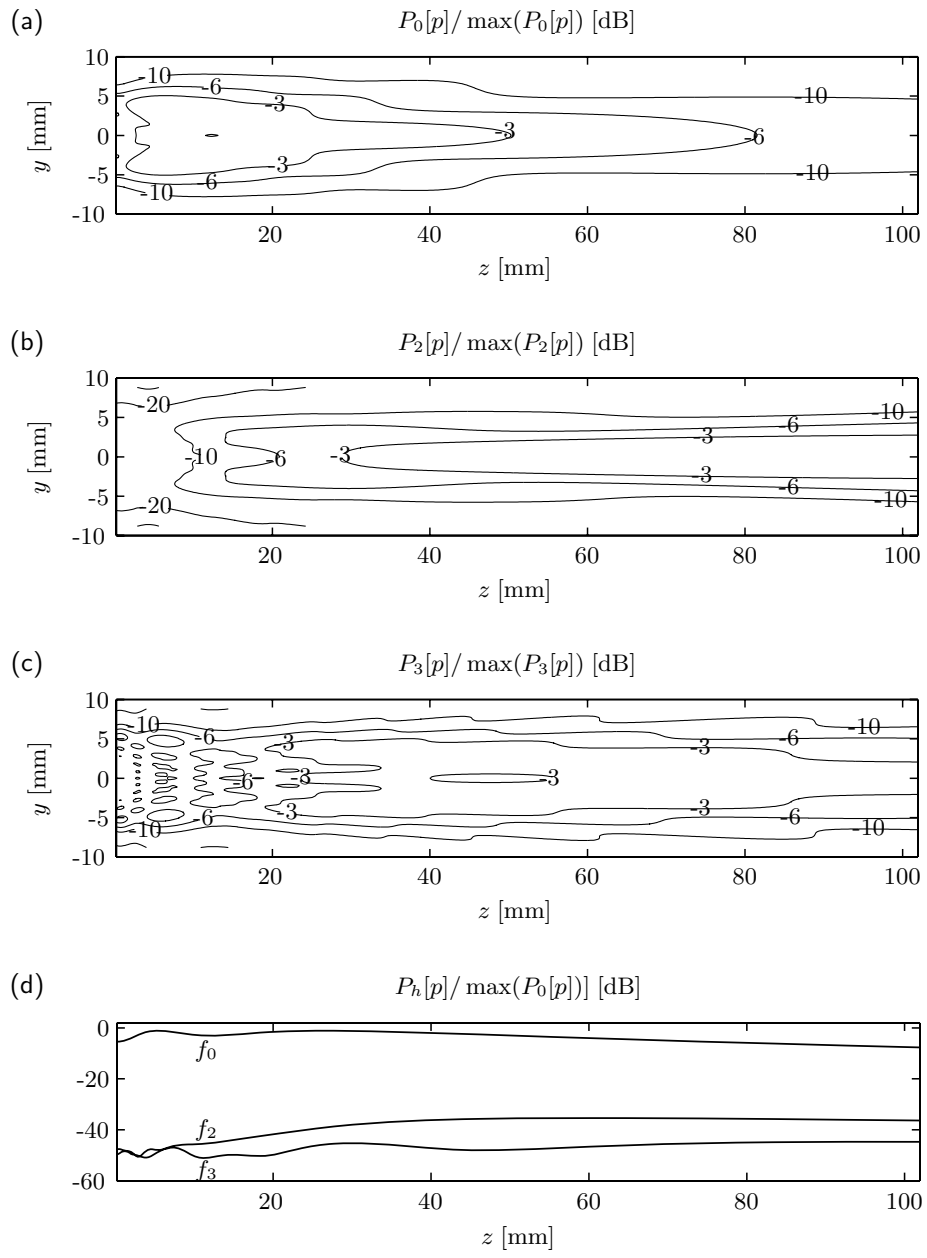

Figure 6.9. Filtered pressure profiles for the rectangular transducer with high-level excitation, obtained from the INCS method. (a) Fundamental filtered profile in the plane $x = 0$. (b) Second harmonic profile in the plane $x = 0$. (c) Third harmonic profile in the plane $x = 0$. (d) On the transducer axis.

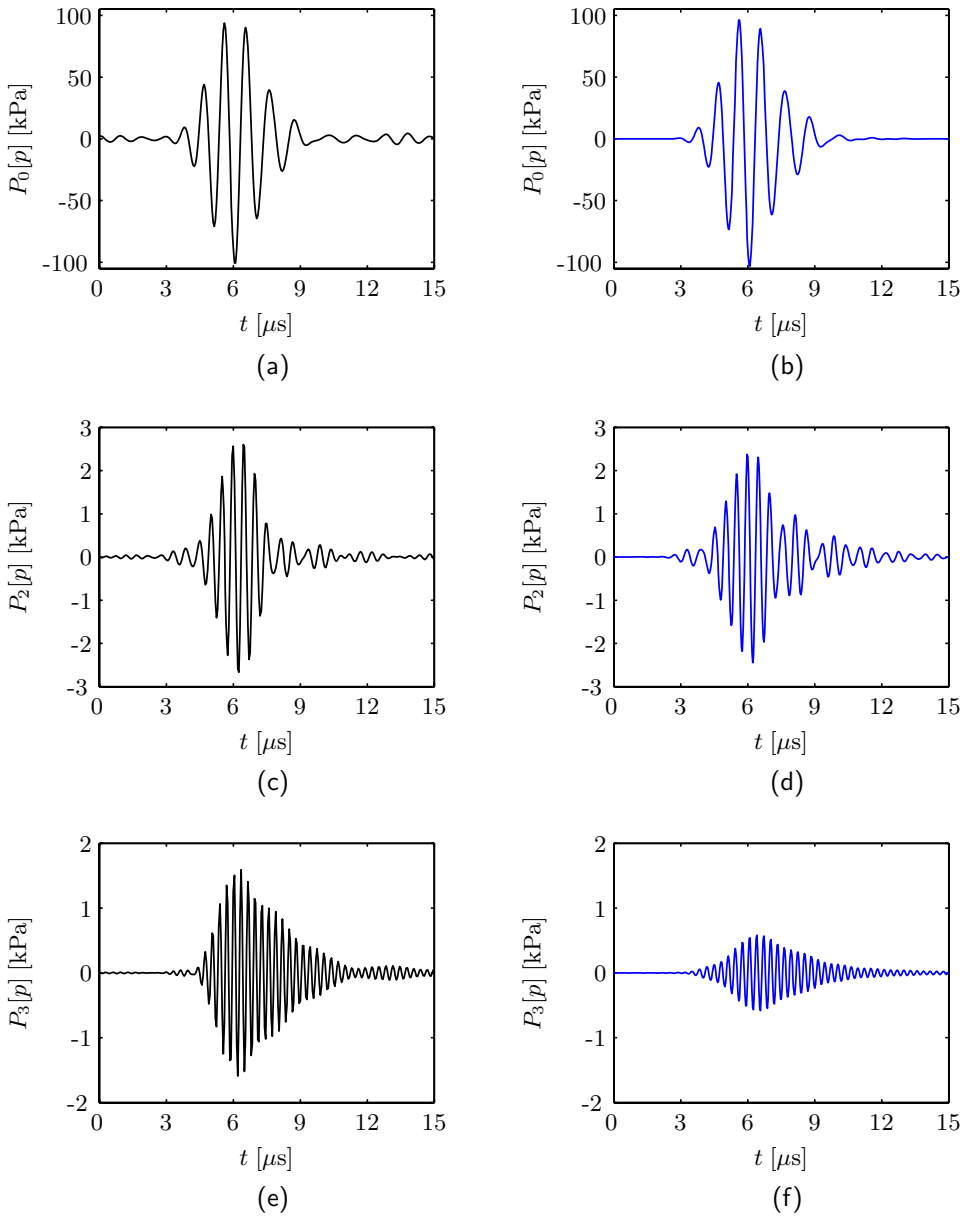

Figure 6.10. Filtered signatures at $z = 50$ mm on the transducer axis for the high-level excitation, as obtained from the measurements (left) and from the INCS method (right). (a,b) Filtered fundamental signatures. (c,d) Filtered second harmonic signatures. (e,f) Filtered third harmonic signatures.

6.3 Discussion

Comparisons with measurements show that the INCS method correctly predicts the measured second harmonic component in the case of a rectangular transducer exciting an acoustic pressure in the order of 100 kPa. The axial and lateral second harmonic pressure profiles were reproduced with an accuracy of 1.2 dB, which is close to the measurement accuracy. The time signatures showed a very good resemblance for the fundamental and the second harmonic component as well. Although the axial and lateral third harmonic pressure profiles on the transducer axis and in the lateral plane $x = 0$ were reproduced well, we cannot judge the performance of the INCS method for this harmonic on the basis of the measurements since the prediction of the source signature from a far-field measurement underestimates the third harmonic that is already present in the source signature.

We saw that an accurate incorporation of the source geometry and the source signature is essential for producing reliable simulation results. For the rectangular transducer under investigation, it proved beneficial to introduce effective width and height parameters and an offset in the z-dimension. If we like to obtain further improvement in the description of the source geometry, as a first possibility we may introduce a spatially dependent amplitude distribution (or apodization) across the source surface, and possibly a spatially dependent time delay of the source signature. However, this approach would still not include the volume effects, reflections and dispersion effects that may arise inside a real transducer. A second alternative would be to replace the idealized source description with a measured pressure across an entire plane. However, since hydrophones exhibit spatial averaging over their active surface, the spatial resolution from acoustic measurements may be insufficient. A third alternative is to use an accurate electromechanical model of the transducer to predict the excited pressure.

Apart from the accurate incorporation of the source geometry, we saw that it is also important to include the correct source signature. We found that the source signature could approximately be obtained from the measured pressure signature on the transducer axis at a low excitation level. This approximation sufficiently accounts for the fundamental component in the source signature, but the third harmonic component that is present in the source signature is underestimated, as expected. Improvement of the estimate of the source signature would be attained by taking a measured pressure at larger distance from the source, but this would go at the cost of

a deteriorated signal-to-noise level. We could think of a number of alternative approaches for obtaining the source signature. Firstly, for large source geometries it may be possible to measure the acoustic pressure very close to the source. For a large source, the body wave and edge wave may still be temporally separated and the source signature can be directly obtained by applying a narrow time window. A second alternative would be to obtain the spatial transfer function of the source signature to the pressure at a certain point and then apply a spatial deconvolution of the measured pressure. This approach requires the absence of nonlinear behavior of the transducer and the electronics. As a third alternative we may again use an electromechanical model of the transducer to find the source excitation.

Despite these considerations on incorporating the source geometry and the source signature, the presented measurements and comparisons have clearly shown that the INCS method is capable of predicting the nonlinear distortion of the acoustic pressure field excited by a rectangular transducer. Together with the theoretical considerations in Chapters 2 and 3, and with the numerical comparisons with other models presented in Chapters 4 and 5, the comparisons with practical results in this chapter provide a further indication of the reliability of the nonlinear acoustic field predictions that are produced by the INCS method.

Chapter 7

Conclusions and discussion

7.1 Conclusions

In this thesis we have developed a numerical method for the computation of the three-dimensional, pulsed acoustic pressure field excited by plane sources of arbitrary geometry in a nonlinear, homogeneous and lossless medium. The Iterative Nonlinear Contrast Source (INCS) method has specifically been designed to cope with large-scale problems (in the order of 100 wavelengths or periods in each spatiotemporal direction) involving low to moderate nonlinear behavior. Moreover, it enables the accurate computation of the higher harmonic frequency components of the acoustic field, even if these are extremely weak as compared to the fundamental acoustic field. Unlike many other methods [72, 82, 85], the INCS method is not based on an implicit or explicit plane wave approximation, and is thus well suited to accurately predict the nonlinear acoustic fields of medical phased array transducers for all steering angles and all observation angles.

The following conclusions may be drawn from the research reported in this thesis:

- We have shown that the acoustic field in a nonlinear medium may be

described by a pair of first-order field equations and a pair of nonlinear constitutive equations. For a homogeneous medium, combination of these leads to a nonlinear wave equation that is valid up to second order in the field quantities. For the progressive fields that occur in our examples, we neglect local nonlinearity effects, and the consequent simplification of the nonlinear wave equation leads to the lossless Westervelt equation.

• We have shown that the Westervelt equation may be solved efficiently by our newly developed INCS method. This method obtains the pulsed, full-wave nonlinear acoustic pressure field of a surface source excited by a pulsed signal. The method consists of two steps:

1. The nonlinear wave problem is formally solved by a Neumann iterative solution, in which the nonlinear term in the Westervelt equation acts as a nonlinear contrast source and provides iterative corrections to the linear approximation of the nonlinear wave problem. Each iterative step in the Neumann scheme is performed by a four-dimensional spatiotemporal convolution integral of the (primary or contrast) source with the Green's function of the linear background medium.
2. For the evaluation of the four-dimensional convolution integral by a discrete convolution sum over a spatiotemporal grid, a maximum temporal frequency of interest is chosen that determines all step sizes of the grid. To attain a grid that is as coarse as possible, the Green's function and the (primary or contrast) source are filtered and windowed in all spatiotemporal dimensions. The filtering operation prevents the aliasing error that would otherwise result in all dimensions from the sampling operation. Thus, we may attain a coarse discretization down to the limit prescribed by the Nyquist-Shannon sampling theorem of two points per wavelength/period of the maximum frequency of interest. The discretized convolution sum is efficiently evaluated using a Fast Fourier Transform (FFT) method. For the contrast source and the pressure field we require a doubling of the source domain by zero-padding in all four dimensions to prevent a wraparound error. For a grid consisting of N points this yields a complexity of the FFT method of the order $2^4 N \log(2^4 N)$. We refer to this second part of the method as the Filtered Convolution (FC) method.

• We have shown that the method is suitable for implementation on a sequential computer as well as on a parallel computer. For a number of linear wave problems, results from the INCS method have been compared with

an analytical solution, with a solution involving a numerical integration and with results from the FieldII program [38, 39]. For a number of nonlinear wave problems, results have been compared with results from methods based on the Burgers equation [15] and on the KZK equation [7, 46], from the ASNLP method [85] and from a finite difference approximation of the Westervelt equation [31, 36]. These results show that the INCS method produces accurate results in all considered cases and that it is capable of efficiently predicting the nonlinear pressure field in a large-scale domain. We conclude that for moderate nonlinear distortion an accurate estimate of the h-th harmonic frequency component is obtained by including $h+1$ harmonics and iterations up to $j = h+1$, and most often it is sufficient to include h harmonics and iterations up to $j = h-1$. The INCS method shows no dependence of the directionality of the wavefield. In case of strong nonlinear distortion the method remains stable, for the one-dimensional wave problem up to the plane-wave shock formation distance. However, since the strongly distorted wavefields may exhibit sharp transitions and therefore would require a large number of harmonics to be incorporated, the accuracy of the INCS method is limited by the cutoff frequency used with the filtering operation. We conclude that because of its reliability, its robustness and the general validity of its solution, the INCS method can be used as a benchmark model for wave problems involving not too strong nonlinear distortion.

- We have shown with a validation experiment employing a rectangular transducer and weak nonlinear distortion that the measured nonlinear acoustic field is predicted very well with the INCS method. Using the plane source description we were capable to reproduce the axial and lateral field profiles of the real transducer for the fundamental frequency component. For the second harmonic component, the axial and lateral profiles and time signatures were reproduced with an error close to the measurement accuracy of 1 dB. For the prediction of the third harmonic component we found that the shapes of the axial and lateral profiles and of the time signature were reproduced accurately. We explained that the underestimation of the third harmonic profile was caused by a limited accuracy in the estimation of the actual source signature used in the experiment.

7.2 Discussion

The presented INCS method is versatile and can be extended in a variety of ways. Within the context of forward-wave problems in linear and nonlinear

acoustics, the following extensions can be thought of:

• We may significantly extend the applicability of the INCS method by including medium attenuation into the model. Up to now we have focused on the accurate incorporation of nonlinear distortion and we have disregarded the medium attenuation. Whereas in a medium like water the attenuation can be safely neglected, in a medium like human tissue this is not the case. We can think of two ways to include medium attenuation in our model. The first way is to include a damping term in the contrast source [73] in a similar way as the nonlinear term from the Westervelt equation. This will provide an iterative correction to the lossless wave problem. The second way is to include attenuation directly in the Green's function of the background medium. The latter approach is discussed in Appendix D.

• We may further extend the applicability of the INCS method by including spatial inhomogeneity in the linear medium parameters ρ_0 and κ_0. This would enable the INCS method to predict the diffraction and scattering of the acoustic fields propagating in heterogeneous media like human tissue. The inhomogeneous parts of the medium parameters can be interpreted as a contrast to the homogeneous wave problem, and can be used to obtain a contrast source term that gives an iterative correction to the homogeneous field solution in a similar way as the nonlinear term from the Westervelt equation. This approach is discussed in Appendix E. In the evaluation of the contrast term due to inhomogeneity, we have to apply a spatial filter to prevent spatial aliasing from occurring. For the accurate prediction of the nonlinear propagation in inhomogeneous media, we may also have to account for the local nonlinear distortion effects that were disregarded by only considering the cumulative nonlinear behavior.

• We may include spatial inhomogeneity in the coefficient of nonlinearity β as well. This may be necessary for the prediction of the nonlinear propagation of acoustic fields in inhomogeneous media like human tissue. In the evaluation of the contrast source, the omission of the spatial filtering as discussed in Sections 4.1 and 5.1, is not allowed anymore.

• We may use an arbitrary volume source instead of a plane surface source. The method is already capable of accounting for this type of source, as we employed volume-type contrast sources in the iterative nonlinear corrections. As an application we can think of acoustic fields generated by an optical source, as occurs in photo-acoustic applications [16].

• We may use a formulation of the nonlinear medium behavior that is differ-

ent from the one incorporated in the Westervelt equation. This may involve the inclusion of the local nonlinearity effects that were discussed in Section 2.5, or the application of an expression for the medium behavior that differs from the one with the coefficient of nonlinearity β as developed in Section 2.3.6. We could do this by employing the INCS method to solve the pair of basic equations Eqs. (2.50) and (2.51) instead of the Westervelt equation. However, this would require the storage of the three components of the acoustic velocity as well as the acoustic pressure, and it would thus increase the memory requirements by a factor four.

- In order to improve the convergence of the iterative scheme in the INCS method, we may employ other iterative schemes than the Neumann solution. Possible candidates are overrelaxation methods, Conjugate Gradient methods or any other Krylov subspace method [23].

The application of the FC method may be fruitfully extended to other wave problems like inverse source and scattering problems, to other physical domains like electromagnetics or elastodynamics, and to any field of research that involves the numerical evaluation of multi-dimensional, large-scale convolution integrals.

This concludes our thesis on the modeling of nonlinear medical diagnostic ultrasound. It is our hope that the research described in this thesis contributes to the further development of medical diagnostic ultrasound equipment, and that the application of the method improves the understanding of the physics underlying the generation and propagation of nonlinear acoustic fields.

Appendix A

Evaluation of the lossless Burgers equation based on a time-base transformation

---

In Chapter 4 we have employed a numerical solution of the Burgers equation as a benchmark solution for the one-dimensional INCS method. The method to obtain and to evaluate the Burgers equation is described in [32]. In this appendix we will shortly present the derivation of the Burgers equation from the Westervelt equation, as well as its implicit solution. Based on this implicit solution, an approximate solution of the Burgers equation can be obtained with the aid of a time-base transformation [15], as will be discussed below.

The lossless Burgers equation is derived from the one-dimensional lossless and source-free version of the Westervelt equation. The latter follows from Eq. (2.70) as [32]

$$\frac{1}{c_0^2}\frac{\partial^2 p}{\partial t^2} - \frac{\partial^2 p}{\partial x^2} = \frac{\beta}{\rho_0 c_0^4}\frac{\partial^2 p^2}{\partial t^2}. \tag{A.1}$$

The introduction of a comoving or retarded time $\tau = t - x/c_0$ in Eq. (A.1), and the consequent transformation of the partial derivatives, yields

$$\frac{2}{c_0}\frac{\partial^2 p}{\partial x \partial \tau} - \frac{\partial^2 p}{\partial x^2} = \frac{\beta}{\rho_0 c_0^4}\frac{\partial^2 p^2}{\partial \tau^2}. \tag{A.2}$$

Within the comoving time frame, the variation of the pressure with respect to x is small. If we neglect the second-order derivative with respect to x in

Eq. (A.2), and we integrate the resulting expression with respect to τ, we obtain the lossless Burgers equation

$$\frac{\partial p}{\partial x} = \frac{\beta\, p}{\rho_0 c_0^3} \frac{\partial p}{\partial \tau}. \tag{A.3}$$

For this differential equation we have an implicit solution of the form

$$p(x,\tau) = f(\phi), \qquad \phi = \tau + \frac{\beta}{\rho_0 c_0^3}\,(x - x_0)\, p(x,\tau), \tag{A.4}$$

where $f(\phi)$ is an arbitrary function and x_0 is an arbitrary constant. Taking $x = x_0$ shows us that $p(x_0,\tau) = f(\tau)$, and therefore we can also write Eq. (A.4) as

$$p(x,\tau) = p[x_0, \tau + \frac{\beta}{\rho_0 c_0^3}\,(x - x_0)\, p(x,\tau)]. \tag{A.5}$$

The introduction of a distance Δx by defining $x = x_0 + \Delta x$ gives us

$$p(x_0 + \Delta x,\tau) = p[x_0, \tau + \frac{\beta}{\rho_0 c_0^3}\,\Delta x\, p(x_0 + \Delta x,\tau)]. \tag{A.6}$$

If we substitute the Taylor expansion of $p(x_0 + \Delta x,\tau)$ around $x = x_0$ in the argument on the right-hand side of Eq. (A.6) and we neglect the higher order terms in Δx, we obtain

$$p(x_0 + \Delta x,\tau) \simeq p[x_0, \tau + \frac{\beta}{\rho_0 c_0^3}\,\Delta x\, p(x_0,\tau)], \tag{A.7}$$

which approximation is valid as long as $p(x,\tau)$ varies slowly enough over the distance Δx. The pressure at $x = x_0 + \Delta x$ is thus obtained from the pressure at $x = x_0$ by transforming the time-base of $p(x_0,\tau)$ with a shift that depends on the magnitude of the pressure field at each time instant. This principle is shown in Fig. A.1 for a pressure field exhibiting a sinusoidal waveform at $x = x_0$. From the figure we clearly observe the waveform steepening effect that was also noted in Subsection 4.3.4. It is also clear that an inconsiderate application of the time-base transformation results in a multivalued waveform. Even before this case, the approximations of lossless propagation and the neglection of the second derivative in x do not hold anymore. If we want to prevent multivaluedness, we may include absorption into the Burgers equation. This may reduce the magnitude of the time shift at time instants where steep slopes are present in the pressure field. In this

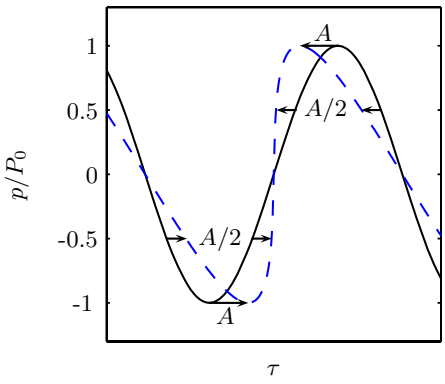

Figure A.1. Time base transformation of a sinusoidal pressure field with an amplitude P_0 given at $x = x_0$ (solid), resulting in the pressure field at a new position $x = x_0 + \Delta x$ (dashed). The maximum shift equals $A = \beta P_0 \Delta x / \rho_0 c_0^3$.

thesis, the situation of a multivalued waveform is prevented by not marching the solution of the Burgers equation beyond the shock formation distance that is given by Eq. (4.11).

The spatial step size Δx is limited by the assumption regarding the slow variation of p that leads to Eq. (A.7). By successive application of Eq. (A.7) we obtain a numerical method that predicts the nonlinear pressure at a position $x = k\,\Delta x$, k being a positive integer, starting from a given source pressure $p(0, \tau) = P_0\, s(t)$ at $x = 0$. Here, P_0 and $s(t)$ respectively are the source pressure amplitude and the source signature, as in Section 4.1. If the source pressure is sampled on a uniform temporal grid, then the time-base transformation results in a temporal axis that is nonuniformly spaced. To recover the uniform grid, the waveform has to be interpolated at the original time instants. For an accurate interpolation, the temporal sampling step size Δt needs to be sufficiently small.

Appendix B

Computational approaches for the efficient evaluation of the INCS method in case of large-scale problems

---

As was noted in Section 1.3, the problem of our interest concerns the evaluation of the pressure field in a large-scale, four-dimensional spatiotemporal domain. Moreover, since the developed INCS method is an iterative method with operations that apply to the full spatiotemporal grid, data needs to be stored for all grid points. This may result in considerable memory requirements. For this reason, a significant part of Chapter 3 was devoted to the development of the Filtered Convolution method, which enables an efficient discretization. Still, the computational grids are of such a size that optimized strategies for reduction of the memory usage are required for the evaluation of the problem. In this appendix we will discuss a number of strategies that either reduce the total spatiotemporal domain size or that minimize the memory demands during the evaluation of the INCS method. We will focus on the evaluation of the convolution sum, as this is the most elaborate operation in the INCS method in terms of memory requirements and computer time.

Evaluation of the four-dimensional convolution sum

First we repeat the four-dimensional discrete convolution sum from Eq. (3.39)

$$\mathcal{L}[S^{(j)}]_{a,b,c,n} = \Delta x^3 \Delta t \sum_{d,e,f} \sum_{m} G_{a-d,b-e,c-f,n-m}\, S^{(j)}_{d,e,f,m}. \tag{B.1}$$

We focus on the case $j \geq 1$, for which $S^{(j)}$ is a source that is distributed over a volume and the operator $\mathcal{L}[S^{(j)}]$ yields the nonlinear field correction $\delta p^{(j)}$. In Eq. (B.1), all quantities denote the spatiotemporally filtered, windowed and sampled forms. Throughout this appendix we will omit the notation developed in Chapter 3 to indicate this. To further simplify the notation, in this appendix we will also omit the superscript (j), and we will use the continuous variables $\boldsymbol{x}$ and t and their Fourier transform counterparts instead of the subscript indices. In this way we focus on the computational evaluation of the convolution sum and we are not distracted by heavy notation.

The spatiotemporal source domain as well as the spatiotemporal domain of interest are given by $[0, \boldsymbol{X}] \times [0, T]$, such that the grids of $\delta p(\boldsymbol{x}, t)$ and $S(\boldsymbol{x}, t)$ coincide and have a size of $A \times B \times C \times N$ points. A straightforward evaluation procedure is presented in Fig. B.1 in the form of a Nassi-Shneiderman structure diagram. The largest memory demand during the numerical evaluation occurs at steps 4 to 7, where we have two complex arrays of 16 $A \times B \times C \times N$ points in memory. The data of $\tilde{\mathcal{L}}[S](\boldsymbol{k}, \omega)$ that is obtained in step 7 may be stored in the array of $\tilde{S}(\boldsymbol{k}, \omega)$. The most elaborate operations in terms of computer time are obtaining $\hat{G}(\boldsymbol{x}, \omega)$ and evaluating the FFT's and IFFT's.

Strategy 1: Use real-to-complex FFT routines

Since the Fourier spectrum of a real function $f(t)$ has the property $\hat{f}(-\omega) = \hat{f}^*(\omega)$, we can save a factor of two in memory usage by only storing the function values for the positive frequencies in $[0, \Omega]$. The FFTW package [27, 28] employs special real-to-complex FFT routines that take care of this. We can only employ this strategy in case of the temporal dimension, since the subsequent transformations involve complex quantities.

1. Obtain $S(\boldsymbol{x}, t)$ employing the windows $[0, \boldsymbol{X}]$ and $[0, T]$
2. Zero-pad $S(\boldsymbol{x}, t)$ in $\boldsymbol{x}$ and t
3. FFT $S(\boldsymbol{x}, t)$ with respect to $\boldsymbol{x}$ and t
4. Obtain $\hat{G}(\boldsymbol{x}, \omega)$ employing the windows $[-\boldsymbol{X}, \boldsymbol{X}]$ and $[-T, T]$
5. Scale $\hat{G}(\boldsymbol{x}, \omega)$ with $1/\Delta t$ and reorder in ω
6. FFT $\hat{G}(\boldsymbol{x}, \omega)$ with respect to $\boldsymbol{x}$
7. $\tilde{\mathcal{L}}[S](\boldsymbol{k}, \omega) := \tilde{G}(\boldsymbol{k}, \omega)\, \tilde{S}(\boldsymbol{k}, \omega)$
8. IFFT $\tilde{\mathcal{L}}[S](\boldsymbol{k}, \omega)$ with respect to $\boldsymbol{k}$ and ω
9. Reduce the support of $\mathcal{L}[S](\boldsymbol{x}, t)$ in $\boldsymbol{x}$ and t
10. Scale $\mathcal{L}[S](\boldsymbol{x}, t)$ with $\Delta x^3 \Delta t$
11. $\delta p(\boldsymbol{x}, t) := \mathcal{L}[S](\boldsymbol{x}, t)$

Figure B.1. Structure diagram for the evaluation of the convolution sum in Eq. (B.1), with the source domain and the domain of interest $[0, \boldsymbol{X}] \times [0, T]$.

Strategy 2: Use efficient evaluation of the convolution sum

The evaluation procedure in Fig. B.1 is not efficient in terms of computation time and memory use, as in step 3 it first declares two large arrays and then performs four-dimensional FFTs on these as a whole, i.e. including all zero-padding regions in $S(\boldsymbol{x}, t)$. We can improve the procedure by addressing each dimension separately [42]. In our case it is most beneficial to apply this strategy only to the temporal dimension. The procedure for this strategy is given in Fig. B.2.

The largest memory demand during the evaluation now occurs at steps 8 to 11, where we have a complex array of $2\,A \times B \times C \times N$ points and two complex arrays of $8\,A \times B \times C$ points in memory. This is considerably less than the memory needed for the procedure in Fig. B.1. The obtained $\tilde{\mathcal{L}}[S](\boldsymbol{k}, \omega_n)$ in step 10 may again be stored in the array of $\tilde{S}(\boldsymbol{k}, \omega_n)$.

Strategy 3: Use a circular temporal axis

The FFT method yields a circular convolution instead of a linear one. As a consequence, to evaluate the linear temporal convolution of the Green's function G with a single-pulse source signature S, we have to extend the support $[0, T]$ of S by zero-padding. In doing so, we prevent the appearance of a wraparound error in the pressure field within the interval $[0, T]$. However,

1. Obtain $S(\boldsymbol{x}, t)$ employing the windows $[0, \boldsymbol{X}]$ and $[0, T]$
2. Zero-pad $S(\boldsymbol{x}, t)$ in t
3. FFT $S(\boldsymbol{x}, t)$ with respect to t
4. For each ω_n
5. Obtain $\hat{G}(\boldsymbol{x}, \omega_n)$ employing the windows $[-\boldsymbol{X}, \boldsymbol{X}]$ and $[-T, T]$
6. Scale $\hat{G}(\boldsymbol{x}, \omega_n)$ with $1/\Delta t$ and reorder in ω
7. FFT $\hat{G}(\boldsymbol{x}, \omega_n)$ with respect to $\boldsymbol{x}$
8. Extend the support of $\hat{S}(\boldsymbol{x}, \omega_n)$ in $\boldsymbol{x}$
9. FFT $\hat{S}(\boldsymbol{x}, \omega_n)$ with respect to $\boldsymbol{x}$
10. $\tilde{\mathcal{L}}[S](\boldsymbol{k}, \omega_n) := \tilde{G}(\boldsymbol{k}, \omega_n)\, \tilde{S}(\boldsymbol{k}, \omega_n)$
11. IFFT $\tilde{\mathcal{L}}[S](\boldsymbol{k}, \omega_n)$ with respect to $\boldsymbol{k}$
12. Reduce the support of $\hat{\mathcal{L}}[S](\boldsymbol{x}, \omega_n)$ in $\boldsymbol{x}$
13. IFFT $\hat{\mathcal{L}}[S](\boldsymbol{x}, \omega)$ with respect to ω
14. Reduce the support of $\mathcal{L}[S](\boldsymbol{x}, t)$ in t
15. Scale $\mathcal{L}[S](\boldsymbol{x}, t)$ with $\Delta x^3 \Delta t$
16. $\delta p(\boldsymbol{x}, t) := \mathcal{L}[S](\boldsymbol{x}, t)$

Figure B.2. Structure diagram for the memory-efficient evaluation of the convolution sum in Eq. (B.1), with the source domain and the domain of interest $[0, \boldsymbol{X}] \times [0, T]$.

if the source signature is periodical with a period T_P we can perform the convolution by taking only one period $t \in [0, T_P)$ of the source signature and using a cyclic convolution with period T_P. In order for the cyclic convolution to yield the correct pressure field solution, we also need the cyclic continuation of the Green's function with a period T_P. This is automatically obtained by omitting the temporal windowing of the Green's function in the temporal Fourier domain. By using the cyclic convolution, the zero-padding region in t is omitted. This results in a total grid size that is a factor of two smaller as compared to the linear convolution with an aperiodic pulse.

The approach for the periodical source signature can also be employed in the case of a single pulse excitation, saving a factor of two in memory demand and computation time. If the temporal support on each spatial position in the domain of interest has a maximum length T, regardless of the time of arrival at that position, then a periodical continuation with a period $T_P = T$ of the source and of the resulting pressure field will never yield an overlap of the original field with its periodically continued counterparts. To

1. Obtain $S(\boldsymbol{x},t)$ employing the windows $[0,\boldsymbol{X}]$ and $[0,T]$
2. Zero-pad $S(\boldsymbol{x},t)$ only in $\boldsymbol{x}$
3. FFT $S(\boldsymbol{x},t)$ with respect to $\boldsymbol{x}$ and t
4. Obtain $\hat{G}(\boldsymbol{x},\omega)$ employing only the spatial window $[-\boldsymbol{X},\boldsymbol{X}]$
5. Scale $\hat{G}(\boldsymbol{x},\omega)$ with $1/\Delta t$ and reorder in ω
6. FFT $\hat{G}(\boldsymbol{x},\omega)$ with respect to $\boldsymbol{x}$
7. $\tilde{\mathcal{L}}[S](\boldsymbol{k},\omega) := \tilde{G}(\boldsymbol{k},\omega)\,\tilde{S}(\boldsymbol{k},\omega)$
8. IFFT $\tilde{\mathcal{L}}[S](\boldsymbol{k},\omega)$ with respect to $\boldsymbol{k}$ and ω
9. Reduce the support of $\mathcal{L}[S](\boldsymbol{x},t)$ in $\boldsymbol{x}$
10. Scale $\mathcal{L}[S](\boldsymbol{x},t)$ with $\Delta x^3 \Delta t$
11. $\delta p(\boldsymbol{x},t) := \mathcal{L}[S](\boldsymbol{x},t)$

Figure B.3. Structure diagram for the evaluation of the convolution sum in Eq. (B.1) with the source domain and the domain of interest $[0,\boldsymbol{X}] \times [0,T]$. The procedure is applicable in case of either a periodical source signal with a period $T_P = T$, or when it may be assumed that the temporal window size T is large enough to prevent the cyclic continuation of the field solution from overlapping with the original field solution.

reconstruct the absolute time axis of the pressure field at a certain point, we multiply the periodical continuation with a window at $[t_0, t_0 + T_P]$, where t_0 is the time of arrival at that point. The evaluation procedure for the cyclic convolution sum is presented in Fig. B.3.

In the cyclic temporal convolution, the total number of points for S is now N instead of $2N$. For $\hat{G}(\boldsymbol{x},\omega)$ this means that the samples in the angular frequency domain are taken at $\omega = n\Delta\omega$ with $\Delta\omega = 2\pi/N\Delta t$ and $n \in [-(N/2), (N-1)/2]$ (division rounded down).

Strategy 4: Use convolutions over skew domains (candy cane method)

As observed in Subsection 5.3.3, for the evaluation of the nonlinear field at a certain point of observation it is sufficient to include the contrast sources in the region in between the primary source and the point of observation. To compute the field in points relatively close to the z-axis, e.g. for an unsteered beam, we can take a block-shaped domain of interest with x and y-dimensions that are approximately equal to the sizes of the primary source, as sketched

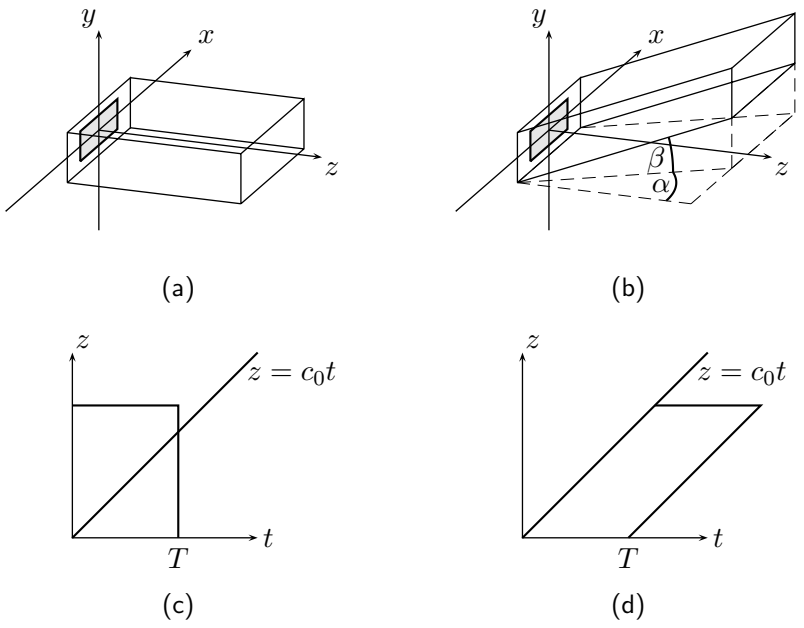

Figure B.4. (a) Block-shaped domain of interest, located around the positive z-axis. (b) Parallelepiped-shaped domain of interest around an axis with azimuth α and elevation β. (c) Time of arrival on the z-axis of a pulse excited at $z = 0$ on $t = 0$, and a stationary "rectangular" domain of interest with duration T. (d) Same situation as in (c), but now with a comoving "parallelogram-shaped" domain of interest with duration T.

in Fig. B.4a. However, for points at a larger distance from the z-axis, e.g. for a steered beam or a grating lobe, we would need block-shaped domains of interest with large x or y-dimensions to cover the region in between the primary source and the point of observation. In this case it is much more efficient to calculate the field in a parallelepiped-shaped domain of interest, with a certain azimuth and elevation, as depicted in Fig. B.4b.

A similar situation occurs in combination with the temporal dimension, as is shown in Figs. B.4c and d. An excitation from the primary source at $z = 0$ on $t = 0$ causes an acoustic pressure field on the z-axis with a time of arrival $t = z/c_0$. When studying the pressure pulse of duration T, it would be more efficient to calculate the field in a temporal window that moves along with the time of arrival. This is achieved by using a parallelogram-shaped domain in the tz-plane.

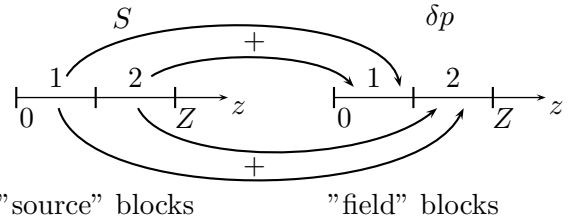

Figure B.5. Illustration of the blockwise evaluation of the convolution over two blocks $[0, Z/2)$ and $[Z/2, Z)$ in the z-dimension.

An efficient method to calculate the convolution over a domain of that is skew in any of the xz, yz and tz-planes and that yields a result in another domain with arbitrary skewness, has been developed by De Koning [42]. This method is called the candy cane method, and for a domain of interest and a contrast source domain with equal skewness, it is equally efficient in memory demand and computation time as the convolution over a rectangular domain of the same volume.

For the temporal dimension, the situation with the comoving domain is comparable to the periodical window used for Strategy 3, in that we can use a much smaller time window than in case of a stationary domain. The differences with Strategy 3 are that for the comoving domain we still need to include a wraparound region, but on the other hand the time window at any spatial position can now be taken below the maximum temporal support of the entire field.

Strategy 5: Use spatiotemporal decomposition and blockwise evaluation

If the domain of interest is too large to allow for the evaluation of the convolution, then we can subdivide the domain into spatiotemporal blocks and we can evaluate the convolution using a blockwise approach. To illustrate this, we consider a blockwise convolution in the z-dimension. For any "field" block, the result of the convolution over a "source" block is evaluated, and the results are added as depicted in Fig. B.5. In the procedure, care should be taken to avoid overlap. The blockwise evaluation of the convolution takes much less memory because of the smaller zero-padding regions and because only the specific source and field correction blocks are needed in core mem-

1. For $v := 0$ to $V - 1$
2. Obtain $S(x, y, z_v, t)$
3. Zero-pad $S(x, y, z_v, t)$ in $\boldsymbol{x}$ and t
4. FFT $S(x, y, z_v, t)$ with respect to $\boldsymbol{x}$ and t
5. For $w := 0$ to $V - 1$
6. Obtain $\hat{G}(x, y, z_{vw}, \omega)$ employing the appropriate windows
7. Scale $\hat{G}(x, y, z_{vw}, \omega)$ with $1/\Delta t$ and reorder in ω
8. FFT $\hat{G}(x, y, z_{vw}, \omega)$ with respect to $\boldsymbol{x}$
9. $\tilde{\mathcal{L}}[S](\boldsymbol{k}, \omega) := \tilde{G}(\boldsymbol{k}, \omega)\, \tilde{S}(\boldsymbol{k}, \omega)$
10. IFFT $\tilde{\mathcal{L}}[S](\boldsymbol{k}, \omega)$ with respect to $\boldsymbol{k}$ and ω
11. Reduce the support of $\mathcal{L}[S](x, y, z_w, t)$ in $\boldsymbol{x}$ and t
12. Scale $\mathcal{L}[S](x, y, z_w, t)$ with $\Delta x^3 \Delta t$
13. Add $\mathcal{L}[S](x, y, z_w, t)$ to $\delta p(x, y, z_w, t)$

Figure B.6. Structure diagram for the evaluation of the convolution sum in Eq. (B.1) with the source domain and the domain of interest $[0, \boldsymbol{X}] \times [0, T]$, using blockwise evaluation over V blocks in the z-dimension. Here, $z_v \in [v\,Z/V, (v+1)Z/V)$, $z_w \in [w\,Z/V, (w+1)Z/V)$ and $z_{vw} \in ((w - v - 1)Z/V, (w - v + 1)Z/V)$.

ory. The procedure for the evaluation of the convolution using a blockwise approach in the z-dimension is given in Fig. B.6.

The approach to evaluate the convolution with a blockwise approach may come at a cost in computation time. Firstly, for a one-dimensional domain with a total of C points, the order of complexity of the blockwise approach with V blocks is $2CV \log(2C/V)$. Compared with an order of complexity of $2C \log(2C)$ for the procedure in Fig. B.1, the increase in computation time becomes considerable for large V. However, the blockwise approach also gives us the option to exclude certain blockwise convolutions that contribute little or nothing at all. We concluded in Subsection 5.3.3 that the contrast sources between the source and the point of observation contribute dominantly to the nonlinear field correction. With the blockwise approach we can therefore benefit from the fact that any source blocks outside this area can safely be disregarded. A second cause for the increase in runtime is introduced if the harddisk is used as an external memory. If between the blockwise convolutions the total contrast source data and the total field correction data are stored on and retrieved from harddisk, then the time needed for data access increases considerably as compared to the

use of core memory. Thirdly, the blockwise approach requires the Green's function to be evaluated more often, which causes a considerable increase of the total computation time.

Strategy 6: Use the symmetry

All primary source geometries used in Chapter 5 exhibit symmetry in the y-dimension, which we can exploit to reduce memory demands and computation time. A primary source that is symmetrical in the y-dimension yields a pressure field that obeys $p(x, y, z, t) = p(x, -y, z, t)$. If the source domain as well as the domain of interest are given by $[0, \boldsymbol{X}] \times [0, T]$, with $[0, \boldsymbol{X}] = [0, X] \times [-Y, Y] \times [0, Z]$, the grids of $\delta p(\boldsymbol{x}, t)$ and $S(\boldsymbol{x}, t)$ coincide and have a size of $A \times 2B \times C \times N$ points. If we obtain the pressure field for $[0, Y]$ only, we may use this field to calculate the contrast sources in $[0, Y]$, but also the contrast sources in $[-Y, 0)$. The required size of the grid of $\delta p(\boldsymbol{x}, t)$ and $S(\boldsymbol{x}, t)$ is thus $A \times B \times C \times N$, as in the straightforward convolution, although the source domain employed in the computation is twice as large. The procedure for the evaluation of the convolution employing symmetry in the y-dimension is presented in Fig. B.7.

This strategy is a special case of Strategy 5, and it works in combination with Strategy 4, as long as the elevation angle $\beta = 0°$. It may also be applied in the x-dimension if we have symmetry in that dimension.

1. Obtain $S(x, y_+, z, t)$
2. Zero-pad $S(x, y_+, z, t)$ in $\boldsymbol{x}$ and t by zero-padding
3. FFT $S(x, y_+, z, t)$ with respect to $\boldsymbol{x}$ and t
4. Obtain $\hat{G}(x, y_{++}, z, \omega)$ employing the appropriate windows
5. Scale $\hat{G}(x, y_{++}, z, \omega)$ with $1/\Delta t$ and reorder in ω
6. FFT $\hat{G}(x, y_{++}, z, \omega)$ with respect to $\boldsymbol{x}$
7. $\tilde{\mathcal{L}}[S](\boldsymbol{k}, \omega) = \tilde{G}(\boldsymbol{k}, \omega)\, \tilde{S}(\boldsymbol{k}, \omega)$
8. IFFT $\tilde{\mathcal{L}}[S](\boldsymbol{k}, \omega)$ with respect to $\boldsymbol{k}$ and ω
9. Reduce the support of $\mathcal{L}[S](x, y_+, z, t)$ in $\boldsymbol{x}$ and t
10. Scale $\mathcal{L}[S](x, y_+, z, t)$ with $\Delta x^3 \Delta t$
11. $\delta p(x, y_+, z, t) := \mathcal{L}[S](x, y_+, z, t)$
12. Obtain $S(x, y_-, z, t)$ from $S(x, -y_-, z, t)$
13. Zero-pad $S(x, y_-, z, t)$ in $\boldsymbol{x}$ and t by zero-padding
14. FFT $S(x, y_-, z, t)$ with respect to $\boldsymbol{x}$ and t
15. Obtain $\hat{G}(x, y_{-+}, z, \omega)$ employing the appropriate windows
16. Scale $\hat{G}(x, y_{-+}, z, \omega)$ with $1/\Delta t$ and reorder in ω
17. FFT $\hat{G}(x, y_{-+}, z, \omega)$ with respect to $\boldsymbol{x}$
18. $\tilde{\mathcal{L}}[S](\boldsymbol{k}, \omega) := \tilde{G}(\boldsymbol{k}, \omega)\, \tilde{S}(\boldsymbol{k}, \omega)$
19. IFFT $\tilde{\mathcal{L}}[S](\boldsymbol{k}, \omega)$ with respect to $\boldsymbol{k}$ and ω
20. Reduce the support of $\mathcal{L}[S](x, y_+, z, t)$ in $\boldsymbol{x}$ and t
21. Scale $\mathcal{L}[S](x, y_+, z, t)$ with $\Delta x^3 \Delta t$
22. $\delta p(x, y_+, z, t) := \delta p(x, y_+, z, t) + \mathcal{L}[S](x, y_+, z, t)$

Figure B.7. Structure diagram for the evaluation of the convolution sum in Eq. (B.1) with the source domain and the domain of interest $[0, X] \times [-Y, Y] \times [0, Z] \times [0, T]$. The procedure is applicable in case of symmetry in the y-dimension. Here, $y_+ \in [0, Y]$, $y_- \in [-Y, 0)$, $y_{++} \in [-Y, Y]$ and $y_{-+} \in (0, 2Y]$.

Appendix C

Derivation of the linear acoustic field of a cylindrical piston transducer causing a pressure jump

---

In this appendix we describe the derivation of the linear acoustic pressure field of a cylindrical piston source causing a pressure jump. From the convolution integral in Eq. (3.7) we derive a single variable integral that can be evaluated with a standard numerical method.

The source under study is an unfocused cylindrical piston source located in the plane $z = 0$ and causing a pressure jump. The piston has $\mathcal{O}$ as its center and R as its radius. It causes a pressure jump that, conform Eq. (5.4), can be described as $\Delta P(x, y, t) = 2P_0\, s(t)\, a(x, y)$ with $a(x, y) = H(R - \sqrt{x^2 + y^2})$. If the pressure jump source of Eq. (3.64) and the three-dimensional Green's function of Eq. (3.9) are substituted into the convolution integral in Eq. (3.7), then an expression is obtained for the linear acoustic pressure $p(\boldsymbol{x}, t)$ in a point of observation $\boldsymbol{x}$, viz.

$$p(\boldsymbol{x}, t) = -\int_{\mathcal{D}_S}\int_{\mathcal{T}_S} \frac{\delta(t - t' - \|\boldsymbol{x} - \boldsymbol{x}'\|/c_0)}{4\pi\,\|\boldsymbol{x} - \boldsymbol{x}'\|}\, \partial_{z'}[\Delta P(x', y', t')\, \delta(z')]\ \mathrm{d}t'\ \mathrm{d}\boldsymbol{x}'. \tag{C.1}$$

With the application of the commutativity property for the convolution, see Eq. (3.66), and by using the sifting property of the delta pulses, we can

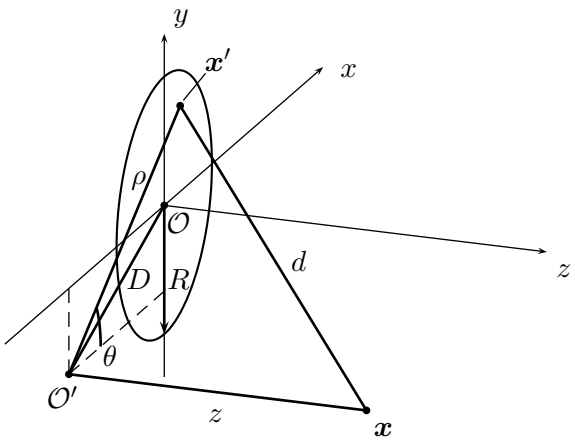

Figure C.1. Geometry of the cylindrical source, showing the source point $\boldsymbol{x}'$ and the observation point $\boldsymbol{x}$, the polar coordinate system (ρ, θ), and several other geometrical variables.

rewrite Eq. (C.1) as

$$p(\boldsymbol{x}, t) = -\partial_z \int_{\mathcal{D}_S} \frac{\Delta P(x', y', t - \|\boldsymbol{x}-\boldsymbol{x}'\|/c_0)}{4\pi \|\boldsymbol{x}-\boldsymbol{x}'\|} \, \mathrm{d}\boldsymbol{x}'. \tag{C.2}$$

where $\boldsymbol{x}' = (x', y', 0)$. We now apply a transformation of $\boldsymbol{x}'$ [33]. First we define the point $\mathcal{O}'$ as the projection of $\boldsymbol{x}$ onto the source plane, i.e. $\mathcal{O}' = (x, y, 0)$. Next, within the source plane we introduce the set of polar coordinates (ρ, θ) with respect to $\mathcal{O}'$ as

$$\rho = \sqrt{(x' - x)^2 + (y' - y)^2}, \tag{C.3}$$

$$\theta = \tan^{-1}\left(\frac{y' - y}{x' - x}\right). \tag{C.4}$$

The polar coordinate system is shown in Fig. C.1. Moreover, we introduce the distance D between $\mathcal{O}$ and $\mathcal{O}'$, the distance d between the observation point $\boldsymbol{x}$ and the source point $\boldsymbol{x}'$, and the retarded time τ as

$$D = \sqrt{x^2 + y^2}, \tag{C.5}$$

$$d = \left\|\boldsymbol{x}-\boldsymbol{x}'\right\| \quad = \sqrt{\rho^2 + z^2}, \tag{C.6}$$

$$\tau = t - \frac{\|\boldsymbol{x}-\boldsymbol{x}'\|}{c_0} = t - \frac{d}{c_0}. \tag{C.7}$$

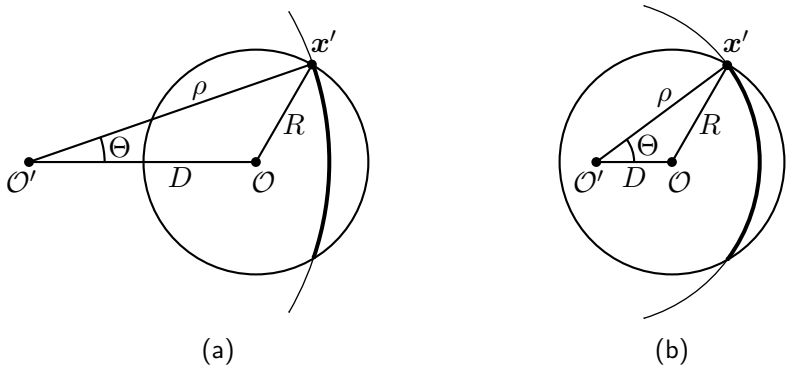

Figure C.2. Determination of the angle $\Theta(\rho)$, for a source point $\boldsymbol{x}'$ on the rim of the cylindrical source. (a) Case $D \geq R$ and $\rho \in [D-R, D+R]$. (b) Case $D < R$ and $\rho \in [R-D, R+D]$; in this case there is no point on the rim for $\rho \in [0, R-D)$.

In the polar coordinate system we have $\mathrm{d}\boldsymbol{x}' = \rho\,\mathrm{d}\theta\,\mathrm{d}\rho$, and by writing out the excitation function, the integral in Eq. (C.2) yields

$$\begin{aligned} p(\boldsymbol{x},t) &= -\partial_z \int_0^\infty \int_0^{2\pi} \frac{\Delta P(\rho,\theta,\tau)}{4\pi\, d}\,\rho\,\mathrm{d}\theta\,\mathrm{d}\rho \\ &= -\partial_z \int_0^\infty \frac{P_0\, s(\tau)}{d} \int_0^{2\pi} \frac{a(\rho,\theta)}{2\pi}\,\mathrm{d}\theta\,\rho\,\mathrm{d}\rho. \end{aligned} \tag{C.8}$$

The geometry function $a(\rho,\theta)$ is derived from $a(x',y')$ as

$$a(\rho,\theta) = H\left(R - \sqrt{[x+\rho\cos(\theta)]^2 + [y+\rho\sin(\theta)]^2}\right). \tag{C.9}$$

Let us now define the function

$$a_\rho(\rho) = \int_0^{2\pi} \frac{a(\rho,\theta)}{2\pi}\,\mathrm{d}\theta. \tag{C.10}$$

The value of this function is determined by that part of the circle with radius ρ and center $\mathcal{O}'$ that falls within the support of $a(x,y)$. We distinguish between two cases that depend on the location of $\mathcal{O}'$, as shown in Fig. C.2. In case $D \geq R$, for $\rho \in [D-R, D+R]$ a part of the circle falls within the support of $a(x,y)$. As may be deduced from Fig. C.2a, the angle $\Theta(\rho)$ is found from the cosine law as

$$\Theta(\rho) = \cos^{-1}\left(\frac{D^2+\rho^2-R^2}{2D\rho}\right), \tag{C.11}$$

Table C.1. The ranges of ρ and the expressions for $a_\rho(\rho)$, for the two cases for D. For all other values of ρ, we have $a_\rho(\rho) = 0$. $\Theta(\rho)$ is given by Eq. (C.11).

Case	Range $[\rho_1, \rho_2]$		
for D	ρ_1	ρ_2	$a_\rho(\rho)$
$D \geq R$	$D - R$	$D + R$	$\Theta(\rho)/\pi$
$D < R$	0	$R - D$	1
$D < R$	$R - D$	$R + D$	$\Theta(\rho)/\pi$

and within this range of ρ, we therefore have

$$a_\rho(\rho) = \frac{\Theta(\rho)}{\pi}. \tag{C.12}$$

In case $D < R$, for $\rho \in [0, R - D)$ the entire circle falls within the support of $a(\rho, \theta)$, and therefore we have $a_\rho(\rho) = 1$. As shown in Fig. C.2b, for $\rho \in [R - D, R + D]$ the angle $\Theta(\rho)$ is again found from the cosine law and is again given by Eq. (C.11). In all cases, the value of $a_\rho(\rho)$ varies between 0 and 1, and $a_\rho(\rho)$ acts as a geometry function. For the different cases for D and ranges $[\rho_1, \rho_2]$ of ρ the corresponding expressions for $a_\rho(\rho)$ are given in Table C.1. Substitution of $a_\rho(\rho)$ into Eq. (C.8) gives us

$$p(\boldsymbol{x}, t) = -\partial_z \int_{\rho_1}^{\rho_2} \frac{P_0\, s(\tau)}{d} a_\rho(\rho)\, \rho \, \mathrm{d}\rho. \tag{C.13}$$

Next, we apply the derivative with respect to z, and with

$$\partial_z \frac{1}{d} = \frac{-z}{d^3}, \tag{C.14}$$

$$\partial_z \tau = \frac{-z}{c_0 d}, \tag{C.15}$$

we arrive at

$$p(\boldsymbol{x}, t) = z\, P_0 \int_{\rho_1}^{\rho_2} \left[\frac{s(\tau)}{d^3} + \frac{\partial_\tau s(\tau)}{c_0\, d^2} \right] a_\rho(\rho)\, \rho \, \mathrm{d}\rho. \tag{C.16}$$

Finally, we change the integration variable from ρ to d. From Eq. (C.6) we obtain $\rho \, \mathrm{d}\rho = d \, \mathrm{d}d$, and this yields

$$p(\boldsymbol{x}, t) = z\, P_0 \int_{d_1}^{d_2} \left[\frac{s(\tau)}{d^2} + \frac{\partial_\tau s(\tau)}{c_0\, d} \right] a_\rho(d)\, \mathrm{d}d. \tag{C.17}$$

Table C.2. The ranges of d and the expressions for $a_\rho(d)$, for the two cases for D. For all other values of d, we have $a_\rho(d) = 0$. $\Theta(d)$ is given by Eq. (C.18).

Case	Range $[d_1, d_2]$		
for D	d_1	d_2	$a_\rho(d)$
$D \geq R$	$\sqrt{(D-R)^2+z^2}$	$\sqrt{(D+R)^2+z^2}$	$\Theta(d)/\pi$
$D < R$	z	$\sqrt{(R-D)^2+z^2}$	1
$D < R$	$\sqrt{(R-D)^2+z^2}$	$\sqrt{(R+D)^2+z^2}$	$\Theta(d)/\pi$

For the different cases for D and ranges $[d_1, d_2]$ of d, the corresponding expressions for $a_\rho(d)$ are given in Table C.2. The angle $\Theta(d)$ employed in this table is derived from Eq. (C.11) as

$$\Theta(d) = \cos^{-1}\left(\frac{D^2 + d^2 - z^2 - R^2}{2\,D\,\sqrt{d^2 - z^2}}\right). \tag{C.18}$$

The integral occurring in Eq. (C.17) is a regular integral that can be evaluated numerically up to any degree of accuracy with an adaptive Lobatto quadrature rule. On the source axis a closed-form solution can straightforwardly be obtained from Eq. (C.13). For this special case we have $\rho_1 = 0$ and $\rho_2 = R$, and in between these bounds $a_\rho(\rho) = 1$. Equation (C.13) then reduces to

$$p(z,t) = -\partial_z \int_0^R \frac{P_0\, s(\tau)}{d}\, \rho \,\mathrm{d}\rho. \tag{C.19}$$

It can be easily shown that

$$\partial_z \frac{s(\tau)}{d} = \frac{z}{\rho}\,\partial_\rho \frac{s(\tau)}{d}, \tag{C.20}$$

and for $z > 0$ Eq. (C.19) therefore results in

$$\begin{aligned} p(z,t) &= -z \int_0^R \partial_\rho \frac{P_0\, s(\tau)}{d}\, \mathrm{d}\rho \\ &= -z\, \frac{P_0\, s(\tau)}{d}\bigg|_{\rho=0}^{\rho=R} \\ &= P_0\, s(t - \frac{z}{c_0}) - \frac{z}{\sqrt{z^2+R^2}}\, P_0\, s(t - \frac{\sqrt{z^2+R^2}}{c_0}). \end{aligned} \tag{C.21}$$

The two terms in this final form are respectively called the body wave and the edge wave. The body wave term resembles a plane-wave starting at $z = 0$, and the edge wave term seems to originate at the edge of the source. At the source, the axial pressure field simply becomes $\lim_{z\downarrow 0} p(z,t) = P_0\, s(t)$. For $z \gg R$, Eq. (C.21) can be approximated by

$$p(z,t) \approx P_0\, s(\tau) - P_0\, s(\tau - \frac{R^2}{2c_0 z}), \tag{C.22}$$

where $\tau = t - z/c_0$. For large z the time difference between the first and the last term, i.e. the term $R^2/2c_0 z$, becomes very small. From this we observe that for $z \to \infty$ we may apply a further approximation

$$p(z,t) \approx \frac{R^2}{2c_0 z}\, \partial_\tau\, P_0\, s(\tau). \tag{C.23}$$

This shows that for large z the waveform of the pressure on the axis resembles the time derivative of the source pulse.

Appendix D

Extension of the INCS method to media with attenuation of a frequency power law type

---

In the development of the INCS method we have disregarded the occurrence of attenuation in the acoustic medium. As we mentioned in Sections 1.3 and 2.5, for water this neglection is allowed in case of not too strong nonlinearity. However, for the linear or nonlinear propagation of acoustic waves through a medium like human soft tissue, attenuation cannot be neglected. For the frequencies considered in this thesis, attenuation in tissue is about a factor 100 higher than in water. In this appendix we will present an approach for including acoustic attenuation in our physical and numerical model. We start with the phenomenology of attenuation in water and in human tissue. Next, we turn our attention to the inclusion of attenuation in the linear basic equations and in the associated Green's function. Subsequently, we discuss the spatiotemporal filtering and windowing of the lossy Green's functions, followed by a description of the numerical evaluation of the resulting expressions. After this we generalize the approach to the nonlinear acoustic wave problem, and finally we show the performance of the approach and the differences with some results presented earlier in this thesis.

Phenomenology of attenuation and dispersion in water and in tissue

When an acoustic wave propagates through a realistic medium, it undergoes attenuation. A plane, harmonic wave traveling in the positive x-direction through a lossy medium can be described by [65]

$$p(x,t) = P_0 \exp[j\omega(t - x/c_0)] \exp(-\alpha x) = P_0 \exp(j\omega t - \gamma x), \tag{D.1}$$

where $\alpha > 0$ is the attenuation coefficient and

$$\gamma(\omega) = j\frac{\omega}{c_0} + \alpha \tag{D.2}$$

is the propagation coefficient. The attenuation coefficient is usually expressed in nepers per centimeter [Np/cm] or decibel per centimeter [dB/cm].[1] For water, α is proportional to the square of the frequency [32, 65]. For human soft tissue, α can usually be described by a frequency power law with a power $1 < b < 2$ up till very high frequencies [19]. For both types of media, the attenuation coefficient can therefore be written as

$$\alpha(\omega) = \alpha_1 |\omega|^b, \quad \alpha_1 > 0,\ 1 < b \leq 2. \tag{D.3}$$

Table D.1 lists typical values for the relevant acoustic medium parameters for water and for several human tissues.

Lossy basic equations and lossy Green's function

When drawing up a mathematical framework for the propagation of acoustic waves through an attenuative medium, two principles must at least be obeyed that are essential to the physical nature of wave propagation. The first principle is that of causality, i.e. a response cannot precede its cause. The second principle is that an excitation always results in a wavefront that travels through the medium with a finite sound speed. In this section we start with the linearized, constitutive equations for a medium with relaxation in the compressibility parameter. Together with the basic acoustic equations, these relations lead to a Green's function of the lossy, linear and homogeneous background medium that respects the two principles of acoustic wave propagation and that expresses a frequency power law type of attenuation.

[1] 1 Np = 8.686 dB.

Table D.1. Acoustic medium parameters for water and for several human tissues, obtained from [19, 65]. The attenuation coefficient a as in the frequency power law af^b is given, from which α_1 follows as $\alpha_1 = a\,(2\pi)^{-b}$. The given numbers are typical values.

Medium type	c_0 $[\mathrm{m\,s^{-1}}]$	ρ_0 $[\mathrm{kg\,m^{-3}}]$	β	a $[\mathrm{Np\,cm^{-1}MHz^{-}}b]$	b
water	1492	998	3.52	2.5×10^{-4}	2.0
blood	1584	1060	4.00	1.6×10^{-2}	1.21
brain	1562	1035	4.28	6.7×10^{-2}	1.3
fat	1430	928	6.14	1.4×10^{-2}	1.0*
liver	1578	1050	4.38	5.2×10^{-2}	1.05
muscle (skeletal)	1580	1041	4.72	6.3×10^{-2}	1.0*

* assumed value

From Eqs. (2.30) and (2.38) the linearized, constitutive equations for a lossless and therefore instantaneously reacting medium are obtained as

$$\dot{\Phi}_k = \rho_0 \partial_t v_k, \tag{D.4}$$

$$\dot{\theta} = -\kappa_0 \partial_t p. \tag{D.5}$$

We introduce an attenuation mechanism in the medium by incorporating relaxation in the compressibility parameter, and because of this the second equation becomes

$$\dot{\theta}(t) = -\kappa_0 \partial_t \int_{-\infty}^{\infty} \chi(t-\tau) p(\tau)\,\mathrm{d}\tau = -\kappa_0 \partial_t \left[\chi(t) *_t p(t)\right], \tag{D.6}$$

where $\chi(t)$ $[\mathrm{s^{-1}}]$ is a normalized compressibility relaxation function and $*_t$ denotes the convolution with respect to time. In this relation, causality demands that the dilatation rate $\dot{\theta}(t)$ is the reaction of the medium to a pressure $p(t)$ imposed on it either before or at the time of the reaction. Therefore we must require that the integrand only yields a contribution for $\tau \leq t$, which means that

$$\chi(t) = 0 \quad \text{for} \quad t < 0. \tag{D.7}$$

In the derivation of the first-order linear acoustic equations (2.55) and (2.56) we have neglected loss mechanisms like viscosity and heat conduction by

making Assumptions 3 and 6. Without going into detail on these issues, we now simply assume that the linear acoustic equations for a lossy medium may be obtained from the inclusion of Eqs. (D.4) and (D.6) in the deformation equation (2.17) and the equation of motion (2.21). This gives [74]

$$\partial_k p(x_j,t) + \rho_0 \partial_t v_k(x_j,t) = f_k(x_j,t), \tag{D.8}$$

$$\partial_r v_r(x_j,t) + \kappa_0 \partial_t \left[\chi(t) *_t p(x_j,t)\right] = q\ (x_j,t). \tag{D.9}$$

Conform the derivation in Section 2.4 these equations yield a lossy, linear wave equation of the form

$$\frac{1}{c_0^2}\partial_t^2[\chi(t) *_t p(x_j,t)] - \partial_k^2 p(x_j,t) = S(x_j,t). \tag{D.10}$$

The Green's function $G(x_j,t)$ for the lossy wave problem is defined as the pressure response to a point source that is located at $x_j = 0$ and that emits an impulse at $t = 0$, i.e.

$$\frac{1}{c_0^2}\partial_t^2[\chi(t) *_t G(x_j,t)] - \partial_k^2 G(x_j,t) = \delta(x_j)\delta(t). \tag{D.11}$$

The lossy Green's function has to obey causality as well, so $G(x_j,t) = 0$ for $t < 0$. Moreover, the lossy Green's function has to yield a wavefront that travels through the medium with a finite speed. This speed should equal the sound speed c_0 of the lossless wave problem.

The Green's function is best solved from Eq. (D.11) by applying integral transforms with respect to x_j and t. As in Section 3.4, we will employ the Fourier transform in the spatial dimensions. For the temporal dimension however, we favor the single-sided Laplace transform, as it provides straightforward conditions to ensure causality and to find the speed of the wavefront. The Laplace transform $\hat{f}(s)$ of an arbitrary, causal function $f(t)$, with $f(t) = 0$ for $t < 0$, is defined by the Laplace transformation pair

$$\hat{f}(s) = \int_0^\infty f(t)\, \exp(-st)\, \mathrm{d}t, \tag{D.12}$$

$$f(t) = \frac{1}{2\pi j} \int_{s_0-j\infty}^{s_0+j\infty} \hat{f}(s)\, \exp(st)\, \mathrm{d}s, \tag{D.13}$$

where s is the complex Laplace parameter. The integration path in the inverse transformation is called the Bromwich contour and s_0 is chosen such

that the contour is located to the right of any singularities of the integrand. Note from comparison with Eqs. (3.19) and (3.20) that the Fourier transform pair of an arbitrary, causal function $f(t)$ is obtained from Eqs. (D.12) and (D.13) by taking the limit $s \to j\omega$ from the right half of the complex s-plane. Since both $\chi(t)$ and $G(x_j, t)$ are causal functions, application of the temporal Laplace and spatial Fourier transformations to Eq. (D.11) yields

$$\left[\frac{s^2}{c_0^2}\hat{\chi}(s) + \|\boldsymbol{k}\|^2\right]\tilde{G}(\boldsymbol{k}, s) = 1, \tag{D.14}$$

and thus we find that the Green's function in the spatiotemporal Fourier domain is given by

$$\tilde{G}(\boldsymbol{k}, s) = \frac{1}{\|\boldsymbol{k}\|^2 + \gamma^2}, \tag{D.15}$$

where

$$\gamma(s) = \frac{s}{c_0}\hat{\chi}^{1/2}(s) \tag{D.16}$$

is the propagation coefficient. Comparison of Eq. (D.15) with Eqs. (3.46) and (3.55) shows that the lossless Green's functions straightforwardly generalize to their lossy forms by substituting $jk = \gamma(s)$. By using this substitution in the lossless, temporal Fourier domain expressions in Eqs. (3.45) and (3.54), we obtain the lossy, temporal Laplace domain forms of the one-dimensional and three-dimensional Green's functions as

$$\hat{G}(x, s) = \frac{\exp(-\gamma(s)\,|x|)}{2\gamma(s)}, \tag{D.17}$$

$$\hat{G}(\boldsymbol{x}, s) = \frac{\exp(-\gamma(s)\,\|\boldsymbol{x}\|)}{4\pi\,\|\boldsymbol{x}\|}. \tag{D.18}$$

In the Laplace domain, the general conditions to be imposed on $\gamma(s)$ and $\hat{\chi}(s)$ are:

1. $\hat{\chi}(s)$ is the Laplace transform of a real function. This means that $\hat{\chi}(s)$ must be real for real values of s.

2. $\hat{\chi}(s)$ is the Laplace transform of a unique, causal function. This condition is imposed by Lerch's theorem [78], stating that $\hat{\chi}(s)$ must at least remain bounded in the real points $s = s_0 + nl$ with $s_0 \geq 0$, $l > 0$ and $n = 0, 1, 2, \ldots$ This condition is certainly satisfied if $\hat{\chi}(s)$ remains bounded on the real axis for $s \geq s_0 \geq 0$.

3. The wavefront travels with a finite wave speed c_0. In the lossless case, the wave speed is obtained as $c_0 = s/\gamma(s)$. In the lossy case, the propagation speed of the wavefront follows from $\gamma(s)$ in the limit $\mathrm{Re}(s) \to \infty$ as

$$c_0 = \lim_{\mathrm{Re}(s)\to\infty} \frac{s}{\gamma(s)} = \lim_{\mathrm{Re}(s)\to\infty} \frac{c_0}{\hat{\chi}^{1/2}(s)}, \tag{D.19}$$

and therefore we have the requirement

$$\lim_{\mathrm{Re}(s)\to\infty} \hat{\chi}(s) = 1. \tag{D.20}$$

Within the bounds set by these conditions, we may construct a propagation coefficient that obeys a frequency power law attenuation, i.e. a function $\gamma(s)$ that for $s \to j\omega$ gives

$$\gamma(j\omega) = \frac{j\omega}{c_0}\hat{\chi}^{1/2}(j\omega) = \alpha(\omega) + j\beta(\omega), \tag{D.21}$$

where $\alpha(\omega)$ satisfies Eq. (D.3). A possible function that fits these requirements is

$$\gamma(s) = \frac{s}{c_0}\left(1 + \frac{c_0\alpha_1 s^{b-1}}{\cos(\pi b/2)[1 + (s/s_1)^a]}\right), \tag{D.22}$$

where a is an integer value with $a > b-1$ and $s_1 \gg 1$. From this expression, the relaxation function is easily obtained. The term $(s/s_1)^a$ in the denominator is necessary to satisfy the general conditions 2 and 3. In this term, the real positive constant s_1 may be very large. Straightforward analysis shows that as long as $|\omega| \ll s_1$

$$\alpha(\omega) \approx \alpha_1 |\omega|^b, \tag{D.23}$$

$$\beta(\omega) \approx \frac{\omega}{c_0} + \alpha_1 \tan(\pi b/2)\omega\,|\omega|^{b-1}. \tag{D.24}$$

Here it has been assumed that the branch cut due to s^{b-1} is located in the left half of the complex s-plane so that one and the same definition for the fractional powers of $\pm j$ can be employed, i.e.

$$(\pm j)^b = \exp(\pm j\pi b/2) = \cos(\pi b/2) \pm j\sin(\pi b/2). \tag{D.25}$$

The dispersion term in $\beta(\omega)$ is the same as the one found by Szabo [64]. Moreover, the relaxation function $\hat{\chi}(s)$ following from Eq. (D.22) is an extension of the Power Law loss model introduced by Strick, which was given for $0 < b < 1$ [62].

Filtering and windowing of the 1D and 3D lossy Green's functions

In the temporal and spatiotemporal Fourier domain versions of the Green's function, attenuation and the accompanying dispersion generally establish themselves by the replacement of the real wavenumber $k = \omega/c_0$ by a complex wavenumber

$$k_\alpha(\omega) = -j\gamma(j\omega) = \beta(\omega) - j\alpha(\omega), \tag{D.26}$$

where $\beta(\omega) = \omega/c(\omega)$ and $\alpha(\omega) > 0$. The spatially filtered forms of the one-dimensional and three-dimensional lossy Green's functions are obtained by the same approach as in Section 3.4, and result in Eqs. (3.48) and (3.57) with k replaced by k_α. The temporal windowing of the Green's functions needs further consideration.

For the one-dimensional Green's function in the lossless, unfiltered case, the windowing operation in Eq. (3.49) involved the subtraction of a step function $H(t-T)$ and the multiplication with the window $H(c_0T - |x|)$. In the temporal Fourier domain this resulted in a windowed Green's function Eq. (3.50),

$$\hat{G}^T(x,\omega) = \frac{\exp(-jk\,|x|) - \exp(-jk\,c_0T)}{2jk}\,H(c_0T - |x|). \tag{D.27}$$

For the lossy case, the multiplication with $H(c_0T - |x|)$ still applies, but the subtraction of $H(t-T)$ that leads to the term $-\exp(-jk\,c_0T)$ in Eq. (D.27) is formally not applicable anymore. If we keep this term and replace k by k_α, we obtain a less ideal window than the one in Eq. (3.28), but the obtained window nevertheless shows a satisfactory performance. Figure D.1 shows the spatiotemporally filtered and temporally windowed, lossy, one-dimensional Green's function for $|x|/c_0 = 10$. The medium is liver and we have used a cutoff frequency $\Omega/2\pi = 20$ and a half window width $T = 40$. In this figure we observe the smooth dropoff at $t = T$ which is due to the smooth window resulting from the replacement of k by k_α in the window term. The tail after $t = T$ does not cause a wraparound error in the field solution if the temporal axis is taken slightly larger than T.

For the three-dimensional Green's function, the temporal windowing operation is much more straightforward. In the lossless, unfiltered case the approach leading to Eq. (3.58) involved only the multiplication with the window $H(c_0T - \|\boldsymbol{x}\|)$, resulting in the temporal Fourier domain expression

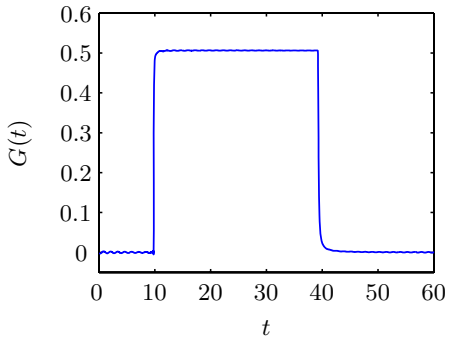

Figure D.1. Plot of the spatiotemporally filtered and temporally windowed lossy, one-dimensional Green's function versus time for $|x|/c_0 = 10$ with $\Omega/2\pi = 20$ and $T = 40$. The medium is liver.

of Eq. (3.59),

$$\hat{G}^T(\boldsymbol{x}, \omega) = \frac{\exp(-jk\,\|\boldsymbol{x}\|)}{4\pi\,\|\boldsymbol{x}\|}\, H(c_0 T - \|\boldsymbol{x}\|). \tag{D.28}$$

For the lossy case, this multiplication still applies, and we only make a small wraparound error in the Green's function due to its lossy tail in the temporal dimension for points where $\|\boldsymbol{x}\| \approx c_0 T$.

In conclusion, for the filtered and windowed Green's functions we may employ the expressions from Eq. (3.51) in the one-dimensional case[2] and from Eqs. (3.60) and (3.61) in the three-dimensional case, with k replaced by k_α.

Evaluation of the 1D and 3D lossy Green's functions

For $|x| = 0$ and $\|\boldsymbol{x}\| = 0$, the numerical evaluation of Eqs. (3.51) and (3.61) for a complex wavenumber causes no problem. However, for other values of x or $\boldsymbol{x}$, the numerical evaluation of the spatial filtering terms in these equations may result in instabilities in case of a complex wavenumber. These are caused by exponential terms in the special functions. These terms cancel in the final result, but yield large intermediate values which are sensitive to numerical error. To prevent these problems, we reformulate the spatial filtering terms

[2]Note that Eq. (3.52) is not needed anymore since in the lossy case k will never become zero.

in Eqs. (3.51) and (3.60) by employing the exponential integral [2, p. 228]

$$E_1(z) = \int_z^\infty \frac{e^{-t}}{t}\,\mathrm{d}t, \qquad |\arg z| < \pi, \tag{D.29}$$

and by using the relations [2, p. 232]

$$\mathrm{Si}(z) = \frac{1}{2j}[E_1(jz) - E_1(-jz)] + \frac{\pi}{2}, \qquad |\arg z| < \frac{\pi}{2}, \tag{D.30}$$

$$\mathrm{Cin}(z) = \frac{1}{2}[E_1(jz) + E_1(-jz)] + \ln z + \gamma, \quad |\arg z| < \frac{\pi}{2}, \tag{D.31}$$

where $\gamma = 0.57721\ldots$ is Euler's constant. With $\cos(k_\alpha\,|x|)$ and $\sin(k_\alpha\,|x|)$ written out in exponential functions and with some reordering of the terms, the one-dimensional, lossy, spatially filtered, temporally windowed Green's function for $|x| > 0$ and $|\mathrm{Re}(k_\alpha)| < K$ becomes

$$\begin{aligned}\hat{G}_K^T(x,\omega) =& \frac{\exp(-jk_\alpha\,|x|) - \exp(-jk_\alpha\,c_0T)}{2jk_\alpha}\,H(c_0T - |x|)\\ &- \frac{\exp(jk_\alpha\,|x|)}{4\pi k_\alpha}\,\Big\{E_1[-j(K-k_\alpha)\,|x|] - E_1[j(K+k_\alpha)\,|x|]\Big\}\\ &- \frac{\exp(-jk_\alpha\,|x|)}{4\pi k_\alpha}\,\Big\{E_1[j(K-k_\alpha)\,|x|] - E_1[-j(K+k_\alpha)\,|x|]\Big\}.\end{aligned} \tag{D.32}$$

Now we define the function

$$E_1'(z) = \exp(z)\,E_1(z), \tag{D.33}$$

which, unlike $E_1(z)$, is well behaved even if $\mathrm{Re}(z) \to -\infty$. With some reordering of the terms in Eq. (D.32), this gives

$$\begin{aligned}\hat{G}_K^T(x,\omega) =& \frac{\exp(-jk_\alpha\,|x|) - \exp(-jk_\alpha\,c_0T)}{2jk_\alpha}\,H(c_0T - |x|)\\ &- \frac{\exp(jK\,|x|)}{4\pi k_\alpha}\,\Big\{E_1'[-j(K-k_\alpha)\,|x|] - E_1'[-j(K+k_\alpha)\,|x|]\Big\}\\ &- \frac{\exp(-jK\,|x|)}{4\pi k_\alpha}\,\Big\{E_1'[j(K-k_\alpha)\,|x|] - E_1'[j(K+k_\alpha)\,|x|]\Big\}.\end{aligned} \tag{D.34}$$

In a similar fashion, the three-dimensional, lossy, spatially filtered, temporally windowed Green's function for $\|\boldsymbol{x}\| > 0$ and $|\mathrm{Re}(k_\alpha)| < K$ becomes

$$\begin{aligned}\hat{G}_K^T(\boldsymbol{x},\omega) =& \frac{\exp(-jk_\alpha\|\boldsymbol{x}\|)}{4\pi\|\boldsymbol{x}\|} H(c_0T - \|\boldsymbol{x}\|) \\ &- \frac{\exp(jk_\alpha\|\boldsymbol{x}\|)}{8\pi^2 j\|\boldsymbol{x}\|} \left\{E_1[-j(K-k_\alpha)\|\boldsymbol{x}\|] - E_1[j(K+k_\alpha)\|\boldsymbol{x}\|]\right\} \\ &+ \frac{\exp(-jk_\alpha\|\boldsymbol{x}\|)}{8\pi^2 j\|\boldsymbol{x}\|} \left\{E_1[j(K-k_\alpha)\|\boldsymbol{x}\|] - E_1[-j(K+k_\alpha)\|\boldsymbol{x}\|]\right\}. \quad \text{(D.35)}\end{aligned}$$

In terms of $E_1'(z)$, this yields

$$\begin{aligned}\hat{G}_K^T(\boldsymbol{x},\omega) =& \frac{\exp(-jk_\alpha\|\boldsymbol{x}\|)}{4\pi\|\boldsymbol{x}\|} H(c_0T - \|\boldsymbol{x}\|) \\ &- \frac{\exp(jK\|\boldsymbol{x}\|)}{8\pi^2 j\|\boldsymbol{x}\|} \left\{E_1'[-j(K-k_\alpha)\|\boldsymbol{x}\|] + E_1'[-j(K+k_\alpha)\|\boldsymbol{x}\|]\right\} \\ &+ \frac{\exp(-jK\|\boldsymbol{x}\|)}{8\pi^2 j\|\boldsymbol{x}\|} \left\{E_1'[j(K-k_\alpha)\|\boldsymbol{x}\|] + E_1'[j(K+k_\alpha)\|\boldsymbol{x}\|]\right\}. \quad \text{(D.36)}\end{aligned}$$

For the evaluation of $E_1'(z)$ at $z \neq 0$ we employ a number of terms of the series expansion [2, p. 229]

$$E_1'(z) = \exp(z)\left[-\gamma - \ln(z) - \sum_{n=1}^{\infty} \frac{(-1)^n z^n}{n\, n!}\right], \quad \text{(D.37)}$$

or a number of terms of the even form of the continued fraction [57]

$$E_1'(z) = \frac{1}{z+1-} \frac{1^2}{z+3-} \frac{2^2}{z+5-} \frac{3^2}{z+7-} \cdots . \quad \text{(D.38)}$$

The two expressions approximate $E_1'(z)$ with different efficiency in different regions of the complex plane. In Fig. D.2, the region is shown where the evaluation of $E_1'(z)$ with an absolute error less than or equal to 10^{-6} is faster with the series expansion than with the continued fraction. This figure is based on a Fortran implementation of both expressions, in which the continued fraction is evaluated with the modified Lentz algorithm [57]. Since in our applications only a small part of all evaluations requires the series expansion, a further optimization of Eq. (D.37) is not opportune.

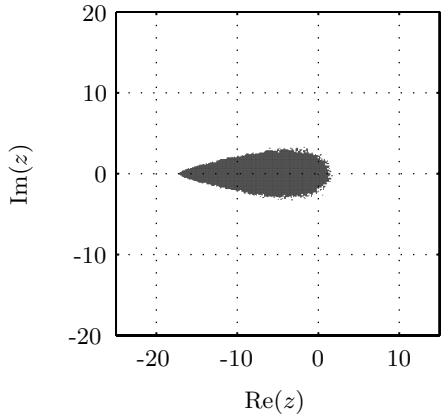

Figure D.2. Region where the evaluation of $E_1'(z)$ with an absolute error less than or equal to 10^{-6} is faster with the series expansion than with the continued fraction.

Extension to nonlinear, lossy wave problems

In the previous sections we have discussed the inclusion of attenuation in the linear wave problem. The extension of the discussion to the nonlinear wave problem is easy if we assume that the attenuation and nonlinear distortion phenomena can be decoupled and treated separately. As was also discussed in Section 2.5, the approach of decoupling attenuation and nonlinear distortion, and thus of disregarding any interaction terms, is common in the modeling of nonlinear acoustic phenomena. The interaction terms are considered to be of third order in the wavefield quantities, and are thus neglected in any second-order considerations. This decoupling, however, does not mean that the field components that are generated by nonlinear distortion are not anymore subject to lossy propagation. In fact, the level of the higher harmonic frequency components will be determined by the combination of nonlinear distortion and attenuation. As described in Subsection 4.3.2, the nonlinear distortion results in the transfer of energy from the lower harmonics to the higher harmonics. At the same time, the frequency-dependent attenuation becomes higher for increasing frequency, thus removing more energy from the higher harmonic frequency components.

The approach of decoupling the attenuation and the nonlinear distortion phenomena enables us to extend the INCS method to lossy media in a simple way. The only modification to the method as presented in Chapter 3

is the replacement of the one-dimensional or three-dimensional lossless, filtered and windowed Green's functions by their lossy counterparts that have been derived in this appendix.

One-dimensional results

We test the lossy INCS method for a one-dimensional configuration by considering a medium with the acoustic parameters of liver, as given in Table D.1. We use the source configuration and the excitation pulse as defined in Section 4.1, i.e. a plane surface source at $x = 0$ exciting a harmonic signal with a Gaussian envelope and with $f_0 = 1$ MHz and $P_0 = 500$ kPa. Further we employ a maximum frequency of interest $F = 6.5$ MHz and a discretization with $D_F = 2$. The first iteration, $j = 0$, yields the linear wavefield solution. Figure D.3a shows the progressive development over distance of the spectral profile of the fundamental component, giving an exponential decay of up to 2.27 dB at $x = 50$ mm. In the same figure, we compare this result with the development of the pressure calculated by the lossy plane-wave solution

$$\hat{p}(x, \omega) = P_0 \hat{s}(\omega) \exp(-jk_\alpha x), \tag{D.39}$$

where $\hat{s}(\omega)$ is the frequency domain source signature and k_α is given by Eqs. (D.22) and (D.26). The profiles show perfect agreement. To investigate the frequency dependence of the attenuation, next we employ a narrowband excitation pulse by setting $T_w = 12/f_0$ and $T_d = 18/f_0$ in the Gaussian envelope of Eq. (4.3), and we vary the center frequency of the source signature f_0 over the range 0.1 MHz to 6.4 MHz. The variation of the spectral profile of the fundamental component at $x = 50$ mm as a function of the center frequency is shown in Fig. D.3b. Again, comparison with the frequency-dependent attenuation obtained with Eq. (D.39) yields a perfect agreement.

Further we compare the lossy and lossless acoustic pulse under strong nonlinear distortion. Again we use liver as the acoustic medium, and for the lossless case we set $\alpha_1 = 0$. We obtain the nonlinear pressure field of the source as first described above, but now with $P_0 = 3$ MPa, and we observe p at the plane wave shock formation distance $x = \bar{x} = 50$ mm. As in Subsection 4.3.4, the maximum frequency of interest is chosen as $F = 6.5$ MHz, the discretization is fixed at $D_F = 2$, and we iterate up to $j = 11$. Figures D.4a to d show the lossless and lossy results as obtained with the INCS method, compared to the results obtained with the solution of the lossless Burgers' equation outlined in Appendix A and computed with $\Delta t = 1/200 f_0$ and the

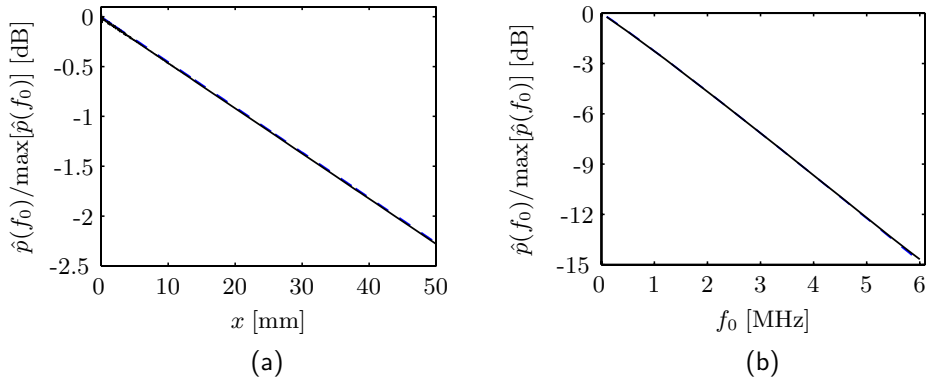

Figure D.3. Spectral profile of the acoustic pressure in a one-dimensional, linear, lossy medium, as obtained by the INCS method (solid) and from the plane wave solution in Eq. (D.39) (dashed). (a) As a function of the distance x, at a fixed center frequency $f_0 = 1$ MHz. (b) As a function of the center frequency f_0, at a fixed distance $x = 50$ mm.

same spatial step size as for the INCS method. We observe that the lossy result shows a strong decrease of the higher harmonic frequency components compared to the lossless result, and that the signature in the time domain is much smoother. The overshoot in the INCS method of the highest harmonic is not so clearly visible in the lossy results, but it may still be present in a reduced form. Figures D.4e and f show the acoustic field at $x = \bar{x}$ for a comparable medium[3] but with $b = 2$. Comparing this with Figs. D.4c and d, which give the result for $b = 1.05$, we see that although the signature is very comparable, the higher harmonics in the case $b = 2$ are strongly attenuated. This shows that in the case of nonlinear propagation, tissue-like medium behavior cannot be accounted for with a square power law type of attenuation.

Three-dimensional results

Finally we investigate the behavior of the lossy INCS method for a three-dimensional configuration. For the medium we use liver, and we obtain the linear and the nonlinear pressure field that is excited by a phased array source causing a pressure jump. The transducer is a 64 element array with element

[3]For this medium, the attenuation coefficient a [Np/cm Mhz^b], as occurs in the power law $a\,|f|^b$, is taken equal to that of liver.

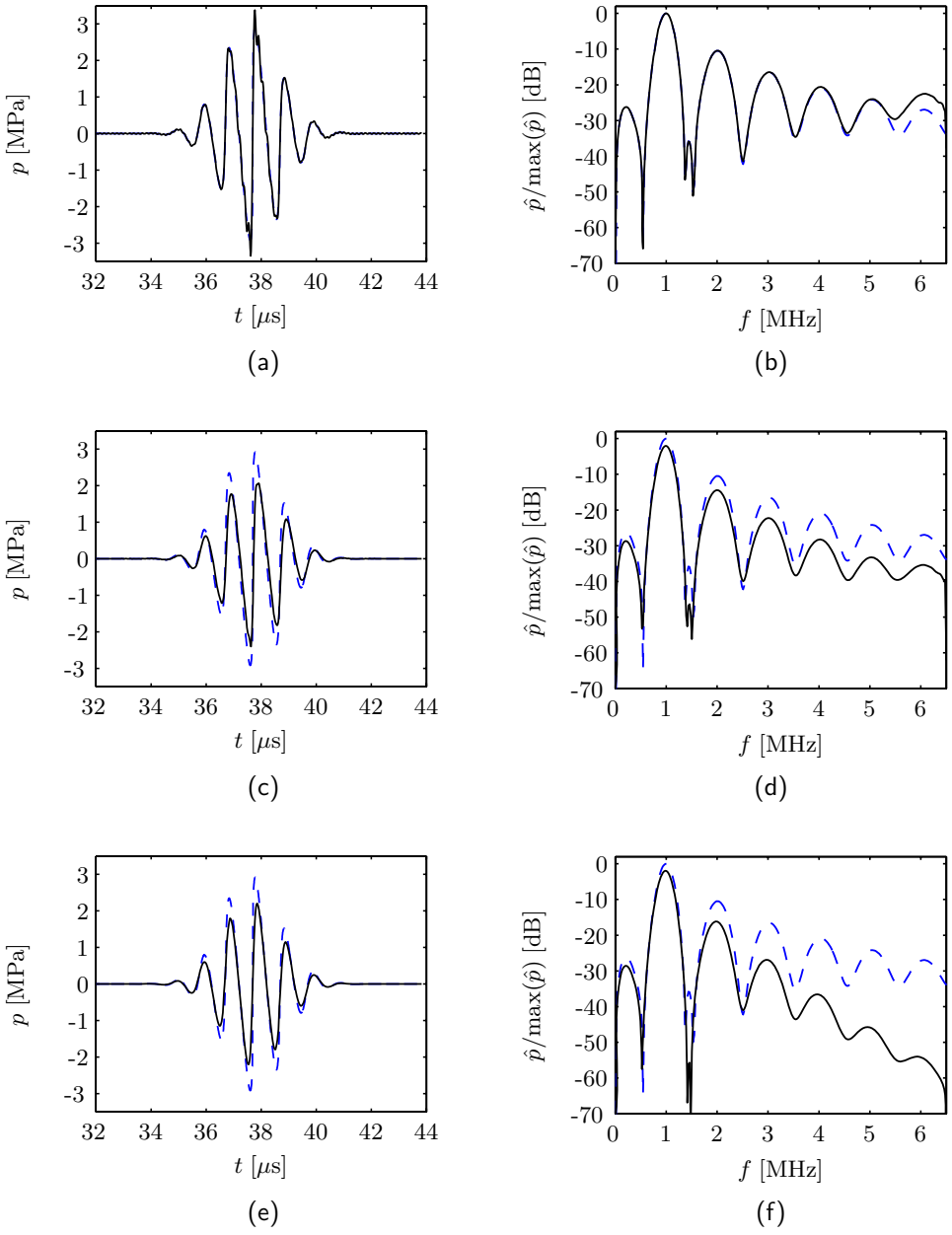

Figure D.4. Acoustic pressure at $\bar{x} = 50$ mm as predicted by the INCS method at $j = 11$ (continuous) and by the lossless Burgers equation (dashed). (a),(b) Lossless medium. (c),(d) Lossy medium with $b = 1.05$. (e),(f) Lossy medium with $b = 2$. The figures on the left show the time domain pulses, and the figures on the right the corresponding frequency spectra.

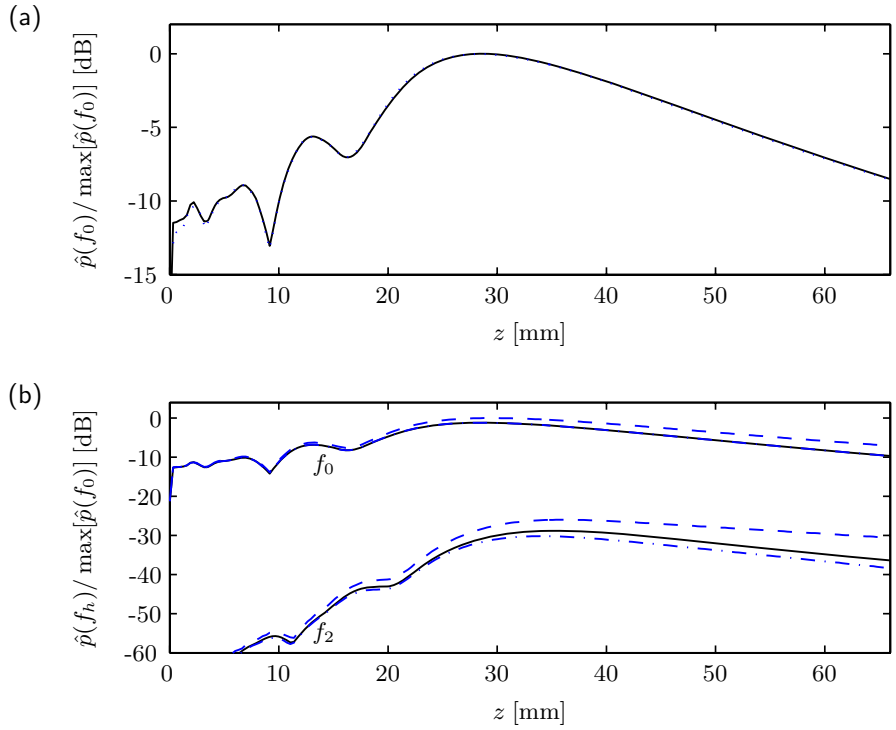

Figure D.5. Spectral profiles on the transducer axis for the phased array transducer. (a) Linear profiles obtained with the INCS method (solid) and the FieldII program (dotted), both for the lossy case with $b = 1.05$. (b) Nonlinear profiles obtained with the INCS method, for the lossy case with $b = 1.05$ (solid), for the lossless case (dashed) and for the lossy case with $b = 2$ (dash-dotted).

parameters $W_{\text{el}} \times H_{\text{el}} = 0.25$ mm $\times$ 12 mm and $d_{\text{el}} = 0.3$ mm. The array is focused at $(x_f, z_f) = (0, 40)$ mm and $z_{\text{ele}} = z_f$. The excitation pulse is a harmonic signal with a Gaussian envelope as defined in Section 4.1 and with $f_0 = 1$ MHz and $P_0 = 250$ kPa. The nonlinear field solution is obtained for a domain of interest with a spatial size of 36 mm $\times$ 18 mm $\times$ 66 mm and a periodical temporal window of 20 μs, a maximum frequency of interest $F = 2.5 f_0$, and a discretization with $D_F = 2$. The linear field is obtained with iteration $j = 0$, and the nonlinear field is estimated with $j = 2$. Figure D.5a shows the lossy, linear field profile on the axis of the transducer, compared

to the lossy, linear field profile obtained with the FieldII program.[4] The profiles show excellent agreement. Figure D.5b shows the nonlinear field profiles of the fundamental and the second harmonic frequency components on the axis of the transducer for the lossy situation with $b = 1.05$, the lossless situation and the lossy situation with a comparable medium[5] with $b = 2$. We observe that compared to the lossless case, in the lossy case with $b = 1.05$ the fundamental component is reduced by 2.4 dB at $z = 60$ mm, and the second harmonic is reduced by 5.0 dB. For the lossy case with $b = 2$, the fundamental component is equally reduced as for the case with $b = 1.05$. This is explained from the fact that the attenuation coefficient a is kept constant, and therefore the damping at 1 Mhz is equal for both lossy cases. However, for the case $b = 2$ the second harmonic component is reduced by 7.0 dB at $z = 60$ mm, showing a stronger decay than for the case $b = 1.05$. Similar to the one-dimensional example in Fig. D.4 this difference will become even larger for the higher harmonic components. This confirms that in case of nonlinear propagation, tissue-like medium behavior cannot be accounted for with a square power law type of attenuation.

Conclusion

From the presented examples we conclude that the lossy INCS method is able of incorporating tissue-like attenuation. Moreover, we conclude that a square power law (with $b = 2$) and a frequency power law (with $b < 2$) result in significantly different nonlinear fields. This shows the importance of an accurate incorporation of the correct attenuation law in the estimation of the nonlinear wavefield from medical phased array transducers.

[4] The FieldII program only allows for inclusion of a linear frequency attenuation law. To match the attenuation in FieldII with our frequency power law, we use a first order Taylor approximation of the frequency power law around the center frequency f_0.

[5] For this medium, the attenuation coefficient a [Np/cm Mhz^b], as occurs in the power law $a\,|f|^b$, is taken equal to that of liver.

Appendix E

Extension of the INCS method to media with inhomogeneity

The methodology of the INCS method can also be applied to problems with spatial inhomogeneity in the medium parameters. In fact, the contrast source formulation employed in the INCS method was inspired by its earlier use in problems with inhomogeneous media. In this appendix we will study the incorporation of inhomogeneous medium parameters in the INCS method. We start with the formulation of the linear wave equation for inhomogeneous media Next we will discuss the solution of this wave equation using the contrast source formulation in combination with the Filtered Convolution method. As an illustration we will finally compute the linear acoustic pressure field in a three-dimensional configuration with a number of objects.

Formulation of the wave equation for inhomogeneous media

We start with the repetition of the linear acoustic equations in Eqs. (2.55) and (2.56)

$$\partial_k p \ + \rho\, \partial_t v_k = f_k, \tag{E.1}$$

$$\partial_r v_r + \kappa\, \partial_t p \ = q, \tag{E.2}$$

where we have used the symbols ρ and κ instead of ρ_0 and κ_0 to indicate that the mass density and compressibility vary in space. We assume that the

medium parameters are time-independent, and therefore we also disregard their variation as a function of the wave quantities. Conform the derivation in Section 2.4 these equations then yield a linear, inhomogeneous wave equation of the form

$$\frac{1}{c^2}\partial_t^2 p - \partial_k^2 p - (\partial_k \rho)\,\partial_t v_k = \rho\,\partial_t q - \partial_k f_k, \tag{E.3}$$

where $c = (\rho\kappa)^{-1/2}$ is the inhomogeneous sound speed. We apply Eq. (E.1) once more to eliminate v_k, and with $(\partial_k \rho)/\rho = \partial_k \ln(\rho)$ we get

$$\frac{1}{c^2}\partial_t^2 p - \partial_k^2 p + [\partial_k \ln(\rho)]\,\partial_k p = \rho\,\partial_t q - \partial_k f_k + [\partial_k \ln(\rho)] f_k. \tag{E.4}$$

Further we assume that c and ρ deviate only locally from the quantities c_0 and ρ_0 of a homogeneous background medium. Assuming that the medium inhomogeneity is only present outside the sources, Eq. (E.4) can be rewritten as

$$\frac{1}{c_0^2}\partial_t^2 p - \partial_k^2 p = S - [\partial_k \ln(\rho)]\,\partial_k p - \left(\frac{1}{c^2} - \frac{1}{c_0^2}\right)\partial_t^2 p, \tag{E.5}$$

where $S = \rho_0 \partial_t q - \partial_k f_k$ is the source term as employed in this thesis.

Solution using a contrast source formulation and the Filtered Convolution method

Just as the nonlinear term in the Westervelt equation can be used as a contrast source that accounts for the nonlinearity in the medium, the last two terms at the right-hand side of Eq. (E.5) can be used as a contrast source

$$S^C(p) = -[\partial_k \ln(\rho)]\,\partial_k p - \left(\frac{1}{c^2} - \frac{1}{c_0^2}\right)\partial_t^2 p \tag{E.6}$$

that accounts for the inhomogeneity of the linear medium. In this appendix we will apply the Neumann iterative scheme to solve the acoustic pressure field for the inhomogeneous wave problem. We assume that the Neumann scheme converges for this kind of contrast, but we have not investigated this aspect.

As explained in Section 3.2, the iterative steps in the Neumann scheme involve the convolution of the Green's function of the background medium with the primary or the contrast source. And as discussed in the remainder

of Chapter 3, the evaluation of the convolution can be performed efficiently with the Filtered Convolution method. One of the steps that is important for the evaluation of the inhomogeneity contrast source is its spatiotemporal filtering. As discussed in Sections 4.2 and 5.2, for the nonlinear contrast source term it generally suffices to only apply a temporal filter. Since the medium inhomogeneity is not coupled to time, the inhomogeneity contrast source must be filtered in the spatial dimensions only. Since the acoustic pressure itself has been obtained by the Filtered Convolution method, the terms $\partial_k p$ and $\partial_t^2 p$ in Eq. (E.6) contain no higher temporal and spatial angular frequencies than Ω and K. However, sampling of the factors $[\partial_k \ln(\rho)]$ and $(c^{-2} - c_0^{-2})$ describing the medium inhomogeneity, and their multiplication with the factors $\partial_k p$ and $\partial_t^2 p$ to obtain the contrast source, could give rise to spatial aliasing. To prevent this, the medium factors and the resulting contrast source need to be filtered in all spatial dimensions with the methods described in Section 3.5.

Illustration

As an illustration, we present simulation results for the linear acoustic wavefield that propagates through a medium with three objects exhibiting inhomogeneity in the sound speed. The contrasts are taken such that they are representative for human tissue, and we neglect the inhomogeneity in the mass density. The homogeneous embedding is water ($\rho_0 = 998\ \mathrm{kg\,m^{-3}}$, $c_0 = 1480\ \mathrm{m\,s^{-1}}$), in which we have placed a homogeneous phase screen with an undulation in the x direction ($c = 0.95c_0$), a water-filled cylinder with a homogeneous wall ($c = 0.95c_0$), and an ellipsoid with a Gaussian distribution of the wave speed ($\max(c) = 1.1c_0$). The distribution of the wave speed in the medium is displayed in Figs. E.1a and E.2a. The term $[c^{-2}(\boldsymbol{x}) - c_0^{-2}]$ in the contrast source is filtered in all spatial dimensions by using the method of Fig. 3.6 with an oversampling factor $a = 2$. In this medium, an acoustic wavefield is generated by a phased array source causing a velocity jump. It is located in the plane $z = 0$ and has its center at the origin. The array consists of 64 elements with parameters $W_{\mathrm{el}} \times H_{\mathrm{el}} = 0.25\ \mathrm{mm} \times 12\ \mathrm{mm}$ and $d_{\mathrm{el}} = 0.3\ \mathrm{mm}$, and it is focused at $(x_f, z_f) = (0, 60)\ \mathrm{mm}$, with $z_{\mathrm{ele}} = z_f$. The signature is a harmonic signal with a center frequency $f_0 = 2\ \mathrm{MHz}$, a Gaussian envelope as used before, and a source pressure amplitude $P_0 = 250\ \mathrm{kPa}$. We have obtained successive approximations $p^{(j)}$ up till $j = 9$ in a computational domain with a spatial size of 42 mm × 16 mm × 60 mm and a comoving temporal window of 24 μs, a maximum frequency of interest $F = 2f_0$, and a

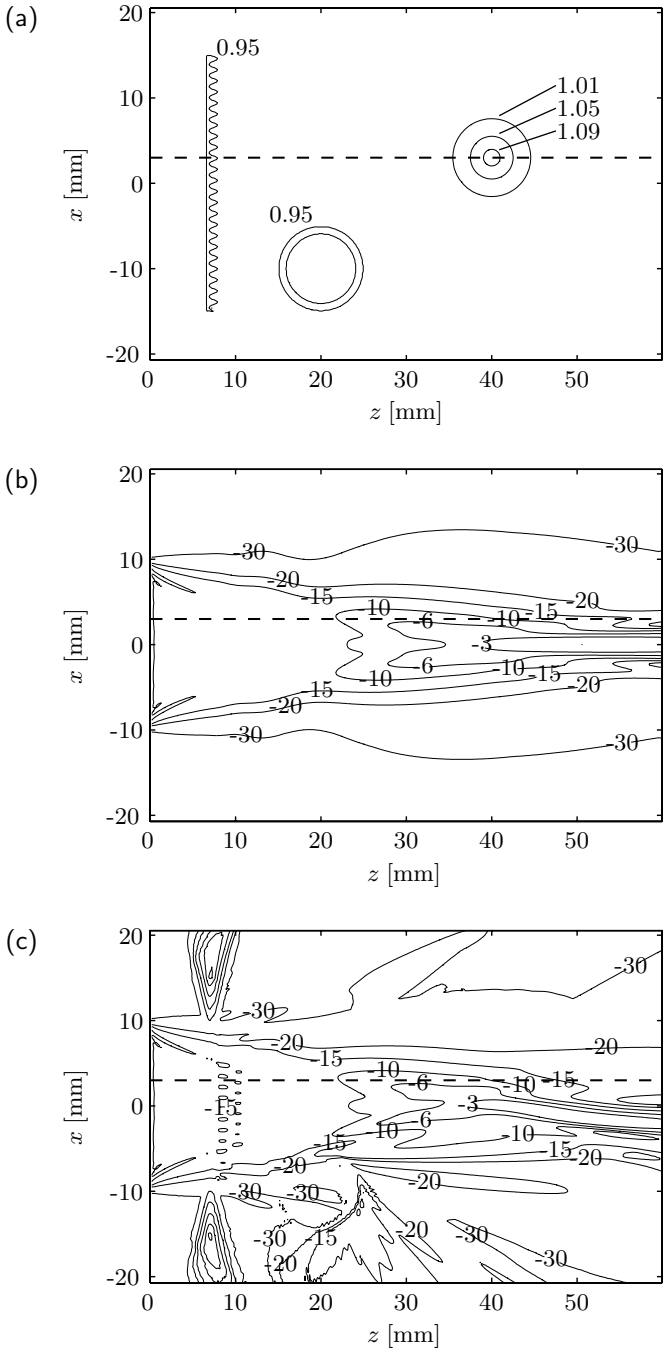

Figure E.1. (a) The wave speed contrast c/c_0 in the inhomogeneous medium. (b) The pressure profile of $p^{(0)}$. (c) The pressure profile of $p^{(9)}$. All figures apply to the plane $y = 0$ mm. The dashed line shows the cross-cuts in Fig. E.2.

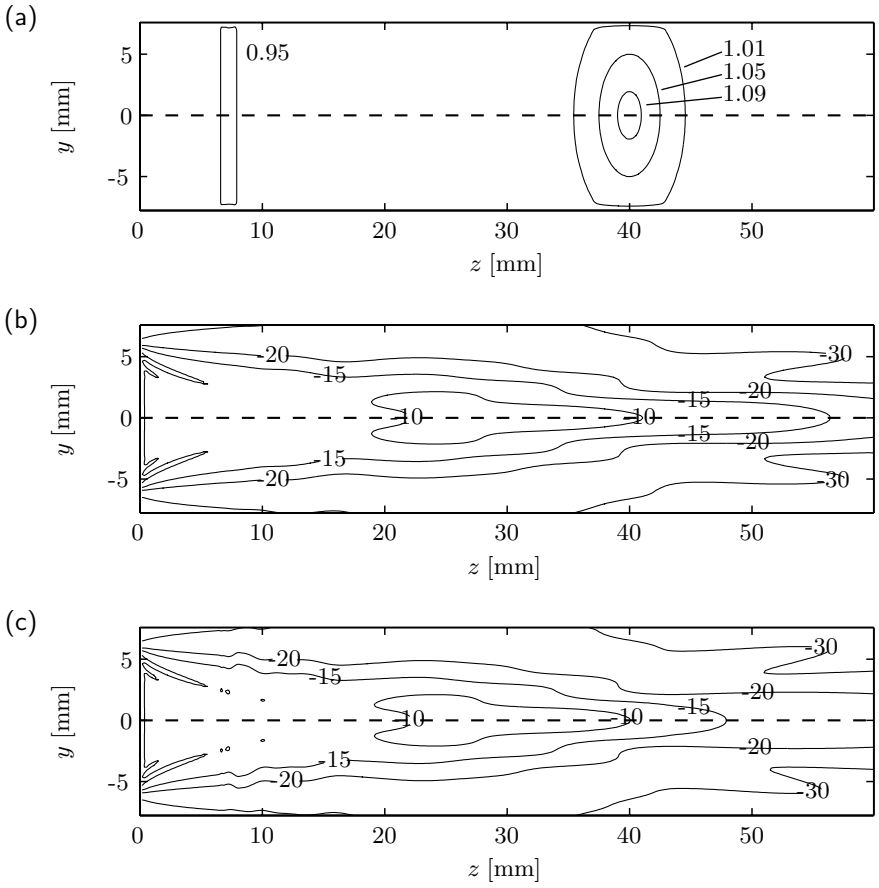

Figure E.2. (a) The wave speed contrast c/c_0 in the inhomogeneous medium. (b) The pressure profile of $p^{(0)}$. (c) The pressure profile of $p^{(9)}$. All figures apply to the plane $x = 3$ mm. The dashed line shows the cross-cuts in Fig. E.1.

discretization with $D_F = 2$. The successive results are almost identical from $j = 5$ to at least $j = 9$, which suggests that convergence has been obtained at $j = 5$. Figures E.1b and E.2b show the profiles of $p^{(0)}$, i.e. the incident field, in the planes $y = 0$ mm and $x = 3$ mm, respectively. In the same figures, the panels c give the corresponding profiles for $p^{(9)}$, which seems to be an accurate approximation to the total field. The results clearly reveal the effect of the objects on the beam shape. The phase screen affects the beam shape by generating an interference pattern just beyond the screen, and by forming small side-lobes with large off-axis angles. The wall of the cylinder acts as a curved waveguide, which captures a part of the beam and radiates it off in the negative x direction. The main effect of the ellipsoid, which acts as a diverging acoustic lens, is the diffraction of the beam in the negative x direction.

Based on the fact that the total field solution barely changes for iterations $j = 5$ to $j = 9$, we conclude that the Neumann iterative solution is capable of handling the inhomogeneities of the kind presented here. However, we have also observed instable behavior for higher numbers of iterations, as well as for larger contrasts. For example, the artefacts at both ends of the phase screen in Fig. E.1c will blow up for high values of j. To avoid these numerical issues, the methodology of the INCS method may be combined with more sophisticated iterative schemes with improved convergence properties, like the successive overrelaxation method or the conjugate gradient method [68].

Bibliography

[1] S.I. Aanonsen, T. Barkve, J. Naze Tjotta, and S. Tjotta, *Distortion and harmonic generation in the nearfield of a finite amplitude sound beam*, J. Acoust. Soc. Am. **75** (1984), no. 3, 749–768.

[2] M. Abramowitz and I.A. Stegun, *Handbook of mathematical functions*, Dover publications, New york, 1968.

[3] M.A. Averkiou, Y.-S. Lee, and M.F. Hamilton, *Self-demodulation of amplitude- and frequency-modulated pulses in a thermoviscous fluid*, J. Acoust. Soc. Am. **94** (1993), no. 5, 2876–2883.

[4] M.A. Averkiou, D.N. Roundhill, and J.E. Powers, *A new imaging technique based on the nonlinear properties of tissues*, Proc. IEEE UFFC, 1997, pp. 1561–1566.

[5] A.C. Baker, A.M. Berg, A. Sahin, and J. Naze Tjotta, *The nonlinear pressure field of plane, rectangular apertures: experimental and theoretical results*, J. Acoust. Soc. Am. **97** (1995), no. 6, 3510–3517.

[6] B.B. Baker and E.T. Copson, *The mathematical theory of Huygens' principle*, Oxford university press, Oxford, 1953.

[7] A. Bouakaz and N. de Jong, *Native tissue imaging at superharmonic frequencies*, IEEE Trans. Ultrason., Ferroelect., Freq. Contr. **50** (2003), no. 5, 496–506.

[8] A. Bouakaz, C.T. Lancée, and N. de Jong, *Harmonic ultrasonic field of medical phased arrays: simulations and measurements*, IEEE Trans. Ultrason., Ferroelect., Freq. Contr. **50** (2003), no. 6, 730–735.

[9] A. Bouakaz, C.T. Lancée, P.J.A. Frinking, and N. de Jong, *Simulations and measurements of nonlinear pressure field generated by linear array transducers*, Proc. 1999 IEEE Ultrasonics, 1999, pp. 1511–1514.

[10] A.I. Burshtein, *Introduction to thermodynamics and kinetic theory of matter*, John Wiley and Sons, New York, 1996.

[11] M.D. Cahill and A.C. Baker, *Numerical simulation of the acoustic field of a phased-array medical ultrasound scanner*, J. Acoust. Soc. Am. **104** (1998), no. 3, 1274–1283.

[12] P.T. Christopher and K.J. Parker, *New approaches to nonlinear diffractive field propagation*, J. Acoust. Soc. Am. **90** (1991), no. 1, 488–499.

[13] ———, *New approaches to the linear propagation of acoustic fields*, J. Acoust. Soc. Am. **90** (1991), no. 1, 507–521.

[14] R. Cleveland and Y. Jing, *Comparison of mechanisms involved in image enhancement of tissue harmonic imaging*, Proc. ISNA17, 2005, pp. 263–266.

[15] R. O. Cleveland, M. F. Hamilton, and al., *Time-domain modeling of finite-amplitude sound in relaxing fluids*, J. Acoust. Soc. Am. **99** (1996), no. 6, 3312–3318.

[16] B.T. Cox and P.C. Beard, *Fast calculation of pulsed photoacoustic fields in fluids using k-space methods*, J. Acoust. Soc. Am. **117** (2005), no. 6, 3616–3627.

[17] A.T. de Hoop, *Handbook of radiaton and scattering of waves*, Academic Press, San Diego, 1995.

[18] J.A. DeSanto, *Scalar wave theory – green's functions and applications*, Springer-Verlag, Berlin, 1992.

[19] F.A. Duck, *Physical properties of tissue*, Academic Press, 1990.

[20] ———, *Nonlinear acoustics in diagnostic ultrasound*, Ultras. Med. Biol. **28** (2002), no. 1, 1–18.

[21] F.A. Duck and H.C. Starrit, *Acoustic shock generation by ultrasonic imaging equipment*, Br. J. Radiol. **57** (1984), 231–240.

[22] F. Dunn and W.D. O'Brien (eds.), *Ultrasonic biophysics*, Dowden, Hutchinson & Ross, Stroudsburg, 1976.

[23] J.T. Fokkema and P.M. van den Berg, *Seismic applications of acoustic reciprocity*, Elsevier, Amsterdam, 1993.

[24] B. Fornberg, *Generation of finite difference formulas on arbitrarily spaced grids*, Math. Comput. **51** (1988), 699–706.

[25] ———, *A practical guide to pseudospectral methods*, Cambridge University Press, New York, 1996.

[26] P.D. Fox, A. Bouakaz, and F. Tranquart, *Computation of steered nonlinear fields using offset KZK axes*, Proc. IEEE Ultrasonics 2005, 2005, pp. 1984–1987.

[27] M. Frigo and S. G. Johnson, *The design and implementation of FFTW3*, Proc. of the IEEE **93** (2005), no. 2, 216–231, special issue on "Program Generation, Optimization, and Platform Adaptation".

[28] M. Frigo and S.G. Johnson, *FFTW 3.0.1 manual*, 2003, (http://www.fftw.org/).

[29] K.-E. Froysa, J. Naze Tjotta, and S. Tjotta, *Linear propagation of a pulsed sound beam from a plane or focusing source*, J. Acoust. Soc. Am. **93** (1993), no. 1, 80–92.

[30] S. Ginter, M. Liebler, E. Steiger, T. Dreyer, and R.E. Riedlinger, *Full-wave modeling of therapeutic ultrasound: nonlinear ultrasound propagation in ideal fluids*, J. Acoust. Soc. Am. **111** (2002), no. 5, 2049–2059.

[31] I.M. Hallaj and R.O. Cleveland, *FDTD simulation of finite-amplitude pressure and temperature fields for biomedical ultrasound*, J. Acoust. Soc. Am. **105** (1999), no. 5, L7–L12.

[32] M.F. Hamilton and D.T. Blackstock (eds.), *Nonlinear acoustics*, Academic Press, San Diego, 1998.

[33] G.R. Harris, *Review of transient field theory for a baffled planar piston*, J. Acoust. Soc. Am. **70** (1981), no. 1, 10–20.

[34] J. Hoffelner, H. Landes, M. Kaltenbacher, and R. Lerch, *Finite element simulation of nonlinear wave propagation in thermoviscous fluids including dissipation*, IEEE Trans. Ultrason., Ferroelect., Freq. Contr. **48** (2001), no. 3, 779–786.

[35] J. Huijssen, *Validation experiments for the Iterative Nonlinear Contrast Source method*, Tech. report, Delft University of Technology, Laboratory of Electromagnetic Research, 2007.

[36] J. Huijssen, A. Bouakaz, M. D. Verweij, and N. de Jong, *Simulations of the nonlinear acoustic pressure field without using the parabolic approximation*, Proc. IEEE Ultrasonics 2003, 2003, pp. 1851–1854.

[37] C.A. Jeffery and P.H Austin, *A new analytic equation of state for liquid water*, J. Chem. Phys. **110** (1999), no. 1, 484–496.

[38] J.A. Jensen, *Field: a program for simulating ultrasound systems*, 10th Nordic-Baltic Conference on Biomedical Imaging, in Medical & Biological Engineering & Computing, vol. 34, 1, no. 1, 1996, pp. 351–353.

[39] J.A. Jensen and N.B. Svendsen, *Calculation of pressure fields from arbitrarily shaped, apodized and excited ultrasound transducers*, IEEE Trans. Ultrason., Ferroelect., Freq. Contr. **39** (1992), no. 2, 262–267.

[40] V.A. Khokhlova, A.E. Ponomarev, M.A. Averkiou, and L.A. Crum, *Effect of absorption on nonlinear propagation of short ultrasound pulses generated by rectangular transducers*, J. Acoust. Soc. Am. **112** (2002), no. 5, 2370.

[41] ———, *nonlinear pulsed ultrasound beams radiated by rectangular focused diagnostic transducers*, Acoust. Phys. **52** (2006), no. 4, 481–489.

[42] J. de Koning, *Parallelizing Parnac*, Technical report number TR06-03, VORtech Computing, 2007.

[43] G.D.C. Kuiken, *Thermodynamics of irreversible processes*, Wiley, New York, 1994.

[44] T. Kujawska, J. Wojcik, and A. Nowicki, *Nonlinear pulsed pressure field from focused rectangular apertures: experimental and numerical simulation results*, Proc. IEEE Ultrasonics 2005, 2005.

[45] V.P. Kuznetsov, *Equations of nonlinear acoustics*, Sov. Phys. Ac. **16** (1971), no. 4, 467–470.

[46] Y.-S. Lee and M.F. Hamilton, *Time-domain modeling of pulsed finite-amplitude sound beams*, J. Acoust. Soc. Am. **97** (1995), no. 2, 906–917.

[47] D.R. Lide (ed.), *Crc handbook of chemistry and physics*, Taylor and Francis, Boca Raton, 2007.

[48] M. Liebler, S. Ginter, T. Dreyer, and R.E. Riedlinger, *Full wave modeling of therapeutic ultrasound: efficient time-domain implementation of the frequency power-law attenuation*, J. Acoust. Soc. Am. **116** (2004), no. 5, 2742–2750.

[49] W. Marczak, *Water as a standard in the measurements of speed of sound in liquids*, J. Acoust. Soc. Am. **102** (1997), no. 5, 2776–2779.

[50] G. Muir and E.L. Carstensen, *Prediction of nonlinear acoustic effects at biomedical frequencies and intensities*, Ultras. Med. Biol. **6** (1980), 341–344.

[51] S. Nakamura, *Applied numerical methods with software*, Prentice Hall, New Jersey, 1991.

[52] J. Naze Tjotta and S. Tjotta, *Interaction of sound waves. part I: Basic equations and plane waves*, J. Acoust. Soc. Am. **82** (1987), no. 4, 1425–1428.

[53] The Numerical Algorithms Group Ltd., Oxford, *NAG Fortran library, mark 21.1*, 2006, (http://www.nag.co.uk/numeric/FL/FLdocumentation.asp).

[54] H.J. Nussbaumer, *Fast fourier transform and convolution algorithms*, Springer-Verlag, Berlin, 1981.

[55] C.L. Phillips and J.M. Parr, *Signals, systems and transforms*, Prentice Hall, New Jersey, 1999.

[56] A.D. Pierce, *Acoustics, an introduction to its physical principles and applications*, McGraw-Hill, New York, 1981.

[57] W.H. Press, S.A. Teukolsky, W.T. Vetterling, and B.P. Flannery, *Numerical recipes in Fortran 77*, 2nd ed., Cambridge University Press, Cambridge, 1996.

[58] G.F. Roach, *Green's functions*, Cambridge university press, Cambridge, 1982.

[59] D. Shanks, *A study of postulates: the "thermodynamic" derivation of the adiabatic gas law*, Am. J. Physics **24** (1956), no. 5, 352–354.

[60] V.W. Sparrow and R. Raspet, *A numerical method for general finite amplitude wave propagation in two dimensions and its application to spark pulses*, J. Acoust. Soc. Am. **90** (1991), no. 5, 2683–2691.

[61] P.R. Stepanishen, *Transient radiation from pistons in an infinite planar baffle*, J. Acoust. Soc. Am. **49** (1971), no. 5B, 1629–1638.

[62] E. Strick, *A predicted pedestal effect for pulse propagation in constant-Q solids*, Geophysics **35** (1970), 386–403.

[63] J.C. Strikwerda, *Finite difference schemes and partial differential equations*, Wadworth&Brooks/Cole, California, 1989.

[64] T.L. Szabo, *Causal theories and data for acoustic attenuation obeying a frequency power law*, J. Acoust. Soc. Am. **97** (1995), no. 1, 14–24.

[65] ———, *Diagnostic ultrasound imaging*, Elsevier academic press, Amsterdam, 2004.

[66] J. Tavakkoli, D. Cathignol, and R. Souchon, *Modeling of pulsed finite-amplitude focused sound beams in time domain*, J. Acoust. Soc. Am. **104** (1998), no. 4, 2061–2072.

[67] P.A. Thompson, *Compressible-fluid dynamics*, McGraw-Hill, New York, 1972.

[68] P.M. Van den Berg and R.E. Kleinman, *Iterative solution of integral equations in scattering problems*, El. Waves and Ult. Nondest. Eval. **4** (1990), no. 10, 57–62.

[69] R.W.C Van der Veeken, *Configurational filtering and sampling methods in the computation of frequency-domain electromagnetic fields*, Delft University Press, Delft, 1987, Phd. thesis.

[70] R.W.C. Van der Veeken and H. Blok, *A configurational filtering and sampling method in the numerical solution of three–dimensional electromagnetic source problems*, J. Electrom. Waves and Appl. **4** (1990), no. 10, 919–943.

[71] T. Varslot, S.-E. Masoy, T.F. Johansen, and B.A.J. Angelsen, *Aberration in nonlinear acoustic wave propagation*, IEEE Trans. Ultrason., Ferroelect., Freq. Contr. **54** (2007), no. 3, 470.

[72] T. Varslot and G. Taraldsen, *Computer simulation of forward wave propagation in tissue*, IEEE Trans. Ultrason., Ferroelect., Freq. Contr. **52** (2005), no. 9, 1473–1482.

[73] M.D. Verweij, *Modeling space-time domain acoustic wavefields in media with attenuation: the symbolic manipulation approach*, J. Acoust. Soc. Am. **97** (1995), no. 2, 831–843.

[74] ———, *Analysis of acoustic loss models with fractional time derivatives using the similarity transformation approach*, Proc. 7th Int. Congress on Sound and Vibration, 2000, pp. 3043–3050.

[75] Visual Numerics, Houston, *IMSL Fortran numerical library user's guide math/library special functions, version 6.0*, 2006, (http://www.vni.com/products/imsl/documentation/fort06/SFUN.pdf).

[76] B. Ward, A.C. Baker, and V.F. Humphrey, *Nonlinear propagation applied to the improvement of lateral resolution in medical ultrasound scanners*, Proc. 1995 International Congress on Acoustics, 1995, pp. 965–968.

[77] F.M. White, *Viscous fluid flow*, 2nd ed., Mc Graw-Hill, New York, 1991.

[78] D.V. Widder, *The Laplace transform*, Princeton U.P., Princeton, 1946.

[79] G. Wojcik, J. Mould, L. Carcione, and S. Ayter, *A study of second harmonic generation by focused medical transducer pulses*, Proc. 1998 IEEE Ultrasonics, 1998, pp. 1583–1588.

[80] G. Wojcik, J. Mould, F. Lizzi, N. Abboud, M. Ostromogilsky, and D. Vaughan, *Nonlinear modeling of therapeutic ultrasound*, Proc. 1995 IEEE Ultrasonics, 1995, pp. 1617–1621.

[81] J. Wojcik, A. Nowicki, P.A. Lewin, P.E. Bloomfield, T. Kujawska, and L. Filipczynski, *Wave envelopes method for description of nonlinear acoustic wave propagation*, Ultrasonics **44** (2006), 310–329.

[82] X. Yang and R.O. Cleveland, *Time domain simulation of nonlinear acoustic beams generated by rectangular pistons with application to harmonic imaging*, J. Acoust. Soc. Am. **117** (2005), no. 1, 113–123.

[83] T. Yano and Y. Inoue, *Strongly nonlinear waves and streaming in the near field of a circular piston*, J. Acoust. Soc. Am. **99** (1996), no. 6, 3353–3372.

[84] E.A. Zabolotskaya and R.V. Khokhlov, *Quasi-plane waves in the nonlinear acoustics of confined beams*, Sov. Phys. Acoust. **15** (1969), no. 1, 35–40.

[85] R.J. Zemp, J. Tavakkoli, and R.S.C. Cobbold, *Modeling of nonlinear ultrasound propagation in tissue from array transducers*, J. Acoust. Soc. Am. **113** (2003), 139–152.

Samenvatting

Modellering van niet-linear medisch-diagnostisch ultrageluid

In de afgelopen 40 jaar is het gebruik van ultrageluidsgolven uitgegroeid tot een veelzijdige standaard techniek in de medische diagnostiek. Deze techniek, bekend als echografie, is gebaseerd op de opwekking van een hoogfrequent akoestisch veld in het menselijk lichaam en het opvangen van het gereflecteerde veld dat ontstaat op weefselovergangen en lichaamsstructuren. Op basis van de informatie in dit gereflecteerde veld kan een beeld worden opgebouwd van de inwendige organen zoals hart, lever, nieren en milt, of van een foetus in de baarmoeder, en zo kunnen structuren en (dis)functionaliteit van het inwendige op non-invasieve wijze door de clinicus worden onderzocht. Recentelijk hebben een aantal revoluties binnen de echografie plaatsgevonden, waarvan het benutten van de eigenschappen van niet-lineaire akoestische golfpropagatie niet de minste is. Voor de verdere ontwikkeling en optimalisatie van echografie-apparatuur is het van groot belang dat dit niet-lineaire akoestische gedrag goed begrepen wordt en voorspeld kan worden. Het doel van het onderzoek dat in dit proefschrift wordt beschreven, is hiertoe een bijdrage te leveren door het ontwikkelen van een numerieke methode die een nauwkeurige voorspelling levert van het niet-lineaire akoestische veld van een medisch-diagnostische *phased-array* transducent.

Vanuit een mathematisch-fysisch perspectief bekeken vindt de niet-lineaire propagatie zijn oorzaak in het inherent niet-lineair zijn van de akoestische basisvergelijkingen, vanwege veldafhankelijk mediumgedrag. In dit proefschrift wordt aangetoond dat een set van twee veldvergelijkingen en

twee niet-lineaire, constitutieve vergelijkingen onder een aantal realistische aannames resulteert in een tweede-orde akoestische golfvergelijking die bekend staat als de Westervelt vergelijking, waarin verliezen zijn verwaarloosd en waaraan een bronterm is toegevoegd.

Op basis van deze niet-lineaire golfvergelijking is een numerieke methode ontwikkeld die geschikt is voor de simulatie van het niet-lineaire akoestische veld in een grootschalige configuratie in het vier-dimensionale ruimte-tijddomein. De grootte-orde van dit domein is 100 golflengtes c.q. periodes in elke dimensie, uitgaande van de hoogste relevante frequentie in het probleem. In verband met de amplitude van de drukvelden die optreden bij medisch-diagnostische toepassingen, is bij de ontwikkeling van de method uitgegaan van een zwak tot matig niet-lineair gedrag. De methode wordt aangeduid als de Iteratieve Niet-Lineaire Contrastbron methode ofwel de *Iterative Nonlinear Contrast Source* (INCS) methode. Deze methode omvat twee stappen:

- Vanwege de veronderstelde zwakke tot matige niet-lineariteit kan de niet-lineaire term in de Westervelt vergelijking worden beschouwd als een veld-afhankelijke *contrastbron* die een correctieve bijdrage levert op de lineaire veldoplossing. De oplossing van het lineaire veldprobleem levert een eerste schatting van het akoestische veld, waarmee ook een eerste schatting van de contrastbron gemaakt kan worden. Een hernieuwde oplossing van het lineaire veldprobleem met inbegrip van de benaderde contrastbron levert een tweede schatting van het akoestische veld. Herhaald toepassen van dit principe resulteert in een iteratieve Neumann oplossing waarvan we aannemen dat deze convergeert naar het exacte niet-lineaire akoestische veld. In de lineaire stap van de iteratieve Neumann oplossing lossen we een voorwaarts bronprobleem op. Hierbij wordt het akoestische veld verkregen via een convolutie van de primaire bron en de contrastbron enerzijds, en de Greense functie van het gelineariseerde, homogene en verliesvrije achtergrondmedium anderzijds.

- Voor een efficiente numerieke bepaling van de convolutie uit de vorige stap, behandelen we de Greense functie en de bronnen in alle ruimte- en tijddimensies met een ideaal filter en een ideaal venster. Hierdoor is het mogelijk een discretizatie toe te passen van twee punten per golflengte c.q. periode, uitgaande van de hoogste relevante frequentie in het probleem, zonder dat *aliasing* optreedt. Voor de numerieke evaluatie van de discrete convolutie gebruiken we een zogenaamde *Fast Fourier Transform* (FFT) methode. Dit resulteert in een schema dat voor grote aantallen

punten per dimensie bijna een orde lager in complexiteit is dan met een directe evaluatie van de discrete convolutie. De tweede stap van de INCS methode duiden we aan als de Gefilterde Convolutiemethode ofwel de *Filtered Convolution* (FC) methode.

In dit proefschrift laten we vervolgens met behulp van een aantal een-dimensionale en drie-dimensionale simulaties het convergentiegedrag zien van de gepresenteerde methode. Vergeleken met een aantal referentiemethodes blijkt de INCS-methode binnen enkele iteraties een nauwkeurig en stabiel resultaat op te leveren in het geval van zwakke tot matige niet-lineariteit. De simulaties tonen ook de bruikbaarheid van de INCS-methode bij een groot ruimte-tijddomein aan. De methode blijkt ongevoelig voor de richting van het akoestische veld, en geeft een nauwkeurige voorspelling voor de afzonderlijke hogere harmonischen die vanwege het niet-lineaire gedrag in het veld aanwezig zijn. In het geval van sterke niet-lineariteit is de methode eveneens stabiel, maar vergeleken met de resultaten van een aantal andere methodes begint de voorspelling vanaf een bepaalde afstand van de bron af te wijken vanwege de toegepaste filtering.

Naast de vergelijking met andere numerieke methoden, toont ook een beschreven validatie-experiment, waarbij het niet-lineaire akoestische veld van een rechthoekige bron wordt gemeten en vergeleken met de voorspelling van de INCS-methode, aan dat de gesimuleerde resultaten zeer goed overeenkomen met het gemeten veld.

Op grond van de beschreven bevindingen concluderen wij dat de INCS methode een zeer betrouwbaar middel is om het niet-lineaire akoestische veld van medisch-diagnostische *phased-array* transducenten nauwkeurig te voorspellen.

Acknowledgements

Although this PhD. thesis has a single author, I could not claim to be the only actor in its realization. First of all I would like to thank prof. dr. ir. P.M. van den Berg to be my promotor and for his time in discussing, reading and correcting the chapters of this thesis. Thank you for the flexibility and for knowing that the door was always open, despite your busy agenda. My sincerest gratitude goes to the copromotor, dr. ir. M.D. Verweij, who has been my guide and mentor throughout these years. Martin, many thanks for the efforts you have invested in me, and for the discussions, both personal and academic, that were always motivating, helpful and interesting, sometimes intense. You have often inspired me to continue investigating and to take that extra step in my research necessary for having reached the current level. Thanks for your thorough and meticulous correction work in the writing process. If I may think of one word that describes you best in your professional life, then it is 'thoroughness'.

I have enjoyed working at the Laboratory of Electromagnetic Research, and I would like to thank the staff and students for creating a good scientific and pleasant environment and for the interested inquiries on the work. It is good to be with people who understand what you are trying to do and why that takes so much time.

The cooperation with the Experimental Echocardiography Laboratory at the Erasmus Medical Center in Rotterdam has been joyful and inspiring for me. The discussions with Nico de Jong, Jerome Borsboom, Guillaume Matte and Paul van Neer kept my feet in the sometimes muddy practice of developing a new ultrasound transducer. Thank you for the great time spent together at a number of IEEE conferences, and at the lab.

Acknowledgements go to Nicole Ruiter and Michael Zapf of the Forschungszentrum Karlsruhe for their great hospitality and for kindly providing me with the measurement setup for the validation measurements.

Acknowledgements go to Mark Roest of VORtech Computing for his continued interest and for the efforts that he has put into the project and in the parallellisation of the code. My thanks also go to Jasper de Koning who has done a great job in the programming of the parallel code.

I would like to thank Koen van Dongen for setting up the internship at the FZK Karlsruhe. Koen, thanks for providing the rectangular transducer and thanks for your inquisitiveness. Some day you will win one other time in our squash matches.

Joris Koeners, the same goes for me in relation to you... Thanks for sharing the 20th floor gossip and for being such a loyal friend during the recent years.

This thesis is dedicated to the most important persons in my life: to my parents, who have always supported and loved me. I could not thank you enough for that. To Elise, my 'better half'. Thank you for your love and companionship. And to the little character in Fig. 1.1b, whom I hope to get to know a lot better in the future.

It is my deepest wish that this work may be to the greater glory of the creator of this world, God our Father through Jesus Christ our Lord. May your name be exalted in heaven and on earth.

Koos Huijssen
Delft, August 2008

About the author

Koos Huijssen was born in Oud-Beijerland, The Netherlands on April 14, 1976. Starting in 1988, he followed secondary education at the Gereformeerde Scholengemeenschap in Rotterdam, from which he obtained the diploma Gymnasium in 1994. In 1995 he started his study Electrical Engineering at the Delft University of Technology, Delft, The Netherlands. During his studies he performed an internship at the Leiden Universitary Medical Center, Leiden, The Netherlands, on the development of a data acquisition and visualisation program for determining the orientation of all parts of the human body. He earned his Msc. degree in 2003 in Telecommunications. The Msc. thesis concerned the development of a cylindrical model for the propagation of nonlinear acoustic waves from medical phased array transducers, and it was conducted in a joint cooperation between the Laboratory of Electromagnetic Research at the Delft University of Technology and the Experimental Echocardiography Laboratory at the Erasmus Medical Center Rotterdam, Rotterdam, The Netherlands. A conference paper describing the developed model was presented on an international conference in 2003. In 2003 he started his PhD. research at the Laboratory of Electromagnetic Research under the supervision of prof. dr. ir. P.M. van den Berg. The research concerned the development of a three-dimensional model for the simulation of nonlinear acoustic waves from medical phased array transducers, and resulted in a computer code suitable for a large-scale, clustered multiprocessor system. For the validation of the developed method, measurements were performed during a summer internship in 2007 at the Forschungszentrum Karlsruhe, Karlsruhe, Germany. The results of the PhD. research are described in the present thesis. The work was also presented on seven international conferences and published in a number of conference and journal papers.

Publications

- M.D Verweij and J. Huijssen, *A filtered convolution method for the computation of acoustic wave fields in very large spatiotemporal domains*, submitted to J. Acoust. Soc. Am., July 2008.

- M.D. Verweij and J. Huijssen, *Performance study of the Iterative Nonlinear Contrast Source method*, Proc. Int. Symp. Nonl. Ac. 18, Stockholm, 2008, pp. 77–80.

- J. Huijssen, M.D. Verweij and N. de Jong, *Comparison of an angular spectrum method and a Green's function method for nonlinear propagation of pulsed acoustic fields from medical phased array transducers*, Proc. IEEE Int. Ultrasonics Symp. 2007, New York, 2007, pp. 1740–1743.

- J. Huijssen and M.D. Verweij, *3D time-domain modeling of nonlinear medical ultrasound with a contrast source method: behavior of the contrast sources*, Proc. Int. Cong. Acoustics 19, Madrid, 2007.

- J. Huijssen, M.D. Verweij and N. de Jong, *3D time-domain modeling of nonlinear medical ultrasound wit an iterative Green's function method*, Proc. IEEE Int. Ultrasonics Symp. 2006, Vancouver, 2006, pp. 2124–2127.

- J. Huijssen and M.D. Verweij, *Numerical solution of nonlinear acoustic wave problems employing a Green's function approach*, Proc. Eccomas CFD 2006, Egmond aan Zee, 2006.

- J. Huijssen and M.D. Verweij, *Iterative numerical solution of nonlinear wave problems*, Proc. Int. Cong. on Sound and Vibration 13, Vienna, 2006.

- J. Huijssen and M.D. Verweij, *Nonlinear constitutive equations derived for fluids obeying an ideal gas, a Tait-Kirkwood or a B/A type equation of state*, Proc. Int. Symp. Nonl. Ac. 17, State College, 2005, pp. 552–555.

- M.D. Verweij and J. Huijssen, *Nonlinear and dissipative constitutive equations for coupled first-order acoustic field equations that are consistent with the generalized Westervelt equation*, Proc. Int. Symp. Nonl. Ac. 17, State College, 2005, pp. 241–244.

- J. Huijssen, A. Bouakaz, M.D. Verweij and N. de Jong,, *Simulations of the nonlinear acoustic pressure field without using the parabolic approximation*, Proc. IEEE Int. Ultrasonics Symp. 2003, Honolulu, 2003, pp. 1851–1854.